Terrestrial biosphere exchange of oxygen and carbon dioxide

Kim Faassen

Propositions

1. Studying the O_2 budget requires representing photosynthesis and respiration separately rather than only considering their net flux.
   (this thesis)

2. Diurnal scale O_2:CO_2 ratios based on atmospheric measurements have up to now been misinterpreted.
   (this thesis)

3. Specializing in a single research topic slows scientific progress.

4. By always using climate change to justify carbon cycle research topics, the value of fundamental research is overlooked.

5. Applauding women for their gender overlooks their achievements.

6. The high number of complaints about Dutch public transport says more about the Dutch people than about the public transport itself.

7. You can only form an opinion about Carnival if you have experienced it yourself.

Propositions belonging to the thesis, entitled
Terrestrial biosphere exchange of oxygen and carbon dioxide

Kim Faassen
Wageningen, 8 July 2025

Terrestrial biosphere exchange of oxygen and carbon dioxide

Kim Faassen

Thesis committee

Promotors
Prof Dr Wouter Peters
Professor in Air Quality and Atmospheric Chemistry
Wageningen University & Research

Prof Dr Jordi Vilà-Guerau de Arellano
Professor of Meteorology
Wageningen University & Research

Co-promotors
Dr Ingrid T. Luijkx
Associate Professor, Meteorology and Air Quality
Wageningen University & Research

Other members
Prof. Dr J.B. Evers, Wageningen University & Research
Dr B.B. Stephens, National Center for Atmospheric Research, USA
Dr habil. C. Gerbig, Max Planck Institute for Biogeochemistry, Germany
Dr S. N. Vardag, Heidelberg University, Germany

This research was conducted under the auspices of the Graduate School for Socio-Economic and Natural Sciences of the Environment (SENSE)

Terrestrial biosphere exchange of oxygen and carbon dioxide

Kim Faassen

Thesis
submitted in fulfilment of the requirements for the degree of doctor
at Wageningen University
by the authority of the Rector Magnificus
Prof. Dr C. Kroeze,
in the presence of the
Thesis Committee appointed by the Academic Board
to be defended in public
on Tuesday 8 July 2025
at 3:30 p.m. in the Omnia Auditorium.

Kim Faassen
Terrestrial biosphere exchange of oxygen and carbon dioxide
XV+231 pages.

PhD thesis, Wageningen University, Wageningen, The Netherlands (2025)
With references, with summary in English and Dutch

DOI 10.18174/681504

Summary

To understand the processes driving trends and variability in atmospheric carbon dioxide (CO_2) levels, it is essential to disentangle this CO_2 signal into the sources and sinks that contribute to it. Global CO_2 levels are influenced by fossil fuel emissions, land-use change, biosphere exchange, and ocean exchange. However, measuring atmospheric CO_2 alone does not allow to distinguish between these contributing processes and additional information is required. Carbon cycle tracers play a key role in providing these extra constraints. Atmospheric oxygen (O_2), is of particular importance as it is inherently linked to CO_2 in carbon cycle processes and therefore offers valuable insights into the carbon cycle at different scales.

In this thesis, we study this link between O_2 and CO_2. This relationship can be quantified using the exchange ratio (ER), which represents the number of moles of O_2 exchanged per mole of CO_2. Each process that links O_2 and CO_2 has a specific ER value, which can be applied across different spatial and temporal scales to improve our understanding of the carbon cycle. On the global scale, the ER of fossil fuel combustion is based on the composition of the fossil fuels that are combusted, and the ER is on average 1.38 ± 0.03. The ER of biosphere exchange is assumed to be 1.1 ± 0.1. These values are used to partition the global carbon sinks into the contributions from the terrestrial biosphere and oceans. However, scarcely available local measurements indicate that the ER of the biosphere might deviate from this value and is not constant but varies across time and space. The ER of the net exchange of the biosphere (ER_{net}) is formed by two larger fluxes: gross primary productivity (GPP) and total ecosystem respiration (TER), each with their individual ER values (ER_a and ER_r respectively). These individual ER values can be used to improve the partitioning of net ecosystem exchange (NEE) into GPP and TER fluxes, a key open question in our field.

This thesis aims to enhance our understanding of how to quantify and apply the O_2:CO_2 ratio of the terrestrial biosphere. Due to the limited availability of observations that simultaneously measure O_2 and CO_2 above vegetation, it remains challenging to assess the validity of assuming a constant ER_{net} value of 1.1 and to determine the drivers of its spatiotemporal variability. Furthermore, there is no clear understanding of how to quantify ER_{net}. Some studies use atmospheric mole fractions of O_2 and CO_2 to determine ER_{net}

(in that case called $\mathrm{ER}_{\mathrm{atmos}}$), while others analyze O_2 and CO_2 surface fluxes based on vertical gradients that directly represent $\mathrm{ER}_{\mathrm{net}}$. Also, elemental composition of vegetation and soils is used to derive O_2:CO_2 ratios (in that case called the Oxidative Ratio, OR). Where observational data are lacking, modeling approaches can bridge the gap between different spatial and temporal scales. However, O_2 had not yet been incorporated in biosphere models to simulate both net O_2 and CO_2 exchange, limiting the interpretation of observational data and understanding of differences between site-specific $\mathrm{ER}_{\mathrm{net}}$ values to the global average value of 1.1. In this thesis, we address these gaps by integrating data from new field campaigns with biosphere and atmospheric models that include O_2, thereby improving our understanding of biospheric O_2 exchange. Ultimately, this understanding can contribute to more widespread use of O_2 to detect and attribute changes in carbon cycle fluxes and reservoirs.

Chapter 2 introduces the measurement techniques and models used throughout this thesis. We present O_2 observations from three new field campaigns conducted in boreal (Hyytiälä, Finland), temperate (Loobos, the Netherlands) and tropical (Amazon, Brazil) forests. In this chapter, we explain the details of the calibration procedures required to obtain continuous measurements from a fuel cell analyzer (Hyytiälä campaign) and flask samples (Loobos campaign). This thesis integrates these measurements with three modeling approaches: (1) the one-box CLASS model, which simulates atmospheric mixing in the boundary layer on a diurnal timescale coupled to the conditions of the three ecosystems; (2) the SiB4 biosphere model, which simulates biospheric fluxes based on carbon pools and plant functional types over multiple years for the whole globe; and (3) the STILT Lagrangian transport model. We have implemented O_2 into each of these three models to generate both atmospheric and surface O_2 and CO_2 flux signals.

Chapter 3 presents an in-depth analysis of our O_2 and CO_2 observations from the Hyytiälä field campaign conducted during the spring and summer of 2018 and 2019. During this campaign we collected continuous O_2 and CO_2 measurements at two heights above the canopy. We determine the best method to infer O_2 and CO_2 surface fluxes from the vertical gradient to calculate the $\mathrm{ER}_{\mathrm{net}}$, ER_{a} and ER_{r}. The results revealed a distinct diurnal cycle in $\mathrm{ER}_{\mathrm{net}}$, with higher values at night and lower values during the day. We then apply the obtained ER values to partition daily NEE into GPP and TER, demonstrating that the O_2-based partitioning method produced results comparable to traditional temperature-based approaches using eddy-covariance.

Chapter 4 evaluates the O_2:CO_2 ratio based on single-height measurements from our Hyytiälä campaign, by combining these observations with the CLASS model. In Chapter 3, we already found that O_2:CO_2 ratios vary significantly depending on whether they are derived from vertical gradients ($\mathrm{ER}_{\mathrm{net}}$) or temporal changes in atmospheric mole fractions ($\mathrm{ER}_{\mathrm{atmos}}$). We use our model to disentangle the $\mathrm{ER}_{\mathrm{atmos}}$ signal and demonstrate why single-height measurements are not suitable to represent surface processes. The results of our CLASS model show that the entrainment of air from the free troposphere into the boundary layer significantly influences the diurnal cycles of atmospheric O_2 and CO_2 mole fractions. Since entrainment is not a coupled O_2 and CO_2 exchange process, it lacks a distinct ER signature which complicates the interpretation of ER_{atmos}. We show that ER_{atmos} only approaches ER_{net} when entrainment become negligible, for example in the late afternoon.

Chapter 5 extends the analysis of Chapters 3 and 4 to other ecosystems by investigating which processes shape the diurnal range of carbon cycle tracers (CO_2, O_2 and $\delta^{13}C$) in temperate (Loobos) and tropical (Amazon) forests. We collected new observations at multiple heights from these locations and combined them with the CLASS model to simulate diurnal cycles for each site. We use these new vertical profile measurements to confirm the conclusion from Chapter 4, that entrainment is a dominant factor in shaping the diurnal range of all carbon cycle tracers. Furthermore, we show that other atmospheric processes, such as subsidence and cloud ventilation, also play a significant role in shaping the diurnal cycles of the carbon cycle tracers. These findings underscore the difficulty of directly linking diurnal variations in carbon cycle tracers to surface exchange processes. We introduce the diurnal range as a metric to evaluate atmospheric transport models as well as trends in long-term atmospheric measurements.

Chapter 6 shifts the focus from short-term diurnal variations to the global spatial scale and temporal variability of ER_{net} over an annual cycle. We incorporate O_2 into the SiB4 biosphere model by applying observation-based estimates for ER_a and ER_r to assimilation and respiration fluxes from carbon pools of different plant functional types. This allowed us to for the first time simulate global biospheric O_2 fluxes with a biosphere model. The resulting ER_{net} values show a clear seasonal and spatial variability, driven by variations in ER_a, ER_r and the ratio between GPP and TER. Consequently, the resulting ER_{net} is not linked anymore to a single biological process, making it difficult to interpret this signal. We subsequently transport the modeled O_2 and CO_2 net biosphere fluxes with the STILT model to assess their impact on atmospheric signals at two stations, Weybourne in the UK and Bialystok in Poland. Our findings suggest that regional variations in ER_{net} can substantially affect O_2 partitioning methods used to estimate changes in fossil fuel CO_2 emissions, especially in areas where the signals are strongly influenced by the biosphere.

Finally, **Chapter 7** synthesizes the key findings of chapters in this thesis, puts them into further context and identifies remaining research gaps. We highlight two major areas for further investigation: (1) the need for additional measurements to better characterize the different definitions and physical interpretations of the O_2:CO_2 exchange of the biosphere and (2) the importance of improving our ability to connect biosphere O_2:CO_2 ratios defined at different spatial and temporal scales. Additionally, we combine our findings about

measurements provided throughout the thesis into a comprehensive list of recommendations for future measurement campaign strategies.

This thesis advances the understanding of the O_2:CO_2 exchange ratio from the terrestrial biosphere. We provide insights and recommendations on how to quantify this ratio and explore its spatial and temporal variability. By combining observations with modeling approaches, we explain the processes that govern O_2:CO_2 ratios and establish links between different temporal and spatial scales. By enhancing our understanding of biospheric O_2 and CO_2 fluxes, we refined O_2 partitioning methods and improved their application for carbon budget assessments from ecosystem to global scales. This opens the door for further application of atmospheric O_2 to constrain the terrestrial biosphere and ocean carbon sinks and to facilitate fossil fuel emissions verification.

Samenvatting

Om beter te begrijpen waar de variaties in koolstofdioxide (CO_2) in de atmosfeer vandaan komen, is het belangrijk om dit signaal te ontleden en de verschillende bronnen te onderscheiden die eraan bijdragen. De CO_2 waardes in de atmosfeer worden beïnvloed door meerdere processen: uitstoot door de verbranding van fossiele brandstoffen, veranderingen in landgebruik, opname en uitstoot door de biosfeer (zoals vegetatie en bodems), en opname door de oceanen. Wanneer we alleen CO_2 meten, worden al deze signalen samengevoegd, waardoor het lastig is om ze uit elkaar te houden. We hebben daarom extra informatie nodig om het CO_2-signaal goed te kunnen interpreteren. Zogeheten koolstoftracers kunnen hierbij helpen. Een voorbeeld van zo'n tracer is atmosferische zuurstof (O_2), omdat O_2 aan CO_2 is gekoppeld in bepaalde processen. Daardoor kan O_2 waardevolle aanvullende informatie bieden over het koolstofbudget van de aarde.

In deze thesis onderzoeken we hoe O_2 en CO_2 met elkaar samenhangen. Die relatie wordt vaak uitgedrukt met een zogeheten uitwisselingsratio (*Exchange Ratio: ER*): de verhouding tussen het aantal O_2-moleculen dat uitgewisseld wordt voor elk CO_2-molecuul. Zo is er bijvoorbeeld O_2 nodig om fossiele brandstoffen te verbranden, waarbij tegelijkertijd CO_2 vrijkomt. De precieze verhouding hangt af van het type brandstof, maar gemiddeld wordt aangenomen dat er 1,38 O_2-moleculen nodig zijn voor elk CO_2-molecuul dat vrijkomt (ER = 1,38). Bij processen in de biosfeer, zoals respiratie en fotosynthese, zien we een andere verhouding. Tijdens respiratie neemt de biosfeer O_2 op en stoot CO_2 uit, terwijl tijdens fotosynthese juist CO_2 wordt opgenomen en O_2 wordt uitgestoten. Gemiddeld genomen geldt hier een constante ER van ongeveer 1,1. De oceaan speelt ook een rol in de koolstofcyclus, maar bij de uitwisseling met de oceaan zijn CO_2 en O_2 niet gekoppeld. Dat maakt de specifieke ER-waarden van fossiele brandstoffen en biosfeerprocessen extra waardevol voor het beter interpreteren van het atmosferische CO_2-signaal. Hiervoor moeten O_2-metingen gelijktijdig met CO_2-metingen worden uitgevoerd.

Uit veldmetingen blijkt echter dat de ER van de biosfeer niet altijd constant is. Deze kan variëren afhankelijk van bijvoorbeeld het type vegetatie, bodemsoort en het seizoen. Omdat er wereldwijd nog maar weinig O_2-metingen zijn gedaan, weten we nog weinig over de oorzaken van deze variaties. Het doel van dit proefschrift is daarom om beter inzicht te krijgen in de O_2:CO_2 verhouding van biosferische uitwisseling en deze nauwkeuriger te kwantificeren. Hiervoor gebruiken we nieuwe O_2-metingen uit veldcampagnes, gecombineerd met atmosferische modellen waarin O_2-uitwisseling is meegenomen. Zo proberen we beter te begrijpen hoe de biosfeer bijdraagt aan het O_2-signaal.

Hoofdstuk 2 beschrijft de meetmethodes en modellen die we in deze thesis gebruiken.We presenteren nieuwe O_2-metingen uit drie veldcampagnes, uitgevoerd in een boreaal bos (Hyytiälä, Finland), een gematigd bos (Loobos, Nederland) en een tropisch bos (Amazoneregenwoud, Brazilië). Ook leggen we uit hoe we de metingen hebben gekalibreerd, vooral voor Hyytiälä en Loobos. De metingen worden gecombineerd met drie modellen: (1) het CLASS model, dat de atmosfeer over 1 dag en voor 1 plek simuleert; (2) het SiB4 model, dat biosfeerprocessen wereldwijd simuleert op basis van verschillende vegetatietypen; en (3) het STILT transport model, dat atmosferisch transport van CO_2 (en nu ook O_2) van de meetlocatie naar de bron terugrekent. We hebben O_2 in alle drie de modellen geïmplementeerd zodat O_2- en CO_2-signalen gelijktijdig kunnen worden gesimuleerd.

Hoofdstuk 3 gaat in op de Hyytiälä-campagne in een boreaal bos in Finland. Hier hebben we O_2 en CO_2 gemeten op twee hoogtes boven het bos. Daarmee konden we verschillende ER-waarden berekenen, waaronder de netto ER (ER_{net}). We zagen een duidelijk dagelijks patroon: hogere ER_{net}-waarden 's nachts en lagere overdag. Deze dagelijkse gang laat duidelijk zien dat de ER waarde op een korte tijdschaal geen constant getal is.

Hoofdstuk 4 analyseert de ER op basis van slechts één meethoogte in Hyytiälä, in tegenstelling tot de twee hoogtes in Hoofdstuk 3. Met het CLASS-model laten we zien dat deze 'één-hoogte ER' (ER_{atmos}) minder geschikt is om biosferische processen te beschrijven, omdat atmosferische menging en andere processen het signaal beïnvloeden. Die processen verstoren de directe koppeling tussen O_2 en CO_2, wat de interpretatie van ER_{atmos} bemoeilijkt. Hiermee laten we zien dat altijd ER_{net} gebruikt moet worden om de ER van de biosfeer aan te geven.

Hoofdstuk 5 breidt de analyse van Hoofdstuk 4 uit naar de gematigde en tropische bossen (Loobos en Amazone). Ook hier combineren we veldmetingen met het CLASS-model. De unieke verticale profielmetingen bevestigen dat atmosferische processen een dominante invloed hebben op de dagelijkse variatie in koolstoftracers. Het model helpt om die atmosferische effecten te kwantificeren en laat zien hoe complex het is om atmosferische signalen direct te koppelen aan processen aan het aardoppervlak.

In **Hoofdstuk 6** verschuiven we de focus van lokale, dagelijkse variaties naar wereldwijde en seizoensgebonden schaal. Hiervoor hebben we O_2 toegevoegd aan het biosfeermodel SiB4. Voor het eerst kunnen we nu wereldwijd de biosferische O_2-uitwisseling simuleren. Het resulterende ER_{net}-signaal laat duidelijke seizoenspatronen zien. Dit komt omdat ER_{net} wordt gevormd door een combinatie van de individuele ER signalen van respiratie en fotosynthese. Daarna gebruiken we het STILT-model om deze uitwisselingen door te rekenen naar twee meetstations. De resultaten laten zien dat regionale verschillen in ER_{net} grote invloed kunnen hebben op schattingen van fossiele CO_2-emissies wanneer gebruik wordt gemaakt van de O_2-methode. Het is daarom belangrijk om rekening te houden met de variaties van de biosfeer ER signalen.

In **Hoofdstuk 7** vatten we de belangrijkste bevindingen samen en schetsen we richtingen voor toekomstig onderzoek. We benadrukken twee grote onderzoeksgebieden die nog verder onderzoek vereisen: (1) er zijn meer metingen nodig om de verschillende O_2:CO_2 ratio's van de biosfeer beter te begrijpen en (2) het is belangrijk dat we de verschillende O_2:CO_2 ratio's beter kunnen verbinden op verschillende tijd- en ruimteschalen.

Deze thesis laat zien hoe het combineren van observaties en modellen leidt tot een beter begrip van de O_2:CO_2-verhouding in de biosfeer. We bieden handvatten voor hoe deze ratio beter gekwantificeerd kan worden, en leggen uit hoe variaties in tijd en ruimte ontstaan. Met deze inzichten kunnen we de O_2-methode verbeteren om het CO_2-signaal in de atmosfeer beter te duiden en zo preciezer te achterhalen welke processen bijdragen aan veranderingen in de atmosfeer.

Contents

Chapter 1

Introduction

1.1 Global carbon cycle

The variations in atmospheric carbon dioxide (CO_2) mole fractions result from different sources and sinks, collectively known as the carbon cycle (Figure 1.1). The primary sources of CO_2 include fossil fuel combustion and land-use changes, which together emit approximately 10.9 PgC/year to the atmosphere over the decade 2013-2022 (Friedlingstein et al., 2023). However, not all emitted CO_2 remains in the atmosphere. Approximately 25% is taken up by the terrestrial biosphere (3.3 PgC/year), while another 25% is taken up by the ocean (2.8 PgC/year). The remaining CO_2 (5.2 PgC/year) accumulates in the atmosphere (Friedlingstein et al., 2023).

The imbalance between sources and sinks in the carbon cycle has led to an increase in atmospheric CO_2 mole fractions, which drives climate change. Since the start of the industrial revolution, atmospheric CO_2 levels have risen by approximately 51%, contributing, along with other greenhouse gases, to a global temperature increase of 1.1°C compared to the pre-industrial temperature (Friedlingstein et al., 2023; Forster et al., 2023; Jones et al., 2023). Rising global temperatures have severe consequences, including more frequent and intense droughts, sea-level rise, and other climate-related impacts (e.g. Seneviratne et al., 2021). Understanding the individual processes contributing to the increase in CO_2 mole fractions is therefore critical to address and mitigate climate change.

The main driver of the increasing atmospheric CO_2 mole fraction is fossil fuel combustion. This process oxidizes carbon-containing compounds, releasing CO_2 into the atmosphere. As shown in Figure 1.1, fossil fuel combustion is the largest annual source of CO_2 emissions, yet it has a relatively small associated uncertainty of 0.5 PgC/year. Emissions from fossil fuel combustion are estimated using bookkeeping methods, which rely on detailed national inventories of fuel usage and emission factors (Andrew, 2020). The amount of bottom-up data available results in a relatively lower uncertainty in the fossil fuel emissions compared to other components of the global carbon budget.

In contrast to fossil fuel emissions, both ocean and terrestrial biosphere uptake have relatively high uncertainties in their sink estimations, compared to the size of the signals. The ocean continuously exchanges CO_2 with the atmosphere as CO_2 dissolves into seawater and gets released again. Once dissolved, CO_2 can be taken up by plankton or react with H_2O. The reaction of CO_2 with H_2O, forming dissolved inorganic carbon, is the largest carbon pool in the global carbon cycle (Figure 1.1). When CO_2 reacts with H_2O it attains a chemical equilibrium with inorganic bicarbonate ions and carbonates. Note however that the slow shift of this chemical equilibrium due to more and more anthropogenic carbon entering the oceans also lowers ocean pH (Haugan and Drange, 1996; Bopp et al., 2013) and dissolves shells and corals made from calcium carbonate (e.g. Bibby et al., 2007; McClintock et al., 2009; Heinze et al., 2015). This destructive effect of our fossil

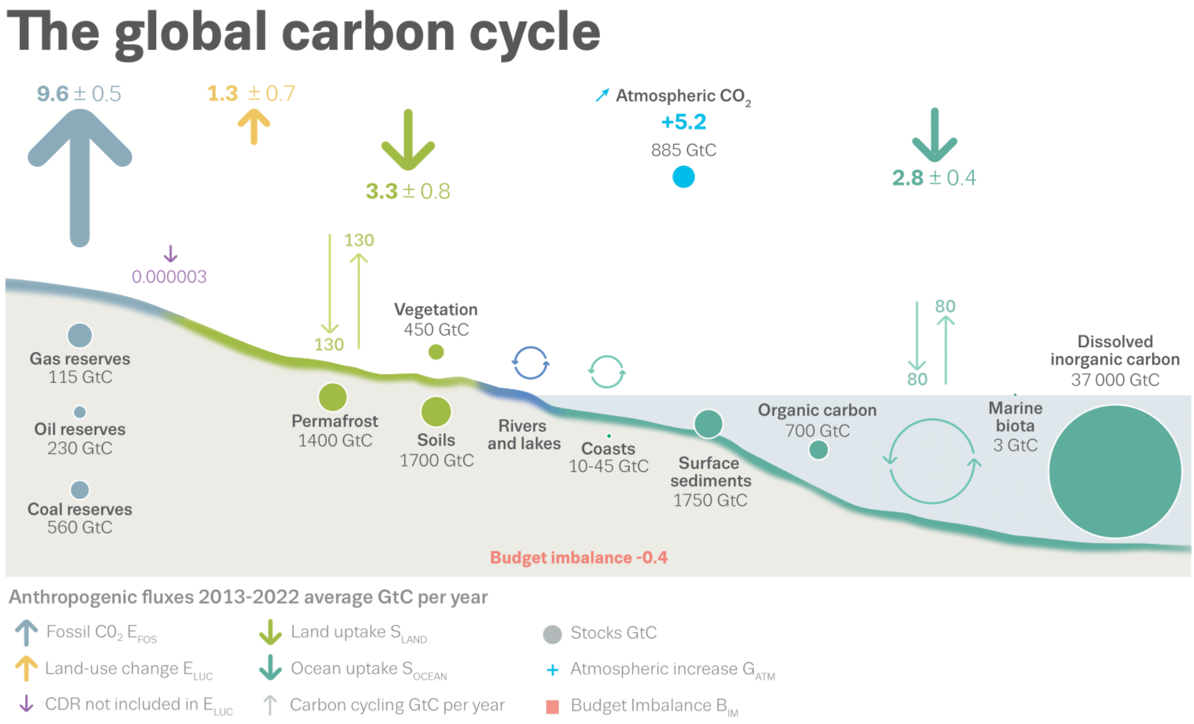

Figure 1.1: Visualization of the different components of the carbon budget between 2013-2022 as shown in Friedlingstein et al. (2023). The arrows indicate the exchange between the surface and the atmosphere and the circles indicate the carbon reservoirs. In this thesis we focus on the terrestrial biosphere exchange (green arrows).

emissions is often overlooked when purely focusing on carbon sinks and climate change. Ocean CO_2 uptake is calculated using global ocean biogeochemical models (GOBMs) and data-based pCO_2 mapping methods, but discrepancies arise between different models as well as between model predictions and observation-based approaches (Hauck et al., 2020). These inconsistencies contribute to the relatively high uncertainty in estimating the ocean's role as a carbon sink.

The land carbon uptake has the highest uncertainty in the global carbon cycle (Figure 1.1). Dynamic global vegetation models (DGVMs) are commonly used to calculate the land uptake, but these models face significant challenges (Sitch et al., 2024). These challenges arise from the high temporal and spatial variability of land carbon uptake, driven by diverse ecosystem responses, past and present land-management by humans, seasonal differences in carbon exchange, and the impacts of past and present extreme meteorological events. As a result, further investigation is crucial to better understand and quantify terrestrial biosphere CO_2 uptake. Therefore, this thesis focuses on the terrestrial biosphere carbon exchange.

1.2 Terrestrial carbon cycle

The biosphere takes up CO_2 through the process of photosynthesis, which is also called assimilation. During photosynthesis, CO_2 and water (H_2O) are converted using sunlight into sugars (glucose; $C_6H_{12}O_6$) and oxygen (O_2) according to the following equation:

$$6CO_2 + 6H_2O \leftrightarrow C_6H_{12}O_6 + 6O_2 \tag{1.1}$$

This reaction is the cornerstone of energy capture for plants, providing them with glucose as a source of chemical energy and producing oxygen as a byproduct. The reaction can also proceed in reverse when plants require energy, in a process known as respiration. During respiration, glucose and oxygen are broken down to release energy, forming carbon dioxide and water. Respiration does not depend on light and occurs continuously when the plant is metabolically active.

As a result, the net CO_2 uptake by the terrestrial biosphere is a balance of two key processes: photosynthesis (also known as Gross Primary Productivity, GPP) and respiration (also known as Total Ecosystem Respiration, TER). This net exchange is represented as:

$$NEE = -GPP + TER \tag{1.2}$$

Where NEE (net ecosystem exchange) is the net flux of CO_2 between the ecosystem and the atmosphere. GPP encompasses the assimilation of CO_2 by plants during photosynthesis. The rate of GPP is influenced by several factors, including light availability, water vapor pressure deficit, temperature, soil moisture, and atmospheric CO_2 concentration (e.g. Farquhar et al., 1980; Von Caemmerer and Farquhar, 1981a; Kaiser et al., 2015; Kaiser et al., 2017). These variables dictate how efficiently plants can capture and use carbon dioxide for growth and energy storage.

TER consists of both autotrophic and heterotrophic respiration processes. Autotrophic respiration originates from vegetation, including leaves, stems and roots. During this process, plants burn sugars produced through photosynthesis to generate the energy required for metabolic activities. In contrast, heterotrophic respiration is driven by microorganisms in the soil that decompose organic carbon pools. These carbon pools can include litter or soil organic matter. While autotrophic respiration primarily relies on recently synthesized sugars, heterotrophic respiration involves the breakdown of carbon pools that were formed over much longer time spans. The rate of TER depends on several factors, such as soil temperature, soil moisture and the size of the different carbon pools (e.g. Kirschbaum, 1995; Ryan and Law, 2005; Curiel Yuste et al., 2007).

NEE can be measured using an Eddy Covariance (EC) system placed above the canopy of the vegetation. An EC system operates at a high frequency (e.g. 10 Hz), capturing turbulent fluctuations in both the vertical or horizontal wind speed and the mole fractions of CO_2. Using the covariance between these two variables, the turbulent flux of CO_2 is determined, providing a direct measure of the net exchange of CO_2 between the ecosystem and the atmosphere (Baldocchi, 2003).

GPP and TER cannot be directly determined from EC NEE measurements alone. Instead, they have to be calculated using indirect methods. Two widely-used approaches are the temperature-based function developed by Reichstein et al. (2005) and the light-based function by Lasslop et al. (2010). The temperature-based method calculates TER using night-time EC measurements of CO_2 and air temperature, with the assumption that GPP is zero during the night. The light-based method splits NEE into GPP and TER by analyzing day-time EC measurements of CO_2 and identifying a hyperbolic relationship with light intensity, which incorporates the effect of water vapor pressure deficit.

The dependency of both methods on meteorological variables and processes, creates uncertainties in partitioning NEE into its gross components (Lasslop et al., 2010). This emphasizes the need for approaches that are independent of meteorological variables and more directly linked to the underlying processes driving the gross fluxes. Various carbon cycle tracers (e.g. carbonyl sulfide, $\delta^{13}C$ offer promising alternative by providing a more direct connection to these processes (Wehr et al., 2016; Whelan et al., 2018; Peters et al., 2018; Koren et al., 2019; Kooijmans et al., 2021). One such tracer is the ratio between O_2 and CO_2 exchange. The advantage of using O_2 is that is directly coupled to CO_2 in respiration and photosynthesis (Equation 1.1).

1.3 Atmospheric O_2

The mole fraction of atmospheric O_2 in dry air in the year 2000 was approximately 209,392 ± 3 parts per million (ppm), or 20.9% (Tohjima et al., 2005). Despite this large background value, changes in atmospheric O_2 happen at ppm level and can be directly linked to opposite changes in atmospheric CO_2. Figure 1.2a illustrates this anti-correlated behavior between O_2 and CO_2, based on atmospheric flask measurements at Mauna Loa (Keeling, 2024). Over this 35-year period, the atmospheric CO_2 mole fraction increases due to fossil fuel combustion and land use change and has a distinct season cycle following from the exchange with the biosphere: higher CO_2 mole fractions occur during the northern hemisphere winter (when TER $>$ GPP) and lower mole fractions occur in summer (when GPP $>$ TER). The O_2 measurements exhibit the opposite pattern, with a decline over time, lower mole fractions in the winter, and higher mole fractions in the summer.

The anti-correlation of atmospheric O_2 and CO_2 can be explained by their connection through several sources and sinks of CO_2 (Figure 1.2b). In the biosphere, this connection is established by photosynthesis and respiration (Equation 1.1). During photosynthesis, CO_2 is consumed and O_2 is produced, whereas during respiration O_2 is consumed and CO_2 is produced. This exchange between the biosphere and the atmosphere drives the seasonal variations observed in Figure 1.2a. Fossil fuel combustion also couples O_2 and

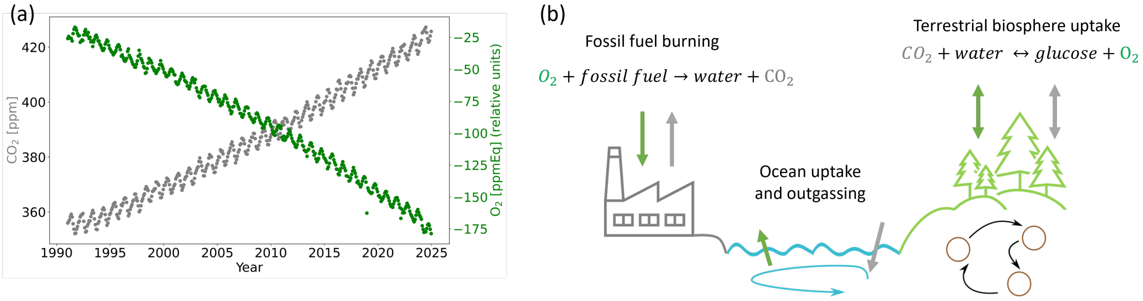

Figure 1.2: Measured O_2 and CO_2 signals at Mauna Loa, obtained through flask measurements by the Scripps Institution of Oceanography (SIO) (Keeling, 2024) (a) and the different components that influence the global budgets of O_2 and CO_2 (b). The green arrows represent O_2 exchange and the grey arrows represent CO_2 exchange. Chapter 2 elaborates on the ppmEq units used to indicate the amount of O_2.

CO_2. When fossil fuels containing carbon are burned, O_2 is consumed and CO_2 is emitted. This process contributes to the observed decrease in atmospheric O_2 mole fractions over time.

For ocean-atmosphere exchange, O_2 and CO_2 exchange processes are decoupled. Within the water, O_2 and CO_2 can be linked through the processes photosynthesis and respiration carried out by plankton. However, the ocean outgassing of O_2 is primarily determined by temperature and therefore occurs independent of CO_2 exchange. Additionally, dissolved CO_2 can react with H_2O to form bicarbonate ions and calcium carbonates in a chemical equilibrium. These reactions do not involve O_2, thereby decoupling the relationship between the two gases in the ocean-atmosphere exchange (Keeling and Shertz, 1992; Keeling and Manning, 2014).

1.4 Measuring atmospheric O_2

Measuring atmospheric O_2 is challenging due to its large background value (209,392 ppm in dry air (Tohjima et al., 2005)) and the relatively small changes that are on the same order of magnitude as CO_2, ranging from approximately 1 to 40 ppm. Capturing these changes requires detecting variations as small as 1/209,392 or 0.0005%. This level of precision is significantly higher than what is needed for CO_2 measurements, where changes occur against a background of around 400 ppm, requiring a precision of 1/400, or 0.25%. In most studies where the link between atmospheric O_2 and CO_2 is evaluated, highly precise O_2 measurements are essential. To achieve the required precision, a specialized approach is used for reporting these measurements.

Atmospheric O_2 concentrations are typically expressed relative to nitrogen (N_2) and compared to a reference value, as defined by (Keeling and Shertz, 1992):

$$\delta(O_2/N_2) = \left(\frac{(O_2/N_2)_{\text{sample}}}{(O_2/N_2)_{\text{reference}}} - 1 \right) \cdot 10^6 \text{ [per meg]} \tag{1.3}$$

Where $(O_2/N_2)_{\text{sample}}$ is the ratio of O_2 to N_2 in the atmospheric sample being measured and $(O_2/N_2)_{\text{reference}}$ is the reference value, as first determined in 1980 by the Scripps Institution of Oceanography (Keeling, 1988; Keeling et al., 2007). It is assumed that $\delta(O_2/N_2)$ primarily reflects changes in O_2, because atmospheric N_2 is less variable than O_2 (Keeling and Shertz, 1992). By measuring O_2 relative to N_2, it becomes possible to detect small changes in O_2 abundance. $\delta(O_2/N_2)$ values are multiplied by 10^6 and expressed in per meg. Chapter 2 provides a more elaborate explanation about the per meg 'units' and how to relate them to CO_2 values expressed in ppm. The current $\delta(O_2/N_2)$ values are negative (Figure 1.2) because atmospheric O_2 mole fractions are lower than the reference value of 1980.

The study by Benedict (1912) was the first to report atmospheric O_2 mole fractions over time, indicating that they remained constant within their measurement precision of 60 ppm. A follow-up study by Machta and Hughes (1970) reaffirmed this finding, showing that the atmospheric O_2 mole fraction could be consistently measured at 20.946% with a similar measurement precision of 60 ppm. However, due to limitations in measurement precision, both studies did not detect the expected decrease in O_2 caused by fossil fuel combustion. Keeling (1988) significantly improved the measurement precision to 1 ppm, using an interferometric technique, enabling Keeling and Shertz (1992) to be the first to report long-term changes in atmospheric O_2 mole fractions. Their work revealed a seasonal cycle and a measurable decline over time. Subsequently, Bender et al. (1994) showed that a mass spectrometer could replicate these patterns and Tohjima (2000) introduced the use of gas chromatography for O_2 measurements, further advancing the field. However, these measurement techniques were not able to perform measurements continuously, instead relying on samples of air to be taken to the laboratory.

Continuous measurement techniques are essential to capture detailed variations in atmospheric O_2 across both time and space. With this goal in mind, Stephens (1999) and Stephens et al. (2003) developed a vacuum ultraviolet (VUV) absorption technique to measure O_2. This method detects changes in O_2 by measuring absorption in the vacuum ultraviolet spectrum, achieving a measurement precision of 6 per meg for 10-second intervals. This technology was further improved by Stephens et al. (2021), reaching a precision of 1.25 per meg for 5-second measurements in stationary conditions. Another continuous measurement technique involves the use of fuel cells. These devices contain a lead cell and an acid electrolyte, which react with O_2 to produce a current proportional to the O_2 mole fraction (see also Chapter 2). Several studies have developed fuel cell-based measurements, achieving a measurement precision of approximately 5 per meg (Stephens et al., 2007;

Thompson et al., 2007; Kozlova and Manning, 2009; Van der Laan-Luijkx et al., 2010; Popa et al., 2010; Ishidoya et al., 2013; Battle et al., 2019).

1.5 Application of O_2 on the large scale

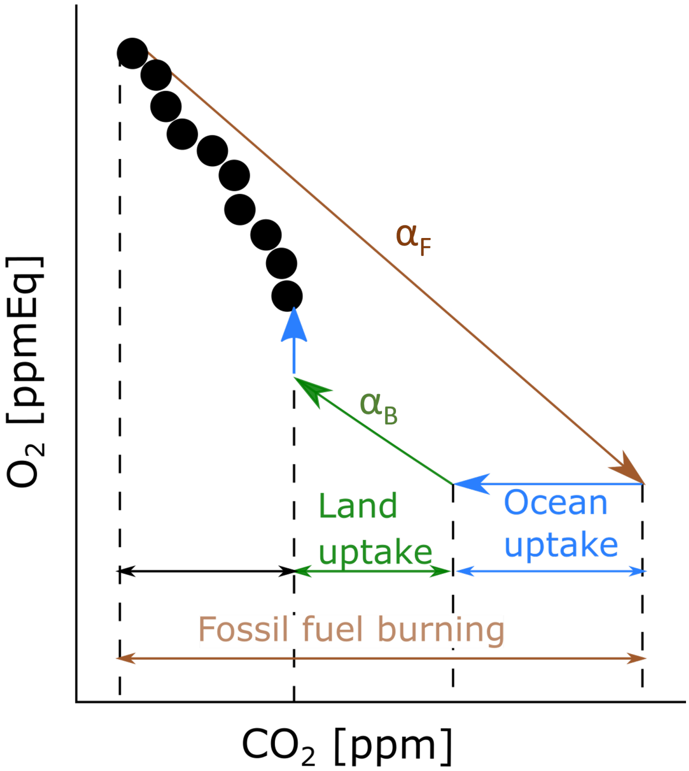

Figure 1.3: Schematic representation illustrating how atmospheric O_2 measurements allow to determine the land and ocean sinks in the global carbon budget on decadal timescales using annually averaged observations. In this schematic, the dots represent annual globally averaged measurements and the arrows depict the fluxes that contribute to forming these atmospheric signals.

Atmospheric O_2 measurements were initially mainly used to estimate the global uptake of CO_2 by the oceans and terrestrial biosphere. This estimation uses the observed trends in global O_2 and CO_2, (see Figure 1.2a) (Keeling, 1988; Keeling and Shertz, 1992; Keeling et al., 1993; Bender et al., 1996; Stephens et al., 1998; Manning and Keeling, 2006). The relationship between the global trends in O_2 and CO_2 can be quantified using the following mass balance equations (Keeling and Shertz, 1992; Keeling and Manning, 2014):

$$\frac{dCO_2}{dt} = F - O - B \tag{1.4}$$

$$\frac{dO_2}{dt} = -\alpha_F F + \alpha_B B + Z_{O_2} \tag{1.5}$$

Where F is the global CO_2 flux from fossil fuel combustion, B is the net terrestrial biosphere uptake of CO_2, O is the net ocean uptake of CO_2 and Z is the net ocean outgassing of O_2.

The parameter α_F is the globally averaged O_2:CO_2 oxidative ratio for fossil fuel burning, and α_B is the globally averaged O_2:CO_2 ratio for biosphere exchange. Currently, α_F is assumed to be 1.38 (Keeling and Manning, 2014), and α_B is assumed to be 1.1, as reported by Severinghaus (1995). This α_B value is based on oxidative ratios of wood samples (see Sect. 1.6). The O_2:CO_2 ratio of the biosphere may be referred to with different terminology depending on the measurement technique used and the temporal scale of the observations. These varying definitions will be discussed in Sect. 1.6 and Sect. 1.7. Note that Eqs. 1.4 and 1.5 are simplifications of the O_2 and CO_2 budgets. They do not take into account the proposed metal correction of the O_2 budget (Battle et al., 2023) and additionally the land-use change fluxes are included into the biosphere fluxes instead of as a separate flux as was discussed in Section 1.1.

Keeling and Shertz (1992) introduced the method to combine Eq. 1.4 and Eq. 1.5 to calculate CO_2 uptake by the biosphere and oceans using atmospheric O_2 measurements. In this approach, F is estimated based on fossil fuel emission inventories and Z_{O_2} is derived from a function incorporating global ocean heat content and N_2 dynamics (Manning and Keeling, 2006). The observed atmospheric O_2 and CO_2 trends from measurement stations that are not influenced by direct source and sink signals (so called background stations) are used to determine dO_2/dt and dCO_2/dt respectively. Consequently, Eq. 1.4 and Eq. 1.5 can be combined to calculate B (biospheric CO_2 uptake) and O (oceanic CO_2 uptake). A schematic overview of this approach is shown in Figure 1.3.

The atmospheric trends of O_2 and CO_2 measured at background stations can also be used to investigate ocean behavior and enhance the understanding of marine biological productivity, as first discussed by Keeling et al. (1993). Oceanic CO_2 uptake and O_2 outgassing are influenced by water temperature and biological production in the ocean (Stephens et al., 1998; Keeling and Manning, 2014). To facilitate the interpretation of oceanic outgassing effects on atmospheric measurements, Stephens et al. (1998) introduced the concept of atmospheric potential oxygen (APO), defined as:

$$APO = \delta(O_2/N_2) + \alpha_B \cdot (\Delta CO_2)/0.2094 \ \ \text{[per meg]} \tag{1.6}$$

Where $\delta(O_2/N_2)$ represents the total atmospheric O_2 signal and ΔCO_2 is the difference between the total atmospheric CO_2 signal with an arbitrary reference. The APO signal is a combined O_2 and CO_2 signal designed to be insensitive to the influence of terrestrial biosphere exchange. By adding $\alpha_B \cdot CO_2$ to O_2, it is assumed that the trend and variations resulting from terrestrial biosphere exchange are removed from the O_2 signal. The study by Stephens et al. (1998) adopted a value of 1.1 for α_B based on the study by Severinghaus (1995). This contrasted the previously hypothesized value of 1.05, proposed by Keeling (1988).

Currently, the budgets described by Eqs. 1.4, 1.5 and 1.6 are frequently applied to enhance our understanding of global CO_2 uptake by the biosphere and oceans, as well as oceanic behavior (Rödenbeck et al., 2008; Tohjima et al., 2019; Friedlingstein et al., 2023; Jin et al., 2023). Beyond these global scale applications, the O_2 method has been further developed to aid in the verification of fossil fuel emissions (Ishidoya et al., 2022a; Pickers et al., 2022; Rödenbeck et al., 2023). In these recent approaches, APO is determined from measurements at sites close to fossil fuel sources, in contrast to background monitoring stations used in earlier methods. By calculating APO, which means removing the biospheric variations based on CO_2, and subtracting the background signal (that includes ocean O_2 outgassing), it is assumed that the remaining peaks in the atmospheric O_2 signal are primarily caused by fossil fuel emissions, and APO therefore allows to identify changes in fossil fuel signals.

A large remaining uncertainty in the atmospheric O_2 budget is associated with oceanic outgassing (Z_{O_2}) (Keeling and Garcia, 2002; Manning and Keeling, 2006; Ishidoya et al., 2012; Keeling and Manning, 2014; Resplandy et al., 2018; Tohjima et al., 2019). This term is influenced by N_2 outgassing (particularly when using measurements of $\delta(O_2/N_2)$) and the global ocean heat content. Both variables are difficult to measure or calculate due to their large spatial and temporal variability.

Another uncertainty in the atmospheric O_2 budget is the value of α_B. In all O_2 partitioning approaches mentioned above, a constant value for α_B is assumed. Typically, the value of 1.1 proposed by Severinghaus (1995) is used, with an associated uncertainty of ± 0.10 (Keeling and Manning, 2014). However, it is important to investigate the constant α_B value because several studies (e.g. Seibt et al., 2004; Ishidoya et al., 2013; Hilman et al., 2022) have demonstrated that the O_2:CO_2 ratio of the terrestrial biosphere varies significantly depending on the location and the temporal scale of the measurement (Sect. 1.6 and Sect. 1.7). Furthermore, local O_2 and CO_2 biospheric measurements have the potential to provide additional O_2 partitioning methods, offering improved insights into the carbon cycle of the biosphere at local spatial scales. (Sect. 1.7). Throughout this thesis we will focus on the O_2:CO_2 ratio of the terrestrial biosphere and improve its quantification.

1.6 The oxidative ratio of the terrestrial biosphere

The constant terrestrial biosphere O_2:CO_2 ratio value (α_B) of 1.1, as used in Eq. 1.5 and Eq. 1.6, is determined using oxidative ratio (OR) measurements. OR values are derived from the elemental composition of organic material by analyzing the quantities of carbon (C), hydrogen (H), oxygen (O) and nitrogen (N) molecules in the material. Assuming that N_2 is the primary source of nitrogen, the OR can be calculated using the following equations (Keeling, 1988; Severinghaus, 1995; Masiello et al., 2008):

$$xCO_2 + \frac{y}{2}H_2O + \frac{w}{2}N_2 \rightarrow C_xH_yO_zN_w + \frac{4x+y-2z}{4}O_2 \tag{1.7}$$

$$OR = -\frac{\Delta O_2}{\Delta CO_2} = -\frac{\frac{4x+y-2z}{4}}{x} = -\frac{4x+y-2z}{4x} \tag{1.8}$$

Where x, y, z and w are the number of elements or molecules from specific organic materials. The resulting OR values were found to be between 0.978 and 1.060 for a range of different organic materials (Masiello et al., 2008). When the primary source of nitrogen shifts to a different compound, such as nitrate (NO_3^-) or ammonium (NH_4^+), the equation above changes accordingly and slightly adjusts the OR value with a maximum increase/decrease of around 0.05 (Seibt et al., 2004; Randerson et al., 2006; Masiello et al., 2008).

Different types of plant material and soil organic matter exhibit varying OR values (Severinghaus, 1995; Masiello et al., 2008; Hockaday et al., 2009; Hockaday et al., 2015; Jürgensen et al., 2021; Worrall et al., 2013; Clay and Worrall, 2015). Sugars in the form of carbohydrates contain equal numbers of molecules of O and C (Eq. 1.1), resulting in an OR of 1.0. Carbohydrates are synthesized by leaves and are abundant in non-woody material (Randerson et al., 2006). Organic materials with a higher carbon content relative to oxygen have OR values above 1.0 (Eq. 1.8). For instance, when vegetation stores carbon as lipids (OR = 1.37) or lignin (OR = 1.14) the carbon-to-oxygen ratio increases, leading to a higher OR (Randerson et al., 2006; Masiello et al., 2008). Woody biomass contains more lipids and lignin and therefore has higher OR values compared to non-woody material. When vegetation dies and decomposes, organic carbon pools are formed in the soil. These pools are gradually broken down by microbial activity. Compounds containing less carbon are easier to decompose and will disappear first, leaving behind the compounds with higher carbon content. This process increases the oxidative state of the soil, thereby raising the OR value over time (Hilman et al., 2022).

OR values are used to determine the α_B value because OR measurements represent processes occurring over long time scales, similar to global O_2 partitioning methods. It is assumed that an OR value reflects the net number of O_2 molecules that are emitted compared to the number of CO_2 molecules that are taken up during the formation of the analyzed organic material. Consequently, the OR provides a representation of O_2 and CO_2 exchange over the time scales relevant to the formation of various organic materials, ranging from a year to decades. It is hypothesized that the terrestrial biosphere signals at global background stations are best represented using the longer time scales of OR measurements (Keeling, 1988; Severinghaus, 1995; Stephens et al., 1998). This assumption aligns with the time scales applied in the global O_2 partitioning methods discussed in Sect. 1.5.

The first estimate of α_B was proposed by Keeling (1988), who hypothesized a value of 1.05 ± 0.02. They based this value on elemental analysis of a few wood samples. Subsequently, Severinghaus (1995) was the first to present accurate OR measurements, assigning a value of 1.1 ± 0.05 to α_B based on OR measurements of wood samples from various plant species. This value for α_B remains widely used in different O_2 partitioning methods (e.g. Manning and Keeling, 2006; Tohjima et al., 2019; Pickers et al., 2022). However, Severinghaus (1995) acknowledged that the soil sample size in their study was too limited to establish a representative value for the global OR. To address this limitation, Worrall et al. (2013) investigated the OR of a wider range of soils and vegetation materials worldwide. By calculating weighted averages for different ecosystems and linking these to measured OR values, they proposed a revised α_B value of 1.04 ± 0.03. Their work was subsequently expanded with a larger dataset of OR values for diverse soil and vegetation types globally, updating the α_B to 1.06 ± 0.06 (Clay and Worrall, 2015).

Using the OR value of 1.1 (Severinghaus, 1995) or 1.06 (Clay and Worrall, 2015) to represent α_B, the global terrestrial O_2:CO_2 ratio in the atmosphere, assumes that α_B remains constant over time and space. However, several studies have demonstrated that the OR varies between ecosystems (Hockaday et al., 2009; Hockaday et al., 2015; Gallagher et al., 2017) and over time (Randerson et al., 2006). Moreover, the use of α_B inherently considers the full time scales over which vegetation and soils are formed. This assumption may no longer hold when applying O_2 partitioning methods on shorter temporal or smaller spatial scales compared to global applications over long time-scales. For example, fossil fuel verification methods (Pickers et al., 2022; Rödenbeck et al., 2023), as discussed in Sect. 1.5, operate on such smaller scales. How to quantify α_B on smaller spatial and temporal scales is not yet understood and local measurements are needed. Analyses of local O_2 and CO_2 measurements can reflect the variability of α_B, and enhance our understanding of the terrestrial O_2:CO_2 ratio across different temporal and spatial scales. We will discuss these next.

1.7 Local measurements of biosphere O_2 and CO_2 exchange

Local measurements of the ratio between the exchange of O_2 and CO_2 above the canopy or with chambers on the vegetation that indicate biospheric exchange are often called the Exchange Ratio (ER) (Seibt et al., 2004). ER measurements differ from the OR in their temporal scales and therefore also in which processes they represent (see Figure 1.4). The OR is derived from elemental analysis of organic material, reflecting the O_2:CO_2 ratio over the time scale during which the organic material was formed. In contrast, the ER represents the O_2:CO_2 ratio of the immediate biospheric exchange observed during the measurements, thus capturing processes on much shorter time scales. Hypothetically, if ER measurements were conducted over the entire period during which organic material forms, the resulting ER signal should align with the OR measurements of the same organic material (Seibt et al., 2004; Randerson et al., 2006; Hockaday et al., 2009; Gallagher et al., 2014). However, this hypothesis has not yet been empirically verified.

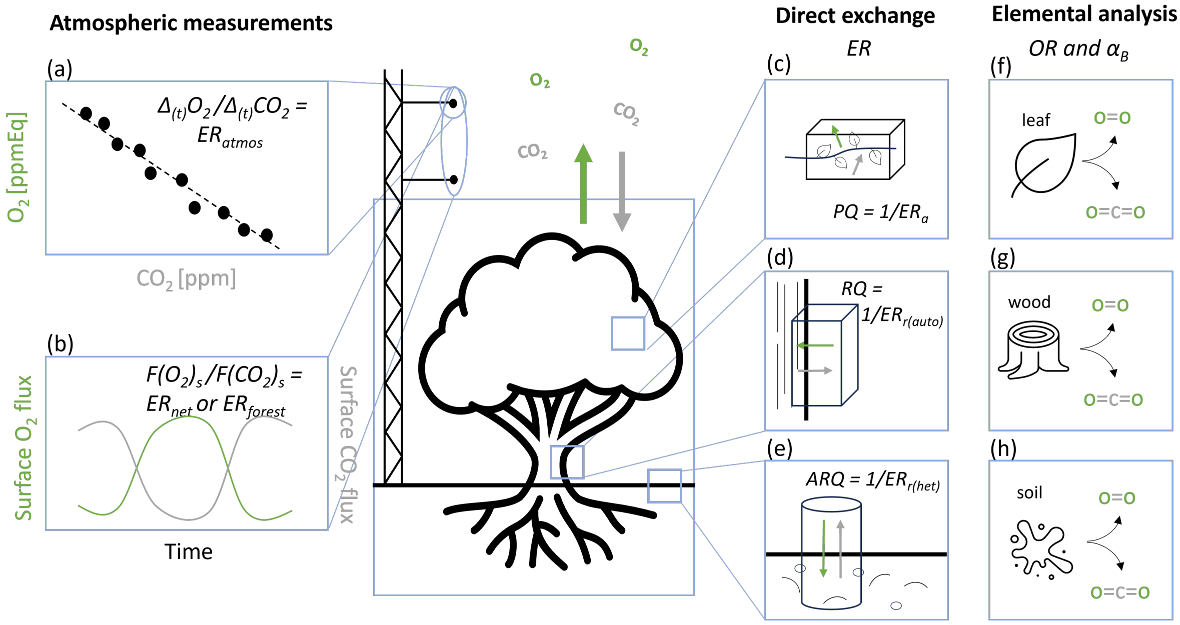

Figure 1.4: Schematic overview of the different O_2:CO_2 ratios that can be measured in and above the biosphere. These signals are categorized into three types of measurements: (1) Atmospheric measurements using a canopy-level measurement tower, where (a) single-height measurements represent the exchange ratio (ER) of the atmosphere (ER_{atmos}) and (b) the turbulent surface flux (F_s) inferred from the vertical gradient of measurements at 2 heights represent the net ER of the forest (ER_{forest} or ER_{net}), (2) direct exchange measurements using branch (c), stem (d) or soil chambers (e) including measurements of the photosynthesis quotient (PQ) or ER of assimilation (ER_a), the respiration quotient (RQ) or ER of autotrophic respiration ($ER_{r(auto)}$), and the apparent respiration quotient (ARQ) or the ER of heterotrophic respiration ($ER_{r(het)}$), and (3) elemental analysis conducted in a lab to determine the oxidative ratio (OR) of different plant or soil materials (f-h). Green colors represent O_2 and grey colors represent CO_2.

1.7.1 Application of O_2 on the local scale

The study by Seibt et al. (2004) was the first to measure changes in atmospheric O_2 and CO_2 mole fractions over a forest canopy within a time span of a few days, using flask samples. Their results demonstrated that the ER resulting from net O_2 and CO_2 exchange derived from the net O_2 and CO_2 surface fluxes of the forest (in this thesis referred to as ER_{net} or ER_{forest}) has a clear diurnal variability, with values around 1.26 during the day and 1.00 during the night. This finding challenges the widely used value of 1.1 to represent O_2:CO_2 biospheric ratios as discussed above in Sect. 1.6. Subsequent studies measuring O_2:CO_2 ratios above the biosphere have confirmed that ER_{net} varies over time and between different measurement locations (Stephens et al., 2007; Ishidoya et al., 2013; Battle et al., 2019).

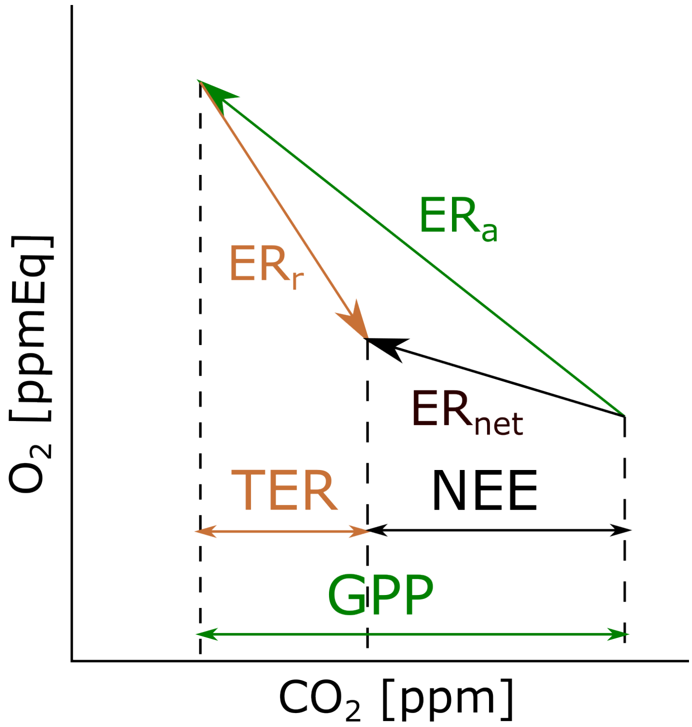

Figure 1.5: Schematic representation illustrating how O_2 allows disentangling the local carbon budget of the biosphere. The horizontal arrows represent the gross fluxes of CO_2: Net ecosystem exchange (NEE), Gross primary productivity (GPP) and total ecosystem respiration (TER). The sloped arrows indicate the O_2:CO_2 ratios associated with a change in mole fraction caused by a specific gross flux, with the exchange ratio for respiration (ER_r), the exchange ratio for assimilation (ER_a) and the exchange ratio of the net exchange of the forest (ER_{forest} or ER_{net}).

To explain the diurnal variability of ER_{net} over time and space, it is necessary to evaluate the processes contributing to ER_{net}. Both GPP and TER form the net exchange of CO_2 and O_2 (See Sect. 1.2). The budgets of the net exchange of O_2 and CO_2 can be combined to derive a definition that characterizes ER_{net} (Seibt et al., 2004; Ishidoya et al., 2013):

$$F(CO_2)_s = NEE = -GPP + TER \tag{1.9}$$

$$-F(O_2)_s = -ER_{net} \cdot NEE = ER_a \cdot GPP - ER_r \cdot TER \tag{1.10}$$

Where $F(CO_2)_s$ is the surface flux of CO_2 above the canopy, $F(O_2)_s$ is the surface flux of O_2 above the canopy, ER_{net} is the ratio between $F(O_2)_s$ and $F(CO_2)_s$, ER_a is the Exchange Ratio of the assimilation processes ($GPP(_{O_2}) : GPP(_{CO_2})$) and ER_r is the Exchange Ratio of the respiration processes ($TER(_{O_2}) : TER(_{CO_2})$). ER_{net} is therefore not linked to a specific process, but rather a combination of the ER values of the gross fluxes contributing to the net signal. Note that in these equations, the signs of the ER values are defined as positive. By understanding the values of ER_a and ER_r, the variability and processes behind ER_{net} can be explained.

Ishidoya et al. (2015) demonstrated that by combining Eqs. 1.9 and 1.10, atmospheric O_2 can be used to partition NEE into GPP and TER. By determining the values for ER_a and ER_r, and inferring the net O_2 and CO_2 fluxes from measurements of their vertical gradients, GPP and TER can be quantified. Figure 1.5 provides a schematic overview of this approach, where the vectors indicate the change in mole fractions of O_2 and CO_2 caused by the specific ER values and CO_2 surface fluxes. It is therefore important to accurately measure the various O_2:CO_2 ratios present within an ecosystem to gain a comprehensive understanding of ER_a and ER_r

1.7.2 The different ER signals of the biosphere

Measurements of ER_a can be conducted in-situ using a branch chamber or in a controlled laboratory setting with a plant chamber (Figure 1.4). Only a limited number of studies have used branch chambers to link ER_a to ER_{net} (Seibt et al., 2004; Ishidoya et al., 2013). Studies focusing on the physiological processes of plants often employ plant chambers. These biology-oriented studies typically use the inverse of ER, referred to as the photosynthesis quotient (PQ), which represents the CO_2:O_2 ratio during photosynthesis (Cousins and Bloom, 2004; Fischer et al., 2015). ER_a values are generally close to 1.0 but can vary depending on factors such as light intensity and the nitrogen source. ER_a remains poorly understood due to the limited number of studies that have investigated it, whether through branch chamber measurements in the field or controlled experiments in the lab.

Multiple measurements are required to determine ER_r due to the variety of processes contributing to the ER_r signal (Figure 1.4). The variability of ER_r can be attributed to two processes, each with their own ER value: autotrophic respiration ($ER_{r(auto)}$) and heterotrophic respiration ($ER_{r(het)}$). $ER_{r(auto)}$ can be quantified by measuring CO_2 and O_2 fluxes from tree stems and roots (Shane et al., 2004; Hicks Pries et al., 2020; Hilman et al., 2022). $ER_{r(het)}$ can be determined by measuring CO_2 and O_2 fluxes from soil that does not contain live vegetation (Angert et al., 2015; Hilman et al., 2022).

Most studies that have measured ER_r signals focus on the biological processes inside the soil or plants. Similar to ER_a, these biology-oriented studies use the inverse of ER, referred to as the respiration quotient (RQ). In soil studies, when O_2 and CO_2 follow different pathways in or out of the soil, the apparent respiration quotient (ARQ) is frequently used instead of RQ. These measurements allow partitioning soil respiration into their autotrophic and heterotrophic components, as $ER_{r(auto)}$ and $ER_{r(het)}$ typically have distinct values (Hicks Pries et al., 2020). The different ER_r values can vary between 0.8 up to values larger than 2.0 depending on temperature and soil type (Angert et al., 2015; Hicks Pries et al., 2020; Hilman et al., 2022). While the ER_r of soils is often associated with soil OR signals, the processes driving the observed ER_r signals remain poorly understood.

Both $\mathrm{ER_a}$ and $\mathrm{ER_r}$ contribute to the overall exchange ratio of the terrestrial biosphere ($\mathrm{ER_{net}}$). For the global and long-term applications of α_b discussed above in Sect. 1.5, it is commonly assumed that $\mathrm{ER_a}$ equals $\mathrm{ER_r}$. However, local-scale measurements indicate that this assumption does not hold on smaller spatial and temporal scales, leading to more variability in $\mathrm{ER_{net}}$ over time and space.

$\mathrm{ER_{net}}$ can be determined by measuring the net surface exchange of both O_2 and CO_2 with the atmosphere (Figure 1.4b). The net surface exchange of CO_2 can be measured directly using eddy covariance (EC) systems above the canopy, integrating all the processes in and below the canopy. However, no system currently available can measure O_2 fluxes with the speed and accuracy required for EC-based measurements. Despite attempts to improve such systems, to date, they have not yet been successful. As a result, the O_2 flux must be determined indirectly by measuring its vertical gradient. Ishidoya et al. (2013) and Ishidoya et al. (2015) were the first to apply this method by measuring O_2 and CO_2 at two heights to infer the surface fluxes of both gases. By dividing the surface fluxes of O_2 and CO_2 for each time step, they calculated $\mathrm{ER_{net}}$ at the corresponding temporal resolution.

Another method to infer the ER signal involves measuring temporal changes of both O_2 and CO_2 mole fractions at a single height (Figure 1.4a). The linear regression of O_2 against CO_2 gives the slope that represents the ER signal (Seibt et al., 2004; Stephens et al., 2007; Battle et al., 2019). In this thesis, we refer to this as the ER of the atmosphere ($\mathrm{ER_{atmos}}$). This ER signal is not only influenced by surface processes but also largely influenced by atmospheric processes, which makes $\mathrm{ER_{atmos}}$ different compared to $\mathrm{ER_{net}}$. To date, only Seibt et al. (2004) and Ishidoya et al. (2013) measured $\mathrm{ER_{net}}$ and their findings show that $\mathrm{ER_{atmos}}$ and $\mathrm{ER_{net}}$ do not result in the same value to indicate the surface ER signal. However, they did not explore the reasons behind this discrepancy. This thesis dives deeper into the comparison between $\mathrm{ER_{atmos}}$ and $\mathrm{ER_{net}}$ and analyzes when these values can be used to indicate surface processes.

Relatively few studies have measured the exchange of both O_2 and CO_2 between the biosphere and the atmosphere (Figure 1.6). These measurement locations include the WLEF tower in the US (Stephens et al., 2007), Harvard forest in the US (Battle et al., 2019), the Takayama tower (TKY) in Japan (Ishidoya et al., 2013), the Zotino Tall Tower Observatory (ZOTTO) in Russia (Kozlova and Manning, 2009), the Bialystok tower in Poland (Popa et al., 2010), Griffin forest in the UK (Seibt et al., 2004), the Ochsenkopf tower in Germany (Thompson et al., 2009) and Reinshof site in Germany (Knohl et al., 2020). These studies vary in the methods used to determine the ER of the biosphere and in the level of detail of their analysis of O_2 data. Consequently, there is still limited understanding of the behavior of the O_2:CO_2 ratio of the biosphere. This knowledge gap complicates the assessment of how the biosphere ER influences O_2 partitioning methods across different temporal and spatial scales. Throughout this thesis we added new

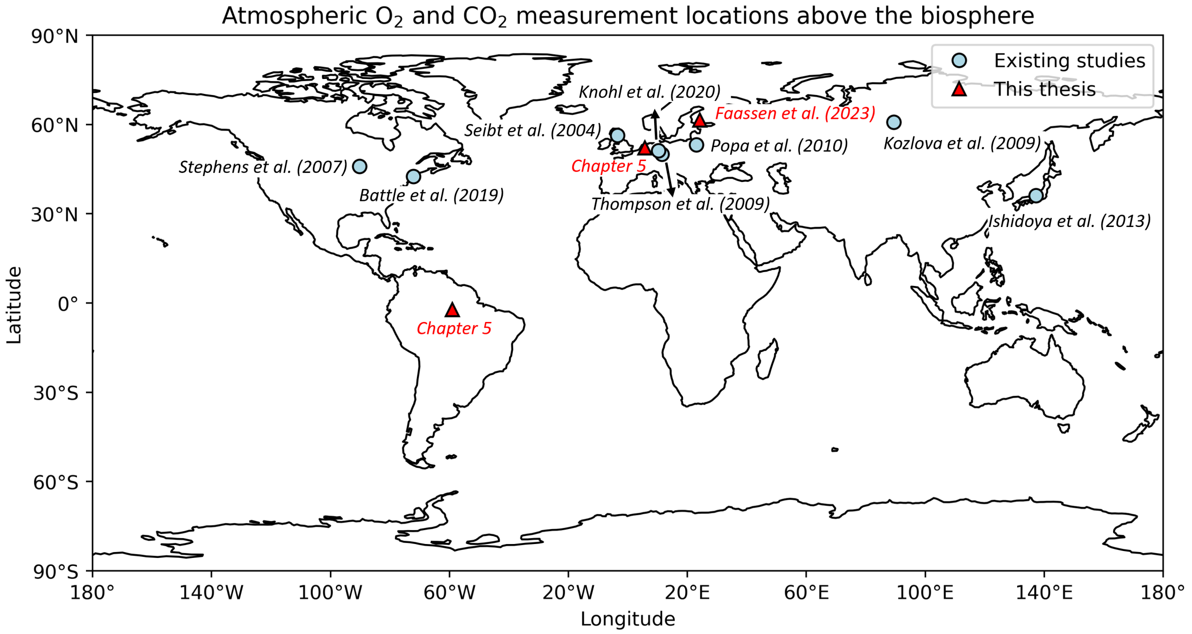

Figure 1.6: Locations worldwide where both O_2 and CO_2 were measured above vegetation.

measurements of O_2 and CO_2 mole fractions above vegetation to increase our knowledge of the biosphere ER (Figure 1.6).

1.8 Research questions and thesis outline

To enhance our understanding of the terrestrial biosphere exchange of O_2 and CO_2, this thesis addresses four key research questions. Each question targets a specific knowledge gap and is explored in a dedicated chapter. We do this by combining observations from 3 measurement campaigns and 3 different types of models with different degree of complexity and acting at different scales. The thesis is outlined as follows.

We continue with Chapter 2 in which we introduce the methods used throughout the thesis. This chapter provides detailed information on: (1) calculating with O_2 per meg values,(2) an introduction to the measurement campaigns used in this thesis, (3) the calibration techniques used for the O_2 measurements in this thesis and (4) an introduction and comparison of the models used in this thesis.

In Chapter 3 we analyze data from our field campaign conducted in southern Finland. As shown in Figure 1.6, there are only a few locations worldwide where the exchange of O_2 and CO_2 between the biosphere and the atmosphere has been measured. To improve our understanding of the ER values of the terrestrial biosphere it is essential to collect more measurements of O_2 and CO_2. One ecosystem that remains understudied in this context is the boreal forest. Accordingly, we evaluate our data collected during campaigns in the spring and summer of 2018 and 2019 in Hyytiälä, Finland.

Similar to the study by Ishidoya et al. (2015), during the Hyytiälä campaigns O_2 and CO_2 were measured continuously at two heights above the canopy using a fuel cell analyzer to measure O_2 and to infer the O_2 and CO_2 surface fluxes. The study by Ishidoya et al. (2015) demonstrated for the first time that O_2 surface fluxes could be used to partition NEE into GPP and TER. Building on this fundamental work, we analyzed in more detail what the optimal method is to calculate O_2 surface fluxes. Additionally, we apply the partitioning method to the boreal forest ecosystem. By analyzing the surface fluxes of O_2 and CO_2 we could also determine the ER_a and ER_r signals of this boreal forest during the campaign. By combining this information, we address the following main research question in Chapter 3:

1. What is the diurnal variability of the O_2 and CO_2 exchange ratio of a boreal forest?

In Chapter 3 we discuss the contrasting values for ER_{net} (the ER based on O_2 and CO_2 fluxes derived from their vertical gradient, in this chapter referred to as ER_{forest}) and ER_{atmos} (the ER based on single height mole fractions of O_2 and CO_2) during the measurement campaigns in Hyytiälä. ER_{net} values were approximately 1.0, while ER_{atmos} values always consistently exceeded 1.0, sometimes even surpassing 2.0. The limited studies available that analyzed ER_{atmos}, have reached differing conclusions about whether this ER value can represent ER_{net} or what the ER_{atmos} value itself means. Seibt et al. (2004) argued that ER_{atmos} cannot be compared with ER_{net} due to atmospheric mixing. Battle et al. (2019) suggested that atmospheric mixing effects can be minimized by using data collected late in the day when mixing is less significant. Ishidoya et al. (2013) measured both ER_{net} and ER_{atmos} and reported little difference between the two signals. However, no studies so far have thoroughly investigated the specific meaning of the ER_{atmos} signal, leaving it unclear whether single-height measurements can accurately represent the O_2:CO_2 ratios originating from the biosphere.

To determine what forms the ER_{atmos} signal, an atmospheric model is required. Previous O_2 modeling efforts have used a simple one-box model (Seibt et al., 2004; Ishidoya et al., 2013) or a multi-layer biosphere model with a fixed atmosphere (Yan et al., 2023). However, these models are not able to disentangle the atmospheric and biospheric signals of O_2 and CO_2. To address this limitation, we employed a more advanced model: the mixed-layer Chemistry Land-surface Atmosphere Soil Slab (CLASS) (Vilà-Guerau de Arellano et al., 2015). The CLASS model allows for a detailed examination of how the ER_{atmos} signal is generated and its sensitivity to micro meteorology. It also allows to connect the ER_{atmos} signal to the ER_{net} signal of the surface processes. By combining the CLASS model with our data from the Hyytiälä campaign, we were able to address the following research question in Chapter 4:

2. What do single height O_2:CO_2 ratios above a forest represent?

The studies in Chapter 3 and 4 focus specifically on the boreal forest in Hyytiälä. As noted earlier, there is a significant need for additional O_2 and CO_2 measurements across different ecosystems. To address this, we examined two additional ecosystems: a temperate and a tropical forest. For the tropical forest, we used our observations from the cloud roots campaign conducted in 2022 in the Amazon, Brazil (Vilà-Guerau de Arellano et al., 2024). For the temperate forest, we analyzed our observations from the Ruisdael campaign, which took place in 2022 in Loobos, The Netherlands. During both campaigns, flask samples were collected from which O_2, CO_2 and $\delta^{13}C$ were measured.

By combining the CLASS model with the observations from the two campaigns, we extend the analysis from Chapter 4 to different ecosystems. This expanded analysis also incorporates the stable isotope $\delta^{13}C$ in CO_2, which, similarly to the O_2:CO_2 ratio, can be used to partition NEE into GPP and TER (Wehr et al., 2016). Using the CLASS model, we disentangle the diurnal cycles of CO_2, O_2 and $\delta^{13}C$ for the two contrasting ecosystems. This detailed analysis allows us to address the following research question in Chapter 5:

3. What influences the diurnal cycles of CO_2, O_2 and $\delta^{13}C$ for two contrasting ecosystems?

To connect the locally measured ER_{net} signals to a biospheric O_2:CO_2 signal on a larger spatial scale (α_B), it is necessary to upscale the biospheric O_2 and CO_2 fluxes to get global spatial and temporal variability. We employed the Simple Biosphere model (SiB4) (Haynes et al., 2019). So far, only Huang et al. (2018) and Ding et al. (2022) have modeled global biosphere O_2 fluxes by linking the OR to CO_2 fluxes. However, Chapter 3 revealed that the O_2 fluxes are strongly influenced by the balance between GPP and TER, as well as their ER_a and ER_r signals. Relying solely on the OR linked to CO_2 fluxes fails to capture the full variability of O_2 fluxes. To address this, we applied distinct ER_r and ER_a values to the TER and GPP fluxes for various plant functional types within the SiB4 model. While our O_2 flux implementation in SiB4 is relatively simple and not yet validated against observational data, it provides an opportunity to evaluate the temporal and spatial variability of α_B. This approach enables us to answer the following first research question in Chapter 6:

4a. What is the temporal and spatial variability of α_B?

Additionally, this theoretical implementation allows us to analyze the impact of a variable α_B on O_2 partitioning methods. We combined the spatially varying biosphere fluxes into an atmospheric signal by transporting the fluxes with the atmospheric Stochastic Time-Inverted Lagrangian Transport (STILT) model (Gerbig et al., 2003). We then focus on the impact of a variable α_B on fossil fuel applications using APO as discussed in Pickers et al. (2022). Ultimately, this answers a second research question for Chapter 6:

4b. What is the effect of a variable α_B over time and space on the APO method for estimating fossil fuel emissions?

We conclude the thesis by synthesizing and discussing the results from all chapters in Chapter 7. This final chapter provides an overview of the similarities and differences of the findings across the chapters and offers recommendations for future research in the field of biosphere O_2 and CO_2 exchange.

Chapter 2

Methods: Measuring and modeling atmospheric O_2

Throughout this thesis, various O_2 modeling and measurement methods are used to address the research questions outlined in Chapter 1. This chapter provides an overview of these methods and gives more detailed information on why and how they were used. Section 2.1 discusses the units used to report atmospheric O_2, and calculations involving O_2, including the significance of accounting for the dilution effect of CO_2 when measuring O_2. I furthermore outline the procedure for converting O_2 measurements from 'per meg' to 'ppm' or 'pm equivalents'. This conversion was consistently applied across all chapters of this thesis. Section 2.3 covers the various calibration techniques applied to obtain the data presented in Chapters 3 and 5. Finally, Section 2.4 focuses on the different models that are used throughout the thesis, including the mixed-layer Chemistry Land-surface Atmosphere Soil Slab (CLASS) model in Chapters 4 and 5, the Simple Biosphere model (SiB4) model and the atmospheric Stochastic Time-Inverted Lagrangian Transport (STILT) model in Chapter 6.

2.1 O_2 units and calculations

Atmospheric O_2 measurements are commonly reported as $\delta(O_2/N_2)$ in 'per meg'. However, in some measurement techniques O_2 is measured as an absolute quantity and not relative to N_2 and in many model applications it is more practical to express O_2 as mole fractions in ppm. To enable comparison between observations, models and for direct O_2 to CO_2 comparison, it is necessary to convert per meg values to mole fractions or vice versa. This conversion is not straightforward because O_2 is not a trace gas; its mole fraction is influenced by other trace gases, leading to potential dilution effects. These effects must be accounted for to ensure accurate representation and comparison of O_2 measurements (Keeling, 1988).

In this Section, we describe the process for converting O_2 across various units, taking into account the dilution effect caused by changes in the CO_2 mole fraction, similar as described by Stephens (1999). Only CO_2 is considered because it exhibits the largest variability in dry air composition. We discuss three scenarios in which the mole fractions of CO_2 and O_2 change individually within an air pocket (Figure 2.1). The air pocket is assumed to consist of 1,000,000 molecules with the following initial composition: 400 CO_2 molecules, 209,392 O_2 molecules and 780,876 N_2 molecules. The remaining 9,332 molecules consist mainly of argon and other species (Tohjima et al., 2005).

For Scenario 1, one molecule of CO_2 is added to the air pocket. The resulting change in the CO_2 mole fraction can be calculated as:

$$\left(\frac{401}{1000001} - \frac{400}{1000000}\right) \approx 1.0 \text{ ppm} \tag{2.1}$$

In Scenario 1, the number of O_2 molecules remains constant at 209,392. However, since the mole fraction of O_2 depends on the total number of molecules in the air pocket, it is

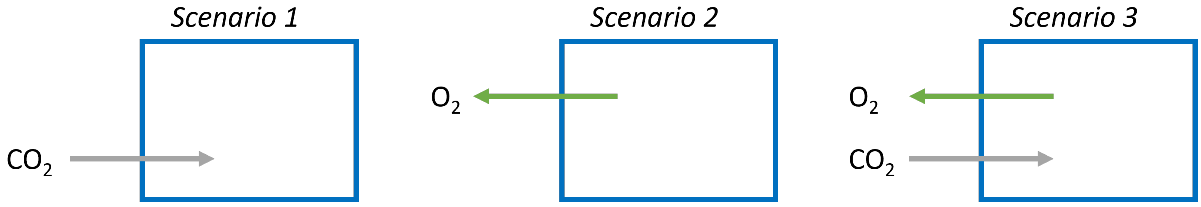

Figure 2.1: Three scenarios in which the amount of O_2 or CO_2 changes with 1 molecule in an air pocket that contains 1,000,000 molecules.

affected by the addition of 1 CO_2 molecule. The change in the O_2 mole fraction is:

$$\left(\frac{209392}{1000001} - \frac{209392}{1000000}\right) \approx -0.21 \text{ ppm} \tag{2.2}$$

Thus, the O_2 mole fraction decreases slightly by 0.21 ppm due to the dilution effect caused by the addition of one molecule of CO_2, even though the number of O_2 molecules remains unchanged. However, the $\delta(O_2/N_2)$ (in per meg), which represents changes in the O_2/N_2 ratio independent of the total air composition, remains unaffected. This is because $\delta(O_2/N_2)$ specifically reflects the relative abundance of O_2 compared to N_2 and is not influenced by changes in the mole fractions of other trace gases, such as CO_2 (Eq. 1.3).

For Scenario 2, one molecule of O_2 is removed from the air pocket. This changes the mole fraction of O_2 due to both the reduction in the number of O_2 molecules and the decrease in the total number of molecules in the air pocket:

$$\left(\frac{209391}{999999} - \frac{209392}{1000000}\right) \approx -0.79 \text{ ppm} \tag{2.3}$$

So when the amount of O_2 is changed by one molecule it will not result in a change of 1 ppm, in contrast to what we saw for CO_2 in Scenario 1. A decrease of one molecule O_2 also affects the O_2 per meg value by:

$$\left(\frac{209391/780876}{209392/780876} - 1\right) \cdot 10^6 \approx -4.776 \text{ per meg} \tag{2.4}$$

This means that in Scenario 2 a change of 0.791 ppm in the O_2 mole fraction corresponds to a change of 4.776 per meg. As a result, a 1 ppm change in the O_2 mole fraction (without a change in the CO_2 mole fraction) corresponds to approximately $4.776/0.791 = 6.04$ per meg change in $\delta(O_2/N_2)$ (Kozlova et al., 2008).

For Scenario 3, one molecule of O_2 is removed and one molecule of CO_2 is added to the air pocket. The resulting change in the O_2 mole fraction is then:

$$\left(\frac{209391}{1000000} - \frac{209392}{1000000}\right) = -1.0 \text{ ppm} \tag{2.5}$$

The change in CO_2 mole fraction is also 1 ppm in Scenario 3 and the change in $\delta(O_2/N_2)$ in per meg stays the same as in Scenario 2:

$$\left(\frac{209391/780876}{209392/780876} - 1\right) \cdot 10^6 \approx -4.776 \text{ per meg} \tag{2.6}$$

The relationship between a change of one O_2 molecule in ppm and per meg 'units' changes now compared to Scenario 2. A 1 ppm change in the O_2 mole fraction (with a change in the CO_2 mole fraction) corresponds to approximately $4.776/1.0 = 4.776$ per meg change in $\delta(O_2/N_2)$, which is the same as $1/O_2 = (1/209{,}392) * 10^6$. The analysis based on Figure 2.1 shows that calculating O_2 values should be handled with care.

Throughout this thesis, we use the conversion factor of $1/O_2$ per meg/ppm to convert from $\delta(O_2/N_2)$ to 'ppm equivalents'. The studies presented in this thesis were conducted above the biosphere. When measuring or modeling in the atmosphere above the biosphere, it is reasonable to assume that changes in O_2 are accompanied by corresponding changes in CO_2 (Keeling, 1988; Stephens, 1999; Kozlova et al., 2008). This aligns with Scenario 3, where both O_2 and CO_2 are altered simultaneously.

2.2 Measuring O_2 and CO_2

Figure 2.2: The measurement towers from which the observations used in this thesis are collected: (a) Hyytiälä tower in Finland, (b) Loobos tower in The Netherlands and (c) ATTO tower in the Amazon in Brazil.

In this thesis, observations from three different measurement locations are presented (Figure 2.2): the Hyytiälä tower in Finland (Chapter 3 and 4), the Loobos tower in The Netherlands (Chapter 5) and the ATTO tower in the Amazon in Brazil (Chapter 5). Each tower is situated in a distinct ecosystem: the Hyytiälä tower in a boreal forest, the Loobos tower in a temperate forest, and the ATTO tower is in a tropical rain forest. Next to the O_2 and O_2 observations, meteorological variables are continuously measured at multiple heights above the canopy at each site. These measurements provide crucial insights into the surface exchange of O_2 and CO_2 and are essential for inferring surface fluxes.

At each location, measurement campaigns were conducted to collect atmospheric O_2 and CO_2 data along with additional meteorological and atmospheric variables, creating a unique dataset for each site. Radiosondes were deployed during each campaign to characterize boundary layer dynamics and measure vertical gradients of temperature and moisture. These measurements are essential for understanding the diurnal variation of O_2 and CO_2.

The setup of O_2 and CO_2 measurements varied across the three locations, providing different insights with each campaign. In Hyytiälä, we conducted continuous O_2 and CO_2 measurements at two heights, allowing to infer their surface fluxes. At Loobos, flask samples were collected both below and above the boundary layer from which O_2 and CO_2 were measured, enabling the quantification of vertical exchange between the free troposphere and the surface. In the Amazon, the combination of cloud characterization and O_2 and CO_2 measurements from flask samples, allowed for assessment of the effect of atmospheric processes, such as cloud-induced mass flow, on the diurnal cycles of O_2 and CO_2.

A complete description of the measurements conducted during each campaign can be found in the respective chapters.

2.3 Calibration of O_2 measurements: Oxzilla and mass spectrometer

Two different measurement techniques to measure atmospheric O_2 were used during the measurement campaigns used in this thesis: continuous measurements using an Oxzilla analyzer (Figure 2.3a) and flask-based measurements analyzed with a mass spectrometer (Figure 2.3b). In Chapter 3, the continuous atmospheric O_2 and CO_2 observations from Hyytiälä were measured with an Oxzilla. Although obtaining this dataset was not part of this thesis, calibration was still required to get the final data presented in 3. This section provides a more detailed explanation of the calibration methodology compared to what is described in Chapter 3. In Chapter 5, flask-based measurements from the Loobos and ATTO tower were analyzed. The flasks taken at the Loobos site were measured using a mass spectrometer at the Center for Isotope Research (CIO) in Groningen. To derive O_2 values from these flask measurements, it was necessary to calibrate the measurements of the mass spectrometer. Since Chapter 5 does not detail the calibration process for the mass spectrometer, a brief explanation is provided in this section (2.3.2). The flasks taken at the ATTO tower were measured and calibrated by the Max Planck Institute for Biogeochemistry in Jena, and their calibration is therefore not part of this thesis. Chapter 5 provides for further details on these measurements.

2.3.1 Oxzilla O_2 measurements and calibration

The Oxzilla measurements follow similar methodologies as described by Stephens et al. (2007), Thompson et al. (2007), van der Laan-Luijkx et al. (2010) and Leeuwen and Meijer

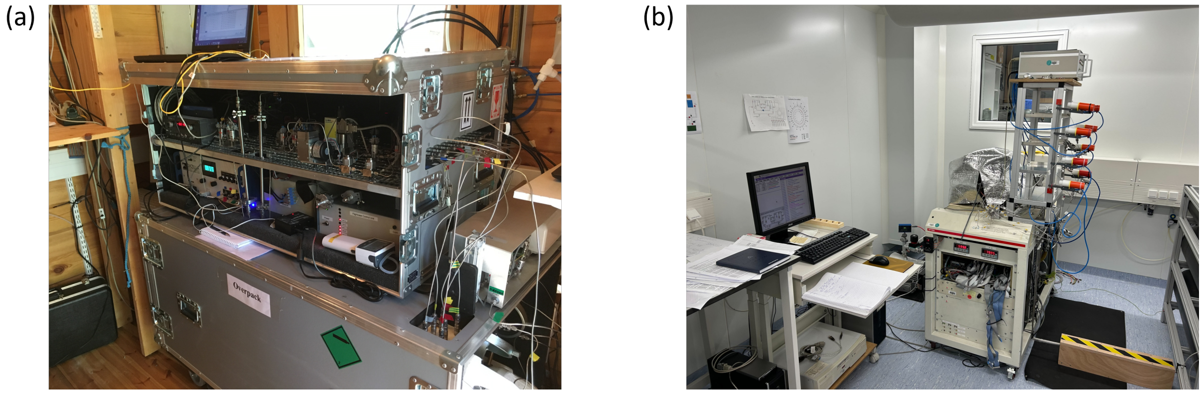

Figure 2.3: The Oxzilla analyzer (a) as described in Chapter 3 and Section 2.3.1, and the mass spectrometer (b) located at the Center for Isotope Research (CIO) in Groningen as described in Section 2.3.2.

(2015). The Oxzilla analyzer uses fuel cells to quantify the amount of atmospheric O_2 through the following electrochemical reaction:

$$O_2 + 2Pb + 4H^+ \rightarrow 2H_2O + 2Pb^{2+} \tag{2.7}$$

The fuel cells consist of lead (acting as the anode) and an acid-based electrolyte. When O_2 comes into contact with the fuel cells, a current is generated as a result of the reaction. Using cylinders with known values of O_2 mole fractions, the electromagnetic signal is converted to determine the mole fraction of O_2 in the air stream.

The Oxzilla is equipped with two fuel cells that operate simultaneously to enhance the accuracy of the device by obtaining a differential signal. Alternately, fuel cell 1 measures the sample air (S_1), which can be either calibration cylinder air or ambient air, while fuel cell 2 measures the reference cylinder (R_2). Subsequently, the sample and reference air streams are switched and fuel cell 2 measures the sample air and fuel cell 1 measures the reference air. The outputs from the two fuel cells are subtracted to produce a Δ signal (S_1 - R_2) or (R_1 - S_2). This approach eliminates machine drift that affects both fuel cells equally. The Oxzilla generates a Δ value every second. The fuel cells are switched every two minutes, to account for potential drift affecting only one of the fuel cells. This switching results in a double difference signal:

$$\Delta(\Delta) = (S_1 - R_2) - (R_1 - S_2) = 2 \cdot (S - R) \tag{2.8}$$

Based on the methods described by van der Laan-Luijkx et al. (2010), the $\Delta(\Delta)O_2$ values are calibrated to obtain $\delta(O_2/N_2)$ values expressed in 'per meg'. Four cylinders are analyzed every 23 hours. The $\delta(O_2/N_2)$ values of these calibration cylinders are determined using the Mass Spectrometer in Groningen on the international scale maintained by the Scripps Institution of Oceanography (SIO2017) (see next section). The $\Delta(\Delta)O_2$ values

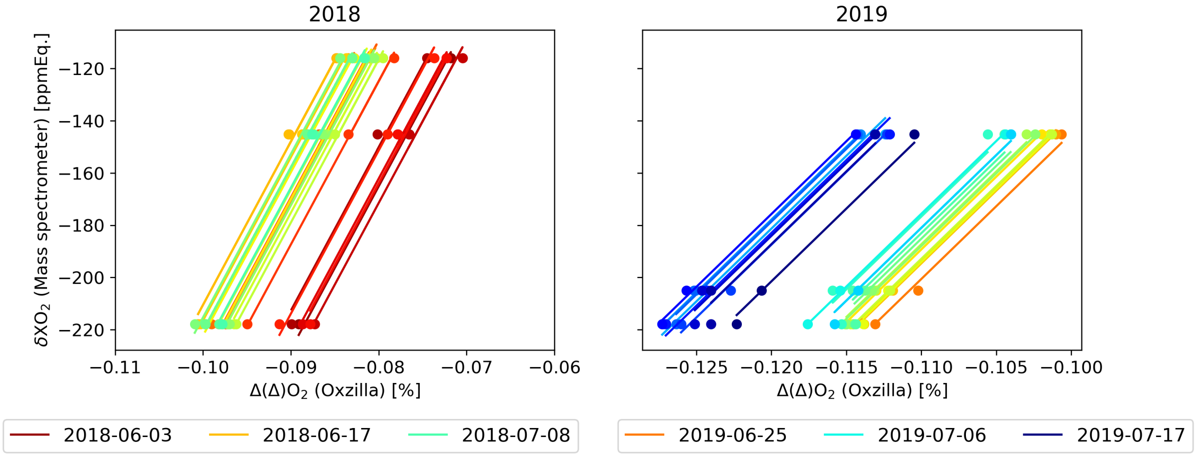

Figure 2.4: The calibration lines for the Oxzilla as calculated using the $\Delta(\Delta)O_2$ values measured by the Oxzilla analyzer (x-axis) and the assigned δXO_2 values (y-axis) obtained from the mass spectrometer. The dots are the calibration cylinders values, with colors indicating the different measurement days taken over time during both the 2018 and 2019 campaign.

of the Oxzilla can be affected by the levels of CO_2 in the sample (see Section 2.1). To compensate for this dilution effect, the $\delta(O_2/N_2)$ values of the calibration cylinders are corrected with the following equation (Keeling et al., 1998; Stephens, 1999):

$$\delta\left(\frac{O_2}{N_2}\right) = \frac{\delta XO_2 + S_{O_2}(\Delta CO_2)}{(1 - S_{O_2}) \cdot S_{O_2}} \tag{2.9}$$

Where S_{O_2} is 0.20946, δXO_2 is the mole fraction of O_2 and ΔCO_2 is the difference between the mole fraction of CO_2 and an arbitrary reference. Only CO_2 is taken into account for the dilution effect because it has the largest effect in dry air (see Sect. 2.3). Three of the four cylinders are used for the calibration procedure, while the fourth is designated as the target cylinder for validation purposes. The $\Delta(\Delta)O_2$ values of the three calibration cylinders, measured by the Oxzilla, are correlated with their respective assigned δXO_2 values (Figure 2.4). The resulting linear regression lines are used to convert the $\Delta(\Delta)O_2$ values of the measured ambient air and the target cylinder into $\delta(O_2/N_2)$ values. The intercepts of the regression lines shift over time due to changes in pressure and when changing reference gases. The instrument response between $\Delta(\Delta)O_2$ and δXO_2 is linear. To get a more accurate value for the slope, we take the mean slope of all the regression lines of the measurement period for each individual campaign (a period of around 6 weeks).

The accuracy and precision of the calibration were assessed using the target cylinder. The precision over time was determined by calculating the difference between the assigned $\delta(O_2/N_2)$ value, measured by the mass spectrometer, and the $\delta(O_2/N_2)$ value measured by the Oxzilla analyzer (Figure 2.5). For the 2019 campaign, the accuracy was 22 per meg between 16-09-2019 and 22-07-2019. The precision was determined using the standard deviation of the $\delta(O_2/N_2)$ values obtained from the Oxzilla analyzer, which was 19 per

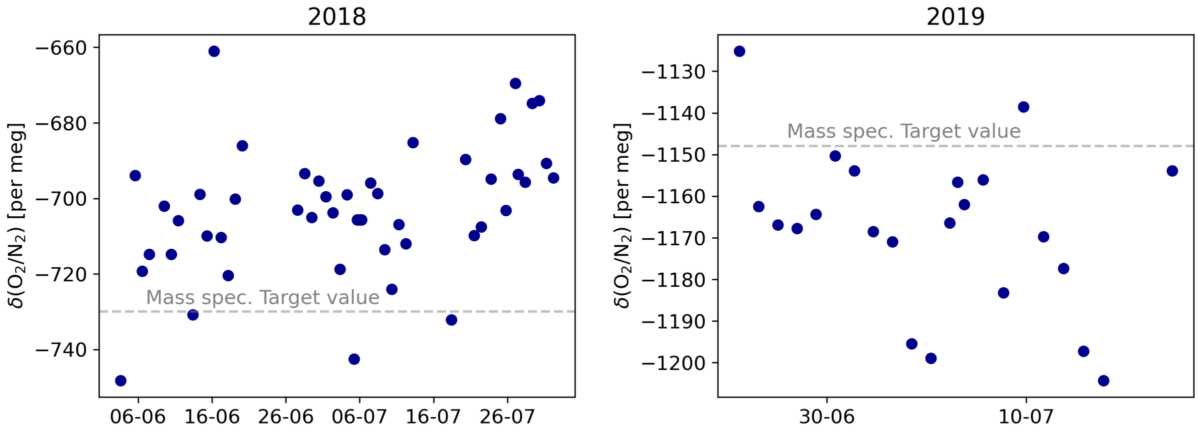

Figure 2.5: The $\delta(O_2/N_2)$ measurements of the target cylinder during the 2018 and 2019 campaign periods. The dots are the $\delta(O_2/N_2)$ values measured by the Oxzilla analyzer and the horizontal dotted lines is the assigned $\delta(O_2/N_2)$ value measured by the mass spectrometer on the SIO2017 scale.

meg for 2019. The precision of our measurements is relatively low compared to 5.0 per meg achieved by previous studies that used a fuel cell analyzer (Battle et al., 2019; Ishidoya et al., 2013; van der Laan-Luijkx et al., 2010; Popa et al., 2010; Pickers et al., 2022). The implications of this are discussed in Chapter 3.

During the 2019 measurement campaign, there was an issue with pressure stability in the instrument. Normally, the MKS differential pressure (PMKS) sensor and regulator ensure a differential pressure between the sample (S) and reference (R) lines of close to 0 mbar. When this works correctly, changes in $\Delta(\Delta)O_2$ values depend only on the sampled air and are not affected by pressure differences between the two lines, as observed during the 2018 campaign (Figure 2.6). However, during the 2019 campaign, the PMKS did not operate properly, resulting in a correlation between the $\Delta(\Delta)O_2$ measurements and the PMKS measurements. We therefore applied a correction to the measured $\Delta(\Delta)O_2$ values for pressure variations, following this relationship:

$$\text{Corrected } \Delta(\Delta)O_2 = \Delta(\Delta)O_2 - 0.095 \cdot \text{PMKS} \tag{2.10}$$

This correction was based on the linear regression line between $\Delta(\Delta)O_2$ measurements and the PMKS measurements for the calibration cylinders (black line in Figure 2.6). The impact of this correction on the measurements is further described in Appendix A3.1 in Chapter 3.

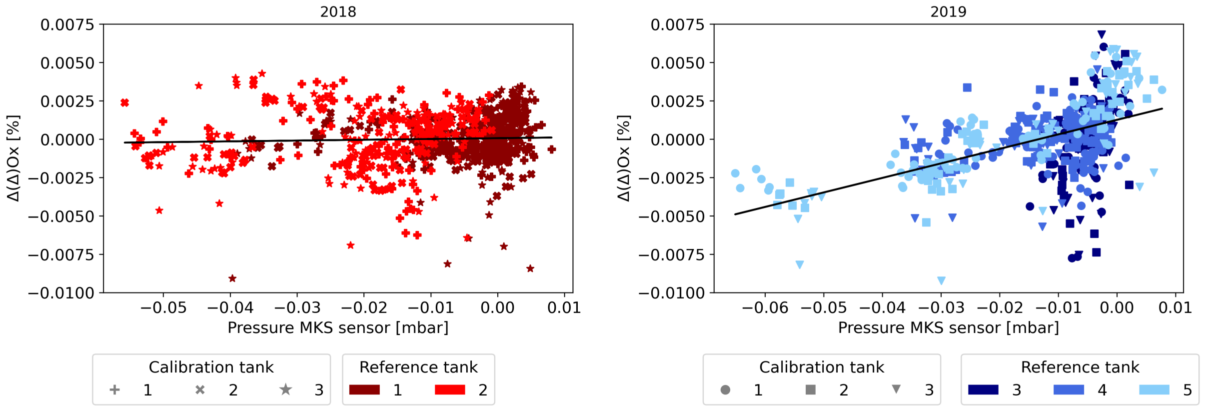

Figure 2.6: Comparison of the relation between $\Delta(\Delta)O_2$ values and the pressure measured by the MKS differential pressure sensor during the Hyytiälä measurement campaigns during 2018 and 2019, indicating an issue during the 2019 campaign. The symbols represent individual calibration cylinders and the colors indicate the periods during which specific reference cylinders were used. The line represents the linear regression trough all the data points.

2.3.2 Mass spectrometer

In comparison with the Oxzilla measurements, the flask measurements are not continuous and were measured on a mass spectrometer. The mass spectrometer directly measures $\delta(O_2/N_2)$ by determining the O_2/N_2 ratio of the sampled air relative to the O_2/N_2 ratio of a machine reference gas. However, the resulting raw $\delta(O_2/N_2)$ values contain artifacts introduced by the machine itself, such as offsets, drifts, and discontinuities between different machine reference gases (the 6123 period vs the 493 period in Figure 2.7a). Additionally, the raw $\delta(O_2/N_2)$ values are not directly measured on the international Scripps Institution of Oceanography (SIO2017) scale and therefore require calibration. For the calibration, we used the working cylinders named 6168, 5279, 4845 and 8160 that were measured against the machine reference cylinders until they were almost empty. The calibration for the measurements used in this thesis covers the period from January 2019 to February 2024, extending the work of van der Laan-Luijkx et al. (2010), Leeuwen and Meijer (2015) and Nguyen et al. (2022).

First, the raw $\delta(O_2/N_2)$ values are filtered to remove outliers (Figure 2.7a). Outliers were filtered using an exclusive filter. In that process, outliers are identified as values that fall outside the range defined by 2.7σ (std) of the mean of the dataset without the outlier, which is around 1% of the data. This process is iteratively repeated until no further outliers remain. Next, the mean $\delta(O_2/N_2)$ value of each working cylinder is calculated for each machine reference cylinder period. This mean value is subsequently subtracted from the filtered raw $\delta(O_2/N_2)$ values. This step allows the different working cylinders to be combined, enabling the determination of the machine's drift and offset (Figure 2.8) based on multiple working cylinders. The drift and offset of the mass spectrometer are

Figure 2.7: The $\delta(O_2/N_2)$ values shown both as both raw data from the mass spectrometer (a) and after calibration to the local Center for Isotope Research (CIO) scale and the international SIO2017 scale (b). Both time series have been filtered to exclude outliers using a filter removing values further than 2.7σ from the mean. The colors represent the working gases and the labels 6123 and 493 indicate the respective machine reference gas periods.

not constant over time. Therefore, calibration periods are identified that have their own drift and offset, as indicated by different colors in Figure 2.8.

Second, the raw $\delta(O_2/N_2)$ values are corrected for both drift and offset across all calibration periods using the working cylinders. Figure 2.9 illustrates this process for a single calibration period. First, a linear regression line is calculated. A drift is identified if the slope of the regression line exceeds 100 per meg/year. In the example shown in Figure 2.9, the drift was -338.4 per meg/year. In this case, the offset is the y-intercept of the starting point of the regression line, 33.4 per meg. If no significant drift is observed in the calibration period, the offset is determined using the mean $\delta(O_2/N_2)$ value of the calibration period period, rather than using the starting point of the fitted slope.

Finally, after correcting for drift and offset using the working cylinders, it is necessary to convert the $\delta(O_2/N_2)$ values to the appropriate scale. Figure 2.7a illustrates that a jump occurs when the same working cylinder is measured against different machine reference cylinders. These jumps are resolved by moving all measurements to a common machine reference cylinder (see Figure A.4 in Leeuwen, 2015). This common machine reference gas is the scale that was defined as the Center for Isotope Research (CIO) scale (Figure 2.7b) using the original machine reference gas 2534 that was in use around 2000. The CIO

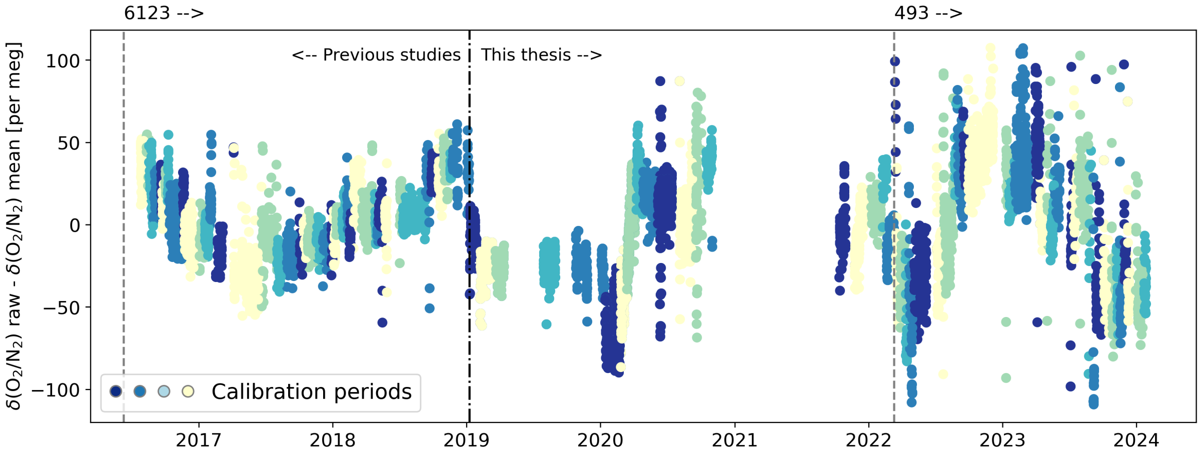

Figure 2.8: The raw $\delta(O_2/N_2)$ values for all working cylinders together with their respective means subtracted for each machine gas period (indicated with the dashed vertical lines). The colors represent the calibration periods, each characterized by a specific offset and drift. The vertical dash-dotted line marks the beginning of the period calibrated in this thesis.

scale standardizes the measurements as if they were measured against the original machine reference gas. This cylinder (number 2534) was used as the primary machine reference gas in 2000, but was eventually depleted. As a result, measurements made using later machine reference gases are now converted back to the equivalent values that would have been obtained with cylinder 2534. However, the CIO scale cannot be directly compared with $\delta(O_2/N_2)$ values from other labs. To enable such comparison, an international scale has to be applied: the Scripps (SIO2017) scale (Figure 2.7b). The SIO scale is applied by measuring 6 cylinders obtained from SIO on the Groningen mass spectrometer. These cylinders were provided by the Scripps Institution of Oceanography laboratory, each with an assigned $\delta(O_2/N_2)$ value on the SIO2017 scale.

The resulting calibration was applied to all measured cylinders and flasks during the measurement period. In this thesis, we used the flasks collected at Loobos in 2022, both from the tower and from aircraft above the forest. The results are shown in Chapter 5.

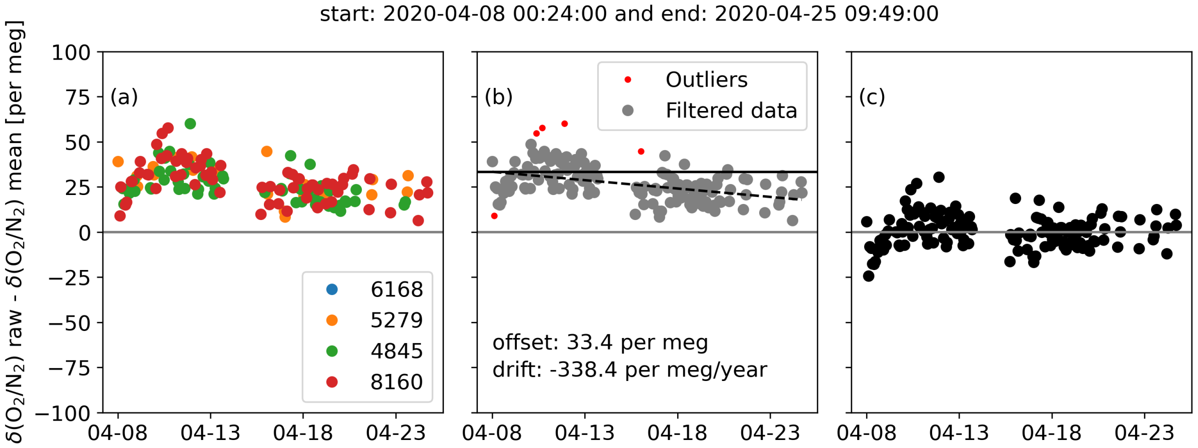

Figure 2.9: An example calibration period illustrating: (a) the raw $\delta(O_2/N_2)$ values from which the mean $\delta(O_2/N_2)$ value for each individual working cylinder was subtracted, here, the 0 line is the mean for the whole machine gas period; (b) a linear regression showing the drift (dotted line) and the offset at the beginning of the period (horizontal solid line); (c) the corrected values from (a) adjusted for both the drift and the offset shown in (b). The resulting values are around 0 per meg, which represents the mean of all working cylinders across this machine reference period.

2.4 Modeling O_2 and CO_2

In this thesis, O_2 biosphere exchange was integrated as new tracer into two models to enhance our understanding of O_2 variability in the atmosphere and for biosphere exchange. Until now, O_2 biosphere fluxes have only been modeled using either a simple one-box model (Seibt et al., 2004) or a multi-layer biosphere model (Yan et al., 2023), both with a fixed O_2:CO_2 ratio in the atmosphere. Both these methods do not include the influence of the atmosphere on the surface, or look at regional variability of O_2 biosphere exchange. To further study these points, we implemented O_2 exchange processes in the mixed-layer Chemistry Land-surface Atmosphere Soil Slab (CLASS) model (Vilà-Guerau de Arellano et al., 2015) and the Simple Biosphere model (SiB4) (Haynes et al., 2019), and we transported the resulting biosphere fluxes with a global atmospheric transport model (TM5, Krol et al., 2005) and regional atmospheric transport model (the Stochastic Time-Inverted Lagrangian Transport (STILT) model, Gerbig et al., 2003). These models provide a more comprehensive framework to study O_2 variability. A schematic representation of the models is shown in Figure 2.10.

In this section, we compare the models used in this thesis with respect to their representation of the atmosphere and the gross fluxes of respiration and assimilation. Detailed explanations of the individual models and their specific implementations are provided in Chapter 4 for the CLASS model and in Chapter 6 for the SiB4 model and the atmospheric transport models.

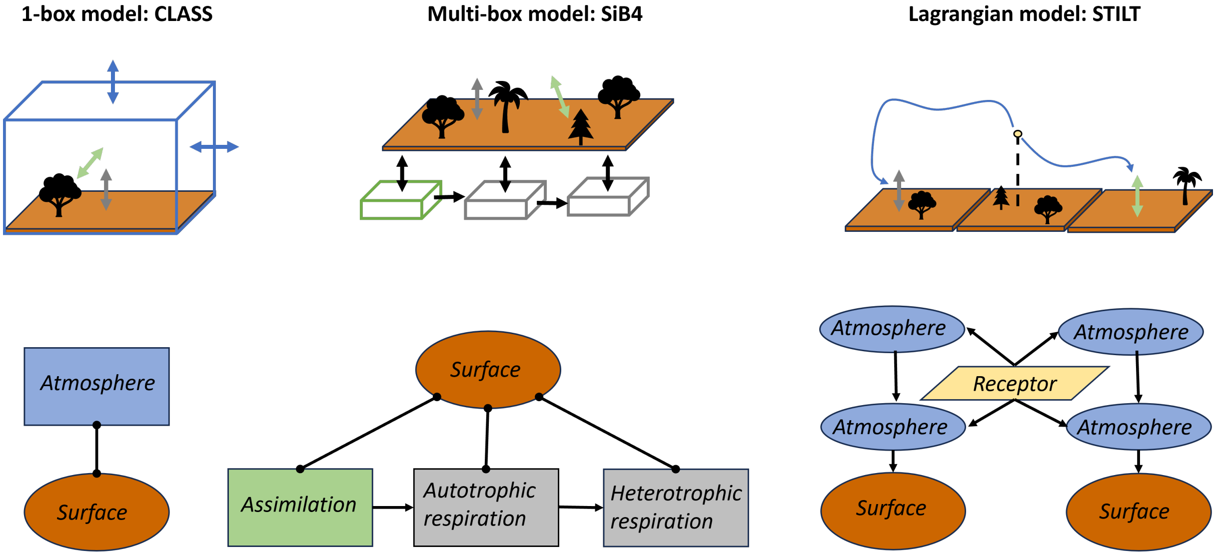

Figure 2.10: Three different models that were used in this thesis: the mixed-layer model CLASS, the biosphere model SiB4 and atmospheric transport model STILT. The 3D boxes in the first row and the rectangles in the bottom row represent the compartments of each model that calculate the carbon storage dynamics over time.

O_2 was incorporated into the models by directly linking it to the gross biosphere CO_2 fluxes. The representation of the gross fluxes differs between CLASS and SiB4 (Figure 2.10). CLASS calculates the assimilation flux using the A-gs approach for a selected vegetation type (Goudriaan et al., 1985), while the soil respiration flux is modeled based on temperature and soil moisture. In contrast, the SiB4 model connects all gross fluxes (Figure 2.10). The assimilation flux in SiB4 is calculated using the Farquhar model for multiple vegetation types at the same time for each grid box (Farquhar et al., 1980). While studies indicate no significant difference between the Goudriaan and Farquhar approaches (Van Diepen et al., 2022), SiB4's inclusion of multiple vegetation types at the same time, allows for a broader range of assimilation fluxes over time and between locations. The respiration flux in SiB4 is more complex than in CLASS, as it depends on the carbon stored within each pool, and the temperature- and moisture dependent turn-over time of each pool. Consequently, SiB4 can be run with more spatial detail and over longer time ranges, such as seasonal cycles, compared to CLASS which is best suitable to analyze a diurnal cycle in detail.

The atmospheric conditions influence the gross fluxes in both the CLASS and SiB4 model. However, the representation of the atmosphere differs between the two. The atmosphere in the CLASS model stores carbon (and oxygen) and interacts directly with the surface (Figure 2.10). In contrast, the atmosphere in SiB4 is prescribed by ERA5 reanalysis data (Hersbach et al., 2020). While the ERA5 meteorological data impacts the surface fluxes, the surface fluxes do not influence the atmosphere. To calculate an atmospheric signal from the SiB4 surface fluxes, an atmospheric transport model is required. By coupling SiB4 with the Langrangian transport model STILT, we generate an integrated atmospheric signal that reflects contributions from multiple SiB4 grid cells, each with distinct surface properties.

The differences among the three models made each suitable for the specific objectives of the studies in this thesis. In Chapter 4 and 5 the goal was to evaluate the diurnal atmospheric signal of O_2 and CO_2. Since CLASS is works best for single-day simulations, it provides an accurate description of the processes contributing to daily atmospheric signals. This made it an ideal model for gaining initial insights into the atmospheric and surface processes shaping the measured O_2 and CO_2 mole fractions. Using STILT for this purpose would have introduced unnecessary complexity for such a short time series. In Chapter 6, we shift the focus to evaluating the O_2:CO_2 ratios of the biosphere for larger scales. This gave us the opportunity to upscale the research to larger scales. Additionally, we wanted to link the surface O_2:CO_2 ratios to those observable in the atmosphere. STILT could provide these insights because the focus extended to time scales beyond a single day.

Further details on the implementation of O_2 in each of these models are provided in the respective chapters.

Chapter 3

Diurnal variability of atmospheric O_2, CO_2 and their exchange ratio above a boreal forest in southern Finland

This chapter has originally been published as:

K. A. P. Faassen, L. N. T. Nguyen, E. R. Broekema, B. A. M. Kers, I. Mammarella, T. Vesala, P. A. Pickers, A. C. Manning, J. Vilà-Guerau de Arellano, H. A. J. Meijer, W. Peters, and I. T. Luijkx (2023). "Diurnal variability of atmospheric O_2, CO_2, and their exchange ratio above a boreal forest in southern Finland". *Atmospheric Chemistry and Physics* 23 (2), 851–876

Abstract

The exchange ratio (ER) between atmospheric O_2 and CO_2 is a useful tracer for better understanding the carbon budget on global and local scales. The variability of ER (in mol O_2 per mol CO_2) between terrestrial ecosystems is not well known, and there is no consensus on how to derive the ER signal of an ecosystem, as there are different approaches available, either based on concentration (ER_{atmos}) or flux measurements (ER_{forest}). In this study we measured atmospheric O_2 and CO_2 concentrations at two heights (23 and 125 m) above the boreal forest in Hyytiälä, Finland. Such measurements of O_2 are unique and enable us to potentially identify which forest carbon loss and production mechanisms dominate over various hours of the day. We found that the ER_{atmos} signal at 23 m not only represents the diurnal cycle of the forest exchange but also includes other factors, including entrainment of air masses in the atmospheric boundary layer before midday, with different thermodynamic and atmospheric composition characteristics. To derive ER_{forest}, we infer O_2 fluxes using multiple theoretical and observation-based micro-meteorological formulations to determine the most suitable approach. Our resulting ER_{forest} shows a distinct difference in behaviour between daytime (0.92 ± 0.17 mol/mol) and nighttime (1.03 ± 0.05 mol mol^{-1}). These insights demonstrate the diurnal variability of different ER signals above a boreal forest, and we also confirmed that the signals of ER_{atmos} and ER_{forest} cannot be used interchangeably. Therefore, we recommend measurements on multiple vertical levels to derive O_2 and CO_2 fluxes for the ER_{forest} signal, instead of a single level time series of the concentrations for the ER_{atmos} signal. We show that ER_{forest} can be further split into specific signals for respiration (1.03 ± 0.05 mol/mol) and photosynthesis (0.96 ± 0.12 mol/mol). This estimation allows us to separate the net ecosystem exchange (NEE) into gross primary production (GPP) and total ecosystem respiration (TER), giving comparable results to the more commonly used eddy covariance approach. Our study shows the potential of using atmospheric O_2 as an alternative and complementary method to gain new insights into the different CO_2 signals that contribute to the forest carbon budget.

3.1 Introduction

To understand how the increasing carbon dioxide (CO_2) levels in the atmosphere will change our climate, we need to know the sources and sinks of CO_2 separately. The main sources are fossil fuel combustion and land-use change and the main sinks are the net uptake by the terrestrial biosphere and the oceans (Friedlingstein et al., 2022). The net terrestrial biospheric sink (net ecosystem exchange, NEE) results from many fluxes of which the two largest are typically gross primary production (GPP) and the total ecosystem respiration (TER). Knowing these gross fluxes separately will allow for better estimates of the changing behaviour of the biosphere carbon sink, as GPP and TER respond differently to climate change and increasing atmospheric CO_2 levels (Cox et al., 2013; Ballantyne et al., 2012).

Using tracers in addition to CO_2 allows us to gain further insights into GPP and TER, without relying on a temperature-based function to parameterize TER as is used for eddy covariance (EC) measurements (e.g. Reichstein et al., 2005). Tracers such as atmospheric O_2 (Keeling and Manning, 2014), as well as COS, $\delta^{13}C$ or $\Delta^{17}O$ have the important advantage of sharing a process or pathway with CO_2 directly (Wehr et al., 2016; Whelan et al., 2018; Peters et al., 2018; Koren et al., 2019; Kooijmans et al., 2021). This allows one to use numerical models to test formulations of processes, such as stomatal and mesophyll exchange, photosynthesis, pool-specific respiration, and even turbulent canopy exchange. Atmospheric O_2 is directly coupled to CO_2 in several processes through the so-called exchange ratio (ER) (Keeling and Manning, 2014; Manning and Keeling, 2006; Keeling et al., 1993). This ER indicates the number of moles of O_2 that are consumed per moles of CO_2 that are produced (or vice versa) and gives a process-specific signature (Keeling, 1988).

On the global scale, the $O_2 : CO_2$ molar ratio ER has been used to derive the global oceanic CO_2 sink and determine the global carbon budget (Stephens et al., 1998; Rödenbeck et al., 2008; Tohjima et al., 2019). This is done by solving the atmospheric budgets of O_2 and CO_2 with the following equations:

$$\frac{dCO_2}{dt} = F - O - B \tag{3.1}$$

$$\frac{dO_2}{dt} = -\alpha_F F + \alpha_B B + Z_{O_2} \tag{3.2}$$

where F is the fossil fuel CO_2 emissions, O is ocean CO_2 uptake, B is the net terrestrial biosphere sink of CO_2 and Z_{O_2} indicates the ocean O_2 outgassing. Symbols α_F and α_B indicate the global ERs for fossil fuel combustion and the net terrestrial biosphere sink, respectively. In these global studies simplified global average values are used for α_F and α_B, where α_F is determined from the global mixture of fuels burned, which results in 1.38 [mol mol^{-1}] (Keeling and Manning, 2014) and α_B was determined by laboratory measurements and a literature study of different plant and soil materials, which resulted in

1.1 [mol/mol] (Severinghaus, 1995). Furthermore, α_B is used to combine O_2 and CO_2 into atmospheric potential oxygen (APO) (Stephens et al., 1998) which is used in determining the ocean carbon sink, and recently it has also been shown to be a suitable tracer to detect fossil fuel emission reductions during the COVID-19 pandemic (Pickers et al., 2022). For these larger-scale applications using APO it is important to have good estimates for the terrestrial biosphere ERs.

On local/ecosystem scales, previous studies have shown that this terrestrial biosphere ER is not a constant value of 1.1 as used on the global scale, and that it shows a certain degree of temporal and spatial variability. These studies either measured the oxidative ratios (ORs) from elemental composition analysis (Worrall et al., 2013; Randerson et al., 2006; Gallagher et al., 2017), or derived the ER from atmospheric concentration measurements (Battle et al., 2019; Seibt et al., 2004; Laan et al., 2014a). Note that there is a distinction in the terminology between ER and OR. The OR indicates the stoichiometry of specific materials, whereas the ER indicates the exchange between the atmosphere and organisms or ecosystems. By using elemental composition analysis, the OR reflects the relationship between O_2 and CO_2 over a longer timescale, of years or decades and only reflects the OR from the materials that are sampled. By using atmospheric concentration measurements for the ER, the ER reflects a shorter time scale compared to the OR, of hourly to daily time periods, and it also reflects a different spatial scale, as the ER includes all processes that are originating from the footprint. The spatial scale that is covered by the ER signal depends on the type of measurements or modelling, i.e. leaf, canopy or ecosystem. Both the OR- and the ER-based studies showed that $O_2 : CO_2$ molar ratio of the biosphere changes per ecosystem and over different time periods. The ER from the gas exchange experiments can furthermore be used for the separation of GPP and TER, using a specific ecosystem ER, which are determined with two alternative approaches (see Fig. 3.1) (Seibt et al., 2004; Stephens et al., 2007; Ishidoya et al., 2013; Ishidoya et al., 2015; Battle et al., 2019). The first is the ER of the atmosphere (ER_{atmos}), which is the ratio of the evolution of the atmospheric O_2 and CO_2 concentration measurements over time, and the second is the ER of the forest (ER_{forest}), which is the ratio of the net surface fluxes of O_2 and CO_2 above the canopy, including all processes occurring below the canopy, including both vegetation and soil exchange. First attempts to estimate ER_{forest} were made using one-box models (Seibt et al., 2004; Ishidoya et al., 2013). More accurate estimates of ER_{forest} would be based on in situ measured O_2 and CO_2 surface fluxes; however O_2 currently cannot yet be measured accurately using EC techniques. Ishidoya et al. (2015) showed the first surface fluxes of O_2 using vertical gradients of O_2, an alternative technique to EC, and CO_2 measurements at two heights above the canopy in the surface layer in a temperate forest in Japan. Their results showed that the ER_{forest} signal could be used to separate the NEE signal into GPP and TER, consistent with the separation method for EC measurements using an empirical function of air temperature.

When using O_2 to separately estimate GPP and TER fluxes, it is important to use the value for ER that represents ecosystem exchange. Seibt et al. (2004) showed that the signal of ER_{atmos} cannot be directly linked to the exchange of carbon in the terrestrial biosphere, because in addition to the biosphere, ER_{atmos} is also affected by advection, boundary layer dynamics, and entrainment (Fig. 3.1). In contrast, Ishidoya et al. (2015) found similar values for ER_{atmos} and ER_{forest}. So far, there is no clear consensus on which signal should be used to indicate the ER of the ecosystem. Furthermore, since atmospheric O_2 measurements are challenging to make, only a few studies exist that measured atmospheric O_2 from flasks (Seibt et al., 2004) or continuously (Ishidoya et al., 2015; Stephens et al., 2007; Battle et al., 2019) above an ecosystem and derive ER signals. The uncertainty and spatial and temporal variability of $O_2 : CO_2$ molar ratio of the biosphere are therefore not well known (Manning and Keeling, 2006; Keeling and Manning, 2014), and knowledge about the difference between ER_{forest} and ER_{atmos}, its variability across difference regions and ecosystems, and how ER_{forest} can be used on both the local and global scale to advance our understanding of the carbon cycle, is still limited. Therefore, more and longer in situ time series of atmospheric O_2 measurements are needed, and further understanding of O_2 and CO_2 exchange above and below the canopy is crucial to continue the pioneering work by Seibt et al. (2004), Stephens et al. (2007), Ishidoya et al. (2015) and Battle et al. (2019) to improve the application of the global biosphere ER, resulting in a better understanding of the carbon balance on local, regional, and global scales.

The aim of this study is to improve upon existing methods to calculate ER_{forest} and get a better comparison of the ER_{atmos} and ER_{forest} signals. We carried out a measurement campaign in Hyytiälä, Finland, for two short periods in spring/summer 2018 and 2019 where both O_2 and CO_2 were measured at two heights with a setup including a differential fuel cell analyser for O_2. We used our measurements to determine the diurnal behaviour of the relation between the concentrations and the fluxes of O_2 and CO_2, by using either one or both measurement heights on the tower. The objectives of this study are the following: (1) to extend the existing continuous O_2 records, (2) to calculate the O_2 surface fluxes in a boreal forest for the first time, (3) to combine the O_2 and the CO_2 fluxes, to calculate ER_{forest} from these fluxes, and to compare the ER_{atmos} and ER_{forest} signals, and (4) use ER_{forest} to estimate GPP and TER fluxes.

In this paper, we first describe the measurement site, experimental setup and methods used to derive O_2 fluxes and the different ER signals (Sect. 3.2). We present the measurements for the whole campaign, and we select a representative day to determine the most suitable approach for deriving O_2 fluxes and to determine ER_{forest} (Sect. 3.3). A detailed evaluation and discussion of our ER_{atmos} and ER_{forest} signals is given in Sect. 3.4. We finalize with our conclusion about the diurnal variability of the ER signals for a representative day of a boreal forest (Sect. 3.5).

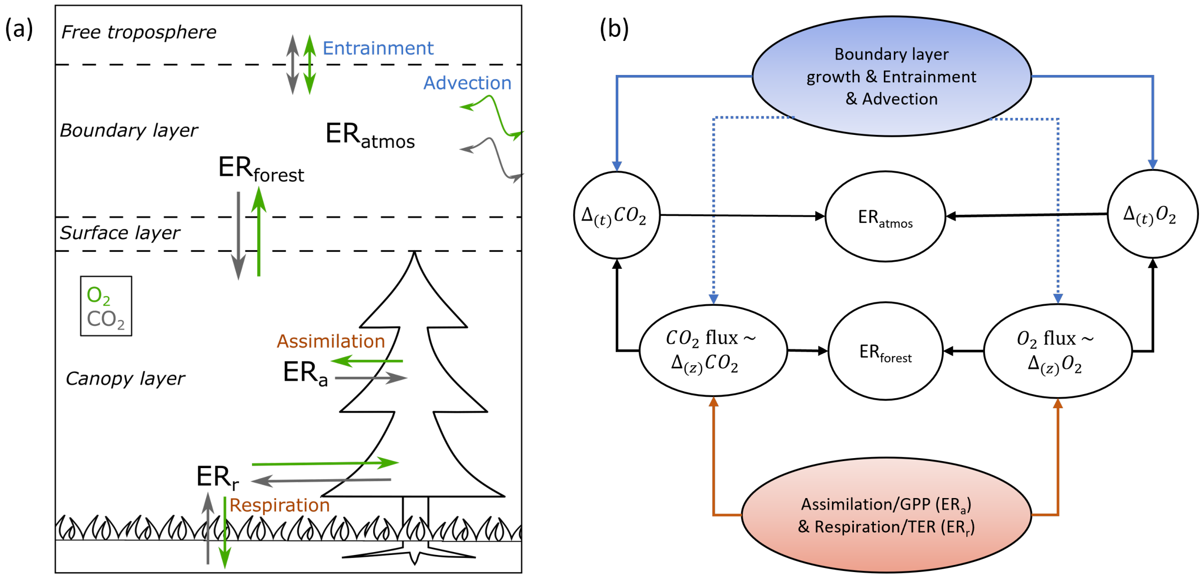

Figure 3.1: Schematic overview of the different $O_2 : CO_2$ exchange ratio signals (ER), measured and analyzed in and above a forest, influenced by the different O_2 and CO_2 fluxes and meteorological processes (a), together with a more detailed look on which processes influence the different ER signals (b). (a) shows the direction of the surface fluxes during the day in the surface layer, which includes the roughness sublayer and the inertial sublayer. During the night the direction of the O_2 and the CO_2 surface fluxes are the other way around. The ER of the atmosphere (ER_{atmos}) is determined from the change over time ($\Delta_{(t)}$) in the O_2 and CO_2 concentration measurements, and the ER of the forest (ER_{forest}) is calculated from the surface fluxes of O_2 and CO_2 which are inferred from ($\sim$) the vertical gradient ($\Delta_{(z)}$). ER_a represents assimilation processes that influence the gross primary production (GPP) flux and ER_r represents respiration processes that influence the total ecosystem respiration (TER) flux. (b) shows the connections between the processes, measurements, and the ERs. Dotted lines indicates smaller influences of the processes that are connected to it compared to solid lines.

3.2 Methods

To determine ER_{atmos} and ER_{forest}, and its diurnal variability, we measured O_2 and CO_2 continuously at two heights above a boreal forest during two short campaigns at Hyytiälä. These ‘OXHYYGEN’ (oxygen at Hyytiälä) campaigns took place in the spring/summer of 2018 (3 June through 2 August) and 2019 (10 June through 17 July). In this section, we describe the measurement site and instrumental setup, as well as the methods used to determine the O_2 and CO_2 fluxes from the measured vertical gradient and the ER signals.

3.2.1 Measurement site

The measurements were made at Hyytiälä SMEAR II forestry station of the University of Helsinki in Finland (61° 51’N, 24°17’ E, +181 m a.m.s.l.; time zone: UTC+2); this site is described in more detail in for example Hari et al. (2013). The SMEAR II station is a boreal site within the European Integrated Carbon Observation System (ICOS) network with atmospheric and ecosystem measurements. The SMEAR II station is located inside a homogeneous forest of Scots pine trees (*Pinus Sylvestris*) with a dominant canopy height of 18 m and some silver birch and aspen trees. The forest floor is covered with mosses and herbs. The soils are podzols on top of glacial till. A large lake is located close (around 550 m) to the measurement site and has a fetch of 250 m over the dominant wind direction of 230°. The footprint of the site is mostly influenced by natural sources, with the atmospheric signal dominated by forest exchange (Carbon Portal ICOS RI, 2022). The measurement site includes several towers, including a 128m tall tower and a 23 m high walk-up tower, where atmospheric variables and gas concentrations are continuously measured. The operational data from this tower are publicly available online at http://avaa.tdata.fi/web/smart/smear/ (last access: 5 January 2022). Our O_2 and CO_2 measurement setup was installed in a cabin at the bottom of the 23 m high tower, and air was sampled from aspirated inlets (Blaine et al., 2006), installed at 23 m in the smaller tower and at 125 m in the tall tower, which are 5 m and 107 m above the canopy height, respectively. We used both levels to calculate the vertical gradient for the flux calculations (Sect. 3.2.3).

3.2.2 Experimental setup

The measurement setup is based on the instrument used in Leeuwen and Meijer (2015), following the methods in van der Laan-Luijkx et al. (2010) and Stephens et al. (2007). O_2 is measured with a Sable Systems "Oxzilla II" fuel cell based instrument and CO_2 is measured with an ABB continuous gas analyser "URAS26", which is a non-dispersive infrared (NDIR) photometer. The gas-handling schematic is shown in Fig. 3.2.

Air was pumped from either 23 or 125 m height to the measurement system at the base of the tower. Both inlet lines were continuously flushed, where either one of the heights is measured by the system with a sample flow of around 120 mL min^{-1} and the other flushed to the room with a higher flow rate of around 2 L min^{-1}, which allows for fast switching between the two heights. We switched between the inlets every half hour to match the EC measurements of ICOS that were already present in the tower and to get a more stable signal of O_2. The air of the selected inlet was first cooled to -60 ° C with a cryogenic cooler to remove water vapour from the air, before entering the system. Second-stage drying of the air streams was done with magnesium perchlorate ($Mg(ClO_4)_2$) traps. The sample air was continuously measured against a reference gas (differentially for O_2, and alternatively for CO_2), and the pressure in both sample and reference lines was matched to be the same using a pressure control system (MKS Instruments, types 223B, 248A, and 250E for the pressure transducers, regulating valve and control system, respectively). The reference and sample lines were switched every 2 minutes between the two fuel cells in the

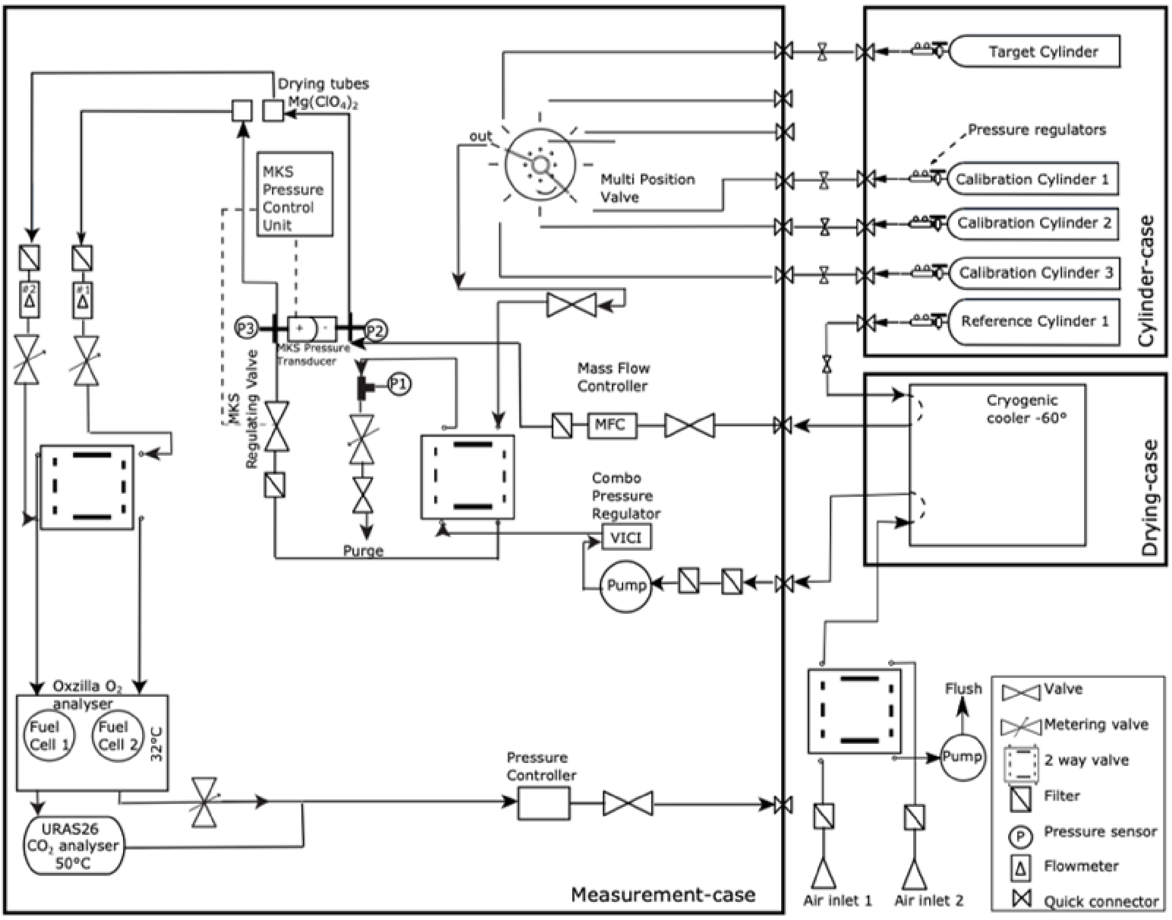

Figure 3.2: Schematic overview of the measurement setup used at Hyytiälä. The setup includes an Oxzilla O_2 fuel cell analyser and a URAS26 NDIR CO_2 analyser. The system measured air sampled from two heights of either 23 or 125 m.

Oxzilla analyser. We measured a set of three calibration cylinders and one target cylinder every 23 hours for half an hour per cylinder.

The measurements of these calibration gases allowed for calibration of our measurements against the international Scripps Institution of Oceanography (SIO) scale for $\delta O_2/N_2$. We did that by using cylinders that are filled in the laboratory at the University of Groningen, where they were calibrated with the primary Scripps cylinders (Nguyen et al., 2022). The O_2 measurements are normally expressed as $\delta O_2/N_2$ ratios in 'per meg' units instead of mole fraction (ppm), since O_2 is not a trace gas because of its high abundance of 20.95%, and therefore the mole fraction varies due to changes of other gases, such as CO_2 (Keeling et al., 1998). $\delta O_2/N_2$ is defined as:

$$\delta(O_2/N_2) = \left(\frac{(O_2/N_2)_{\text{sample}}}{(O_2/N_2)_{\text{reference}}} - 1\right) \cdot 10^6 \text{ [per meg]} \tag{3.3}$$

For simplicity, in this paper we use the term O_2 instead of $\delta O_2/N_2$, and we use the term ‘concentration’ rather than ‘mole fraction’ when discussing both CO_2 and O_2. Equation (3.3) indicates a change compared to a reference level. Negative values therefore indicate concentrations of O_2 lower than the reference value. To allow for comparison of changes in CO_2 and O_2 directly, we converted the units of O_2 from per meg to ppm equivalents (ppmEq), where a change of 1 ppm CO_2 corresponds to a 4.77 per meg change in O_2 (Tohjima et al., 2005; Kozlova and Manning, 2009).

We modified the method described in van der Laan-Luijkx et al. (2010), to calibrate the measurements. The raw CO_2 measurements have a frequency of one measurement per 6 s, the raw O_2 measurements have a frequency of one measurement per second and both give one value every 4 min in the form of ΔCO_2 and $\Delta(\Delta)O_2$, respectively. CO_2 is measured on a single cell instrument, and therefore, ΔCO_2 is the difference between the 2 min averages of the sample air (S) and the reference cylinder (R), giving (S-R). For the 2 min averaged CO_2 measurements, the last 78 s of each 2 min period were used. Note that for CO_2, the NDIR system is different compared to other systems used and therefore does not need a zero gas (Pickers et al., 2017). O_2 is measured on a double-cell instrument and therefore gives a double differential signal. The $\Delta(\Delta)O_2$ is the difference between the 2 min averaged difference between S and R and the 2 min averaged difference between R and S ((S-R)-(R-S)). For the 2 min averaged O_2 values, the last 100 seconds of each 2 min period are used. In 2019, the MKS pressure control valve was not functioning optimally, which led to a small instability in the differential pressure between the sample and reference lines. We therefore corrected the 4 min values of $\Delta(\Delta)O_2$ for this deviation measured by the MKS differential pressure sensor (PMKS), by multiplying $\Delta(\Delta)O_2$ with (0.095 x PMKS), which we derived based on the measurements of the calibration cylinders. In 2018, there was no instability in the pressure control valve, and therefore, no correction was applied in that year. The PMKS deviations correlated with temperature and increased towards the end of the 2019 campaign. Figure A3.1 in Appendix A3.2 shows that the highest corrections were made during the midday at the end of the campaign. The O_2 vertical gradient is hardly affected by the correction as it is the difference between measurements at two heights that are both undergoing the same deviation.

For both CO_2 and O_2, the 4 min values were subsequently used to calculate half-hourly means, where we excluded the first 4 min value after the heights are switched, together with the measurements that did not fall inside the boundary based on the median absolute deviation (MAD) (Rousseeuw and Verboven, 2002). For every half-hourly mean, a standard error is calculated (see Eq. (3.4)) which is used in further analysis to determine the uncertainty of our measurements.

The linear calibration response functions for both O_2 and CO_2 were calculated for every measurement period of the calibration cylinders, which was about every 23 hours. For the response functions, we used a constant slope based on the mean of all the calibration slopes measured in the specific year. The y intercept of the response functions were interpolated to the time of the measurement, based on the two calibrations bracketing the measurement time. To facilitate the comparison of the O_2 and CO_2 measurements of the two heights and allow for flux calculations based on the vertical gradient, we interpolated the data to one measurement for every 30 min for each height. Based on the target cylinders, measured during the calibration period, the stability of the long-term measurements was determined (Table 3.1). A different target cylinder, with different composition of air for 2019 compared to 2018, was used, which resulted in different outcomes for the standard deviation (SD) and the mean difference for these periods. The mean difference is calculated from the target measurements at Hyytiälä compared to the calibrated values using the SIO cylinders in Groningen. The measurement period of 2018 was also longer and so more points were included for the SD and mean difference calculations. The long-term measurement precision of this device throughout the duration of the two measurement campaigns compared to the recommendations of the World Meteorological Organization (WMO) will be further discussed in Sect. 3.4.1.

Table 3.1: The mean difference and the standard deviation (SD) of the target cylinder measurements of O_2 and CO_2 for the 2018 and 2019 periods separately, together with the number of data points used to calculate these specific values.

	2018 (3 June through 1 August)			**2019** (16 June through 17 July)		
	SD	Mean difference	Number of points	SD	Mean difference	Number of points
O_2 [per meg]	16	28	53	19	22	22
CO_2 [ppm]	0.07	0.7	53	0.07	0.5	22

3.2.3 Data analysis

For the analyses presented in this paper, we needed representative diurnal cycles of O_2 and CO_2. We looked for a representative day in 2019 when little to no clouds were present; no unexpected behaviour in the diurnal cycles for potential temperature, specific humidity, or CO_2 occurred (e.g. caused by advection); and when the O_2 data showed a clear difference between the two measurement heights. We used data from 2019 instead of 2018 as 2018 saw a large-scale drought in Europe, and 2019 was less extreme and closer to a typical boreal summer (Peters et al., 2020). However, no single representative day could be found in our 2019 record, when the O_2 data showed a clear negative vertical gradient during the day and positive during the night, in combination with the above-mentioned meteorological criteria. We therefore choose a sequence of days to create an aggregate day based on the average of several days, which is representative for this time of the year in Hyytiälä, following the same method used by Ishidoya et al. (2015). The main criterion was that the vertical O_2 gradient had to be negative during the day, and the negative relationship between the change of O_2 and CO_2 concentrations over time at 23 m was present during the entire day. This resulted in selecting the period of 7 through 12 July 2019 to create the representative day which we used in all subsequent analyses. The half-hourly values for the representative day are the averages of the data points of the individual half-hourly values for each day in the selected period. Each time step has an uncertainty that is based on the error propagation of the standard error (SE) of the 30 min averages for each day in the aggregate and is calculated for each time step with

$$SE_{aggr} = \frac{\sqrt{\sum SE_{day}^2}}{n} \tag{3.4}$$

where n is the number of days included in the aggregate, $\mathrm{SE_{day}}$ is the standard error of the 30 min average of each individual day, and the $\mathrm{SE_{aggr}}$ is the resulting standard error of a 30 min value for the representative aggregate day.

For the representative day, the two $O_2 : CO_2$ exchange ratio (ER) signals, $\mathrm{ER_{atmos}}$ and $\mathrm{ER_{forest}}$, were determined. $\mathrm{ER_{atmos}}$ is based on O_2 and CO_2 concentrations and is expressed as:

$$ER_{atmos} = -\frac{\Delta_{(t)}O_2}{\Delta_{(t)}CO_2} \tag{3.5}$$

where both $\Delta_{(t)}\mathrm{O_2}$ and $\Delta_{(t)}\mathrm{CO_2}$ are the change in concentration over a selected time period (t). This is a unitless quantity as it represents mol O_2 per mol CO_2. $\mathrm{ER_{atmos}}$ was determined by the slope of a linear regression between the concentration of O_2 and CO_2 at the same height over a specific time period (Seibt et al., 2004; Stephens et al., 2007; Ishidoya et al., 2013; Battle et al., 2019). The selected time periods were based on the period when O_2 and CO_2 had the highest negative correlation. Throughout the day, this could be divided into three periods when different processes dominate (Fig. 3.1). It starts with the period during the night when the atmosphere is stable and when respiration becomes the dominant surface flux (P1); therefore, the CO_2 concentration increases and the O_2 concentration decreases. Subsequently, when the sun starts to rise, the boundary layer height starts to grow and entrainment of air from the free troposphere influences the surface measurements (P2) (Vilà-Guerau de Arellano et al., 2004). Here the CO_2 concentration decreases rapidly and the O_2 concentration increases rapidly. Finally, the period starts when the effect of boundary layer dynamics and entrainment decreases and the assimilation flux dominates (P3); here, the CO_2 concentration decreases less rapidly and the O_2 concentration increases less rapidly. We calculated an $\mathrm{ER_{atmos}}$ signal with Eq. (3.5), for the nighttime (P1), the daytime (by either focusing on only P3 or both P2 and P3), and the complete day (P1 + P2 + P3). The exact boundaries of these periods have to be estimated. To be certain about the exact times that should be taken as the boundaries for each period, an atmospheric model is needed.

$\mathrm{ER_{forest}}$ is based on O_2 and CO_2 fluxes and is expressed as

$$ER_{forest} = -\frac{F_{O_2}}{F_{CO_2}} \tag{3.6}$$

where both F_{O_2} and F_{CO_2} are the net mean turbulent surface fluxes above the canopy of O_2 and CO_2 over a selected time period (Seibt et al., 2004; Ishidoya et al., 2015). We derive the fluxes of O_2 and CO_2 using the vertical gradient (see next paragraph and Eq. (3.7)). The selected time periods for ER_{forest} were chosen such that the transition periods between the nighttime with a stable atmosphere (when the respiration flux dominates) and the daytime with a well-mixed atmosphere (when assimilation dominates) were excluded. By excluding the transition periods, we removed the periods when the gradients of both CO_2 and O_2 were close to zero. This was done because a very small gradient makes it difficult to calculate a flux and therefore the ER_{forest} and also because during this period entrainment is the most dominant process. The exact duration of the transition periods was based on the maximum and minimum of both the friction velocity and the height of 27 m (z) divided by the Monin Obukov length (L). The friction velocity and (z/L) indicate the measure of turbulence of the atmosphere (Stull, 1988). The mean of the remaining data points of the CO_2 and O_2 flux during the stable atmosphere period was used to calculate the ER_{forest} signal of the night, and the mean of the remaining data points of the CO_2 and O_2 flux during the mixed atmosphere period was used to calculate the ER_{forest} signal of the day. The ER_{forest} for the entire day is taken as the average CO_2 and O_2 flux over the entire day. For this average, no periods are excluded, and all the data points over the 24 h are taken into account. Taking the average daily fluxes to derive ER_{forest} is a slightly different approach compared to the study by Ishidoya et al. (2015), who use the regression line between $\Delta_{(z)}O_2$ and $\Delta_{(z)}CO_2$ to determine ER_{forest}.

Currently, unlike for CO_2, the O_2 flux cannot be measured directly with an EC system. Instead, the flux can be inferred from the flux-gradient method. To calculate the flux of a certain scalar (ϕ) with the flux-gradient method, the following equation was used (Stull, 1988):

$$F_\phi = -K_\phi \cdot \frac{\partial\overline{\phi}}{\partial z} \tag{3.7}$$

where F_ϕ is the surface flux of ϕ, K is the exchange coefficient and $(\partial\overline{\phi}/\partial z)$ is the vertical gradient of $\overline{\phi}$. To determine the O_2 flux with Eq. (3.7) (where $\overline{\phi} = \overline{O_2}$), the exchange coefficient of O_2 (K_{O_2}) needs to be determined. Ishidoya et al. (2015) assumed that K_{O_2} = K_{CO_2} and determined K_{CO_2} by dividing the CO_2 flux, measured with EC, by the CO_2 vertical gradient between two measurement levels. However, the exchange coefficient can also be determined with other methods that, for example, only need two measurement heights for the vertical gradient. In this study, we explore these different options for calculating K_{O_2}. The EC measurements of the CO_2 flux were used as a reference, to determine the most suitable approach. The most suitable approach to infer the O_2 flux is then used for both K_{CO_2} and K_{O_2}. During this study we derive the surface flux in the surface layer (Fig. 3.1), and we assume that the surface flux stays constant in this surface layer, which consists of the roughness sublayer and the inertial sublayer.

We categorized the methods to determine the most suitable K into two groups: the observation-based approach (also called the K-theory (Stull, 1988) or the modified Bowen ratio method (Meyers et al., 1996)) and the theoretical approach (following the similarity theory (Dyer, 1974)). For the observation-based methods, we determined the exchange coefficient (K) in Eq. (3.7) by dividing a flux measured at 27 m, using an EC system, by a three-height (16 m, 67 m, and 125 m) vertical gradient of a specific scalar. Ishidoya et al. (2015) used this approach to calculate their O_2 flux, using the CO_2 flux and vertical gradient of two levels. Next to CO_2, we also calculated K using potential temperature (θ) for the observation-based approach.

For the theoretical approach, the K in Eq. (3.7) is determined with the Monin-Obukov similarity theory (MOST) (Dyer, 1974), where logarithmic surface layer scaling applies for K and empirical similarity functions are used to describe the effect of atmospheric stability. In addition, we used a correction which takes into account the effect of the roughness sublayer (see Appendix for details). The SMEAR II data at 27 m were used for the calculations with MOST. When only two heights for the gradient calculations are available, there is an option to integrate Eq. (3.7) (Ridder, 2010). We tested both the application with and without integration in this study. We used the ICOS data, available at the SMEAR II station, for the K calculations. For the CO_2 EC measurements, we used the gap-filled data to correct for the storage below the measurement height of the EC. Gap-filling was applied when the friction velocity (u*) was below 0.4 m s^{-1} (Kulmala et al., 2019). Appendix A3.1 gives a more elaborate explanation and provides equations of the different methods used to determine the exchange coefficients used in this study.

Finally, we select the K_ϕ from either the observation-based or the theoretical approach that produced CO_2 flux results from our CO_2 vertical gradient measurements that showed the best comparison to the EC CO_2 flux measurements. This K was used to calculate the O_2 and CO_2 fluxes, together with the vertical gradient from measurements collected during our campaigns. For our campaigns, we only have O_2 and CO_2 measurements at two heights (23 m and 125 m), which means that $\partial\overline{\phi}/\partial z$ changes into $\Delta\overline{\phi}/\Delta z$ and the gradient was calculated with finite differences.

After both the CO_2 and O_2 fluxes were determined, resulting in $\mathrm{ER_{forest}}$, we subsequently calculated the $O_2 : CO_2$ exchange ratio signals for the assimilation processes ($\mathrm{ER_a}$) and the respiration of the ecosystem ($\mathrm{ER_r}$) with the following equations (Seibt et al., 2004; Ishidoya et al., 2015):

$$NEE = -GPP + TER \tag{3.8}$$

$$NEE \cdot ER_{\mathrm{forest}} = -GPP \cdot ER_{\mathrm{a}} + TER \cdot ER_{\mathrm{r}} \tag{3.9}$$

where NEE is the net ecosystem exchange, GPP is the gross primary production and TER is the total ecosystem respiration. GPP and TER are always positive by definition, representing uptake and release by the ecosystem, respectively. Therefore, when GPP is larger than TER the resulting negative NEE values represent carbon uptake by the ecosystem. First, we assumed that nighttime NEE is equal to TER, which meant that the nighttime ER_{forest} signal is equal to ER_r. We assumed that the processes that contributed to the ER_r keep the same ratio between O_2 and CO_2 during the entire day and therefore we used a constant ER_r for the entire day. We base this assumption on studies that showed that the variability of ER_r highly depends on the bulk soil respiration (Hilman et al., 2022; Angert et al., 2015). No large changes occur in the soil temperature and the soil moisture during our (representative) diurnal cycle; therefore, we assume that the ER_r of the bulk soil respiration stays relatively constant, and with that the ER_r of the ecosystem also stays constant over the entire day. Subsequently, we calculated ER_a, for both the entire diurnal cycle and the daytime using Eq. (3.9) with the corresponding ER_{forest} and the constant ER_r. We used ICOS NEE EC measurements from the SMEAR II station at a level of 27 m in the 128 m high tower. The GPP fluxes at Hyytiälä are calculated with either of the following two approaches: (1) when NEE EC measurements are available, GPP is calculated as the difference between the NEE EC measurements and the respiration flux, which is calculated using a temperature function; or (2) when NEE EC measurements are not available, GPP is calculated using an equation that is based on the air temperature and light (photosynthetically active radiation (PAR)). A more detailed description of these calculations is given by Kulmala et al. (2019) and Kohonen et al. (2022).

By estimating ER_r and ER_a of this boreal forest, we created the opportunity to apply atmospheric O_2 measurements to separate NEE into GPP and TER (the O_2 method). We calculated ER_r and ER_a for the representative day using Eqs. (3.8) and (3.9), and we use these to calculate GPP and TER for another representative day. We selected 13 through 15 June to create a new second aggregate day and to calculate a new ER_{forest} signal for the entire day (see Fig. 3.3 d and e) for a detailed view on the measurements of those days). These three days were chosen because in 2019 they showed the clearest diurnal cycle of O_2 and a negative O_2 gradient, aside from 7 through 12 July, used above. We assume here that the ER_r and ER_a calculated for the period from 7 through 12 July are representative for the period from 13 through 15 June. Studies show that the ER_r (Hilman et al., 2022) and ER_a (Bloom, 2015; Fischer et al., 2015) values vary with changing soil and atmospheric conditions. The periods for both representative days are relatively close in time and therefore have similar conditions in the soil and the atmosphere, and we can therefore assume that the ER_r and ER_a values based on the 7 through 12 July data can also be applied to the 13 through 15 June period. By using the ER_r and ER_a determined for the first representative day (7-12 July), and ER_{forest} and NEE for the second representative day (13-15 June), we calculated GPP and TER from NEE for this second representative day. By comparing the GPP and TER fluxes of the O_2 method to the GPP and TER fluxes of the temperature-based function of ICOS (EC method), we could demonstrate how accurate the O_2 method is (Sect. 3.3.4). Both Seibt et al. (2004) and Ishidoya et al. (2015) also applied the O_2 method; however, both these studies used chamber measurements to first determine ER_a and ER_r and then used Eqs. (3.8) and (3.9) to infer GPP and TER. Unfortunately, we did not have chamber measurements of both O_2 and CO_2 available and therefore we used Eq. (3.8) and (3.9) to calculate ER_a and ER_r. This means that these two equations can be used in two ways: to determine the ER_a and ER_r signal, or to separate NEE into GPP and TER.

The footprint of the calculated O_2 and CO_2 surface fluxes that also represents the footprint of the ER_{forest}, ER_r and ER_a signals for the representative aggregate day is shown in Fig. A3.2 in Appendix A3.2. The footprint is based on the method by Kljun et al. (2015), where for the height, the geometric mean between 125 and 23 m is used. The footprint analysis shows that the surface fluxes are mainly influenced by the forest surrounding the tower and that the lake located close to the tower is not influencing the signal. The footprint of the O_2 and CO_2 concentrations and therefore the footprint of the ER_{atmos} signal can be found in the document by (Carbon Portal ICOS RI, 2022). This concentration footprint analysis shows that with an average wind direction of north to northeast during 7 through 12 July 2019, the concentrations measured are mainly originated from forest exchange, with hardly any influence of urban sources.

Table 3.1 in Appendix A3.2 gives a complete overview of which data are used for each part of this research for the two different aggregate days.

3.3 Results

3.3.1 O_2 and CO_2 time series

The calibrated half-hourly measurements of O_2 and CO_2 for 2018 and 2019 are shown in Fig. 3.3, together with the vertical gradients between the two measurement heights. The O_2 measurements are shown here converted from per meg to ppmEq, which is to allow for comparison of the diurnal variability for CO_2, and to calculate the ER signals. The differences between the 23 and 125 m measurements are observable for both CO_2 and O_2. During both campaigns in 2018 and 2019, the diurnal behaviour of the O_2 concentrations are anticorrelated with the CO_2 concentrations. This anticorrelation between O_2 and CO_2 is also visible from the gradient measurements, despite the relatively high uncertainty of the O_2 measurements as described in Sect. 3.2.2 and further elaborated on in Sect. 3.4.1. The period 7 through 12 July 2019 shows the most clear negative relationship between the O_2 gradient and the CO_2 gradient, and it also had the most suitable meteorological conditions and was therefore selected for the aggregate representative day (Sect. 3.2.3). The period 13 through 15 June shows a less clear anticorrelation between the vertical gradients of O_2 and CO_2 (Fig. 3.3 d and e), but with clear diurnal cycles of O_2 and CO_2 suitable for the purpose of our second aggregate day (see Sect. 3.3.4).

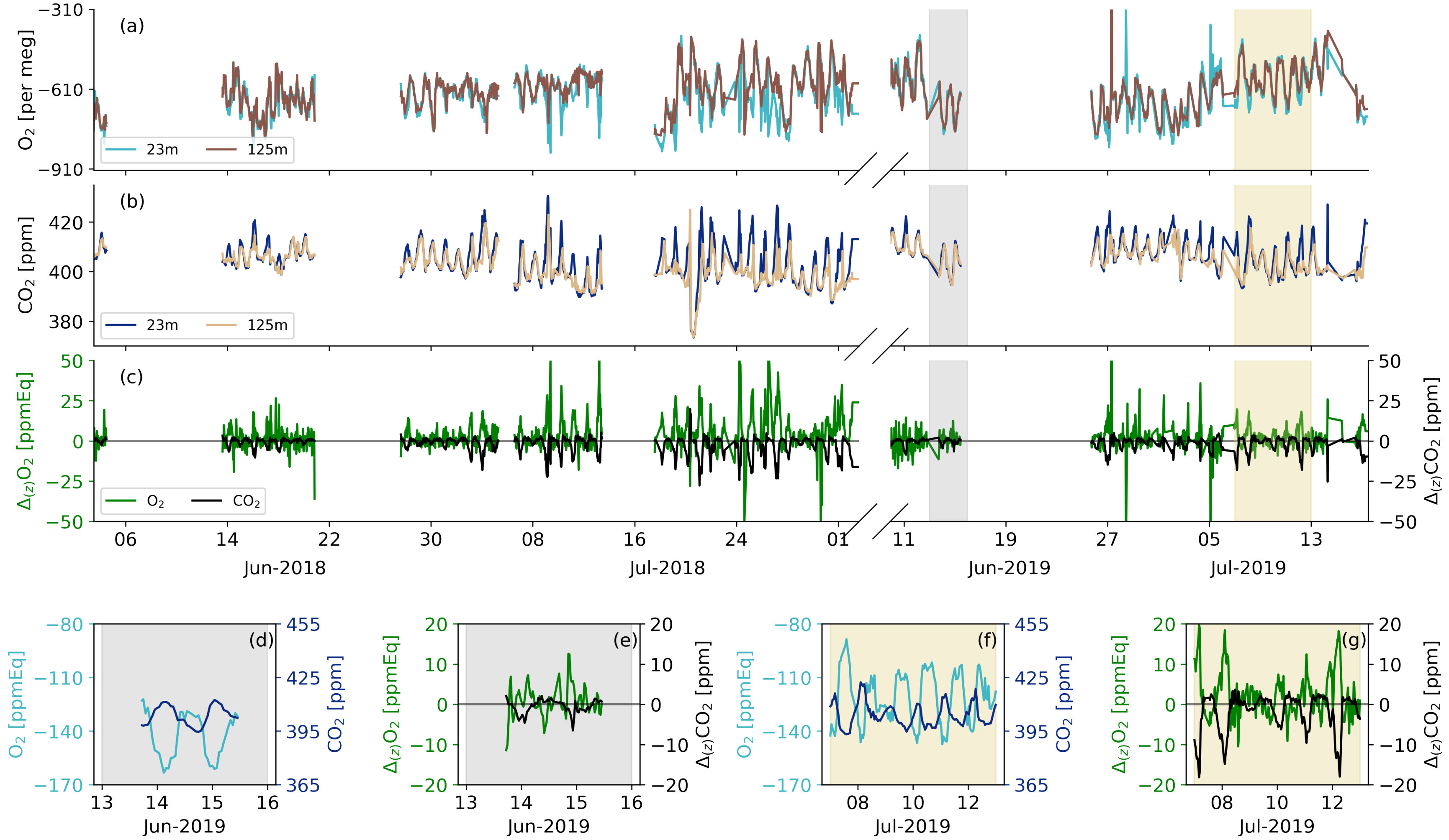

Figure 3.3: The half-hourly average O$_2$ (a) and CO$_2$ (b) concentrations at Hyytiälä for spring/summer of 2018 and 2019 for the 125 and 23 m height levels, together with the vertical gradient ($\Delta_{(z)}$) between these two heights (c) for both O$_2$ and CO$_2$. The shaded areas indicates the dates that were selected for the aggregate representative day (7 through 12 July 2019: yellow) and the second representative day to test the O$_2$ method (13 through 15 June 2019: grey). The selected days for the aggregate representative days are shown in more detail for the 23 m measurements and the gradients for 13 through 15 June (d) and (e) and for 7 through 12 July (f) and (g) for both O$_2$ and CO$_2$.

3.3.2 Diurnal cycles

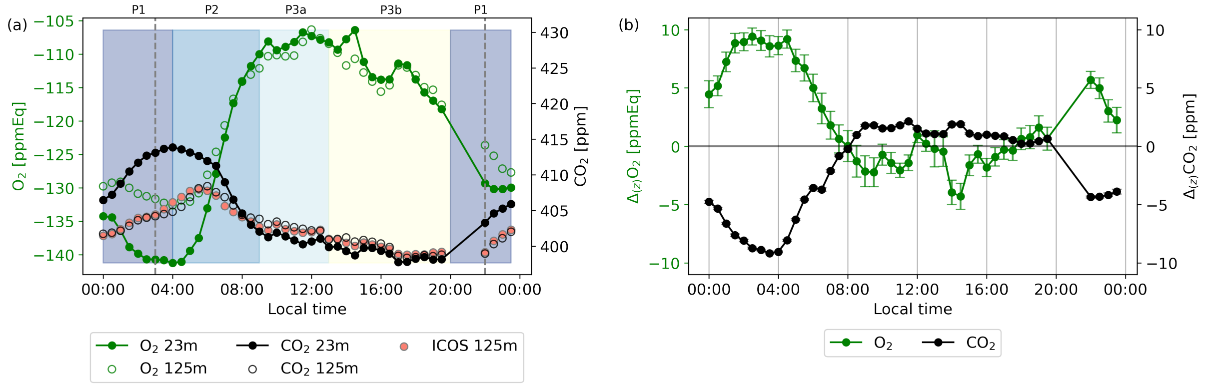

Figure 3.4: Diurnal cycles in local wintertime (LT; time zone UTC+2) (all times in this paper are given in local time unless stated otherwise) of the O_2 and CO_2 concentrations for the 23 and 125 m height levels (a) and the vertical gradient between both levels with the uncertainty of both O_2 and CO_2 of the representative day, taken as the average values of 7 through 12 July 2019 (b). The CO_2 measurements of the ICOS setup are shown in (a) for comparison with the CO_2 setup measured during our campaigns. The shaded colours indicate the selected different periods when the most dominant processes are the following: stable atmosphere and respiration (00:00-04:00, P1); entrainment, boundary layer growth, and assimilation (04:00-09:00, P2); convective conditions and assimilation (09:00-13:00, P3a); and the same as P3a plus a remaining artefact for the O_2 measurements after the pressure correction as explained in the text (13:00-20:00, P3b). The vertical dotted lines indicate the sunrise (03:00) and sunset (22:00). The error bars in panel (b) are half-hourly standard errors based on the error propagation of the standard errors of the data points in (a) (not shown), which were based on Eq. (3.4).

The measurements of O_2 and CO_2 and their vertical gradient for the representative day, are shown in Fig. 3.4. There are no measurements between 20:00 and 22:00 because the calibration cylinders were measured during this period. For 7 through 12 July, we used a fixed calibration time, as radiosondes were launched (not shown) during this period, and we wanted to make sure we captured the morning transition to compare with these radiosondes. Note that the daylight length at Hyytiälä is long at this time of the year, with sunrise at 03:00 and sunset at 22:00. We compared our CO_2 observations with ICOS CO_2 measurements at the same height, which shows that both instruments compare well overall, with a mean difference of 0.70 ± 0.65 ppm during the period 7 through 12 July. The comparison between the two devices was a bit difficult because of the different timing of the measurements. The diurnal cycles of O_2 and CO_2 (Fig. 3.4a) clearly show anticorrelated behaviour between CO_2 and O_2, which is especially visible during nighttime (23:00 - 04:00) and the morning transition (05:00 - 13:00).

Figure 3.4 shows four different periods that can be linked to the periods to calculate ER_{atmos}, described in Sect. 3.2.3. P1 is visible between 23:00-04:00, where respiration starts to dominate the signal and therefore the O_2 concentration decreases and the CO_2 concentration increases, in a decreasing boundary layer height dominated by thermal stratification. P2 becomes visible around 04:00 and stops around 09:00, where entrainment, the growing boundary layer, and the onset of photosynthesis causes a steep increase in the O_2 concentration and a steep decrease in the CO_2 concentration. P3 can be divided into P3a and P3b and is visible between 09:00-20:00. Between 09:00-13:00 (P3a), the photosynthesis flux starts to dominate, and both the O_2 and CO_2 concentration increase and decrease less rapidly. Between 13:00-20:00 (P3b), the O_2 concentration starts to decrease, while the assimilation flux still dominates, which is a remaining artefact from the pressure correction that we applied due to the instability of the MKS pressure transducer (see Sect. 3.2.2). As shown in Fig. A3.1 in Appendix A3.2, higher daytime temperatures cause larger PMKS deviation and therefore the effect of the pressure correction is largest during the midday, leading to a larger uncertainty in the observations in that time period. The boundary of 20:00 between P3b and P1 was difficult to determine as we missed some measurements due to the calibration period and the remaining measurements around this time have a deviation caused by the pressure transducer. Measurements at both levels show this same diurnal behaviour; however, it is more pronounced closer to the vegetation (the 23 m level).

The difference between the two heights results in a vertical gradient (Fig. 3.4b). Similar to the diurnal cycle of the concentrations, the diurnal cycles of the gradients of O_2 and CO_2 also show anticorrelated behaviour. At 08:00, the CO_2 gradient changes from negative to positive, and the O_2 gradient changes from positive to mostly negative, reflecting CO_2 being transported downwards and O_2 upwards, respectively. The magnitude of the gradient depends on the degree of vertical mixing. The sign of the gradients changes during the day, because the lowest level (23 m) is more directly influenced by forest carbon exchange compared to the highest level (125 m). Around the time of sunset, the CO_2 gradient changes from positive to negative, and the O_2 gradient changes from negative to positive, because the lowest measurement level (23 m) is now influenced more by respiration processes of the forest and soils compared to the highest measurement level (125 m). The error bars are based on the error propagation of the standard errors of each half-hourly data point, that were calculated with Eq. (3.4). The gradient of O_2 is hardly affected by the PMKS correction (see Fig. A3.1), as measurements at both heights are affected similarly.

By using Eq. (3.5), we calculated four distinct ER_{atmos} signals for different periods throughout the day at 23 m, as well as to a smaller degree at 125 m (Fig. 3.5 and Table 3.3). The same periods as shown in Fig. 3.4 are visible in Fig. 3.5. This results in an ER_{atmos} during the night (P1) of 1.22 ± 0.02 and two different possibilities for the ER_{atmos} signal during daytime. By combining both P2 and P3a, we get a signal of 2.28 ± 0.01, and by focusing only on P3a, which excludes the entrainment and the boundary layer dynamics, we get a signal of 1.10 ± 0.12. Last, by combining all the periods (P1, P2,

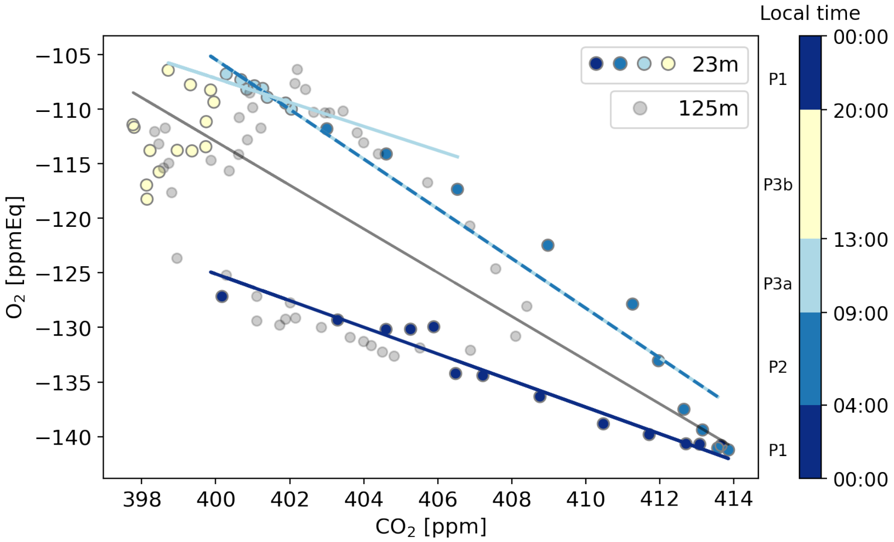

Figure 3.5: The O_2 concentration plotted against the CO_2 concentration for the representative day in local wintertime (LT; time zone UTC+2), with the 23 m level in coloured points per period representing different dominant process and with the 125 m level in grey points. The dominant processes are the following: respiration (00:00-04:00), entrainment (04:00-09:00), assimilation (09:00-13:00), and a remaining artefact after the pressure correction due to the instability of the MKS pressure transducer becomes visible (13:00-20:00). The linear regression lines indicate the exchange ratio of the atmosphere (ER_{atmos}) during the time with a specific dominant process.

P3), we get a signal for the complete day of 2.05 ± 0.03. The uncertainties given here only represent the uncertainty of the slopes from the regression lines in Fig. 3.5. The high values for the ER_{atmos} signal of the entire day and the daytime signal that includes entrainment and the boundary layer dynamics are not very realistic to represent an ER for the forest, and this shows that we should be careful when using ER_{atmos}. This will be elaborated on in Sect. 3.4.2.

3.3.3 Flux calculations for CO_2 and O_2

We explored four alternative methods to derive the O_2 flux from the vertical gradient of the two measurement levels, as described in Sect. 3.2.3. Figure 3.6 shows both the theoretical and the observation-based approaches that were used to calculate the CO_2 flux, in comparison to the ICOS EC CO_2 flux measurements at 27 m on the tower. By comparing these approaches to the EC measurements, we determined which method is most suitable to calculate the O_2 flux. The CO_2 flux measured by the EC system stays positive until around 05:00, when the respiration fluxes are the most dominant and the nocturnal boundary layer is shallower. After 05:00, the CO_2 flux of the EC system becomes negative, and the forest begins to take up CO_2 instead of emitting it. The assimilation fluxes increase and exceed the respiration fluxes, the boundary layer starts to grow, and

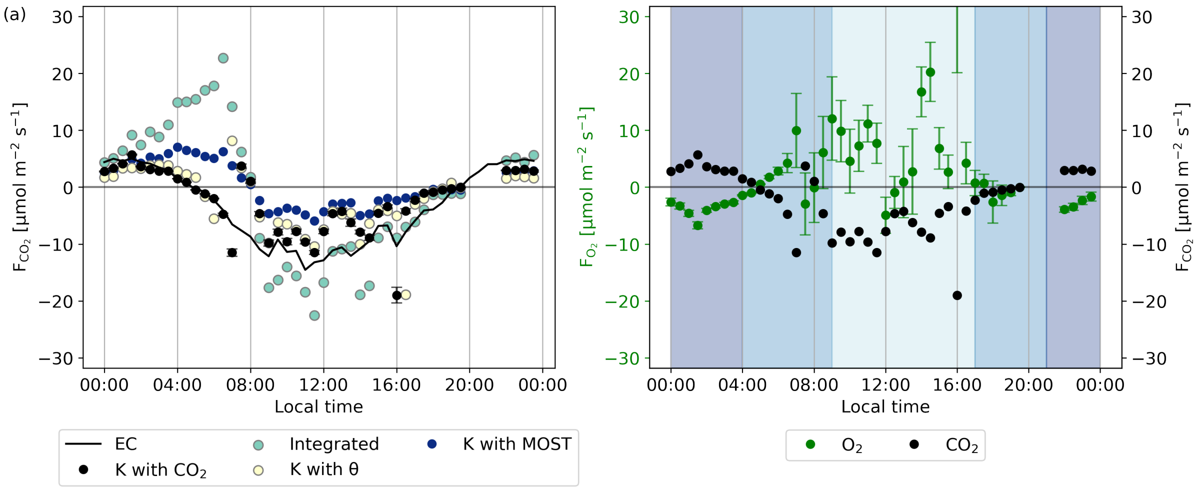

Figure 3.6: The CO_2 flux (a) calculated with different methods for the representative day, as described in Sect. 3.2.3, compared to the CO_2 flux of the ICOS EC measurements. (b) The comparison between the O_2 and CO_2 flux calculated using the method that gave the best results for the CO_2 flux calculations (using the exchange coefficient K with CO_2), for the representative day. The shaded colours indicate the regions that were selected for the following: the night signal (21:00-04:00), the day signal (09:00-17:00), and the remaining regions (04:00-09:00 and 17:00-21:00), with the time in local wintertime (LT; time zone UTC+2). The error bars of (b) are based on the error propagation of the standard error of the 30 min values for the representative day, which are based on Eq. (3.4).

air with lower CO_2 concentrations is entrained from the free troposphere. After 20:00, the CO_2 flux of the EC system becomes positive again as the assimilation fluxes decrease, and the respiration signal begins to dominate again while the boundary layer height decreases. We expect to find this diurnal pattern and the sign change in our calculations of the CO_2 flux from the vertical gradient method as well.

First, we discuss the theoretical methods that are indicated in Fig. 3.6 with 'K with MOST' and 'Integrated' approaches (see Sect. 3.2.3). The MOST and the integrated methods both overestimate the CO_2 flux during the night, between 0:00 and 05:00. In addition the resulting CO_2 flux decreases and becomes negative too late in the day compared to the EC measurements. The CO_2 fluxes of the MOST and integrated methods evolve from a positive flux to a negative flux around 8:00. This is 3 h later than the CO_2 flux from the EC measurements. During the day, between 08:00 and 15:00, the MOST method underestimates the CO_2 uptake and the integrated method overestimates it. Table 3.2 shows that both MOST and the integrated methods have the highest mean difference and root mean square error (RMSE) compared to the observation-based approaches. We discuss this further in Sect. 3.4.3. As a result of this analysis, we decided to not use the theoretical approach to calculate the O_2 flux.

Table 3.2: The mean difference and the root mean square error (RMSE) of the comparison between the EC CO_2 flux measurements at 27 m in the tower and the CO_2 flux calculated with different methods for the exchange coefficient K, based on the ICOS data, each using the vertical gradient of CO_2 at 23 and 125 m of our campaign data.

Approach for K	Mean difference [μmol m^{-2} s^{-1}]	RMSE [μmol m^{-2} s^{-1}]
Integrated	5.21	7.81
K with MOST	4.98	5.83
K with θ	3.71	4.83
K with CO_2	2.80	3.88

Secondly, we analyse the observation-based approaches that are indicated in Fig. 3.6 with 'K with θ' (where K is established using ICOS vertical gradients of potential temperature and the sensible heat flux) and 'K with CO_2' (where K is established using ICOS CO_2 vertical gradients and CO_2 EC data). The observation-based approaches showed a better comparison with the EC observations in determining the CO_2 flux compared the to theoretical approach. Both the θ and the CO_2 methods represent satisfactorily the nocturnal CO_2 flux between 0:00 and 5:00. After 5:00, the fluxes calculated by both methods start to decrease and change sign around the correct time (5:00) from a positive to a negative flux. During the day between 8:00 and 15:00, both the θ and the CO_2 methods underestimate the CO_2 flux but not as much as the theoretical methods. Table 3.2 also shows that both the θ and the CO_2 methods have the lowest mean difference and RMSE. Based on the smaller mean difference and RMSE, as well as the direct link of CO_2 with O_2, we decided to proceed with the method where K is calculated with the ICOS data of CO_2, instead of the ICOS θ data. This K was then multiplied with our measured O_2 vertical gradient between 23 and 125 m to calculate the O_2 flux. Section 3.4.3 presents a more complete discussion on the different methods to determine the most suitable K.

The resulting O_2 flux calculated with the exchange coefficient K based on the ICOS CO_2 data is shown in Fig. 3.6b. The uncertainties are based on the error propagation of the standard errors of the O_2 and CO_2 data per time step as calculated with Eq. (3.4), in Eq. (3.7). We do not calculate an uncertainty for K, as this is not the dominating term contributing to the total uncertainty. The daytime flux values have a high variability, but the inferred fluxes appear physically realistic and promising for one of the first attempts to calculate O_2 fluxes. During the night, between 0:00 and 5:00, the O_2 flux signal has a relatively stable negative value, because the forest consumes O_2 for the respiration processes. Similarly, CO_2 is released during the night, leading to a positive CO_2 flux. After 5:00, the O_2 flux becomes positive and shows a higher variability. Overall, the O_2 flux is positive during the day, which indicates that the forest produces O_2 as the assimilation rate is higher than the respiration rate. The high variability of the O_2 flux compared to the CO_2 flux is caused by the less precise measurements of the O_2 vertical gradient compared to the CO_2 gradient (Fig. 3.4). The measurement precision needed to measure the difference between the two levels is very high, and therefore impacts the measurement of the gradient of O_2. The nighttime values of the O_2 flux are therefore more reliable than the daytime values, since the difference between the two heights is larger and due to the more stable atmospheric conditions at night.

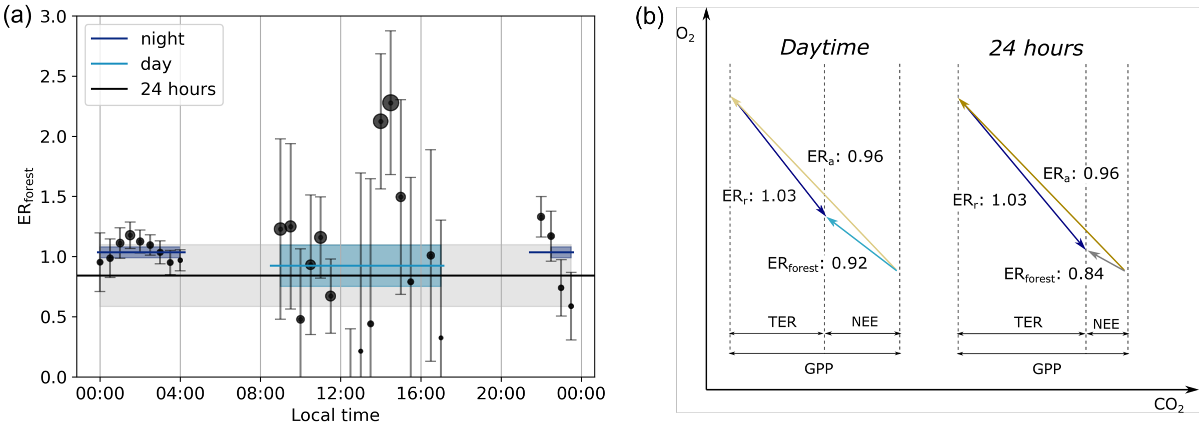

Figure 3.7: The half-hourly exchange ratio of the forest (ER_{forest}) and the resulting averaged ER_{forest} for the entire day (black line), the night between 21:00-4:00 (dark blue line) and the day between 9:00-17:00 (light blue line) of the representative day (a) with the time in local wintertime (LT; time zone UTC+2). The size of the dots indicates the size of the absolute O_2 flux, and the shaded bands indicate the uncertainties of the different ER_{forest} signals. Note that the ER_{forest} lines do not match with the average of the dots in the specific time period, because the lines are based on the averaged fluxes. These different ER signals are presented in a vector diagram format with the carbon fluxes, gross primary production (GPP), total Ecosystem respiration (TER) and net ecosystem exchange (NEE), and the ER of the assimilation processes (ER_a), and the ER of the respiration processes (ER_a) (b).

By using Eq. (3.6), we find three different ER_{forest} signals throughout the day (Fig. 3.7 and Table 3.3). The selected time periods based on the criteria described in Sect. 3.2.3 are between 09:00-17:00 for the daytime and between 21:00-04:00 for the nighttime (Fig. 3.6). This results in a nighttime ER_{forest} signal of 1.04 ± 0.04, a daytime ER_{forest} signal of 0.92 ± 0.17 and an ER_{forest} signal for the entire 24 h of 0.83 ± 0.24. Note that this 24 h value is not the average of the day and night ER_{forest} signals or from all the 30 min ER_{forest} signals, because we used the averaged fluxes. This means that the ER_{forest} signals based on high flux values, indicated in Fig. 3.7 with larger symbols, contribute more to the averaged ER_{forest} signals compared to the lower flux values. Figure 3.7b illustrates that when combining surface fluxes with different sign, we cannot just average the corresponding ER signals (see Sect. 3.4.4). The individual ER_{forest} values of every 30 min show a clear difference between the daytime and nighttime. The ER_{forest} values during the nighttime are relatively stable. The $\mathrm{ER_{forest}}$ values during the daytime show more variability, caused by the high variability of the O_2 flux during daytime (Fig. 3.6). The uncertainty of the $\mathrm{ER_{forest}}$ signals is determined by the propagation of the standard error of the aggregate 30 min data (based on Eq. (3.4)), in Eqs. (3.7) and (3.6).

3.3.4 GPP and TER calculations

Table 3.3: The exchange ratio for the atmosphere ($\mathrm{ER_{atmos}}$: Sect. 3.2, the forest ($\mathrm{ER_{forest}}$: Sect. 3.3, and assimilation and respiration ($\mathrm{ER_a}$ and $\mathrm{ER_r}$: Sect. 3.3 for different time periods of the representative day. The time periods used to calculate the signals are: (09:00-13:00) for day and (23:00-04:00) for night of $\mathrm{ER_{atmos}}$, and (09:00-17:00) for day and (21:00-04:00) for night of $\mathrm{ER_{forest}}$, $\mathrm{ER_r}$, and $\mathrm{ER_a}$. Note that the uncertainty for $\mathrm{ER_{atmos}}$ does not represent the same uncertainty as for $\mathrm{ER_{forest}}$, since the first is the error of the fit, and the second is based on error propagation of the half-hourly measurements.

	$\mathrm{ER_{forest}}$	$\mathrm{ER_r}$	$\mathrm{ER_a}$	$\mathrm{ER_{atmos}}$
Night	1.03 ± 0.05	1.03 ± 0.05		1.22 ± 0.02
Day	0.92 ± 0.17	1.03 ± 0.05	0.96 ± 0.12	1.10 ± 0.12
24 hours	0.84 ± 0.26	1.03 ± 0.05	0.96 ± 0.11	2.05 ± 0.03

We found the ER signals for assimilation ($\mathrm{ER_a}$) and respiration ($\mathrm{ER_r}$) by using Eq. (3.9) (Fig. 3.7b and Table 3.3). The assumption that $\mathrm{ER_r}$ stays constant throughout the day seems reasonable, because the $\mathrm{ER_{forest}}$ values stay stable during the night. Therefore the $\mathrm{ER_r}$ signal becomes 1.03 ± 0.05. A more elaborate discussion of this assumption can be found in Sect. 3.4.5. $\mathrm{ER_a}$ of the daytime is 0.96 ± 0.11, which indicates the $\mathrm{ER_a}$ signal of the boreal forest when the surface fluxes are the highest. The $\mathrm{ER_a}$ signal of the entire diurnal cycle is 0.95 ± 0.11, which also includes the assimilation processes during sunrise and sunset. Figure 3.7b shows all these ER signals and how they change throughout the day, together with their carbon fluxes. $\mathrm{ER_a}$, $\mathrm{ER_r}$ and the resulting $\mathrm{ER_{forest}}$ signals are more realistic compared to the $\mathrm{ER_{atmos}}$ signals. We will elaborate on these differences in Sects. 3.4.4 and 3.4.5.

By using Eqs. (3.8) and (3.9) for a second representative day (13 through 15 June), with the $\mathrm{ER_a}$ and $\mathrm{ER_r}$ signals determined from the representative day, we show in Fig. 3.8 that the O_2 method compares well with the EC method. This means that the O_2 method could potentially be used to separate NEE into GPP and TER on any day when good simultaneous CO_2, O_2 and NEE measurements are available. The difference between the CO_2 fluxes determined with the O_2 method and the EC method of both the GPP and the TER flux are around 0.5 μmol m^{-2} s^{-1}, which is less than 6 % of the total gross flux. The difference is relatively small, which means that the O_2 method compares well with the EC methods to separate NEE into GPP and TER. The different error bars in Fig. 3.8) show how sensitive the O_2 method is to the accuracy of $\mathrm{ER_{forest}}$. By changing $\mathrm{ER_{forest}}$ by 0.2, the GPP estimation by the O_2 method changes by 4 μmol m^{-2} s^{-1}, and by changing

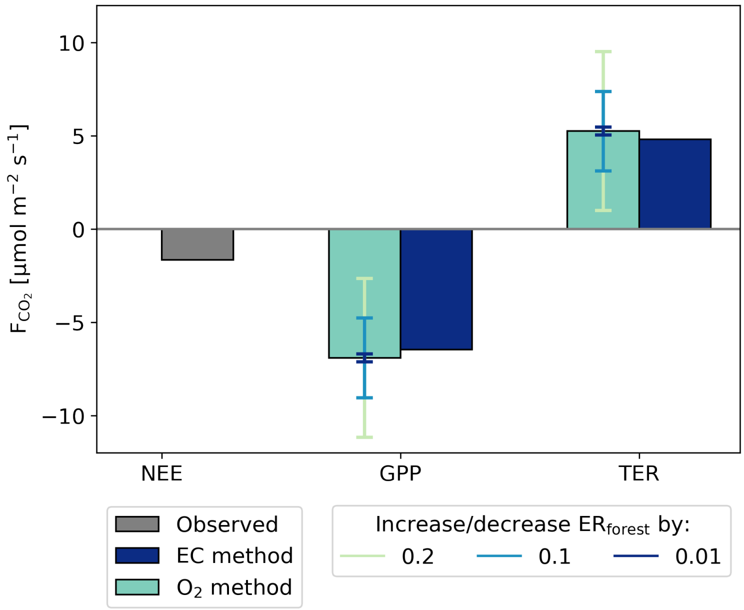

Figure 3.8: The CO_2 fluxes of a second representative day (13 through 15 June) for net ecosystem exchange (NEE), gross primary production (GPP) and total ecosystem exchange (TER) based on two different methods: the EC method and the O_2 method. The different error bars indicate an increase/decrease of 0.2, 0.1, or 0.01 for the exchange ratio of the forest (ER_{forest}) used in the O_2 method.

ER_{forest} by only 0.01, the GPP estimation changes by 0.2 μmol m^{-2} s^{-1}. The effect of changing ER_{forest} on TER has the same effect on GPP. This shows that the O_2 method is quite sensitive to ER_{forest} and should be measured accurately, with a suggested precision of around 0.05. With a precision of 0.05 for ER_{forest} the GPP and TER fluxes derived with the O_2 method stay in the same range as the GPP and TER fluxes determined with the EC method. The application of the O_2 method will be further discussed in Sect. 3.4.5.

3.4 Discussion

We aimed to advance understanding of the $O_2 : CO_2$ exchange ratio and its diurnal variability over a boreal forest by continuously measuring both O_2 and CO_2 concentrations at two heights above the canopy. These measurements gave us the possibility to compare the ER_{atmos} and ER_{forest} signal of an aggregate representative day and compare the boreal forest signals to previous studies in different ecosystems. Our ER_{atmos} signal changed between the day (2.28) and the night (1.22) and had an overall diurnal signal of 2.05. For the ER_{forest} signal, we needed to determine the O_2 and CO_2 surface fluxes based on the two heights. Different flux-calculating methods were compared. The O_2 flux was calculated with the method that resulted in the best comparison to EC fluxes for CO_2, where we found that the exchange coefficient K based on the CO_2 data was most suited.

The resulting ER_{forest} signal showed again differences between the day (0.92) and night (1.04) and the overall diurnal ER_{forest} was 0.83. For these differences and variability in the ER signals, different aspects of the uncertainty have to be taken into account, on which we elaborate in the next sections.

3.4.1 Measurement uncertainty

By analyzing the mean difference and standard deviation of the target cylinder values between 16 June 2019 and 17 July 2019 (Table 3.1), we see that the values are relatively high. Previous studies that used a fuel cell analyser for continuous atmospheric O_2 measurements (Battle et al., 2019; Ishidoya et al., 2013; van der Laan-Luijkx et al., 2010; Popa et al., 2010; Pickers et al., 2022), achieved measurement precision of around 5 per meg. The WMO recommends a compatibility goal of 2 per meg; however, this is difficult to achieve and so the extended compatibility goal is 10 per meg for the worldwide O_2 monitoring network (Crotwell et al., 2020), which shows that our long-term measurement precision of 19 per meg is relatively poor. This poor measurement precision could have been caused by several reasons. The O_2 values of the calibration cylinders that were used were relatively far apart, making it more difficult to measure the values around the target cylinder value. For 2018 we used calibration cylinders with the following values (on the SIO scale): -628.53 per meg -816.17 per meg, and -1208.28 per meg and for 2019 we used cylinders with values: -729.96 per meg, -816.17 per meg, and -1208.28 per meg. The cabin in which the instrument and cylinders were located was not well insulated, which created unstable temperature conditions that might have affected the stability of the cylinders (Keeling et al., 2007). The calibrations of our representative aggregate day took place during the night; therefore, large temperature changes during the day might have affected daytime stability of the reference cylinder. Furthermore, tiny leakages in the setup might have influenced the measurements. Due to the relatively short period for these campaigns and the remote location, it is not possible to trace back the cause of this large uncertainty. This high uncertainty resulted in a larger uncertainty of the vertical gradient of the two heights of the O_2 measurements. However, in this study we are mostly interested in the diurnal variability of the ER signal and differences between ER_{atmos} and ER_{forest}; therefore, the long-term stability of the measurements are less relevant here compared to other O_2 studies.

To reduce the effect of the high measurement uncertainty and derive a more statistically robust signal of the vertical gradient, we created an aggregate representative day based on days with similar weather and atmospheric conditions. The increased statistics of this representative aggregate day decrease the effect of the low measurement precision. We also move away from the reality of one specific day but rather focus on an average situation and variability of the ER signal above a boreal forest based on O_2 and CO_2 measurements at two levels. Given that very few previous studies focused on deriving forest ER signals globally, our analysis helps to gain further understanding of the diurnal variability and the difference between ER_{atmos} and ER_{forest}, which will be discussed in the following sections.

3.4.2 ER_{atmos} signal in comparison to previous studies

Despite the uncertainty in our measurements, there are clear differences between the slopes of O_2 and CO_2 throughout the diurnal cycle (Fig. 3.5). Three different ER_{atmos} signals are visible, with two signals for the day (2.28 ± 0.01 and 1.10 ± 0.12) and one for the night (1.22 ± 0.02) slope (Table 3.3). Note that the uncertainty of these values is based on the slope of the fitted line in Fig. 3.5 and does not represent the uncertainty in the stability of our measurements indicated in Table 3.1. The difference between day and night values of ER_{atmos} was expected, because different processes (i.e. respiration, assimilation and entrainment) with different ER signals play a role at different times during the diurnal cycle. To exclude as much as possible the effect of entrainment and the boundary layer dynamics during the morning transition, we will from now on refer to the 1.10 value as the day ER_{atmos} signal, which is the signal derived from period P3a. ER_{atmos} for the complete day results in 2.05 ± 0.03.

Table 3.4: The different exchange ratio (ER) signals of previous studies are given, with the ER of the atmosphere (ER_{atmos}), the ER of the forest (ER_{forest}), the ER of the respiration processes (ER_r) and the ER of the assimilation processes (ER_a). Bat, 2019 is short for (Battle et al., 2019), Ish, 2015 represents (Ishidoya et al., 2015), Ish, 2013 represents (Ishidoya et al., 2013), and Sei, 2004 represents (Seibt et al., 2004).

	ER_{atmos}[a]			ER_{forest}[b]				
Study	Day	Night	24 h	Day	Night	24 h	ER_r	ER_a
This study	1.10 ± 0.12	1.22 ± 0.02	2.05 ± 0.03	0.92 ± 0.17	1.03 ± 0.05	0.84 ± 0.26	1.03 ± 0.05	0.96 ± 0.12
Bat, 2019	1.02 ± 0.01	1.12 ± 0.01						
Ish, 2015				< 1.0	> 1.0	0.86 ± 0.04	1.11 ± 0.01	1.0
Ish, 2013	0.87 ± 0.02	1.03 ± 0.02	0.94 ± 0.01	≈ 0.98	≈ 1.11	0.89	1.11 ± 0.01	1.02 ± 0.03
Sei, 2004[c]			1.01 ± 0.06	1.24 ± 0.06	1.01 ± 0.02	1.26 ± 0.05	0.94 ± 0.04	1.19 ± 0.12
Sei, 2004[d]	1.14 ± 0.19	1.16 ± 0.02	1.03 ± 0.05					

[a] An ER signal is classified as ER_{atmos} when the ER signal is based on one concentration measurement of O_2 and CO_2.

[b] An ER signal is classified as ER_{forest} when the ER signal is based on surface fluxes from either an 1-box model or vertical gradient flux calculations.

[c] The ER signals of the location Griffin Forest of Seibt et al. (2004) are used here.

[d] The ER signals of the location Harvard Forest of Seibt et al. (2004) are used here.

When comparing our ER_{atmos} signals to those from Battle et al. (2019), Ishidoya et al. (2013), and Seibt et al. (2004) (Table 3.4), we note several similarities but also some differences regarding the specific values of the ER_{atmos} signals. Our daytime signal of 1.10 is similar to 1.02, 0.87, and 1.14 from the previous studies respectively, as is our nighttime signal of 1.22 compared to 1.12 (Battle et al., 2019), 1.03 (Ishidoya et al., 2013), and 1.16 (Seibt et al., 2004). However, our 24 h ER_{atmos} signal of 2.05 shows an unrealistically high number which clearly does not indicate the ER of the forest only. A typical ER_{atmos} signal for a 24 h period lies around 1, as is shown in Table 3.4 and by Stephens et al. (2007) and Manning (2001). Our 24 h ER_{atmos} value includes the measurement points of the period that is influenced by entrainment and boundary layer dynamics (P2), for which period we found an ER signal of 2.28. The large influence of entrainment and boundary layer dynamics made it difficult to be very precise about the specific time periods to choose for P3. Moving the selected time boundaries of P3a from 9:00 to 9:30 or from 13:00 to 12:30 leads to ER_{atmos} values of 0.88 or 1.75, respectively. The large changes in the daytime ER_{atmos} due to small changes in the time boundaries show the high uncertainty of the daytime ER_{atmos}. Therefore, our measurements provide a confirmation of earlier indications (Seibt et al., 2004) that ER_{atmos} is an unreliable estimate for the ER of a forest, and we recommend to use ER_{forest}.

Instead, ER_{atmos} also represents how O_2 and CO_2 are influenced by the boundary layer dynamics and entrainment (Fig. 3.1). The high ER_{atmos} values cannot be explained by signals from other sources, such as fossil fuel combustion or exchange with the lake, as both are not represented in the footprint of our measurements (see Sect. 3.2.3). Furthermore, we have shown that these high values are not an artefact from the instability of the pressure stabilization, as preliminary analysis of the ER_{atmos} values from our 2018 measurements also show values higher than 2.0 (not shown). Although we cannot fully rule out remaining artefacts in the calibration due to, for example, temperature changes in the measurement cabin, we suggest that the more plausible explanation is that ER_{atmos} is highly influenced by atmospheric processes, such as entrainment. The entrainment of air from either the residual layer (early in the morning transition) or the free troposphere (after the residual layer is dissolved) could impact the ER_{atmos} as different sources of air are mixed. The residual layer contains air from the day before and could be affected by horizontal advection, whereas the air in the free troposphere originates from different background sources. These difference sources can have different ER signals and therefore create a mixture of air where O_2 and CO_2 are influenced differently. These air masses affect O_2 differently compared to CO_2 in the boundary layer, and an ER_{atmos} signal will arise that cannot be linked directly to one specific process. Even though entrainment processes also occur at locations of previous studies, we still find differences in ER_{atmos}. We suggest that this can be explained by difference in measurement height compared to the canopy height and different sources of background air in the free troposphere at the measurement location. For the ER_{atmos} signal during P2 at 125 m, we find a value of 3.40, even higher than the ER_{atmos} signal of 2.28 at 23 m, which indicates that the influence of entrainment increases when measuring further away from the canopy and as a result the ER_{atmos} signals show higher values. Further insights into the contributions of each process to ER_{atmos} cannot be estimated from the measurements alone, and would require using an atmospheric model.

3.4.3 Uncertainties in the CO_2 and O_2 flux calculations

By comparing the theoretical and observation-based methods, we determined that the most suitable method to calculate both the CO_2 and O_2 fluxes was to use the observation-based method with CO_2 data (Sect. 3.3.3). Figure 3.6 and Table 3.2 show that the theoretical methods (MOST and integrated) resulted in a change of the CO_2 flux that was late compared to the EC measurement. This delay has been described before and is caused by the time it takes before the turbulence can mix the CO_2 gradient driven by stable nocturnal stratification conditions and establish the corresponding gradient to how turbulent the atmosphere is (Casso-Torralba et al., 2008a). When the heights of the gradient are closer together, the delay is less pronounced. However, the measurement heights used during our campaign are relatively far apart (125 and 23 m), and the EC flux is measured at 27 m. The 125 m measurement is even located outside the surface layer during the morning transition. This made the flux-gradient method (as described in Eq. (3.7)) less applicable, which assumes that the surface flux stays constant in the surface layer (Dyer, 1974).

Since during our campaign we only measured at two heights, we missed information on the logarithmic profile originating from the canopy top, which resulted in an underestimation of the flux using the K with MOST method. This was solved by integrating the MOST equation (‘integrated method’). With the integrated method, the gradient is assumed to be logarithmic and the total flux increases compared to the MOST calculation (Paulson, 1970). However, with the large difference between the two measurement heights, the integrated approach still overestimated the CO_2 flux compared to the EC measurements during both the day and the night. Also, the delay in the timing of the sign change of the gradient cannot be solved with this integrated method. We also explored the effect of adding a roughness surface layer (RSL) in the flux calculations of the theoretical methods, by adding an extra factor that accounts for this layer (not shown in the results) (Ridder, 2010). The contribution of the RSL did not improve our results, because it also includes the delay of the gradient which was causing the largest deviation in the theoretical methods (Table 3.2).

By applying both observation-based methods, using either θ or CO_2 to infer the exchange coefficient K, we did not find this delay in the timing of the gradient and the observation-based methods therefore resulted in derived fluxes close to the EC measurements. Here it has to be noted that the ICOS EC measurements of CO_2 that we used as a benchmark for the most suitable flux calculation approach, were also used in calculating K with CO_2, which makes the comparison of these approaches to the CO_2 flux not fully independent. Note that we first derive K with the vertical CO_2 gradients calculated from ICOS CO_2 observations at three vertical levels, and we apply this to our own measurements of the CO_2 vertical gradient with an independent instrument (Table 3.1). As a result, there is not a full circularity when comparing the obtained fluxes to the EC CO_2 measurements to select which method for calculating K we use. Most previous studies that determined fluxes based on the gradient approach used θ to calculate K (Stull, 1988; Mayer et al., 2011; Wolf et al., 2008; Bolinius et al., 2016; Brown et al., 2020), because θ is the driver of convective turbulence. However, because O_2 is directly linked to CO_2 and because our statistics (Table 3.2) indicated that the CO_2 method resulted in a better comparison to the EC fluxes, we decided to use the ICOS CO_2 data at three levels and the CO_2 EC measurements to calculate K. This K together with the measurements of two heights by our instrument during our campaign were used to calculate both the CO_2 and the O_2 fluxes used in our study. We also tested the impact of using only two vertical levels of the ICOS CO_2 concentrations to calculate K (not shown), which was also the case in the only previous study that derived O_2 fluxes. Ishidoya et al. (2015) derived O_2 fluxes for a temperate forest in Japan using two vertical levels at 18 and 27 m height for both O_2 and CO_2 concentrations. Our comparison of deriving K based on two vertical levels (23 and 125 m), resulted in an underestimation of the gradient and thus an overestimation of K, and as a consequence the calculated CO_2 flux was overestimated. Therefore the three levels of ICOS CO_2 concentrations measurements proved to be vital in our flux calculations here. We still missed the logarithmic profile at the surface with only the two vertical campaign measurements and as a result we slightly underestimated the final CO_2 and O_2 flux. Therefore, we recommend to always measure at at least three heights of CO_2 and O_2 inside the surface layer when they are meant to be used for flux calculations.

Our final O_2 flux (Fig. 3.6) shows a clear diurnal cycle, with the expected behaviour of negative values in the night (O_2 consumption for respiration) and a positive flux during the day (O_2 release during assimilation). The nighttime fluxes are more stable and give a clear signal due to the larger vertical gradient. K is more difficult to determine during the night as the EC measurements are less representative due to the low level of turbulence. However, the largest contributor to the uncertainty is our own O_2 measurements, and the larger gradient allows us to better establish the O_2 flux. The larger variability of the daytime O_2 fluxes is caused by the smaller gradient of the O_2 concentration measurements during the day (Fig. 3.3), when the atmosphere is more well mixed and when the difference between the two heights becomes smaller. The relatively large measurement uncertainty made it difficult to measure these small differences between the two heights and increased the noise in the fluxes. The measurement noise resulted in O_2 gradient variations that were not tied to the CO_2 gradient variations, and this degraded the correlation between the two fluxes. Despite this larger variability, we still find a clear diurnal behaviour, which allowed us to calculate ER_{forest}. Note that the uncertainties of the surface fluxes of O_2 and CO_2 are only based on the measurements from our campaigns, and we did not include the uncertainties that are related to the calculations of K based on the ICOS data. However, the uncertainty in K is relatively small compared to the other terms in the calculation, and the final uncertainty of estimates is dominated by the measurement uncertainty of O_2. Omitting the uncertainty associated with K therefore leads to a minor underestimate of the full uncertainty.

3.4.4 ER_{forest} signal compared to previous studies

Our resulting ER_{forest} signal changes throughout the diurnal cycle, with specific daytime (0.92 ± 0.17), nighttime (1.03 ± 0.05), and overall (0.84 ± 0.26) values (Fig. 3.7 and Table 3.3). The individual nighttime values show a smaller uncertainty due to the already explained effect of the larger gradient during the stable atmospheric conditions of the night. In contrast, the individual daytime values show a larger uncertainty due to the smaller gradient during the unstable atmospheric conditions of the day. We therefore used averaged values for the daytime and nighttime signals to derive the ER_{forest} values. While the daytime signal excludes the entrainment and the boundary layer dynamics during the morning transition, these effects are still included in the overall ER_{forest} signal. Note that the overall 24 h signal is not the average of the daytime and nighttime signal. The nighttime ER_{forest} signal represents a negative O_2 flux and a positive CO_2 flux, whereas the daytime ER_{forest} signal represents a positive O_2 flux and a negative CO_2 flux. This means that the daytime and nighttime surface fluxes influence the atmosphere differently; therefore, these ER_{forest} values cannot be averaged to calculate the overall ER_{forest} signal. By first calculating the average overall O_2 and CO_2 fluxes and then dividing these, we derive the overall ER_{forest} signal correctly.

When comparing our ER_{forest} signals to previous studies of Seibt et al. (2004), Ishidoya et al. (2013) and Ishidoya et al. (2015) (Table 3.4) we notice that the difference between the daytime and the nighttime values that we found and the specific values of the different ER_{forest}, has some similarities and some differences. Our results, along with those by Ishidoya et al. (2013) and Ishidoya et al. (2015) (night: 1.11 and day: 0.98), show that the ER_{forest} signal of the nighttime is higher than the daytime signal, whereas Seibt et al. (2004) (day: 1.24 and night: 1.01) show the opposite behaviour. Our results are most similar to the signals of both Ishidoya et al. (2013) and Ishidoya et al. (2015), especially if we take our uncertainty range into account. The 24 h signals are difficult to compare as we used a different method to determine the overall ER_{forest} signal compared to Ishidoya et al. (2015). In this study we use average fluxes instead of a linear regression through either the O_2 and CO_2 fluxes or vertical gradient and we thereby take into account the size of the fluxes that contributes most to the ER signal, which results in a flux-weighted average ER_{forest}. We note again that we need to distinguish between daytime and nighttime signals, and we cannot just average them. Figure 3.7 illustrates the need to take averages in consistent meteorological and biological periods that are characterized by similar turbulence regimes and similar signs of the O_2 and CO_2 exchange. For example, combining a small negative O_2 flux with a high ER, with a large positive O_2 flux with a lower ER, results in a smaller O_2 flux compared to when the ERs of both fluxes would have been the same. When we take into account our uncertainty, the complete day signal of 0.84 ± 0.26 comes close to the globally used average ER of the biosphere of 1.1 (Severinghaus, 1995). However, the specific value suggests that the overall ER_{forest} signal of this boreal forest lies somewhat lower than 1.1, i.e. closer to 1.0. The difference in ER_{forest} signals between studies can be explained with the different ER_a and ER_r signals, which we discuss in Sect. 3.4.5.

The ER_{forest} and ER_{atmos} signals are not identical; therefore, they do not represent the same information (Table 3.3). The ER_{atmos} signals are higher compared to the ER_{forest} signals; the 24 h signals especially show a large difference. Despite the higher numbers, the day and night signals of ER_{atmos} and ER_{forest} both show the same pattern, where the daytime signal is lower compared to the nighttime signal. When comparing these differences to previous studies we find that not all studies find the same results. The difference between ER_{forest} and ER_{atmos} was not found by Ishidoya et al. (2013). In contrast, Seibt et al. (2004) found a difference between ER_{forest} and ER_{atmos} (Table 3.4). A reason for this could be the measurement height of ER_{atmos}. When ER_{atmos} is determined closer to the canopy and inside the roughness sublayer, it will be more influenced by the surface processes compared to measurements at higher levels, which are seeing more integrated signals of all processes that influence the concentrations inside the atmospheric boundary layer (i.e. forest exchange and non-local processes like entrainment). To get a clear answer to this question, we should further investigate to what extent ER_{atmos} is influenced by entrainment and boundary layer dynamics and under which conditions they can come close to ER_{forest}. We already show that excluding the morning transition (P2) helps to improve the ER_{atmos} signal. However, as already stated, it is difficult from the measurements alone to determine if the ER_{atmos} signal is influenced only by the surface during this period. An atmospheric model would therefore be needed to find how ER_{atmos} can be derived from a single measurement height and to allow for comparison with previous studies that measured at one height to determine the ER of the forest (Battle et al., 2019; Laan et al., 2014a; Stephens et al., 2007). We are currently applying a specific mixed-layer atmospheric model to further investigate this.

3.4.5 The ER_a and ER_r signals

To further understand the relationship between O_2 and CO_2, we cannot use the ER_{forest} signal alone. To look in more detail into the processes driving the variations, we calculated the exchange ratios of respiration (ER_r) and assimilation (ER_a) (Table 3.3 and Fig. 3.7). ER_r was taken as the ER_{forest} nighttime signal (1.03 ± 0.05), by assuming that only respiration influences the ER_{forest} signal during the night and that the ER_r signal stays constant throughout the entire day. This means that both the heterotrophic and autotrophic respiration are included in ER_r, and the same components are respired in the same ratios throughout the day to keep ER_r a constant value. The studies that looked at the ER_r of an ecosystem (Hilman et al., 2022; Angert et al., 2015; Hicks Pries et al., 2020) only focused on longer timescales than the diurnal cycle. It is therefore not possible to derive diurnal variability of ER_r from these previous studies. We would expect some changes in ER_r as temperatures change during the day, and the respiration of plants involves photorespiration during daytime and dark respiration during nighttime. However, as the study by Hilman et al. (2022) showed, the variability of ER_r mainly depends on the bulk soil respiration and therefore depends on the soil temperature and soil moisture. No large changes in temperatures or soil moisture were detected during the period of the representative aggregate day; therefore, it is unlikely that the ER_r significantly changed in that period. To get a more detailed view on how the ER_r of an ecosystem changes throughout the day, more research is needed on the variability of ER_r including from plant respiration by chamber measurements.

The variability of ER_r between locations highly depends on the soil properties (Angert et al., 2015), which makes it difficult to compare with the few studies available (Seibt et al., 2004; Ishidoya et al., 2013) that measured ER_r with chamber measurements on a brown soil. The soil in our study area is a podzol, which is characterized by a high acidity with little organic matter (Buurman and Jongmans, 2005). The OR of podzols is around 1.08 (Worrall et al., 2013), and the ER of acid soils is expected to be around this OR, because carbon cannot easily dissolve into the groundwater (Angert et al., 2015), and we therefore conclude that our ER_r value of 1.04 is realistic.

We looked at two options to calculate ER_a: the ER_a based only on the daytime measurements (between 09:00 and 17:00: 0.96 ± 0.12) and ER_a based on all measurements (throughout the 24 h period: 0.96 ± 0.11). Both numbers are close to 1, which is often assumed as a standard value for ER_a (Ishidoya et al., 2015; Severinghaus, 1995). Next to that, a value of ER_a close to 1 means that ammonium is used as a source for nitrogen instead of nitrate (Bloom et al., 1989; Bloom et al., 2012). Ammonium is indeed a larger source for nitrogen compared to nitrate in Hyytiälä (Korhonen et al., 2013). The OR of needle leaves (and plant material in general) appears to be always close to 1.0 (Jürgensen et al., 2021), which again confirms our ER_a signals. We did not observe differences between the two ER_a signals. The transition periods between the night and the daytime were difficult to measure, because the gradient then becomes close to zero, which means there could be a possibility that next to ER_{forest}, ER_a also has a diurnal cycle. Again, there are only a few studies that looked at the variability of ER_a (Fischer et al., 2015; Bloom et al., 1989; Bloom et al., 2012; Bloom, 2015). The available studies show that ER_a depends on light (Fischer et al., 2015) and the source of nitrogen in the soil (Bloom, 2015). These changes in ER_a happen when the changes in the atmosphere and the soil are sudden and persist for a longer time compared to a diurnal cycle. We can therefore say that the ER_a also does not change drastically during the day. To get a more detailed overview of ER_a, more precise measurements are needed with uncertainties lower than 0.1 for the ER signals. However, the similar values of ER_a that we find for the daytime and 24 h measurements show that ER_a is hardly affected by entrainment during the morning transition and it would suggest that the morning transition is less of an issue for ER_{forest} than for ER_{atmos}.

By applying the O_2 method to a new aggregate day, we showed that the O_2 method gives results similar to the EC method to partition NEE and derive the GPP and TER fluxes (Fig. 3.8), with estimates of the uncertainties of the O_2 method. The EC method also contains uncertainties in its approach because of the reliance on a function of temperature, and should therefore not necessarily be assumed to be the truth (Reichstein et al., 2005). Despite the uncertainty of both the O_2 method and the EC method, both methods give similar results for the CO_2 flux of GPP and TER. In our comparison of the O_2 and EC methods, there is a minor degree of circularity, as we use the EC GPP estimates to estimate ER_a. By applying it to another representative day, we prevent a full circularity (Table 3.1). In this campaign, we unfortunately could not determine the ER_a and ER_r signals independently from EC, which would be recommended for a full comparison. This would have been possible by using chamber measurements. We expect only minor changes in ER_a from branch/leaf chamber measurements compared to the values we derived, because our ER_a is in the range of expected values compared to previous studies (e.g. Jürgensen et al., 2021; Bloom, 2015; Fischer et al., 2015). The satisfactory comparison between the O_2 and the EC methods for the partitioning of the fluxes shows the potential of the O_2 method. The largest challenge for this method is to determine ER_{forest} with large enough accuracy, as this value is most variable and most difficult to determine based on the small O_2 gradients that we observed. Figure 3.8 shows that the ER_{forest} signal should be measured with an uncertainty of 0.05 or less to get results within the uncertainty range of the EC method. When such high accuracy is reached, the O_2 method has the potential to provide an alternative method for the separation of GPP and TER without relying on the regularly used temperature-based function as used for the EC method. Ishidoya et al. (2015) showed similar results, where the O_2 method also produced GPP and TER comparable to the EC method and the magnitude of the GPP and TER fluxes highly dependent on the derived ER_a and ER_r signals.

To allow for an independent comparison between the flux partitioning with the EC method and the O_2 method, such as was done by using $\delta^{13}CO_2$ by Wehr et al. (2016), we recommend measuring the ER_r and ER_a signals directly with chamber measurements (Seibt et al., 2004; Ishidoya et al., 2013). We also recommend to add at least one additional measurement height for the O_2 and CO_2 concentrations below the canopy to apply the storage correction for both the O_2 and the CO_2 fluxes (Aubinet et al., 2012) and to add a measurement in the free troposphere to better evaluate the effect of entrainment. Despite the high dependency on the accuracy of the ER, this study showed again, as did (Ishidoya et al., 2015), that the O_2 method can be used to get a better understanding of the carbon cycle. To further develop this method, we need to expand the O_2 measurements for longer time series and more locations, and to analyse how ER_{forest} varies over longer timescales, which can improve the global average value of ER (α_B) of 1.1 as used in global carbon budget studies such as Manning and Keeling (2006).

3.5 Conclusion

By continuously measuring atmospheric O_2 and CO_2 concentrations at two heights in Hyytiälä, Finland, we gained new insights into the diurnal variability of O_2 and CO_2 above a boreal forest, quantified by interpreting their exchange ratio (ER). We showed that the signal based on one measurement height of the O_2 and CO_2 concentrations (ER_{atmos}) is not representative for the exchange between the forest and the atmosphere only, but it instead includes other processes such as entrainment as well. To derive the ER of the forest specifically (ER_{forest}), we first determined the surface fluxes above the canopy of O_2 and CO_2 using the vertical gradient between the two measurement heights. We found that the most suitable method to calculate both the O_2 and CO_2 surface fluxes was to use the exchange coefficient calculated from the eddy covariance (EC) CO_2 flux and the vertical gradient of CO_2 measurements at three heights above the canopy. The ER_{forest} signals that resulted from the ratio of the mean O_2 and CO_2 fluxes varied between the daytime (0.92 ± 0.17 mol mol^{-1}) and nighttime (1.03 ± 0.05 mol mol^{-1}). The different ER_{forest} signals were composed of the ER of respiration (ER_r: 1.03 ± 0.05 mol/mol) and the ER of assimilation (ER_a: 0.96 ± 0.12 mol/mol). With these findings, we show improved methods to derive O_2 forest fluxes and to derive the variability in the different ER signals over a representative diurnal cycle. The ER_{forest} signal shows a clear diurnal cycle for this boreal forest, and the overall ratio is lower than 1.1 that is used in global carbon budget calculations. Finally, we show that these ER signals can be used to separate net ecosystem exchange (NEE) into gross primary production (GPP) and total ecosystem respiration (TER).

With only a few data sets of continuous measurements of both O_2 and CO_2 concentrations over forests, our data set is of high importance, specifically the availability of measurements at two heights that allow for calculation of O_2 and CO_2 fluxes. Our analyses can serve as a starting point for follow-up research using coupled land surface-atmosphere models to distinguish and quantify contributions of different processes to ER_{atmos} and ER_{forest} signals. Further understanding of these differences will help to fully exploit the advantages of atmospheric O_2 when unravelling the different components in the carbon cycle.

Data availability. The data used in this study are available from https://doi.org/10.18160/SJ3J-PD38. (Faassen and Luijkx, 2022).

3.6 Appendix

A3.1 Equations to calculate the Exchange Coefficient, K

Observation-based method

The gradient between three points is calculated with the following equation:

$$\overline{\phi}(z) = a \cdot z^2 + b \cdot z + c \tag{A3.1}$$

$$\left(\frac{\partial \overline{\phi}(z)}{\partial z}\right) = 2 \cdot a \cdot z + b \tag{A3.2}$$

where z [m] is the height above the displacement height (d [m]) (d is taken as: 2/3 $\cdot$ canopy height); $\overline{\phi}$ is the average variable where the line is fitted through; and a, b and c are the resulting fitted parameters. When only two vertical measurements are available, the gradient was determined using finite differences.

Theoretical approach

For the MOST method, the following equations were used (Physick and Garratt, 1995):

$$K = \frac{\kappa \cdot z \cdot u_*}{\Phi_H(\frac{z}{L})\phi_{rsl}(\frac{z}{L})} \tag{A3.3}$$

where K is the exchange coefficient [m^2 s^{-1}], $\kappa = 0.4$ is the von Kármán constant, u_* [m s^{-1}] is the friction velocity, Φ_H [-] indicates the stability function, and ϕ_{rsl} [-] indicates the contribution of the roughness sublayer (RSL). The Φ_H was calculated with the following (Dyer, 1974):

$$\Phi_H\left(\frac{z}{L}\right) = \left(1 - 16\frac{z}{L}\right)^{-1/2} \qquad \text{when z/L} < 0 \tag{A3.4}$$

$$\Phi_H\left(\frac{z}{L}\right) = 1 + 5\frac{z}{L} \qquad \text{when z/L} > 0 \tag{A3.5}$$

where L [m] is the Obukov length, which was based on the following equation (Dyer, 1974):

$$L = \frac{-u_*^3}{\kappa(\frac{g}{\theta_v})(\overline{w'\theta'_v})} \tag{A3.6}$$

where θ_v [K] is the virtual potential temperature, $\overline{w'\theta'_v}$ [K m s^{-1}] is the virtual surface heat flux, and g [m s^{-2}] is the acceleration due to gravity. Because the flux was measured close to the canopy, the roughness surface layer (RSL) could become important. The RSL needs an additional length scale (ϕ) and can be calculated with the following equation (Ridder, 2010):

$$\phi_{HRSL}\left(\frac{z}{z_*}\right) = 1 - e^{-\mu\frac{z}{z_*}} \tag{A3.7}$$

Here z_* [m] indicates the height of the RSL above the displacement height and we take that as (2 $\cdot$ canopy height-d) and μ is a constant of 0.95 [-].
By integrating Eq. (3.7) with Eq. (A3.3) for K, we get the following equation that was used for the integrated method (Physick and Garratt, 1995):

$$\phi(z_2) - \phi(z_1) = \frac{(\overline{w'\phi'})}{\kappa \cdot u_*} \left[ln\left(\frac{z_2}{z_1}\right) - \Psi_H\left(\frac{z_2}{L}\right) + \Psi_H\left(\frac{z_1}{L}\right) + \psi_{RSL}\left(\frac{z}{L}, \frac{z}{z_*}\right) \right] \quad \text{(A3.8)}$$

where Ψ_H [-] represents the integrated stability functions for heat and ψ [-] is the integrated function to account for the roughness sublayer (RSL) effect. Ψ_H was calculated with (Paulson, 1970):

$$\left.\begin{aligned} \Psi_H\left(\frac{z}{L}\right) &= 2ln\left(\frac{1+x^2}{2}\right) \\ x &= (1-16z/L)^{1/4} \end{aligned}\right\} \qquad \text{when z/L} < 0 \quad \text{(A3.9)}$$

$$\Psi_H\left(\frac{z}{L}\right) = -5\frac{z}{L} \qquad \text{when z/L} > 0 \quad \text{(A3.10)}$$

The function of the integrated RSL length scale (ψ_{RSL}) [-] was calculated with (Ridder, 2010):

$$\psi_{RSL}\left(\frac{z}{L}, \frac{z}{z_*}\right) \approx \Phi_H\left[\left(1 + \frac{\nu}{\mu z/z_*}\right)\frac{z}{L}\right]\frac{1}{\lambda}ln\left(1 + \frac{\lambda}{\mu z/z_*}\right)e^{-\mu z/z_*} \quad \text{(A3.11)}$$

where ν and λ are both parameters, taken as 0.5 and 1.5, respectively.

A3.2 Figures and Tables

Table 3.1: The data used to calculate different variables that we calculated in our study for the two aggregate days. (a) indicates the data that were used for the first representative aggregate day during 7 through 13 July 2019 and (b) indicates the data that were used for the second aggregate day between 13 and 15 June 2019. The data used are mostly from the period of the respective aggregate day, except when indicated otherwise.

(a)	**Data used during the analysis of the aggregate day between 7 through 12 July 2019** [a]					
	(1) ER_{atmos}	(2) Exchange coefficient (K)	(3) Surface flux of O_2 and CO_2	(4) ER_{forest}	(5) ER_a and ER_r	(6) GPP and TER
Data used:	· O_2 from campaign at 23 m · CO_2 from campaign at 23 m	· EC CO_2 flux · CO_2 gradient based on three heights from ICOS (125 m, 67 m, 16 m)	· K (2) · CO_2 or O_2 gradient based on two heights from campaign (125 m, 23 m)	· CO_2 flux (3) · O_2 flux (3)	· ER_{forest} (4) · EC CO_2 flux · GPP from ICOS database	-

(b)	**Data used during the analysis of the aggregate day between 13 through 15 June 2019** [a]					
	(7) ER_{atmos}	(8) Exchange coefficient (K)	(9) Surface flux of O_2 and CO_2	(10) ER_{forest}	(11) ER_a and ER_r	(12) GPP and TER
Data used:	-	· EC CO_2 flux · CO_2 gradient based on three heights from ICOS (125 m, 67 m, 16 m)	· K (8) · CO_2 or O_2 gradient based on two heights from campaign (125 m, 23 m)	· CO_2 flux (9) · O_2 flux (9)	· ER_a (7-12 July) (5) · ER_r (7-12 July) (5)	· ER_{forest} (10) · EC CO_2 flux · ER_a (5) · ER_r (5)

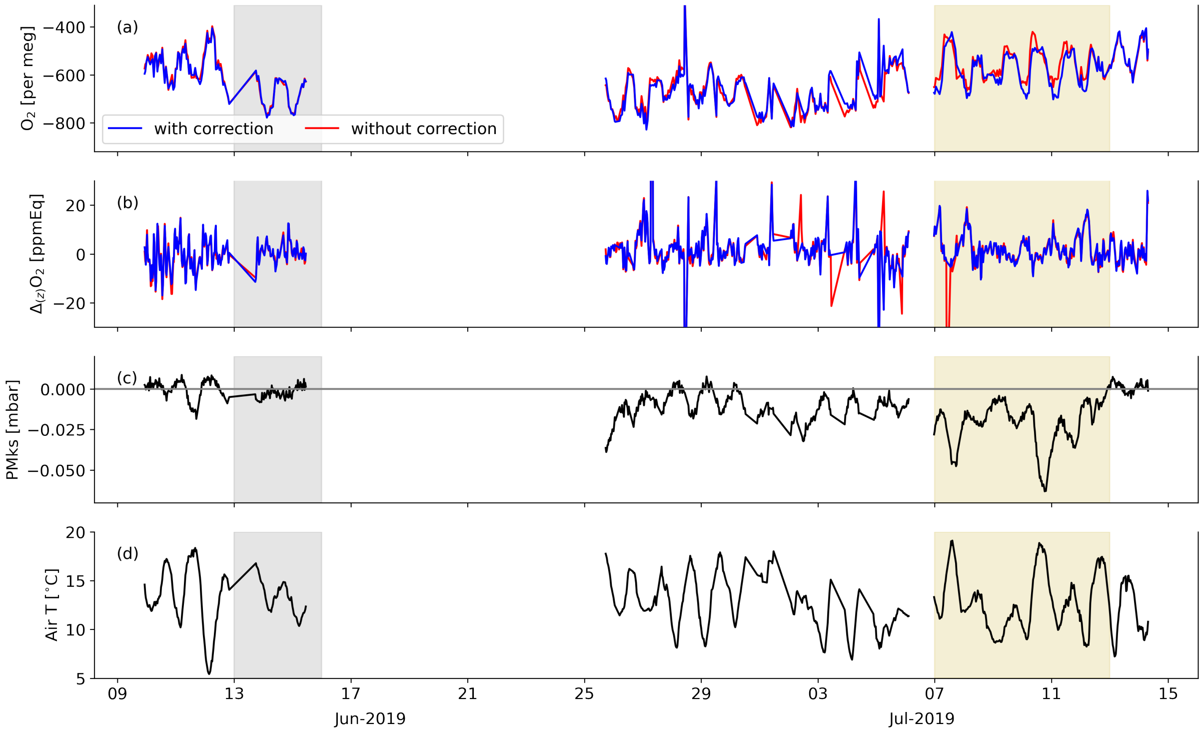

Figure A3.1: The corrected and uncorrected half-hourly average O_2 concentrations at 23 m for the PMKS deviations (a), together with the corrected and uncorrected gradient of O_2 (b). The time series for the 2019 measurement period of the PMKS (c) and the air temperature (d) are also shown. The shaded areas indicate the dates that were selected for the two aggregate representative days, i.e. 13 through 15 June (grey) and 7 through 12 July 2019 (yellow).

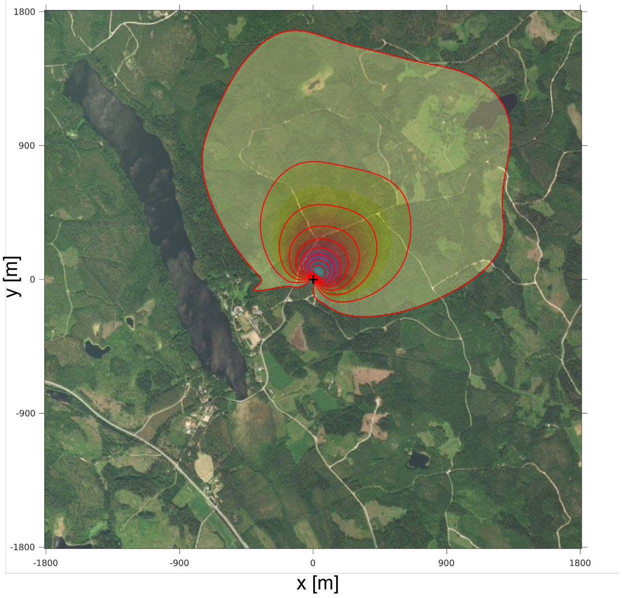

Figure A3.2: The footprint of the O_2 and CO_2 surface fluxes at 53.6 m height (which is the geometric height), determined with the gradient method, for the days during 7 through 12 July 2019 at Hyytiälä. The lines and contours indicate the contributions to the footprint from 10% to 90% in steps of 10%. The plus sign (+) indicates the location of the tower. This figure was created with the method of Kljun et al. (2015)

Chapter 4

Separating above-canopy CO_2 and O_2 measurements into their atmospheric and biospheric signatures

This chapter has originally been published as:

K. A. P. Faassen, J. Vilà-Guerau de Arellano, R. González-Armas, B. G. Heusinkveld, I. Mammarella, W. Peters, and I. T. Luijkx (2024b). “Separating above-canopy CO_2 and O_2 measurements into their atmospheric and biospheric signatures”. *Biogeosciences* 21 (12), 3015–3039

Abstract

Atmospheric tracers are often used to interpret the local CO_2 budget, where measurements at a single height are assumed to represent local flux signatures. Alternatively, these signatures can be derived from direct flux measurements or by using fluxes derived from measurements at multiple heights. In this study, we contrast interpretation of surface CO_2 exchange from tracer measurements at a single height to measurements at multiple heights. Specifically, we analyse the ratio between atmospheric O_2 and CO_2 (exchange ratio, ER) above a forest. We consider the following two alternative approaches: the exchange ratio of the forest ($\mathrm{ER}_{\mathrm{forest}}$) obtained from the ratio of the surface fluxes of O_2 and CO_2 derived from measurements at multiple heights, and the exchange ratio of the atmosphere ($\mathrm{ER}_{\mathrm{atmos}}$) obtained from changes in the O_2 and CO_2 mole fractions over time measured at a single height. We investigate the diurnal cycle of both ER signals to better understand the biophysical meaning of the $\mathrm{ER}_{\mathrm{atmos}}$ signal. We have combined CO_2 and O_2 measurements from Hyytiälä, Finland, during spring and summer of 2018 and 2019 with a conceptual land–atmosphere model to investigate the behaviour of $\mathrm{ER}_{\mathrm{atmos}}$ and $\mathrm{ER}_{\mathrm{forest}}$. We show that the CO_2 and O_2 signals as well as their resulting ERs are influenced by climate conditions such as variations in soil moisture and temperature, for example during the 2018 heatwave. We furthermore show that the $\mathrm{ER}_{\mathrm{atmos}}$ signal obtained from single-height measurements rarely represents the forest exchange directly, mainly because it is influenced by entrainment of air from the free troposphere into the atmospheric boundary layer. The influence of these larger-scale processes can lead to very high $\mathrm{ER}_{\mathrm{atmos}}$ values (even larger than 2), especially in the early morning. These high values do not directly represent carbon cycle processes, but are rather a mixture of different signals. We conclude that the $\mathrm{ER}_{\mathrm{atmos}}$ signal provides only a weak constraint on local-scale surface CO_2 exchange, and that $\mathrm{ER}_{\mathrm{forest}}$ above the canopy should be used instead. Single-height measurements always require careful selection of the time of day and should be combined with atmospheric modelling to yield a meaningful representation of forest carbon exchange. More generally, we recommend always measuring at multiple heights when using multi-tracer measurements to study surface CO_2 exchange.

4.1 Introduction

Rising atmospheric CO_2 levels resulting from fossil fuel combustion and land-use change emissions, which are moderated by uptake by the terrestrial biosphere and oceans, require comprehensive assessment of carbon exchange at local and global scales (Friedlingstein et al., 2022). Atmospheric O_2 serves as a valuable tracer, enhancing our understanding of carbon exchange due to the close linkage between O_2 and CO_2 in carbon cycle processes such as fossil fuel combustion, photosynthesis, and respiration (Manning and Keeling, 2006; Worrall et al., 2013; Keeling and Manning, 2014; Bloom, 2015; Hilman et al., 2022). The exchange ratio ($\mathrm{ER} = -O_2/CO_2$), , denoted as the number of moles of O_2 exchanged per mole of CO_2, represents the specific link between O_2 and CO_2 for different processes (Keeling et al., 1998). Long-term O_2 and CO_2 measurements allow us to derive the global ocean carbon sink (Stephens et al., 1998; Rödenbeck et al., 2008; Tohjima et al., 2019) and to estimate changes in fossil fuel emissions (Pickers et al., 2022; Ishidoya et al., 2020; Rödenbeck et al., 2023).

For global applications, a constant ER of 1.1 ($\mathrm{mol\,mol^{-1}}$) is assumed for the terrestrial biosphere (Severinghaus, 1995). However, the ER of terrestrial biosphere exchange is not uniform at smaller scales; it varies between ecosystems and over time (Angert et al., 2015; Bloom, 2015; Battle et al., 2019; Hilman et al., 2022). Measuring the ERs of ecosystems and the underlying gross processes facilitates the partitioning of net ecosystem exchange (NEE) into gross primary production (GPP) and total ecosystem respiration (TER) (Ishidoya et al., 2015; Faassen et al., 2023), which is still challenging (Reichstein et al., 2005). The ER for net ecosystem exchange can be determined from the ratio of the net turbulent surface fluxes of O_2 and CO_2 above the canopy, referred to as $\mathrm{ER_{forest}}$ (see Fig. 4.1). The O_2 surface fluxes can be inferred from the vertical gradient: the difference between O_2 mole fraction measurements at multiple heights, together with a turbulent exchange coefficient. Currently, available instruments do not allow eddy covariance (EC) O_2 measurements. The $\mathrm{ER_{forest}}$ signal predominantly represents forest exchange occurring in and below the canopy (small-scale processes), comprising the individual ERs of TER ($\mathrm{ER_r}$) and GPP ($\mathrm{ER_a}$) (Ishidoya et al., 2013; Ishidoya et al., 2015; Faassen et al., 2023). Alternatively, the net ecosystem ER has been estimated based on measurements of O_2 and CO_2 mole fractions in the atmosphere at a single height above the canopy. This is referred to as $\mathrm{ER_{atmos}}$ (Fig. 4.1) and is defined as the change in O_2 and CO_2 mole fractions over time (Seibt et al., 2004; Battle et al., 2019; Faassen et al., 2023).

In our recent study (Faassen et al., 2023), we presented a comprehensive comparison of the diurnal behaviour of $\mathrm{ER_{forest}}$ and $\mathrm{ER_{atmos}}$ using measurements collected above a boreal forest in Hyytiälä, Finland. Our analysis revealed that during the afternoon (the photosynthesis-dominant period in Fig. 4.1), the $\mathrm{ER_{atmos}}$ signal approaches the $\mathrm{ER_{forest}}$ value, although they did not converge completely. Furthermore, we showed that during the entrainment-dominant period (see Fig. 4.1), the $\mathrm{ER_{atmos}}$ signal strongly exceeded the

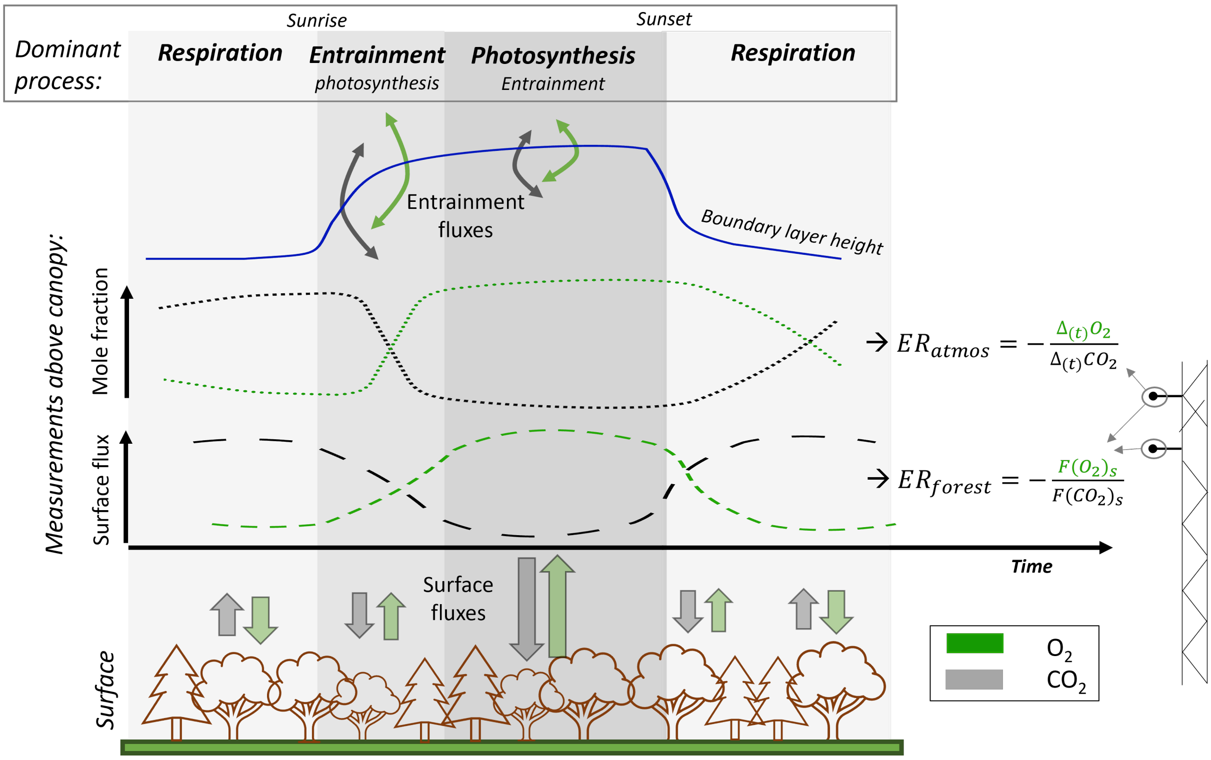

Figure 4.1: Schematic overview of diurnal cycles of the surface fluxes and mole fractions of atmospheric O_2 and CO_2 above a forest canopy. The figure illustrates the dominant processes throughout the day, with forest exchange dominating the nocturnal and afternoon periods, while early morning signals are primarily influenced by entrainment of air from the residual layer or the free troposphere. The surface fluxes of O_2 and CO_2 result in the exchange ratio signal of the forest (ER_{forest}), while the changes in the mole fractions of O_2 and CO_2 over time can lead to variations of the exchange ratio signal of the atmosphere (ER_{atmos}). Note that the term “surface fluxes” refers to the fluxes from the surface layer, which includes the vegetation layer including the top of the canopy. The surface layer is the lowest 10 % of the boundary layer, where the surface directly influences the atmospheric boundary layer.

expected ER value for biosphere exchange, which is typically around 1.1 (Severinghaus, 1995), and even surpassed 2.0. Such high ER values (> 2.0) cannot be attributed to a single process such as photosynthesis, respiration, or fossil fuel combustion, as their ER values are below 2.0. We proposed that the high ER_{atmos} signal was likely influenced by large-scale processes, specifically the entrainment of air from the free troposphere into the boundary layer (Faassen et al., 2023). Seibt et al. (2004) and Yan et al. (2023) also argue that ER_{atmos} cannot capture the ER signal of a forest. In contrast, in the studies by Ishidoya et al. (2013) and Ishidoya et al. (2015), ER_{forest} and ER_{atmos} do result in similar values when small-scale processes dominate over large-scale processes. In Faassen et al. (2023), we concluded that an atmospheric model was needed to interpret the observed diurnal signals of ER_{atmos} and ER_{forest}. The current study delivers this model-based analysis.

Until now, atmospheric O_2 above forest canopies has primarily been modelled with relatively simple one-box models that use only the surface components, lacking implementation of boundary layer dynamics such as entrainment and boundary layer growth (Seibt et al., 2004; Ishidoya et al., 2013). Understanding how mole fractions and, consequently, how ER_{atmos} evolves throughout the day requires accounting for these critical processes. Yan et al. (2023) recently modelled O_2 and CO_2 within and below a canopy using a multi-layer model and showed that ER_{atmos} and ER_{forest} have diurnal and annual patterns. However, ER_{atmos} was treated as a constant value above the canopy and boundary layer dynamics were not accounted for. To expand on the work by Yan et al. (2023) and gain further insight into the diurnal ER_{atmos} behaviour above a canopy, in this study, we use the mixed-layer Chemistry Land-surface Atmosphere Soil Slab (CLASS) model (Vilà-Guerau de Arellano et al., 2015). In short, the model is able to represent the thermodynamics and biophysical processes associated with the diurnal variation in the boundary layer and can provide insights into the processes contributing to ER_{atmos} formation. Additionally, the model facilitates the analysis of ER_{atmos} behaviour under more extreme conditions such as droughts or heatwaves.

In this study, we aim to enhance our understanding of single-height O_2 and CO_2 measurements and the resulting ER_{atmos} signal, as observed above the canopy, and we propose a new relationship between the ER_{atmos} and ER_{forest} signal. We seek to determine whether single-height O_2 and CO_2 measurements can be employed to estimate the ecosystem's ER despite the aforementioned limitations. Additionally, we explore whether the ER_{atmos} signal constrains boundary layer dynamics, and we identify cases where large-scale processes (e.g. entrainment of background air) influence the signal of small-scale processes (e.g. NEE) by analysing different diurnal regimes of ER_{forest} and ER_{atmos}. We combine measurements from campaigns in Hyytiälä, Finland, during spring and summer of 2018 and 2019 with an analysis of the mixed-layer CLASS model. This combined approach allows us to address the following research questions: (1) when does ER_{atmos} represent local forest exchange processes and become equal to ER_{forest} and (2) what is the underlying physical explanation for the high ER_{atmos} values observed in the recent study by Faassen et al. (2023)?

In this paper we first derive a theoretical relationship between ER_{atmos} and ER_{forest} that can help us to understand which components influence the diurnal cycle of ER_{atmos} and when ER_{atmos} should indicate the same processes as ER_{forest} (Sect. 4.2). To evaluate the diurnal cycle of ER_{atmos} we combine observational data with the CLASS model (Sect. 4.3). We then show the model evaluation and the ER_{atmos} and ER_{forest} model results in Sect. 4.4.2, and we analyse different cases to explain the diurnal behaviour of ER_{atmos} during distinct periods of the day and investigate when ER_{atmos} represents forest exchange (Sect. 4.4.3). Next, we place our results in perspective and show how ER_{atmos} should (not) be used (Sect. 4.5). Finally, we present our conclusions on the physical explanations for the differences between the diurnal behaviour of both ER_{atmos} and ER_{forest}.

4.2 Fundamental concepts

4.2.1 The mixed layer theory

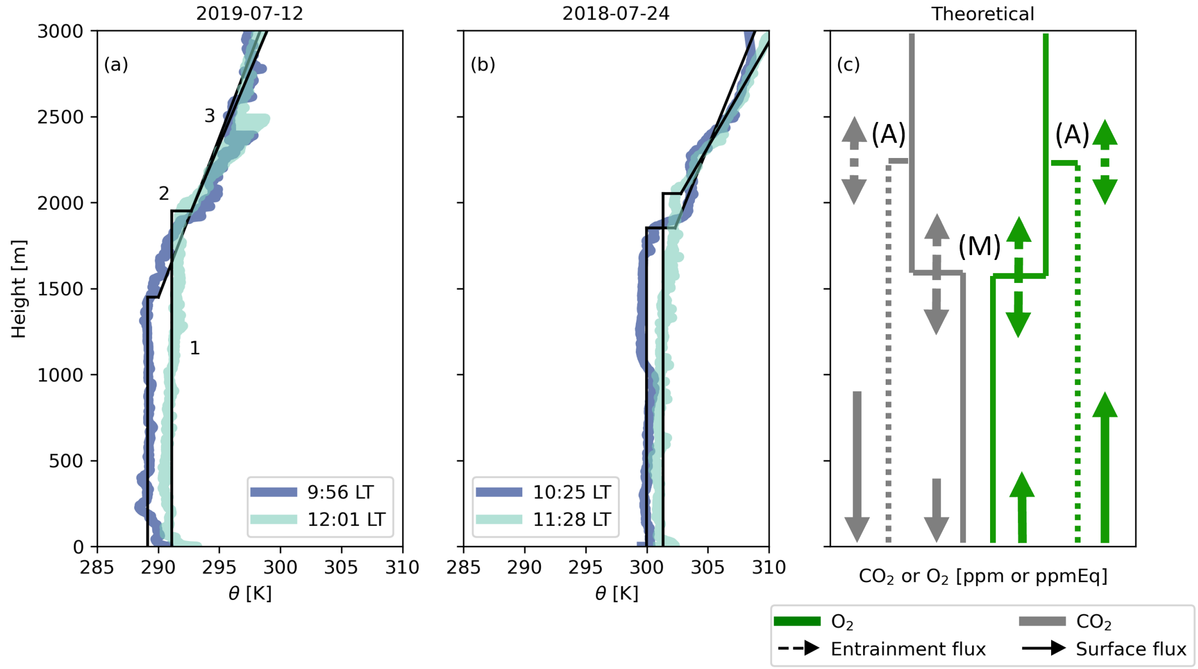

Figure 4.2: Vertical profiles of potential temperature (θ) measured by radiosondes at Hyytiälä on 12 July 2019 **(a)** and 24 July 2018 **(b)**. The observations are conceptualized (black lines) to show (1) the well-mixed profiles at different time steps, (2) the jumps between the boundary layer and the free troposphere, and (3) the lapse rate in the free troposphere; 1, 2, and 3 are used to initialize the CLASS model. Panel **(c)** gives the theoretical vertical profiles of O_2 and CO_2 for the early morning (M) and late afternoon (A). The sizes of the arrows indicate the effects of entrainment (dashed lines) and the surface fluxes (solid lines) on the vertical profiles.

The CLASS land–atmosphere model (Vilà-Guerau de Arellano et al., 2015) is based on the mixed-layer theory which assumes that scalars (such as O_2, CO_2, θ) are constant with height in the atmospheric boundary layer (Lilly, 1968b; Tennekes, 1973). Figure 4.2 illustrates these assumptions for potential temperature (θ), O_2, and CO_2. Within the mixed-layer theory, no distinct surface layer exists, and a capping inversion links the mixed-layer value (the bulk constant value) with the lapse rate of the free troposphere. This inversion, termed the "jump" ($\Delta_{\text{(ft-bl)}}$), represents the difference of a scalar (e.g. the CO_2 mole fraction) between the atmospheric boundary layer and the free troposphere. The free troposphere is represented by a linear change of the scalar with height (the lapse rate).

CLASS describes the well-mixed layer with a scalar constant in height (Fig. 4.2). This scalar (ϕ) can then be solved in the mixed layer with the following equation (Vilà-Guerau de Arellano et al., 2015):

$$\frac{\partial \phi}{\partial t} = \frac{(\overline{w'\phi'})_s - (\overline{w'\phi'})_e}{h} - adv(\phi) \tag{4.1}$$

where $\partial\phi/\partial t$ is the tendency (i.e. change over time) of a generic well-mixed scalar, w' are the deviations of the mean for w which is the vertical wind speed, and ϕ' are the deviations from the mean for a scalar ϕ. The term $(\overline{w'\phi'})_\mathrm{s}$ is the surface flux of ϕ and represents the small-scale processes, $(\overline{w'\phi'})_\mathrm{e}$ is the entrainment flux, h is the boundary layer height, and adv(ϕ) is the horizontal advection of scalar ϕ into the well-mixed layer. In contrast to the local surface exchange, $(\overline{w'\phi'})_\mathrm{e}$ and adv(ϕ) represent large-scale processes.

The entrainment flux is dependent on the entrainment velocity and the jump:

$$(\overline{w'\phi'})_e = -w_e \cdot \Delta_{(ft-bl)}\phi = \left(\frac{\partial h}{\partial t} - w_{sub}\right) \cdot \Delta_{(ft-bl)}\phi \tag{4.2}$$

where w_e is the entrainment velocity, $\Delta_{\text{(ft-bl)}}\phi$ is the jump between the free troposphere and the atmospheric boundary layer, and w_sub is the mean vertical subsidence velocity normally associated with high-pressure systems. We assume w_sub to be negligible, because our focus does not lie on the influence of synoptic scale processes.

$\Delta_{\text{(ft-bl)}}\phi$ changes over time (see Fig. 4.2) and depends on the surface fluxes and the air that is entrained from the free troposphere (see Eq. 4.1):

$$\frac{\partial \Delta_{(ft-bl)}\phi}{\partial t} = \gamma_\phi \cdot w_e - \frac{\partial \phi}{\partial t} \tag{4.3}$$

where γ_ϕ is the lapse rate of ϕ in the free troposphere and $\partial\phi/\partial t$ is the change over time of the well-mixed scalar ϕ (i.e. in the boundary layer).

Lastly, the growth of the boundary layer height $\left(\frac{\partial h}{\partial t}\right)$ effectively determines the entrainment velocity and therefore the entrainment flux of a certain scalar. The growth of the boundary layer is caused by the virtual potential temperature (θ_v), also called buoyancy:

$$\frac{\partial h}{\partial t} = -\frac{(\overline{w'\theta_v'})_e}{\Delta_{(ft-bl)}\theta_v} + w_{sub} \tag{4.4}$$

where θ_v is the virtual potential temperature (i.e. potential temperature of dry air) and w_sub is the subsidence velocity. For more details on these equations, see Vilà-Guerau de Arellano et al. (2015) and Sect. 4.3.2 and Appendix A4.2 for the application of O_2.

4.2.2 Theoretical relationship between $\mathbf{ER_{atmos}}$ and $\mathbf{ER_{forest}}$

The ER signal of the forest ($\mathrm{ER_{forest}}$) is defined as (Faassen et al., 2023)

$$ER_{forest} = -\frac{(F_{O_2})_s}{(F_{CO_2})_s} \approx -\frac{-K_\phi \cdot \Delta_{(z)}O_2/\Delta z}{-K_\phi \cdot \Delta_{(z)}CO_2/\Delta z} \tag{4.5}$$

where $(F_{O_2})_\mathrm{s}$ and $(F_{CO_2})_\mathrm{s}$ are the mean net turbulent surface fluxes of O_2 and CO_2, respectively, over a certain time period above the canopy and can be derived from the vertical gradient of O_2 ($\Delta_{(z)}O_2$) and CO_2 ($\Delta_{(z)}CO_2$) measurements at two heights together with an exchange coefficient following the K-theory (K_ϕ) (Faassen et al., 2023). Note that the K-theory does not apply when one of the measurement levels is inside the canopy. For readability, we write the surface fluxes for both O_2 and CO_2 as F_ϕ, instead of $(\overline{w'\phi'})_\mathrm{s}$ that was used above for the general theory.

The ER signal of the atmosphere (ER_atmos) is defined as (Faassen et al., 2023)

$$ER_{atmos} = -\frac{\partial O_2/\partial t}{\partial CO_2/\partial t} \approx -\frac{\Delta_{(t)}O_2}{\Delta_{(t)}CO_2} \tag{4.6}$$

where $\Delta_{(t)}O_2$ and $\Delta_{(t)}CO_2$ are the changes in the O_2 and CO_2 mole fractions over time (tendencies) at a single height. Linear regression between O_2 and CO_2 can be applied, and the slope gives the ER_atmos value for a certain event or time period. For this study, linear regression was applied for the three periods described in Sect. 4.4.2 for the observations (1 value per 30 min) and the CLASS model output (1 value per 10 s).

According to the mixed-layer theory described above, the tendencies in Eq. (4.6) depend on the surface and entrainment fluxes, together with the boundary layer height (h) (see Eq. 4.1). Equation (4.6) can be rewritten by implementing Eq. (4.1):

$$ER_{atmos} = -\frac{((F_{O_2})_s - (F_{O_2})_e)/h}{((F_{CO_2})_s - (F_{CO_2})_e)/h} \tag{4.7}$$

where $(F_{O_2})_\mathrm{s}$ and $(F_{CO_2})_\mathrm{s}$ are the net surface fluxes of O_2 and CO_2, and $(F_{O_2})_\mathrm{e}$ and $(F_{CO_2})_\mathrm{e}$ are the entrainment fluxes of O_2 and CO_2, respectively. For simplicity, we ignored the advection term in Eq. (4.1) here, but we will add it later (Eq. 4.9). As shown in Eq. (4.2), the entrainment flux depends on the entrainment velocity (w_e) and the jump between the free troposphere and the boundary layer ($\Delta_{\text{(ft-bl)}}\phi$). Combining the definition of ER_forest (Eq. 4.5) with Eq. (4.2) allows us to rewrite Eq. (4.7) as

$$ER_{atmos} = ER_{forest} \cdot \left(\frac{1 + \frac{w_e \cdot \Delta_{(ft-bl)}O_2}{(F_{O_2})_s}}{1 + \frac{w_e \cdot \Delta_{(ft-bl)}CO_2}{(F_{CO_2})_s}} \right) = ER_{forest} \cdot \left(\frac{1 + \beta_{O_2}}{1 + \beta_{CO_2}} \right) \tag{4.8}$$

where $\Delta_{\text{(ft-bl)}}O_2$ and $\Delta_{\text{(ft-bl)}}CO_2$ are the jumps of O_2 and CO_2 between the free troposphere and the boundary layer, and β_ϕ is the ratio between the entrainment flux and the surface flux (Vilà-Guerau de Arellano et al., 2004). Equation (4.8) shows a clear relationship between ER_atmos and ER_forest following the mixed-layer theory.

Using the definition of Eq. (4.1), we can extend Eq. (4.8) to include the effect of advection of O_2 (adv_{O_2}) and CO_2 (adv_{CO_2}), which is, next to entrainment, the second important large-scale process influencing the O_2 and CO_2 values:

$$ER_{atmos} = ER_{forest} \cdot \left(\frac{1 + \beta_{O_2} + \frac{h}{(F_{O_2})_s} \cdot adv_{O_2}}{1 + \beta_{CO_2} + \frac{h}{(F_{CO_2})_s} \cdot adv_{CO_2}} \right) \tag{4.9}$$

Note that in this paper, we mostly focus on cases without advection. We include it here for completeness and discuss the influence of advection in Sect. 4.5.2.

In Appendix A4.1 we analyse Eq. (4.8) by determining when $\mathrm{ER}_{\mathrm{atmos}}$ would theoretically be close to $\mathrm{ER}_{\mathrm{forest}}$ during the day. We show that the β values are of particular importance here: when the β's of O_2 and CO_2 are equal or very small, $\mathrm{ER}_{\mathrm{atmos}}$ gives the same signal as $\mathrm{ER}_{\mathrm{forest}}$. To fully unravel the diurnal variations of $\mathrm{ER}_{\mathrm{atmos}}$ under realistic conditions and identify influencing factors, we need to analyse a real case. Therefore, we study two observed situations by means of the CLASS coupled land–atmosphere model, which we will describe in Sect. 4.3.2.

4.3 Methods

In this section we describe the measurements that were used in this study, together with the mixed-layer model used to evaluate the $\mathrm{ER}_{\mathrm{atmos}}$ and $\mathrm{ER}_{\mathrm{forest}}$ signals.

4.3.1 Hyytiälä 2018 and 2019 measurement campaigns

The observational data were obtained from the SMEAR II Forestry Station of the University of Helsinki in Finland, located in Hyytiälä, Finland (61°51′ N, 24°17′ E, +181 MSL) (Hari et al., 2013). The SMEAR II station serves as a measurement site within a boreal forest equipped with a 128 m tower for continuous measurements of atmospheric variables, fluxes, and greenhouse gas mole fractions. These data are accessible at `https://smear.avaa.csc.fi/` (last access: 24 June 2024). The tower is situated in a homogeneous Scots pine forest, with an average canopy height of 18 m and podzolic soil. The measurement site is predominantly influenced by the surrounding forest and is minimally impacted by signals of fossil fuel combustion (Faassen et al., 2023). For a comprehensive description, see Hari et al. (2013).

During the spring and summer of 2018 (3 June until 2 August) and 2019 (10 June until 17 July), two measurement campaigns, referred to as OXHYYGEN (Oxygen in Hyytiälä), were conducted at Hyytiälä. Continuous measurements of both O_2 and CO_2 mole fractions were taken at two heights (125 and 23 m). O_2 was measured using an Oxzilla II fuel cell analyser, and CO_2 was measured with a non-dispersive infrared (NDIR) photometer (URAS26). Further details on these measurements and the measurement systems are given in Faassen et al. (2023). The measurement precision for O_2 was 19 per meg, and for CO_2 it was 0.07 ppm. Although the precision for O_2 is relatively poor compared to previous studies, it is still adequate for studying the diurnal timescale, as shown in Faassen et al. (2023).

O_2 measurements are typically expressed as $\delta O_2 \,/\, N_2$ ratios in per meg units due to the high abundance of O_2 in the atmosphere (20.946 %) classifying it as a non-trace gas. For direct comparison with CO_2 and implementation into our model, we convert per meg to ppm equivalents (ppmEq) by multiplying with the standard mole fraction of O_2 in air of 0.20946 (Keeling et al., 1998).

During the OXHYYGEN campaigns, radiosondes were launched on multiple days several times per day to quantify the impact of boundary layer dynamics on the O_2 and CO_2 diurnal cycles. The radiosondes (Windsond, model S1H3-R, Sweden) measured vertical profiles of air pressure, wind speed, wind direction, relative humidity, and temperature, with flight heights reaching a maximum of 4500 m and rising rate of about $1.7\,\mathrm{m\,s^{-1}}$. The measurements have an accuracy of 1.0 hPa for air pressure, 5 % for wind speed, 0.2 °C for temperature, and 1.8 % for relative humidity. The temperature and humidity probe has a response time of 6 s, effectively averaging over about 10 m of altitude. For our analysis, we computed vertical profiles of potential temperature (θ) and specific humidity (q) based on pressure, temperature, and relative humidity measurements. Based on the vertical profile of vertical temperature, we also determine the boundary layer height with the parcel method (Kaimal and Finnigan, 1994). Figure 4.2 shows examples of vertical profile measurements of θ for 12 July 2019 and 24 July 2018.

4.3.2 Modelling setup in CLASS

Implementation of CO_2 in CLASS

CLASS serves as a fundamental tool that enables further understanding of specific processes within the atmospheric boundary layer. Several studies have shown that CLASS is successful in reproducing observational data (Vilà-Guerau de Arellano et al., 2012; Vilà-Guerau de Arellano et al., 2019; Schulte et al., 2021). The study of Ouwersloot et al. (2012b) specifically showed that CLASS is able to reproduce the boundary dynamics at the Hyytiälä measurement site. Within CLASS, the vegetation is described using a big-leaf model. The surface stomatal conductance that is representative for the canopy is up-scaled from leaf stomatal conductance by integrating over the leaf area index and incorporating soil moisture. The leaf stomatal conductance is calculated with the A-g_s model. The A-g_s model relates leaf stomatal conductance (g_s) to the net leaf CO_2 assimilation (A) (Jacobs et al., 1996; Ronda et al., 2001). The model computes the dependence of g_s and A on the internal CO_2 mole fraction, the amount of light, the atmospheric temperature, the vapour pressure deficit, and the soil water content at the root zone. Finally, the canopy net CO_2 assimilation is obtained with a function that is inspired by Fick's law of diffusion, based on the difference in the atmospheric CO_2 and internal CO_2 mole fractions, the aerodynamic resistance, and the surface stomatal conductance. The soil respiration is implemented as a function of soil temperature and soil moisture (Vilà-Guerau de Arellano et al., 2012). Combining the net assimilation (A_n) of the plants at canopy level and the soil respiration flux results in the net ecosystem exchange (NEE). This means that the model does not produce exactly the GPP and TER fluxes. The differences between A_n and GPP, and soil respiration and TER, are not directly relevant for our study and we therefore refer to GPP and TER in the following sections, as these terms are more commonly used in the atmospheric CO_2 community. The water cycle is connected to the CO_2 cycle through the surface stomata and the soil moisture inhibition functions for assimilation and respiration.

Implementation of O_2 in CLASS

To model both ER_{forest} and ER_{atmos}, we incorporated the surface flux and the atmospheric mole fraction of O_2 into the CLASS model. We represent the surface flux of O_2 by multiplying the ER of assimilation (ER_a) and the ER of respiration (ER_r) with the CLASS-calculated CO_2 fluxes at the canopy scale. We used the observationally derived ER_a and ER_r values as previously determined in Faassen et al. (2023) for the same site, which were 0.96 and 1.03, respectively. The net surface flux of O_2 was then resolved with the following equation:

$$F(O_2)_s = F(CO_2)_a \cdot -ER_a + F(CO_2)_r \cdot -ER_r \tag{4.10}$$

where $F(O_2)_s$ is the net O_2 surface flux above the canopy, $F(CO_2)_a$ is the net assimilation flux, and $F(CO_2)_r$ is the soil respiration flux. The change of atmospheric O_2 over time was resolved with Eq. (A4.1) (similar to Eq. 4.1) and the entrainment flux is based on Eq. (A4.2) (see also Eq. 4.2). Note that the ER_a from Faassen et al. (2023) was based on GPP fluxes, and this ER_a is now linked to the net assimilation flux (GPP minus the photo- and dark respiration) of the model (Jacobs et al., 1996; Ronda et al., 2001). Seibt et al. (2004) and Ishidoya et al. (2013) showed that ER_a values based on net assimilation have similar values compared to the 0.96 based on GPP. We therefore do not expect this discrepancy to influence our results.

It is important to note that the resulting ER_{forest} signal is not the (weighted) average between ER_a and ER_r, as was also shown by Faassen et al. (2023). The ER_{forest} signal results from the TER and GPP fluxes with different sizes and signs, each with their own ER signals (ER_r and ER_a, respectively). Figure 4.3 shows that the resulting ER_{forest} signal does not necessarily fall within the range of the ER_a and ER_r signals, because the TER and GPP have opposite signs of the O_2 and CO_2 fluxes. This counter-intuitive situation can also occur for combining signals with different isotopic signatures (Miller and Tans, 2003).

Initial conditions

We determined initial and boundary conditions for two cases to constrain the model to the observations. One case was based on the year 2019 (base case) and the other case was based on the year 2018 (characterized by a warm summer in Finland; Peters et al., 2020; Lindroth et al., 2020). Using the two years to initialize CLASS, we were able to better constrain the vegetation's response in the CLASS model under extreme conditions.

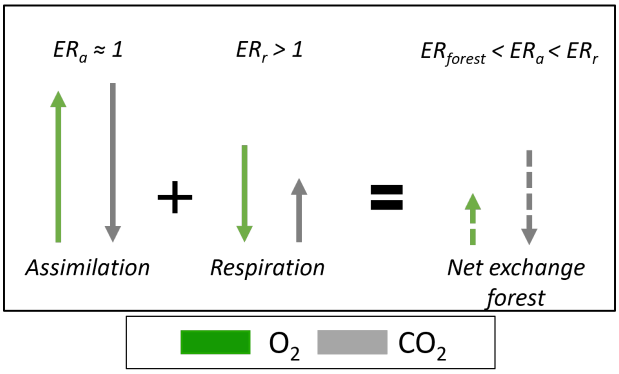

Figure 4.3: Schematic overview of how two processes with different ER signals produce a combined ER signal that is not necessarily the average of the two processes nor necessarily falls within the range of the two combined ER signals. This is due to the different signs of the O_2 and CO_2 fluxes. The example is given for combining the ER signal of assimilation (ER_a) and respiration (ER_r) into ER_{forest} and uses values from our study that are by coincidence larger and smaller than 1.

For each year, we selected one representative day for initialization and validation of the CLASS model. We used 10 July 2019 for the base case and an aggregate between 28 and 29 August 2018 for the warm case. The initial and boundary conditions for initialization of the CLASS runs can be found in Tables A4.2 and A4.3 in the Appendix. Note that the initial jumps ($\Delta_{(\text{ft-bl})}$) of O_2 and CO_2 are based on the best fit between the model and the observations during the day, as direct observations of the jumps were not available. A detailed discussion can be found in Sect. 4.5.3.

We deliberately made only minimal adjustments for the initialization of the 2018 case compared to the 2019 base case to ensure consistency. We assumed that the initial relative humidity remained constant at 80 % regardless of temperature variations, similar to the studies of Vilà-Guerau de Arellano et al. (2012) and Heerwaarden and Teuling (2014).

We adjusted several parameters of the A-g_s land–surface scheme and the soil respiration to improve the agreement between the surface fluxes of the model and the observations in Hyytiälä for both the base case (2019) and the warmer case (2018) (Table A4.2). We decreased the mesophyll conductance (g_m: $2\,\text{mm}\,\text{s}^{-1}$) to better match pine forest conditions (Gibelin et al., 2008; ECMWF, 2014; Visser et al., 2021). Furthermore, the reference temperature of g_m ($T_{2(g_m)}$: 305 K) was increased to reduce afternoon plant stress and to make the CLASS run more comparable with the observations. Lastly, we adjusted the curvature of the drought-response curve (c_β) from zero to 15 % (Combe et al., 2015), given that several studies have demonstrated the pine forest in Hyytiälä to be relatively resilient to lower soil moisture values, thus necessitating a higher (c_β) value (Gao et al., 2017; Lindroth et al., 2020).

Sensitivity analyses

We conducted two sensitivity analyses to gain a deeper understanding of the ER_{atmos} behaviour under varying conditions and to identify factors that lead to a smaller difference between ER_{atmos} and ER_{forest}. Specifically, we looked at changes in ER_{atmos} resulting from changing the different components of Eq. (4.8). The first sensitivity analysis uses the 2019 base case and investigates the effect of background air with a different composition by altering the initial jumps of O_2 and CO_2. By changing only the initial jump and keeping the rest of the 2019 case the same, we simulate situations in which the free troposphere mole fractions of O_2 and CO_2 have changed. In the second sensitivity analysis we examined the impact of climate conditions by modifying the soil moisture and air temperature, mimicking the conditions observed during the 2018 heatwave. Table A4.1 presents the variables used for initializing four cases for these two sensitivity studies.

4.4 Results

In this section, we first show our results for the validation of the CLASS model using observations (Sect. 4.4.1). Subsequently, we discuss the diurnal variability of both the ER_{forest} and ER_{atmos} signals (Sect. 4.4.2). We identify three distinct periods throughout the day in which ER_{atmos} shows large variability (Sect. 4.4.2). We address the large ER_{atmos} that we find in both the observations and the model results (Sect. 4.4.2). Finally, we perform sensitivity analyses to study the effects of changing large-scale conditions, in order to show that our findings are not only valid for a single day (Sect. 4.4.3).

4.4.1 Validation of the O_2 and CO_2 model results

Overall, the modelled O_2 and CO_2 diurnal cycles match well with the observational data. Figures A4.3 and A4.2 in Appendix A4.3 show that CLASS accurately reproduces the diurnal cycles and captures the O_2 mole fraction changes on a daily timescale for both 2018 and 2019 (Fig. A4.3b and c). The figure shows that the differences between the two years are relatively small and indicate that the boundary layer dynamics and the surface fluxes are well represented in CLASS. To accurately replicate the rapid decrease of CO_2 and the sharp increase of O_2 during the rapid growth of the atmospheric boundary layer (between 06:30 and 11:30), we adjusted the jump between the boundary layer and the free troposphere ($\Delta_{(\text{ft-bl})}$) for both O_2 (30 ppmEq) and CO_2 (8 ppm), ensuring that the model aligned with the measurements. Based on values from previous studies, it is realistic for the CO_2 jump to range between 8 and 40 ppm (Vilà-Guerau de Arellano et al., 2004; Casso-Torralba et al., 2008b). While there are limited data available to validate the jump of O_2, based on preliminary results of a campaign in Loobos, the Netherlands, a jump of 30 ppmEq for O_2 seems reasonable. Our chosen combination of O_2 and CO_2 jumps remains an uncertain component in our analysis and will be further discussed in Sect. 4.5.3.

4.4.2 Diurnal variability of ER_{atmos} and ER_{forest} in 2018 and 2019

In this section we discuss the diurnal variability of the ER_{atmos} signal for the 2018 and 2019 cases. First we focus on the budget components (GPP, TER, and entrainment) that influence the O_2 and CO_2 signals (Sect. 4.4.2). To complete the analysis, we support the numerical analysis with Eq. (4.8) to gain a more comprehensive understanding of the underlying processes driving the ER_{atmos} signal for the 2019 case (Sect. 4.4.2).

The three distinct periods of the ER_{atmos} signal during daytime

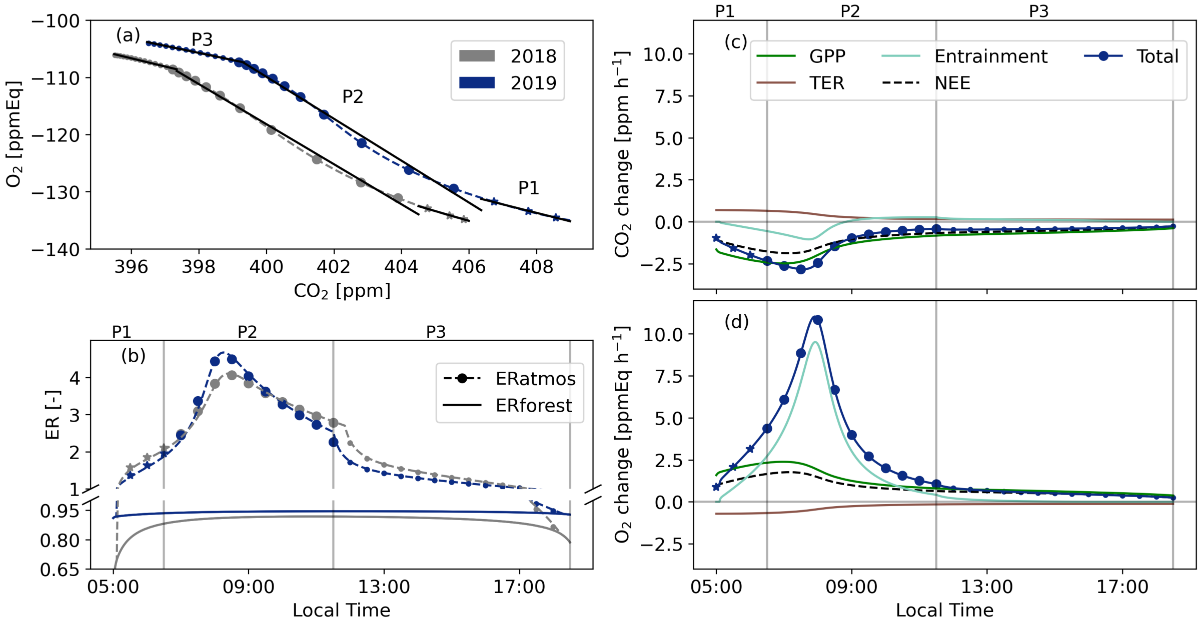

Figure 4.4: Diurnal cycles of O_2 and CO_2 mole fractions **(a)** and ER_{atmos} and ER_{forest} **(b)** as modelled with CLASS for the selected days in 2018 and 2019. We identify three distinct periods based on panels **(c)** and **(d)**, which show the tendencies for the 2019 case (change over time) for CO_2 and O_2 for each process that influences their mole fractions (Eq. 4.1): P1 05:00–06:30, P2 06:30–11:30, and P3 11:30–18:30 LT. The symbols represent half-hourly averaged values of the CLASS model output.

The ER_{atmos} signals obtained for the 2018 and 2019 experiments display large variability throughout the daytime (panels a and b in Fig. 4.4). We identify three distinct periods during the day based on the processes shown in Fig. 4.4c and d: (1) the early morning regime (P1, 05:00–06:30 LT) characterized by an increasing net CO_2 flux into the forest but a non-growing boundary layer (Fig. A4.3a), during which the ER_{atmos} signal during P1 is still relatively close to ER_{forest}; (2) the entrainment-dominant period (P2, 06:30–11:30 LT), where air from a residual layer or air masses from the free troposphere are entrained into the boundary layer and significantly influence the signals, leading to large ER_{atmos} values with an average greater than 3 and extreme values reaching close to 5; (3) the afternoon period (P3, 11:30–18:30 LT), where surface processes dominate the observed signals and

ER_{atmos} moves slowly back towards ER_{forest} and becomes more consistent with values expected for surface processes. The ER_{atmos} values during the three identified periods show good agreement between the observations and the model results (Table 4.1). This analysis confirms from a model perspective that values above 2 for ER_{atmos}, as we reported in Faassen et al. (2023), are indeed possible. Figure 4.4c and d give first indications of what could cause these high values for ER_{atmos}: high influence of entrainment and a different behaviour of the tendencies that influence O_2 compared to CO_2. In the next section we discuss the diurnal behaviour of ER_{atmos} in more detail by using Eq. (4.8).

We find that ER_{forest} is much less variable throughout the day than ER_{atmos} (Fig. 4.4b). In the early morning and later afternoon, the ER_{forest} value is lower than during the midday period. This is caused by a TER flux (with a higher ER signal) almost equal to the GPP flux (with a lower ER signal) caused by low sunlight (Fig. 4.3). At midday, the assimilation of CO_2 by the canopy, with a lower ER signal, becomes increasingly dominant, causing the ER_{forest} signal to move closer to the ER_a value.

Table 4.1: ER_{atmos} (calculated as the slope of the O_2 and CO_2 mole fractions) and ER_{forest} values for the selected days in 2018 and 2019 for both observations (Obs) and the CLASS model for the three selected periods (P1: 05:00–06:30, P2: 06:30–11:30, and P3: 11:30–19:30 LT). The uncertainties in the observed ER_{atmos} and ER_{forest} signals are determined following Faassen et al. (2023). Note that due to limited observational data, we were unable to derive ER_{atmos} values for P1 and P2 in 2018 and for P1 in 2019. NA signifies not available.

	ER_{atmos} (P1)		**ER_{atmos} (P2)**		**ER_{atmos} (P3)**		**ER_{forest} (P1-P3)**	
Year	Obs	Model	Obs	Model	Obs	Model	Obs	Model
2018	NA	1.72	NA	3.50	1.67 ± 0.51	1.43	0.87 ± 0.07	0.90
2019	NA	1.48	3.33 ± 0.31	3.66	1.23 ± 0.10	1.24	0.86 ± 0.06	0.94

Explanation of the large ER_{atmos} values

Analysing the diurnal cycle of the different components of Eq. (4.8) for the 2019 case reveals that the peak value of ER_{atmos} during P2 is caused by the higher β values (the entrainment flux divided by the surface flux) for O_2 compared to CO_2 (Fig. 4.5). The difference between β_{O_2} and β_{CO_2} is a result of the high $\Delta_{(ft\text{-}bl)}O_2 \, / \, \Delta_{(ft\text{-}bl)}CO_2$ ratio (higher than 3). The terms $\Delta_{(ft\text{-}bl)}O_2$ and $\Delta_{(ft\text{-}bl)}CO_2$ represent the jump across the boundary layer top, and each has a different diurnal cycle caused by a different surface flux (Fig. 4.5c and g). The different diurnal cycles for the jumps lead to an increase in the $\Delta_{(ft\text{-}bl)}O_2 \, / \, \Delta_{(ft\text{-}bl)}CO_2$ ratio, consequently raising the ratio between the β values. This effect is further amplified by a higher surface flux of CO_2 compared to O_2, caused by an ER_{forest} value that is slightly lower than 1. The peak value of ER_{atmos} during P2 occurs when both w_e and the $\Delta_{(ft\text{-}bl)}O_2 \, / \, \Delta_{(ft\text{-}bl)}CO_2$ ratio are high and the surface fluxes are still relatively low. This combination contributes to the distinctive peak in ER_{atmos} observed during P2.

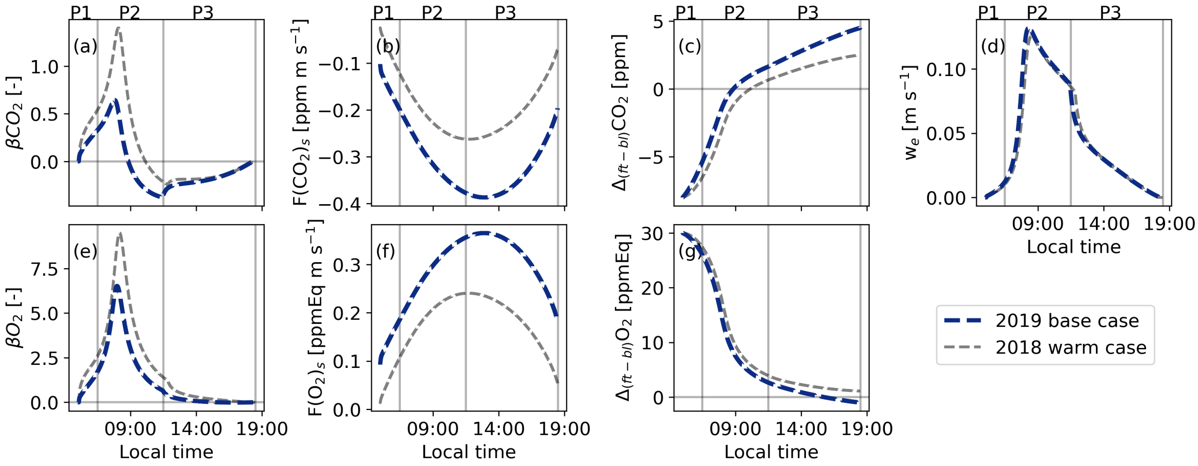

Figure 4.5: Diurnal variability of the different components of Eq. (4.8) for the base case (2019) and the warm case (2018) derived using the CLASS model. Panels **(a)** and **(e)** show the β values for CO$_2$ and O$_2$, where β is the entrainment flux divided by the surface flux (Eq. 4.8); panels **(b)** and **(f)** show the net surface flux; panels **(c)** and **(g)** show the jumps between the free troposphere and the boundary layer ($\Delta_{\text{(ft-bl)}}$); and panel **(d)** shows the entrainment velocity (w_{e}). The vertical lines represent three distinct periods: 05:00–06:30 (P1), 06:30–11:30 (P2), and 11:30–18:30 LT (P3).

Later in the afternoon (P3), both β values gradually decrease and become similar, resulting in an ER$_{\text{atmos}}$ signal that becomes closer to ER$_{\text{forest}}$. This indicates that ER$_{\text{atmos}}$ becomes more representative for surface processes (see also Appendix Sect. A4.1). This decrease in P3 is primarily caused by a reduction in the entrainment velocity (w_{e}) (Fig. 4.5d), indicating slow growth of the atmospheric boundary layer at end of the day (Fig. A4.3). Additionally, the β values become more similar because $\Delta_{\text{(ft-bl)}}$O$_2$ moves closer to $\Delta_{\text{(ft-bl)}}$CO$_2$ during this period (Fig. 4.5c and g), as caused by the mixing of air with the surface.

The ER$_{\text{atmos}}$ signals exhibit higher values than the theoretical analysis in Appendix Sect. A4.1, because the diurnal cycles of the components of Eq. 4.8 are taken into account (Fig. A4.1 vs. Fig. 4.5). Each component of Eq. (4.8) follows its individual diurnal cycle, leading to higher ER$_{\text{atmos}}$ values. Consequently, ER$_{\text{atmos}}$ integrates individual contributions of several processes, particularly during P2, since it is dominated by the influence of mixing with large-scale processes. Careful consideration is needed when interpreting the ER$_{\text{atmos}}$ signal during this period. During P3 the ER$_{\text{atmos}}$ signal appears to align with ER$_{\text{forest}}$ at the end of the day. However, in the 2019 case, this alignment was only observed for a very short period.

We find only small differences in the diurnal behaviour of the ER$_{\text{forest}}$ and ER$_{\text{atmos}}$ signals between the 2018 and 2019 cases (Figs. 4.4 and 4.5). The ER$_{\text{forest}}$ value is lower in 2018 compared to 2019, specifically in the early morning and at the end of the day. This can be attributed to a higher respiration flux caused by the elevated air and soil temperatures during that day in 2018 (Fig. A4.3e). A higher TER flux compared to the GPP flux will decrease the $\mathrm{ER}_{\mathrm{forest}}$ value (Fig. 4.3). While we do not have direct measurements of ER_{r} and ER_{a} for 2018 and 2019, it is likely that the overall diurnal cycle pattern of $\mathrm{ER}_{\mathrm{forest}}$ in Fig. 4.4b (low $\mathrm{ER}_{\mathrm{forest}}$ values in the morning and afternoon, higher $\mathrm{ER}_{\mathrm{forest}}$ values during midday) for both years would have remained consistent. Previous studies suggest that ER_{r} is generally higher than ER_{a}, even under different atmospheric conditions (Angert et al., 2015; Fischer et al., 2015; Hilman et al., 2022). The effect of a warmer and dryer environment on the $\mathrm{ER}_{\mathrm{atmos}}$ signal will be further quantified in Sect. 4.4.3 with a more extreme case.

4.4.3 Sensitivity analyses: effects of changing large scale conditions

With the next two sensitivity analyses, we evaluate whether our findings for the 2019 case are exceptional or whether they can also occur under different (large-scale) conditions. We therefore analyse days with different initial conditions compared to our 2019 and 2018 cases. We focus on the effect of changes in background air (Sect. 4.4.3) and the effect of changes in climate conditions (soil moisture and air temperature, Sect. 4.4.3). With these sensitivity analyses, we show the complexity of the $\mathrm{ER}_{\mathrm{atmos}}$ signal and all the processes by which it can be influenced. Fig. 4.6 is used to illustrate how $\mathrm{ER}_{\mathrm{atmos}}$ is formed by the different components of Eq. (4.8).

Effects of changing background air on ER_{atmos}

Changing the background air in the free troposphere by decreasing the initial jump ratio or the jump sizes of O_2 and CO_2 compared to the 2019 case moves the $\mathrm{ER}_{\mathrm{atmos}}$ signal closer to $\mathrm{ER}_{\mathrm{forest}}$ during P2 and P3 (Fig. A4.4). A lower jump ratio than in the 2019 case but still relatively high jump values ($\Delta_{\text{(ft-bl)}}O_2 = 30\,\text{ppmEq}$ and $\Delta_{\text{(ft-bl)}}CO_2 = -20\,\text{ppm}$) lead to a decrease in the peak of $\mathrm{ER}_{\mathrm{atmos}}$ during P2 and bring $\mathrm{ER}_{\mathrm{atmos}}$ closer to $\mathrm{ER}_{\mathrm{forest}}$ during P3 (yellow line in Fig. A4.4). As the jump ratio decreases, β_{O_2} becomes less dominant and closer to β_{CO_2}. When the O_2 and CO_2 β values become closer, the $\mathrm{ER}_{\mathrm{atmos}}$ value also moves closer to $\mathrm{ER}_{\mathrm{forest}}$ (Fig. 4.6). However, this does not necessarily mean that the surface has become more dominant, since the $\Delta_{\text{(ft-bl)}}$ values are still relatively high.

Reducing the jump sizes of both O_2 and CO_2 ($\Delta_{\text{(ft-bl)}}O_2 = 10$ and $\Delta_{\text{(ft-bl)}}CO_2 = -8$) still results in a relatively high peak for $\mathrm{ER}_{\mathrm{atmos}}$ during P2 and brings $\mathrm{ER}_{\mathrm{atmos}}$ closer to $\mathrm{ER}_{\mathrm{forest}}$ during P3 (purple line in Fig. A4.4). Including the diurnal cycle of the jumps accounts for the effect that the CO_2 jump changes from a negative to a positive value during the day. When the initial CO_2 jump is lower, the sign change occurs earlier in the day and leads to a more negative β_{CO_2} value. This leads to higher $\mathrm{ER}_{\mathrm{atmos}}$ values during P2 (Fig. 4.6). In contrast, a lower jump size would cause the $\mathrm{ER}_{\mathrm{atmos}}$ signal to move more quickly towards $\mathrm{ER}_{\mathrm{forest}}$ during P3, because the surface fluxes dominate over the lowered entrainment flux.

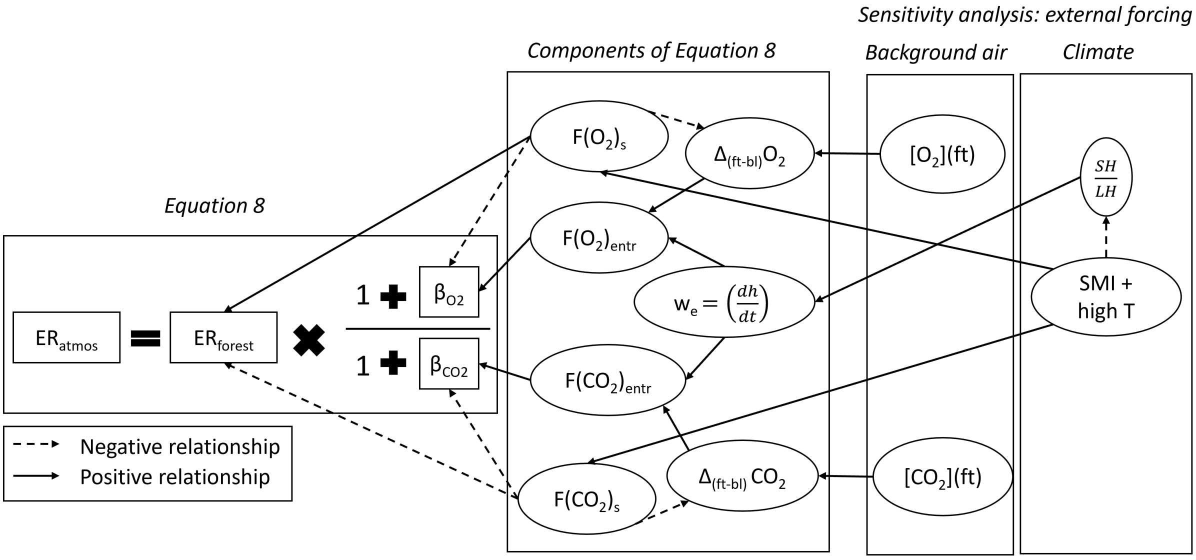

Figure 4.6: Components of Eq. (4.8) and how these influence the ER$_{\text{atmos}}$ signal, including the exchange ratio of the forest (ER$_{\text{forest}}$), the ratio between the net surface flux (F_{s}) and the entrainment flux (F_{entr}) which result in β, the jump between the free troposphere and the boundary layer (Δ(ft-bl)), and the entrainment velocity (w_{e}). The right part of the figure shows the variables that are changed in the two sensitivity analyses: the background air in the free troposphere ([O$_2$](ft) and [CO$_2$](ft)) and the initial soil moisture index (SMI) in combination with a high initial potential temperature (θ_0), which will influence the ratio between the sensible heat flux (SH) and the latent heat flux (LH) at the surface. The dotted arrows indicate a negative influence and the solid arrows indicate a positive influence.

Guided by our theoretical and numerical results and constrained by observations, a high ER$_{\text{atmos}}$ signal during the entrainment-dominant period (P2) can therefore be a result of two cases:

1. The $\Delta_{\text{(ft-bl)}}\text{O}_2$ is substantially larger compared to $\Delta_{\text{(ft-bl)}}\text{CO}_2$ and, therefore, β_{O_2} dominates over β_{CO_2}.
2. $\Delta_{\text{(ft-bl)}}\text{CO}_2$ changes sign from negative to positive and, as a result, β_{CO_2} becomes negative, resulting in a denominator closer to zero.

Changes in the background air result in a distinct change in the diurnal pattern of ER$_{\text{atmos}}$. The difference between the ER$_{\text{atmos}}$ and ER$_{\text{forest}}$ signals could therefore provide extra information on the changes of large-scale processes. This is further discussed in Sect. 4.5.2.

Effect of climate conditions on ER$_{atmos}$ and ER$_{forest}$

By studying the influence of changes in air temperature and soil moisture index (SMI: [soil moisture – w_{wilt}]/[$w_{\text{fc}} - w_{\text{wilt}}$]) on the ER$_{\text{atmos}}$ signal (see Fig. 4.7), we gain insights into how climate conditions can effect $\mathrm{ER}_{\mathrm{atmos}}$ compared to $\mathrm{ER}_{\mathrm{forest}}$. This allows us to study the effects of seasonality or future climate with dryer and warmer conditions. The 2018 case already showed how the $\mathrm{ER}_{\mathrm{atmos}}$ signal could change with decreasing SMI and increasing temperature compared to a more normal year in 2019 (Figs. 4.4 and 4.5). As a next step, we evaluate the full range of how $\mathrm{ER}_{\mathrm{atmos}}$ could change and how $\mathrm{ER}_{\mathrm{atmos}}$ compares to $\mathrm{ER}_{\mathrm{forest}}$. Given the same net radiation, a higher SMI enhances soil respiration, photosynthesis, and latent heat fluxes, and thus decreases the sensible heat flux because of the energy balance closure. This therefore leads to smaller boundary layer growth and, as a result, decreases the entrainment velocity (see Fig. 4.6). In addition, higher air temperatures accelerate both photosynthesis and respiration up to a threshold (Jacobs et al., 1996), resulting in increased GPP and TER fluxes. A lower SMI in combination with higher temperatures can stress plants, leading to decreased O_2 and CO_2 surface fluxes and an enhanced sensible heat flux. This will increase boundary layer growth and the entrainment velocity (Eqs. 4.2 and 4.4). Note that there are also minor changes in $\mathrm{ER}_{\mathrm{forest}}$ when the SMI and air temperature change as a result of GPP and TER changes.

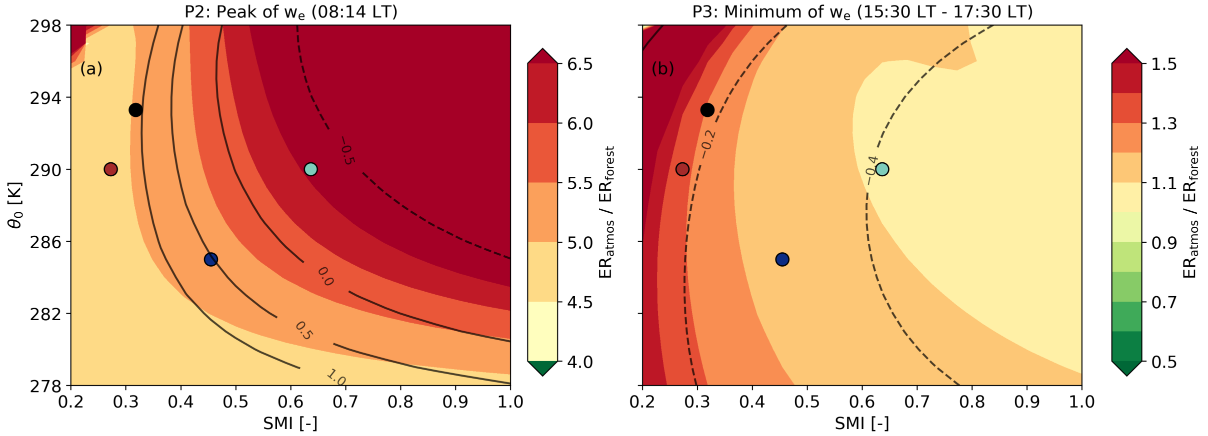

Figure 4.7: Evaluation of the ratio between $\mathrm{ER}_{\mathrm{atmos}}$ and $\mathrm{ER}_{\mathrm{forest}}$ as a function of two key variables that show the effect of a drier and warmer climate: the soil moisture index (SMI) and the initial potential temperature (θ_0). Two periods in the day are analysed: **(a)** during the maximum value of w_e at 08:14 LT (P2) and **(b)** at the end of the day between 15:30 and 17:30 LT, when w_e is minimal (P3). The black lines in panel **(a)** indicate β_{CO_2}, which is the ratio between the entrainment and the surface flux. The black lines in panel **(b)** indicate net CO_2 surface flux values in $\mathrm{ppm\,m\,s^{-1}}$. The coloured symbols (brown and light blue) indicate the example cases that are also shown in Fig. A4.5, the black dot is the 2018 case, and the dark blue dot the 2019 case.

Increasing or decreasing the SMI in combination with changes in air temperature makes the diurnal variability of $\mathrm{ER}_{\mathrm{atmos}}$ more complex, because all components of Eq. (4.8) are now affected (Figs. 4.6 and 4.7). We focus on two particular locations in the parameter space shown in Fig. 4.7: a low soil moisture (red symbol) and a high soil moisture case (green symbol), both with higher temperatures compared to the 2019 case (Fig. A4.5).

A lower soil moisture of $0.14\,\mathrm{m^3\,m^{-3}}$ (SMI = 0.27) with an air temperature of 290 K decreases ER_{atmos} during P2 and increases ER_{atmos} during P3 compared to the 2019 base case (red lines in Fig. A4.5 and red symbol in Fig. 4.7). The lower ER_{atmos} values during P2 are primarily a consequence of a more dominant entrainment flux. Due to a decrease in the O_2 and CO_2 surface fluxes because of stressed plants, both the $\Delta_{(\text{ft-bl})}$ values for O_2 and CO_2 change more slowly and remain high. Higher $\Delta_{(\text{ft-bl})}$ values, along with a higher entrainment velocity caused by higher sensible heat flux, lead to elevated entrainment fluxes. By increasing both the O_2 and CO_2 entrainment fluxes and decreasing the O_2 and CO_2 net surface fluxes, the β values increase and the ratios of the β values move towards the $\Delta_{(\text{ft-bl})}$ ratios. As a result, ER_{atmos} also moves towards the $\Delta_{(\text{ft-bl})}$ ratios multiplied with the ER_{forest} signal (Fig. 4.6). This is similar to the effect observed when increasing the initial jumps of both O_2 and CO_2 (Sect. 4.4.3). The β values stay high during P3 because of the low net O_2 and CO_2 surface fluxes. Therefore, the ER_{atmos} signal also remains close to the ratio of the $\Delta_{(\text{ft-bl})}$ values during P3 and the ER_{atmos} signal does not approach ER_{forest} (Fig. 4.6).

In contrast, a higher soil moisture of $0.22\,\mathrm{m^3\,m^{-3}}$ (SMI = 0.64) with an air temperature of 290 K increases the ER_{atmos} signal during P2 and decreases the ER_{atmos} signal during P3 compared to the 2019 base case (green lines in Fig. A4.5 and green symbol in Fig. 4.7). This is consistent with the effect observed when lowering the initial $\Delta_{(\text{ft-bl})}$ value (Sect. 4.4.3).

In addition to the conclusions in Sect. 4.4.3 on the causes of the high ER_{atmos} signals during P2, the sensitivity analyses for changing climate conditions showed that the large differences between ER_{atmos} and ER_{forest} at the end of the day (P3) can be caused by

1. A substantially larger $\Delta_{(\text{ft-bl})}O_2$ compared to $\Delta_{(\text{ft-bl})}CO_2$, causing β_{O_2} to dominate over β_{CO_2}.
2. High β_{O_2} and β_{CO_2} values because of high O_2 and CO_2 entrainment fluxes and/or low net O_2 and CO_2 surface fluxes.

Our two sensitivity analyses show that several factors, including the entrainment velocity, the $\Delta_{(\text{ft-bl})}$ values and their ratio, and the net surface flux of CO_2, can significantly influence the diurnal behaviour of ER_{atmos}. When using ER_{atmos} as an indication of ER_{forest}, these four factors should be carefully considered. This is crucial to correctly interpret ER_{atmos} values and to understand the underlying processes that influence the carbon exchange above a forest canopy.

4.5 Discussion

In this section we first address the evaluation of the CLASS model (Sect. 4.5.1). Secondly, we elaborate on the issues we found with ER_{atmos} and how this value should (and should not) be used (Sect. 4.5.2). Thirdly, we discuss the importance of the differences between the free troposphere and boundary layer values for O_2 and CO_2 (Sect. 4.5.3). Finally, we put our work in perspective by comparing it to other studies using atmospheric O_2 (Sect. 4.5.4) and to studies on other carbon cycle tracers (Sect. 4.5.5).

4.5.1 Evaluation of the CLASS model

Our implementation of O_2 in the CLASS model could be improved in future studies. Similar to the approach used by Yan et al. (2023), both the ER_r and ER_a signals were kept constant and did not account for potential variations under different climate conditions. To advance our understanding of the ER signals over forest canopies, it is crucial to incorporate ER signals that can respond to varying soil and atmospheric conditions. For instance, the ER_r of soil respiration depends on air temperature and soil moisture (Hilman et al., 2022; Angert et al., 2015), while ER_a is primarily influenced by light at leaf level and nitrogen availability in the soil (Bloom, 2015; Fischer et al., 2015). Additionally, in our current implementation, we did not include the ER for stem respiration (ER_{stem}) (Hilman and Angert, 2016) due to the absence of stem respiration in the CLASS model.

While we utilized CLASS in this study as a proof of concept to demonstrate how ER_{atmos} can change during the day; employing a more elaborate model could allow for more detailed exploration of these ER_{atmos} dynamics and the contributions of various processes. Models with more vertical levels could simulate vertical gradients and analyse differences in the ER_{atmos} signal at various heights, similar to the approach used in Yan et al. (2023). Implementing more vertical levels provides the opportunity to determine the dominance of large-scale processes over small-scale surface processes at different measurement heights. By incorporating a canopy into the model, the surface resistance could be accounted for, enhancing the accuracy of the modelled surface fluxes. Furthermore, exploring larger temporal and spatial scales could yield valuable insights into the variability of ER_{forest} over time and space, in contrast to our CLASS model that is only valid during the day when the SH flux is larger than zero. Increasing the temporal scale gives the opportunity to improve estimates of ER_{forest}. This also has the potential to improve estimates of the global biospheric ER, currently taken to be 1.1 (Severinghaus, 1995).

4.5.2 How ER_{atmos} should be used

Single-height O_2 and CO_2 measurements and their ER_{atmos} signal should be analysed very carefully when using ER_{atmos} as an indicator of surface exchange. During the complete diurnal cycle, ER_{forest} should be utilized as the primary indicator of the ER signals from the surface, while ER_{atmos} should not be used for this purpose. In situations where only one height measurement is available, and therefore only ER_{atmos} can be obtained, a first estimate of ER_{forest} could be made using ER_{atmos}. The ER_{atmos} signal at the end of the day should then be used to avoid the large influence of entrainment earlier in the day. However, any analysis or discussion based on this estimation should include a comprehensive examination of how entrainment might have influenced the ER_{atmos} signal. This also applies for less representative or non-typical days where the mixed-layer theory may be difficult to apply. An example of such a case is given by Casso-Torralba et al. (2008b), where it is shown that entrainment is still important on a non-typical day when polluted air influences the diurnal CO_2 measurements.

Several studies have shown that ER_{atmos} can also serve as an indicator of potential advection from carbon source/sink regions (Ishidoya et al., 2020; Ishidoya et al., 2022a). However, caution should be exercised when directly inferring the specific source based solely on the ER_{atmos} value. Equation (4.9) shows that mixing advected air with the air above a forest will result in an ER_{atmos} signal that cannot be directly linked to the source of the advected air. This is because mixing two ER signals with opposite fluxes does not result in a weighted average (Fig. 4.3). Advection of a source with a known ER signal but with different magnitudes can therefore give different ER_{atmos} values. A solution could be to include other tracers in the analysis such as NO_x or CO (Liu et al., 2023a).

When two or more measurement heights of O_2 and CO_2 are available and ER_{forest} can therefore be derived, the ER_{atmos} of a single height could be used to provide extra information on large-scale processes by analysing the difference between ER_{atmos} and the ER_{forest} signal. During the day, ER_{atmos} provides insights into larger-scale processes, while ER_{forest} reflects local or small-scale processes. Therefore, any discrepancy between ER_{atmos} and ER_{forest} indicates a significant influence of large-scale processes. Nonetheless, the exact difference between ER_{atmos} and ER_{forest} should not be used as an indication of the strength of the influence of large processes. To get more detail on how the large scale processes change between days, the diurnal cycle of ER_{atmos} has to be compared during the entrainment dominant period (P2) and the surface-dominant periods (P3). During P2, an increase in the difference between ER_{atmos} and ER_{forest} may be due to either a low β_{CO_2} or a change in the jump ($\Delta_{(ft\text{-}bl)}$) ratio. If the cause is the former (low β_{CO_2}), the ER_{atmos} signal during P3 should be closer to ER_{forest}. If the latter applies (a high jump ratio), ER_{atmos} should remain well above ER_{forest} in P3.

4.5.3 Different $\Delta_{(ft-bl)}$

Knowing the vertical profile of O_2 and CO_2, especially during sunrise, is essential to gain a more comprehensive understanding of the formation of different jump ratios ($\Delta_{(ft\text{-}bl)}O_2 \,/\, \Delta_{(ft\text{-}bl)}CO_2$) and to better interpret the diurnal behaviour of the ER_{atmos} signal. However, due to a lack of observational data, we cannot validate the vertical profile of O_2 and CO_2 and the jump ratios. We therefore strongly recommend that future measurement campaigns include vertical measurements of both species. This can, for example, be achieved by flask sampling from aircraft, as we did in a recent campaign in the Netherlands, the preliminary results of which confirm that the values we have used here are realistic. Previous studies have also measured vertical profiles of O_2 and CO_2, but they primarily focused on well-mixed profiles during daytime or profiles over the ocean (Morgan et al., 2019; Stephens et al., 2021; Ishidoya et al., 2022b). Hence, careful consideration of the timing and location of the vertical measurements is important to advance our knowledge of the diurnal behaviour of ER_{atmos}.

In the absence of observational data, we show with hypothetical situations that various jump ratios become possible (Fig. 4.8). Both the O_2 and CO_2 jumps are formed as a result of three processes: the mixed-layer value before sunset, the surface flux during the night, and the free troposphere value with the lapse rate (we assume the lapse rate to be $0\,\mathrm{mol\,m^{-1}}$ for CO_2 and O_2). Most cases indicate that $\Delta_{(ft\text{-}bl)}O_2$ is larger than $\Delta_{(ft\text{-}bl)}CO_2$ above a forest, primarily because ER_{forest} is higher than 1.0 during the night ($ER_r > 1.0$), as was shown in previous studies (Ishidoya et al., 2013; Angert et al., 2015; Hilman et al., 2022). It is noteworthy that the movement of the mixed-layer values from sunset to sunrise in Fig. 4.8 differs from its depiction in Fig. 4.2c, where the focus was primarily on the transition between sunrise and sunset. We ignore the effect of subsidence (caused by mesoscale or synoptic processes) on the jump evaluation in this analysis, because it is likely of less importance compared to the other three processes.

It is highly likely that the jump ratio between O_2 and CO_2 cannot be directly linked to a specific ER for a certain process because of the interplay between the three processes that form the O_2 and a CO_2 jump (Fig. 4.8d). The likelihood of both $\Delta_{(ft\text{-}bl)}O_2$ and $\Delta_{(ft\text{-}bl)}CO_2$ being zero at the end of the day is low, because the surface flux during the day would form a jump (Fig. 4.8c). Additionally, it is possible that $\Delta_{(ft\text{-}bl)}O_2$ is smaller than $\Delta_{(ft\text{-}bl)}CO_2$ at the end of the day (Fig. 4.8d) due to the daytime ER_{forest} being smaller than 1.0. Consequently, O_2 will exhibit a faster movement across the zero line, resulting in a significantly larger $\Delta_{(ft\text{-}bl)}O_2 \,/\, \Delta_{(ft\text{-}bl)}CO_2$ ratio compared to ER_r.

Decoupling between the free troposphere and the boundary layer can lead to a scenario in which $\Delta_{(ft\text{-}bl)}CO_2$ becomes larger than $\Delta_{(ft\text{-}bl)}O_2$ (Fig. 4.8e). This can occur, for example, when the influence of fossil fuel sources causes a decrease in the O_2 mole fraction and an increase in the CO_2 mole fraction in the free troposphere, but large surface fluxes from the forest prevent such changes from occurring in the boundary layer. The jump ratio in this case again cannot be attributed to a single process. Some studies have demonstrated that decoupling between the boundary layer and the free troposphere can occur, leading to different ER signals (Sturm et al., 2005; Laan et al., 2014b).

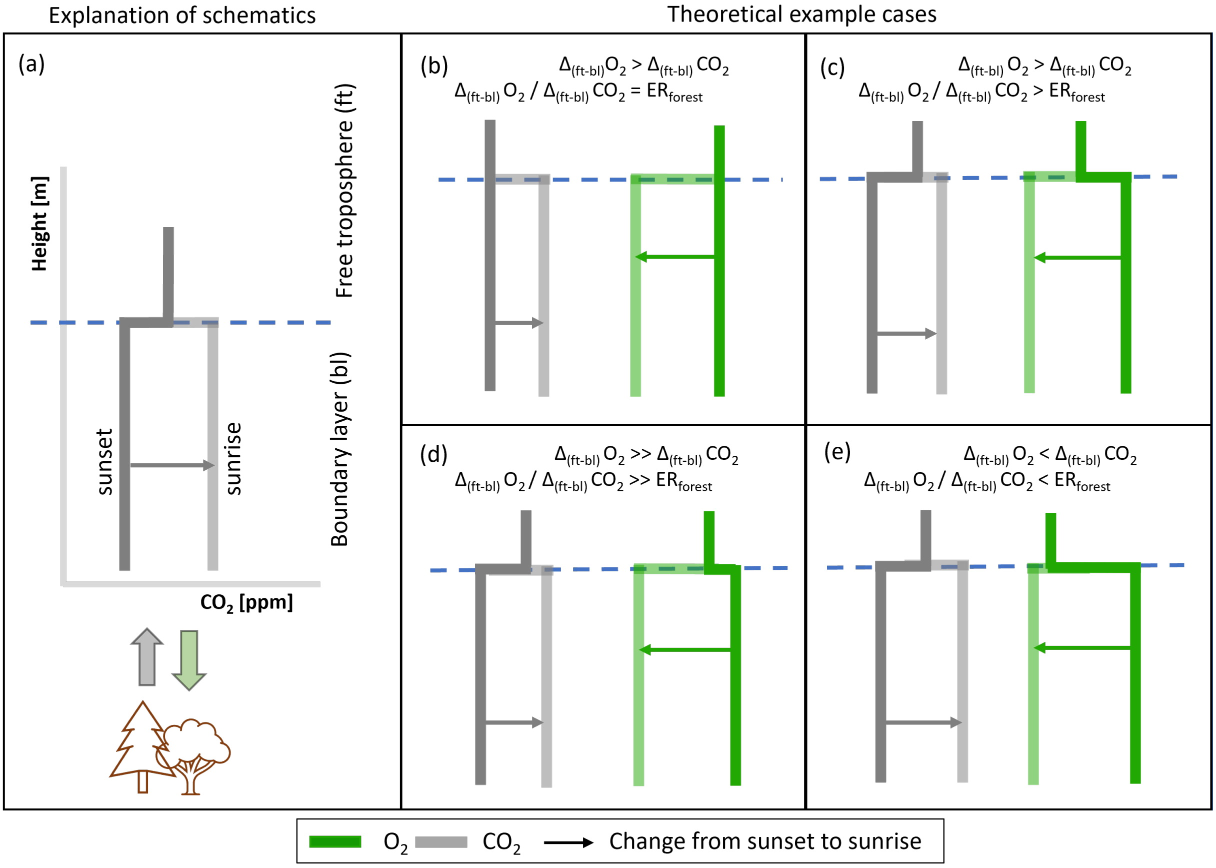

Figure 4.8: Schematic overview of how different ratios of the jumps of O_2 ($\Delta_{(\text{ft-bl})}O_2$) and CO_2 ($\Delta_{(\text{ft-bl})}CO_2$) are formed in the nighttime and how the ratio relates to the exchange ratio of the forest (ER_{forest}). Panel **(a)** gives an explanation of the schematics and the other panels show four possibilities of different jump ratios ($\Delta_{(\text{ft-bl})}O_2 / \Delta_{(\text{ft-bl})}CO_2$): **(b)** the jump ratio is equal to ER_{forest}, **(c)** the jump ratio is larger than ER_{forest}, **(d)** the jump ratio is much larger than ER_{forest}, **(e)** the jump ratio is smaller than ER_{forest}. The bold lines represent the vertical profile just after sunset and the shaded lines represent the vertical profile just before sunrise.

4.5.4 Comparison with other studies

To the best of our knowledge, no previous studies have reported such high deviations of ER_{atmos} from ER_{forest} or ER_{atmos} values higher than 2 for above-forest-canopy measurements, as we found in Faassen et al. (2023). Only Liu et al. (2023b) found a non-linear relationship between O_2 and other tracers that was difficult to explain. While some differences between ER_{atmos} and ER_{forest} have been observed in previous studies, these differences typically fall within a region of 0.5 (Seibt et al., 2004; Ishidoya et al., 2015; Battle et al., 2019; Yan et al., 2023). A possible reason for these smaller differences could be that most studies do not focus on such detailed diurnal analyses of ER_{atmos} for specific days, but rather aggregate data from multiple days, which could mitigate the extreme effects of entrainment by combining various jump possibilities. However, even in the study by Stephens et al.

(2007), in which measurements at different heights are shown, no discernible difference in the $\mathrm{ER}_{\mathrm{atmos}}$ signal for various diurnal cycles was observed, a finding that contrasts with our own analysis. The height at which measurements are made also influences the resulting $\mathrm{ER}_{\mathrm{atmos}}$ signal. Closer to the canopy, the influence of entrainment is lower and $\mathrm{ER}_{\mathrm{atmos}}$ is closer to $\mathrm{ER}_{\mathrm{forest}}$ compared to measurements further away from the canopy (Faassen et al., 2023). However, we still found a high $\mathrm{ER}_{\mathrm{atmos}}$ value of 2.28, even at a level just above the canopy (Faassen et al., 2023). Large values for $\mathrm{ER}_{\mathrm{atmos}}$ have only been found at high-latitude measurement stations (Sturm et al., 2005), due to the influence of the ocean.

There are several possibilities that might explain a constant $\mathrm{ER}_{\mathrm{atmos}}$ signal during the day which are not shown in our study. One possibility is that entrainment dominates throughout the day, caused by high jumps. If both the O_2 and CO_2 jumps are extremely high while the surface flux remains low, the $\mathrm{ER}_{\mathrm{atmos}}$ value reflects the ratios between the jumps. In this scenario, $\mathrm{ER}_{\mathrm{atmos}}$ cannot be used as an accurate indicator for the surface processes. Another explanation could be that the $\mathrm{ER}_{\mathrm{forest}}$ signal is exactly 1.0 and entrainment is relatively low. When $\mathrm{ER}_{\mathrm{forest}}$ equals 1.0, the diurnal cycle of the jumps would respond similarly. Together with a low entrainment flux (resulting from low jumps), it could lead to a constant $\mathrm{ER}_{\mathrm{atmos}}$ value. Additionally, when the peak of $\mathrm{ER}_{\mathrm{atmos}}$ occurs rapidly, there is a possibility that a low measurement precision would miss the extreme changes of $\mathrm{ER}_{\mathrm{atmos}}$. However, even in such cases, $\mathrm{ER}_{\mathrm{atmos}}$ would still be influenced by entrainment, although its impact may be less discernible. It is crucial to note that in all these cases, $\mathrm{ER}_{\mathrm{atmos}}$ remains influenced by entrainment to varying degrees.

Our study provides evidence that $\mathrm{ER}_{\mathrm{atmos}}$ is almost always influenced by large-scale processes and their diurnal variability, specifically entrainment, making it important to exercise caution when using it as an indicator of surface ER processes. Instances where $\mathrm{ER}_{\mathrm{atmos}}$ remains constant throughout the daytime and serves as a reliable indication for $\mathrm{ER}_{\mathrm{forest}}$ are likely rare. In comparison to previous studies (Seibt et al., 2004; Stephens et al., 2007; Ishidoya et al., 2013; Battle et al., 2019), it is unclear why Faassen et al. (2023) yields such extreme values for $\mathrm{ER}_{\mathrm{atmos}}$ while the other studies do not show this, even though our modelling study here confirms the extreme $\mathrm{ER}_{\mathrm{atmos}}$ values. Therefore, we recommend conducting more studies or performing detailed analyses of existing O_2 and CO_2 datasets to gain a better understanding of how changes in $\mathrm{ER}_{\mathrm{atmos}}$ vary with time and space.

4.5.5 Comparison with other multi-tracer analyses

The impact of changes in large-scale conditions such as entrainment on multi-tracer analyses above forest canopies extends beyond atmospheric O_2, encompassing other carbon cycle tracers such as carbon and oxygen isotopes (δ^{13}C and δ^{18}O) (Wehr et al., 2016) and carbonyl sulfide (COS) (Whelan et al., 2018). Caution is required when employing methods of determining ratios between two species (e.g. leaf relative uptake for COS and the ratios between different isotopes) that rely solely on single-height measurements. However, the influence of entrainment on these ratios would be less extreme compared to that on the ER_{atmos} signal, because both COS and isotopes move in the same direction as CO_2 itself. This is differs from the situation with O_2, which always moves in the opposite direction to CO_2. When both species that form the ratio move in the same direction, ratios of different processes could be averaged and a one-height measurement is more readily interpretable. Nevertheless, entrainment would still cause the two compounds that form the ratio to behave differently. We therefore emphasize the need to separately analyse the composition of the signal for each compound when ratios are analysed.

Furthermore, we demonstrate in this study the potential of using ER_{atmos} as an indicator of the extent of large-scale processes. Additional tracers can strengthen this approach. Also $\delta^{13}C$, $\delta^{18}O$, and COS signals exhibit differences between the surface and the free troposphere. Similar to O_2, the onset of entrainment causes these signals to mix, yielding insights into how large-scale processes influence the carbon cycle above a canopy (Berkelhammer et al., 2014; Vilà-Guerau de Arellano et al., 2019). By combining various tracers for CO_2, we can create a comprehensive picture of the effects of small- and large-scale processes that influence carbon exchange.

4.6 conclusions

We used a mixed-layer model to analyse the diurnal behaviour of two exchange ratio ($ER = -O_2 \,/\, CO_2$) signals above a forest canopy: the ER of the atmosphere (ER_{atmos}, determined from the change over time of O_2 and CO_2 mole fraction measurements at a single height above the canopy) and the ER of the forest (ER_{forest}, determined from O_2 and CO_2 fluxes derived from the vertical gradient observations at two levels). We disentangled the biophysical processes influencing ER_{atmos} to interpret single-height O_2 and CO_2 measurements and to evaluate how ER_{atmos} and ER_{forest} can be used to constrain carbon exchange above the canopy. The analysis is supported by the derivation of a new theoretical relationship that connects ER_{atmos} and ER_{forest} and by the use of a mixed-layer model that reproduces the O_2 and CO_2 diurnal cycles coupled to the dynamics of the atmospheric boundary layer. By combining the model with observations from a boreal forest during the two contrasting summers of 2018 and 2019, we found three distinct regimes during the day for ER_{atmos}.

We find that the entrainment of air from the free troposphere leads to a diurnal cycle in ER_{atmos}, resulting in three distinctive regimes: P1 at the start of the day, when the boundary layer has not yet started to grow; P2 when entrainment of air from the free troposphere into the boundary layer is dominant; and P3 at the end of the afternoon, when entrainment becomes negligible. ER_{atmos} can exhibit high values during P2 that cannot be attributed to an ER signal from a single process. During P3, ER_{atmos} becomes closer to ER_{forest}, and is therefore more representative of the forest exchange.

The large diurnal variability in ER_{atmos} shows that single-height O_2 and CO_2 measurements are insufficient as an indication of the O_2 / CO_2 ratios of forest exchange. Our theoretical relationship between ER_{atmos} and ER_{forest} and the model results show that the large diurnal variability is a result of the different behaviours of the O_2 and CO_2 diurnal cycles, which results in ER_{atmos} values that cannot be attributed to a single process. To estimate the ER signal of the surface fluxes from above-canopy measurements, ER_{forest} should be used and, therefore, O_2 and CO_2 signals need to be measured at at least two heights to allow fluxes to be calculated from the vertical gradient. A single measurement height for O_2 and CO_2 could still be used to indicate the presence of advection of other carbon sources. However, the resulting ER_{atmos} signal should be analysed with care, taking into account the diurnal variability and the fact that the resulting ER is not necessarily the average of the individual ER signals of the contributing processes.

When O_2 and CO_2 measurements are available from two different heights, the relationship between ER_{atmos} and ER_{forest} during P2 and P3 could provide valuable information about the changes in large-scale carbon processes (e.g. entrainment) and their influence on the smaller-scale processes of the surface. A discrepancy between ER_{atmos} and ER_{forest} shows that large-scale processes occur together with small-scale processes at the surface. The difference between ER_{atmos} and ER_{forest} should be analysed with care, as the size of the difference is not a direct indication of the size of the influence of the large-scale processes. Differences between ER_{forest} and ER_{atmos} could be caused by several factors: changes in the size of the entrainment flux, the net surface flux or the difference between the free troposphere and the boundary layer (the “jump”) for O_2 and/or CO_2, or changes in the jump ratio between O_2 and CO_2.

In conclusion, single-height O_2 and CO_2 measurements need to be analysed with care, accounting for their dependence on canopy processes (represented by ER_{forest}) but also for their capacity to integrate large-scale processes, resulting in values that cannot be attributed to a single process. To represent the forest exchange, the ER_{forest} signal based on measurements at at least two heights should be used instead.

Data availability. The data used in this study are available from https://doi.org/10.18160/SJ3J-PD38 (Faassen and Luijkx, 2022). The model code for the CLASS model can be found in https://classmodel.github.io/.

4.7 Appendix

A4.1 Evaluation of the theoretical relationship between ER_{atmos} and ER_{forest}

In this section, we analyse Eq. (4.8) to explore the response of ER_{atmos} to changes in the variables in this equation and to investigate when ER_{atmos} aligns with ER_{forest} and thereby accurately reflects local processes. Based on Eq. (4.8), the ER_{atmos} signal equals ER_{forest} when the β values of O_2 and CO_2 are equal. We can define four different regimes where the β values change significantly. As depicted in Fig. 4.1, we can define two regimes based on the entrainment velocity: an entrainment-driven (left panels in Fig. A4.1) and a photosynthesis-driven regime (right panels in Fig. A4.1). To complete the analysis, we considered two distinct cases for the jump of O_2 (top versus bottom panels).

Based on Eq. (4.8), we systematically varied $\Delta_{\text{(ft-bl)}}CO_2$ and $(F_{CO_2})_s$ over plausible ranges and kept the other variables constant. As a result, we derived ER_{forest} / ER_{atmos} ratios for these four regimes, where a value of 1.0 now indicates that ER_{atmos} is equal to ER_{forest}. The selected values and ranges for the four different cases were informed by initial conditions from the Hyytiälä case studied in Faassen et al. (2023) and the corresponding model simulations presented in Sect. 4.3.2.

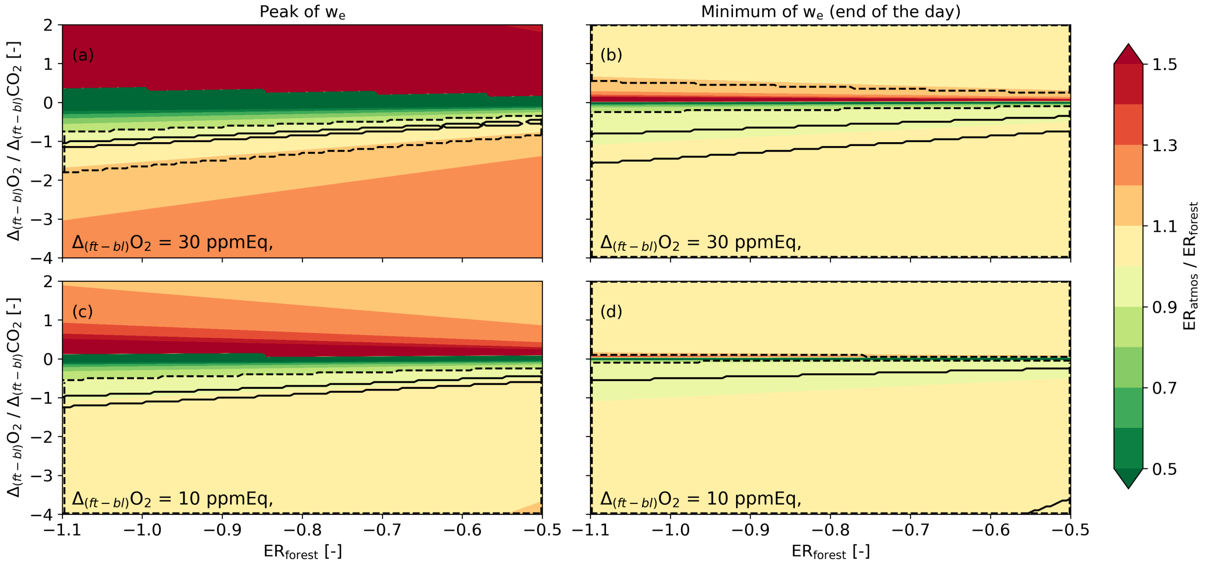

Figure A4.1: Analysis of Eq. (4.8) for the entrainment- and photosynthesis-driven regimes. The ratio between ER_{forest} and ER_{atmos} is evaluated based on changes in ER_{forest} and the ratio of the jumps of O_2 and CO_2 between the free troposphere and the boundary layer ($\Delta_{\text{(ft-bl)}}$) for four cases: with a high entrainment velocity ($w_e = 0.10\,\mathrm{m\,s^{-1}}$) **(a, c)** and a low entrainment velocity ($w_e = 0.01\,\mathrm{m\,s^{-1}}$) **(b, d)**, and for situations with a high O_2 jump ($\Delta_{\text{(ft-bl)}}O_2 = 0.30$ ppmEq) **(a, b)** and a low O_2 jump ($\Delta_{\text{(ft-bl)}}O_2 = 0.10$ ppmEq) **(c, d)**. The O_2 surface flux $F(O_2)_s$ is kept constant for all the panels at $8.5\,\mu\mathrm{mol\,m\,s^{-1}}$.

There are a few situations where the β values of O_2 and CO_2 are equal and these are indicated in Fig. A4.1 as the area between the black solid (ER_{atmos} deviates $< 1\,\%$ from ER_{forest}) and dashed lines (ER_{atmos} deviates $< 10\,\%$ from ER_{forest}):

1. *During the photosynthesis dominant regime.* When the entrainment velocity (w_e) is close to zero, both β values become zero. This is likely at the end of the day (right panels in Fig. 4.1).
2. *When the β values for O_2 and CO_2 become equal, which happens when* $\Delta_{(ft\text{-}bl)}O_2 \,/\, \Delta_{(ft\text{-}bl)}CO_2 = ER_{forest}$. A specific case is when $\Delta_{(ft\text{-}bl)}O_2 = \Delta_{(ft\text{-}bl)}CO_2$. In this instance, ER_{forest} has to be 1.0 for the β values of O_2 and CO_2 to become equal. The β values of O_2 and CO_2 become closer during the lower O_2 jump case (lower panels in Fig. 4.1).

The last situation only occurs under very specific conditions when the ratio of the O_2 and CO_2 entrainment and surface fluxes are the same. This is visible in the left panels of Fig. A4.1, where only a small part of the graph shows values of ER_{atmos} close to ER_{forest} (indicated by the area between the solid lines). In contrast, during low entrainment velocities at the end of the afternoon, it is more likely that the ER_{atmos} values become close to ER_{forest}, and this is shown by the larger area in the right panels of Fig. A4.1. Low entrainment velocities could also occur when the growth of the boundary layer is reduced due to subsidence, although we do not focus on this specific case in this study.

There are also differences between ER_{atmos} and ER_{forest} that arise from variations in the β values. Figure A4.1 demonstrates that substantial differences between ER_{atmos} and ER_{forest} originate due to differences in the entrainment fluxes of both species. When $\Delta_{(ft\text{-}bl)}O_2$ exceeds $\Delta_{(ft\text{-}bl)}CO_2$, this implies a dominant entrainment flux of O_2 over CO_2 and β_{O_2} deviates further from β_{CO_2} (Eq. 4.8). This effect is almost absent when the jumps themselves are lower, because the ER_{atmos}/ER_{forest} ratio stays around 1 (Fig. A4.1c). Moreover, when $\Delta_{(ft\text{-}bl)}CO_2$ transitions from negative to positive, the sign of β_{CO_2} also changes, subsequently elevating the ER_{atmos} values (Eq. 4.8).

ER_{atmos} can also become smaller than ER_{forest} when $\Delta_{(ft\text{-}bl)}CO_2$ is larger than $\Delta_{(ft\text{-}bl)}O_2$ (Fig. A4.1). This difference results in a large value for β_{CO_2} compared to β_{O_2}, causing the ER_{forest} value to be multiplied by a factor of less than 1 and leading to a lower ER_{atmos} value than ER_{forest} (Eq. 4.8). By assessing ER_{atmos} and ER_{forest} values, we can see whether $\Delta_{(ft\text{-}bl)}O_2$ exceeds $\Delta_{(ft\text{-}bl)}CO_2$ ($ER_{atmos} > ER_{forest}$) or vice versa ($ER_{atmos} < ER_{forest}$).

This illustrative analysis, based on prescribed values in Eq. (4.8) and Fig. A4.1, provides an initial estimate of the variability in ER_{atmos}. However, it lacks insights into the diurnal behaviour of the individual components of Eq. (4.8) and their potential combinations.

A4.2 Implementation of O_2 in CLASS

The following equation shows the implementation of the tendency (change over time) of O_2 into CLASS:

$$\frac{dO_2}{dt} = \frac{F_{O_2(s)} - F_{O_2(e)}}{h} + adv_{O_2} \tag{A4.1}$$

where $F_{\mathrm{O_2(s)}}$ is the net surface O_2 flux at the canopy, $F_{\mathrm{O_2(e)}}$ is the O_2 entrainment flux, h is the boundary layer height, and $\mathrm{adv}_{\mathrm{O_2}}$ is the advection term. The surface flux is calculated with Eq. (4.10) and the entrainment flux is based on the following equation (see also Eq. 4.2):

$$F_{O_2(e)} = -w_e \cdot \Delta_{(ft-bl)} O_2 \tag{A4.2}$$

where w_{e} is the entrainment velocity and $\Delta_{\text{(ft-bl)}}O_2$ is the jump of O_2. The jump of O_2 was determined the same way as for CO_2, by tuning the initialization of the jump until the decrease or increase of CO_2 / O_2 of the model matched with the observational data.

A4.3 Validation of CLASS

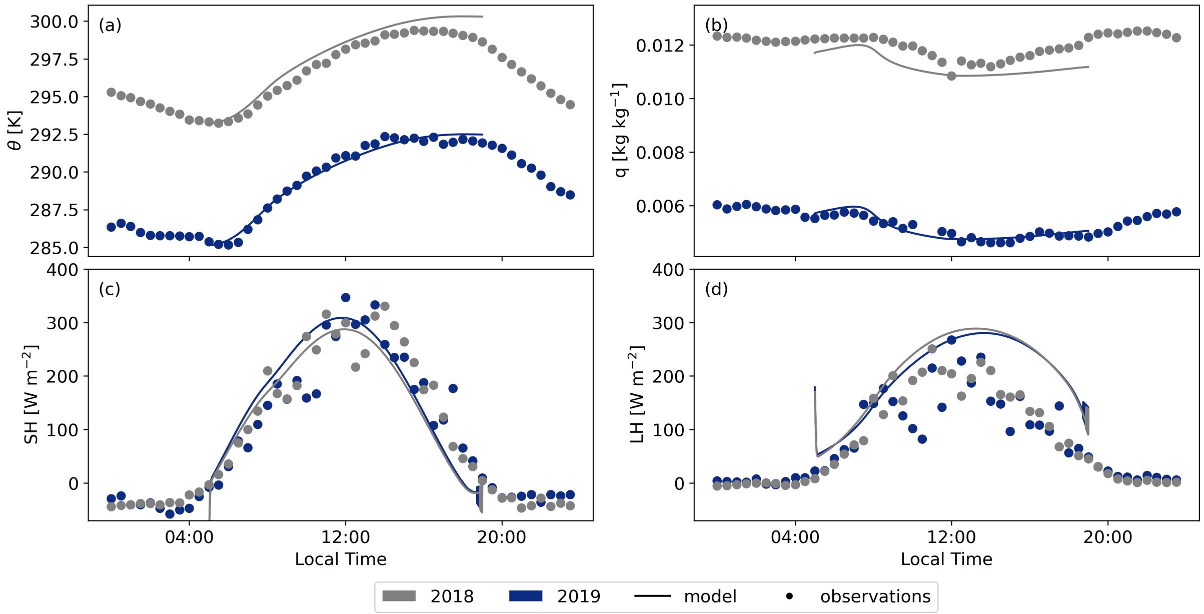

Figure A4.2: Comparison between the 2019 and 2018 cases modelled with CLASS with the observational data for the potential temperature (θ) **(a)**, specific humidity (q) **(b)**, sensible heat flux (SH) **(c)**, and latent heat flux (LH) **(d)**.

Figures A4.3 and A4.2 present a comparison between the model output of CLASS and the corresponding measurements for the representative days of 2018 and 2019, assessing various parameters. Both figures demonstrate that the model compares well to the observed data. CLASS accurately follows the observed temperature increase (Fig. A4.2a). A constant difference of approximately 8K between 2018 and 2019 is seen for both the model and the observations. This persistent difference is attributed to a heat wave rather than a drought in Hyytiälä, as a drought would have intensified the divergence between the 2018 and 2019 simulations throughout the day. Moreover, CLASS adequately models specific humidity for both years, assuming an initial relative humidity of 80 % for 2018 (Fig. A4.2b). The sensible heat flux (Fig. A4.2c) and latent heat flux (Fig. A4.2d) exhibit minimal differences between the 2018 and 2019 simulations. The accurate representation of atmospheric properties in CLASS consequently results in a satisfactory representation of boundary layer height development for both years in comparison to the observed data from radiosondes (Fig. A4.3a)

The various CO_2 fluxes simulated by CLASS exhibit a high level of agreement with the observational data for both 2018 and 2019 (Fig. A4.3d and e). While there are subtle differences evident between the observations for the two years, CLASS adeptly captures these nuances. Consequently, the model provides an accurate representation of plant behaviour under both normal and warmer conditions. The elevated temperatures (+8 K) and slightly reduced soil moisture ($-0.03\,\mathrm{m^3\,m^{-3}}$) contribute to a slightly higher GPP and TER flux. Our study reaffirms that the vegetation in Hyytiälä did not undergo any stress during the 2018 European drought, which would have resulted in a lower GPP and lower latent heat flux (Lindroth et al., 2020).

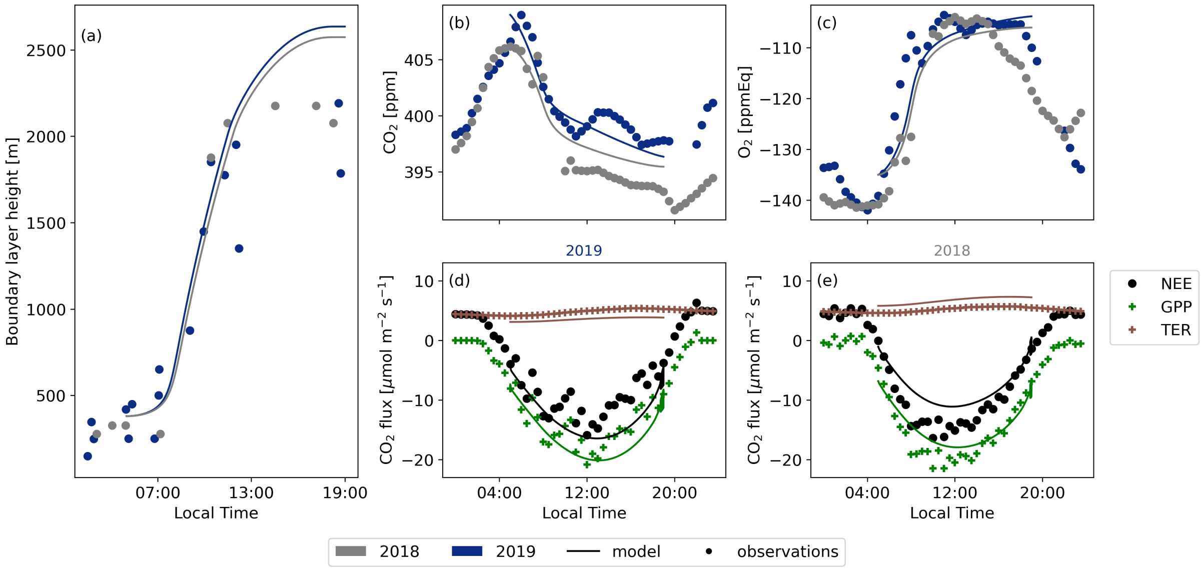

Figure A4.3: Comparison between the 2019 and 2018 cases modelled with CLASS using the observational data for the boundary layer height **(a)**, CO_2 **(b)**, O_2 **(c)**, the 2019 CO_2 surface fluxes **(d)**, and the 2018 CO_2 surface fluxes **(e)**.

For the 2018 case, we altered only a few initial conditions (see Table A4.3). However, both the decrease in CO_2 and the increase in O_2 during the day exhibit close similarity between the model and the observations. This outcome underscores that even with minimal changes in the initial conditions for the 2018 case and while keeping the other variables constant (e.g. the jumps), we can successfully replicate a realistic new day based on the base case.

It is important to note that only the net ecosystem exchange (NEE) data are obtained directly from eddy covariance measurements. The gross primary production (GPP) is inferred from a light- and temperature-based function and the total ecosystem respiration is calculated as the residual between NEE and GPP (Kulmala et al., 2019; Kohonen et al., 2022). This distinction may explain the challenge in aligning the TER flux of the observations with the model, as the model exhibits notable discrepancies from the observations for the 2018 and 2019 cases. The model's simulated respiration increase based on temperature appears more extreme compared to the observations. However, several studies (Lindroth et al., 2008; Gao et al., 2017; Heiskanen et al., 2023) indicate that the model's increase in TER between 2018 and 2019 is slightly too high, while the change based on observations is too low. As a result, it is plausible that the true respiration flux lies somewhere between the model output and the observational data.

A4.4 Figures and Tables

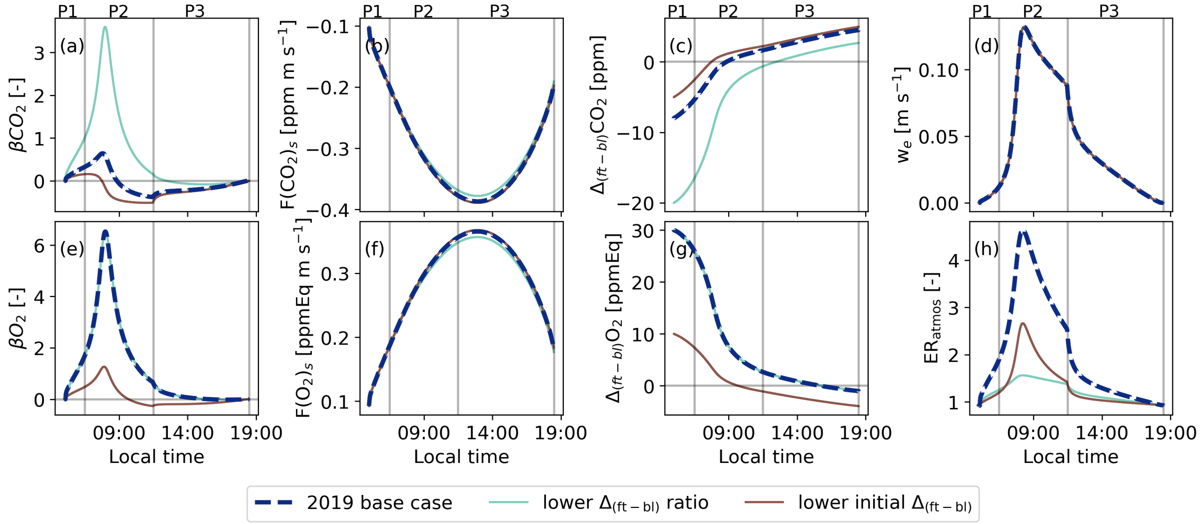

Figure A4.4: Similar to Fig. 4.5 but now for the base case (2019) and the background sensitivity studies with a lower jump ratio between O_2 and CO_2 (lower $\Delta_{\text{(ft-bl)}}$), and with a lower initial jump for CO_2 (lower initial $\Delta_{\text{(ft-bl)}}$). The diurnal variability of the exchange ratio of the atmosphere is now added (ER_{atmos}: (h)).

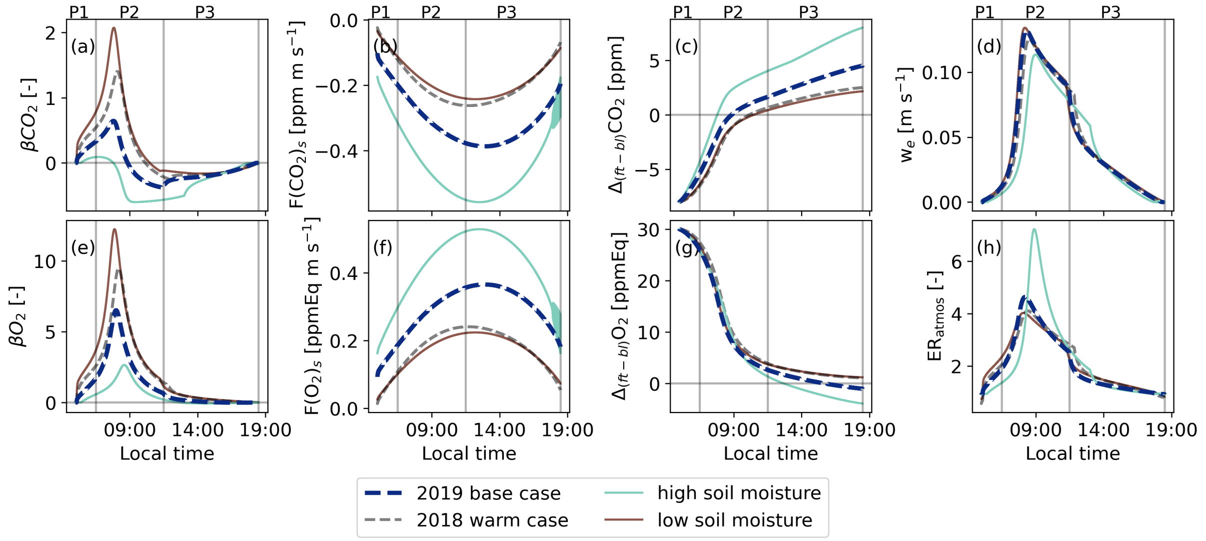

Figure A4.5: Similar to Fig. 4.5 but now for the base case (2019) and the dry and warm sensitivity studies with a high soil moisture and a low soil moisture, both with higher air temperatures compared to the 2019 base case. The diurnal variability of the exchange ratio of the atmosphere is now added (ER_{atmos}: (h)).

Table A4.1: The initial conditions used for the three sensitivity analyses compared to the initial conditions for the 2019 base case. The subscript (0) indicates the first time step.

Variable	2019 base	background air		climate	
		lower $\Delta_{(ft-bl)}$ ratio	lower intial $\Delta_{(ft-bl)}$	high SMI	low SMI
$\Delta_{(ft-bl)}O_{2(0)}$ [ppmEq]	30	30	10	2019 case	2019 case
$\Delta_{(ft-bl)}CO_{2(0)}$ [ppm]	-8	-20	-5	2019 case	2019 case
θ_0 [K]	285.2	2019 case	2019 case	290	290
Soil moisture [m^3 m^{-3}]	0.18	2019 case	2019 case	0.22	0.14

Table A4.2: Initialization of the CLASS model for the 2019 base case based on 10 July 2019. The initialization is based on the SMEAR II data (Hari et al., 2013), our OXHYYGEN campaign data (radiosondes or O_2 and CO_2 measurements) (Faassen et al., 2023), and studies that show ranges for parameters for the plants and soil (Lindroth et al., 2008; ECMWF, 2014; Vilà-Guerau de Arellano et al., 2015).

Parameter [Source]	Description	Initial value
Lat	Latitude [deg]	61.51
Lon	Longitude [deg]	24.17
DOY	Day of year [-]	191
t_0	Starting time [UTC]	3
h_1	Initial boundary layer height [m]	380

Continues next page

h_2	Height of the residual layer [m]	2016
P	Surface pressure [hPa]	988.72
Temperature:		
θ_0	Initial potential temperature [K]	285.15
$\Delta\theta_0$	Initial potential temperature jump [K]	2.4
$\lambda\theta_1$	Potential temperature lapse rate of residual layer [K m^{-1}]	0.0023
$\lambda\theta_2$	Potential temperature lapse rate of free troposphere [K m^{-1}]	0.0057
Specific humidity:		
q_0	Initial specific humidity [kg kg^{-1}]	5.7 x 10^{-3}
Δq_0	Initial specific humidity jump [kg kg^{-1}]	-1.2 x 10^{-3}
λq_1	Specific humidity lapse rate of residual layer [kg kg^{-1} m^{-1}]	-8.3 x 10^{-7}
λq_2	Specific humidity lapse rate of free troposphere [kg kg^{-1} m^{-1}]	-2.3 x 10^{-6}
Carbon:		
$CO_{2,0}$	Initial $CO_{2,0}$ mole fraction [ppm]	409
$\Delta CO_{2,0}$	Initial CO_2 jump [ppm]	-8
λCO_2	CO_2 lapse rate of free troposphere [ppm m^{-1}]	0
Oxygen:		
$O_{2,0}$	Initial O_2 [ppm]	-135
$\Delta O_{2,0}$	Initial O_2 jump [ppm]	30
λO_2	O_2 lapse rate of free troposphere [ppm m^{-1}]	0
Vegetation:		
LAI	Leaf Area Index [-]	3.3
C_{veg}	Vegetation cover [-]	0.9
$r_{c,min}$	Minimum resistance transpiration [s m^{-1}]	500
$r_{s,soil,min}$	Minimum resistance soil evaporation [s m^{-1}]	250
g_D	VPD correction factor for surface resistance [-]	0.03
$z_{0,m}$	Roughness length for momentum [m]	2.0
$z_{0,h}$	Roughness length for heat and moisture [m]	2.0
α	albedo [-]	0.10
R_{10}	Respiration at 10 degrees [mg CO_2 m^{-2} s^{-1}]	0.148
g_m	Mesophyl conducatance [mm s^{-1}]	2
T_{2gm}	reference temperature to calculate gm [K]	305
C_β	Curvature of response curve to drought [-]	0.15
Soil:		
T_s	Initial surface temperature [K]	287.7
$T_{soil,1}$	Initial top soil temperature [K]	284.2
$T_{soil,2}$	Initial deeper soil temperature [K]	282.0
w_{sat}	Saturated volumetric water content [m^3 m^{-3}]	0.5

Continues next page

w_{fc}	Volumetric water content field capacity [m^3 m^{-3}]	0.30
w_{wilt}	Volumetric water content wilting point [m^3 m^{-3}]	0.08
w_g	Volumetric water content of top soil layer [m^3 m^{-3}]	0.18
w_2	Volumetric water content of deeper soil layer [m^3 m^{-3}]	0.12
a	Clapp and Hornberger retention curve parameter [-]	0.387
b	Clapp and Hornberger retention curve parameter [-]	4.05
p	Clapp and Hornberger retention curve parameter [-]	4
CG_{sat}	Saturated soil conductivity for heat [K m^{-2} J^{-1}]	3.22×10^{-6}
$C1_{sat}$	Coefficient force term moisture [-]	0.082
$C2_{ref}$	Coefficient restore term moisture [-]	3.9
Λ	Thermal diffusivity skin layer [-]	5

Table A4.3: Adjustments for the 2018 case (warm case) compared to the 2019 values shown in Table A4.2. Only the initial potential temperature (θ_0), initial soil moisture (w_g), and CO_2 mole fraction ($CO_{2,0}$) are adjusted based on the aggregate of 28 and 29 July 2018. It was assumed that the initial relative humidity stayed constant at 80 % with increasing temperatures; therefore, the initial specific humidity was also adjusted.

Parameter	Description	Initial value
θ_0	Initial potential temperature [K]	293.3
$T_{soil,1}$	Initial top soil temperature [K]	θ_0 - 2
$T_{soil,2}$	Initial deeper soil temperature [K]	θ_0 - 3
q_0	Initial specific humidity [kg kg^{-1}]	f(θ_0)
w_g	Volumetric water content of top soil layer [m^3 m^{-3}]	w_2 - 0.04
w_2	Volumetric water content of deeper soil layer [m^3 m^{-3}]	0.15
$CO_{2,0}$	Initial CO_2 mole fraction [ppm]	406

Chapter 5

Tracing diurnal variations of atmospheric CO_2, O_2 and $\delta^{13}CO_2$ over a tropical and a temperate forest

This chapter is based on:

K. A. P. Faassen, R. González-Armas, G. Koren, G. Agmuas Adnew, H. van Asperen, H. de Boer, S. Botía, V. S. de Feiter, O. Hartogensis, B. G. Heusinkveld, L. M. Hulsman, R. W. A. Hutjes, S. P. Jones, B. A. M. Kers, S. Komiya, L. A. T. Machado, G. Martins, J. B. Miller, W. Mol, M. van der Molen, R. Moonen, C. Q. Dias-Junior, T. Röckmann, H. Snellen, I. T. Luijkx, and J. Vilà-Guerau de Arellano (under review). "Tracing diurnal variations of atmospheric CO_2, O_2 and $\delta^{13}CO_2$ over a tropical and a temperate forest". *Geophysical Research Letters*

Abstract

We present a comprehensive dataset of the diurnal variability of atmospheric CO_2, O_2 and $\delta^{13}CO_2$ above the canopies of two markedly different ecosystems: the Amazon tropical forest and the Loobos temperate forest. Using a coupled forest-atmosphere model constrained by our tower-based and aircraft observations, we demonstrate that atmospheric processes, including entrainment, subsidence, and cloud ventilation, significantly contribute to the amplitude or diurnal range (DR) of carbon cycle tracers. We show that atmospheric processes can contribute more than twice as much as surface processes to DR. Neglecting the influence of atmospheric processes leads to large errors in the interpretation of the diurnal variability of these tracers. We propose DR metric that integrates surface and non-surface dynamics to 1) evaluate atmospheric transport models of carbon cycle tracers and to 2) understand carbon cycle processes and their trends on site level by studying the variability of DR throughout time.

5.1 Introduction

Advancing our understanding of the terrestrial carbon cycle is critical for reducing uncertainties in the global carbon budget (e.g. Friedlingstein et al., 2023; Piao et al., 2020). Measuring and modeling terrestrial carbon cycle exchange processes is complex due to the integration of multiple processes and scales. Carbon cycle tracers disentangle and quantify these processes. Here, we focus on atmospheric carbon dioxide (CO_2), oxygen (O_2) and the isotope composition of CO_2 ($\delta^{13}CO_2$). The O_2/CO_2 exchange ratios and the $\delta^{13}CO_2$ value have been used in previous studies to partition terrestrial carbon cycle processes (Ishidoya et al., 2015; Faassen et al., 2023; Seibt et al., 2008; Wehr et al., 2016).

Understanding the diurnal cycles of these carbon cycle tracers is crucial to correctly apply partitioning methods or to correctly represent them in high spatiotemporal resolution atmospheric models (Yi et al., 2004; Kretschmer et al., 2014; Bonan et al., 2024). The diurnal cycle of atmospheric tracers is influenced by both surface and atmospheric processes. For CO_2, the relative importance between surface and atmospheric processes on the diurnal cycle has been quantified before (e.g. Denning et al., 1996; Larson and Volkmer, 2008; Pino et al., 2012; Williams et al., 2011; Schuh and Jacobson, 2023). They stressed the key role of entrainment of air with a different atmospheric composition from the free troposphere (FT) into the atmospheric boundary layer (ABL) on the diurnal variability. While the influence of entrainment on the diurnal cycles of O_2 and $\delta^{13}CO_2$ has been acknowledged, its significance has not yet been quantified (Bowling et al., 2005; Faassen et al., 2023) due to a lack of observational evidence for combined tracers both in and above the atmospheric boundary layer.

In this paper, we provide this observational evidence, discuss the common patterns in the diurnal cycles of different tracers and propose a new metric. More specifically, we study the interplay between surface exchange, entrainment, subsidence, and cloud ventilation processes. We present two unique and comprehensive sets of atmospheric CO_2, O_2, $\delta^{13}CO_2$ observations and a large number of supporting micro-meteorological and radiosonde measurements, for two contrasting ecosystems: a needle leaf forest in a temperate climate zone (Loobos, The Netherlands Dolman et al. (2002)) and a tropical forest (Amazon, Brazil Andreae et al. (2015)). We introduce the metric DR (Diurnal Range), or diurnal amplitude, defined as the difference between the daily maximum and minimum value of a given carbon cycle tracer, to evaluate the diurnal cycle. DR is inspired by the Diurnal Temperature Range (DTR) which is used to study climate variations and the capability of models to simulate these accurately (e.g. Qu et al., 2014; Adekanmbi and Sizmur, 2022; Huang et al., 2023). We use the coupled land-atmosphere model (the Chemistry Land-surface Atmosphere Soil Slab model, CLASS Vilà-Guerau de Arellano et al. (2015)) to interpret the observations and to study the sensitivity of DR to surface and atmospheric processes.

5.2 Methods

Our analysis is based on the comparison of our comprehensive observations from a temperate (Loobos, the Netherlands) and a tropical (Amazon Tall Tower Observatory: ATTO, Brazil) forest with a forest-atmosphere coupled model. We collected measurements at the Loobos site (52.1664° N, 5.7436° E) at a 36-meter tower (Dolman et al., 2002; Elbers et al., 2011) (https://maq-observations.nl/). At the ATTO site (2.1819° S, 59.0217° W) we collected measurements at three heights at the tall tower (80 m, 100 m, 321 m) (Andreae et al., 2015; Botía et al., 2022; Vilà-Guerau de Arellano et al., 2024). Meteorological variables, including radiation, surface energy, CO_2 fluxes and CO_2 mole fractions were continuously measured at both sites. In 2022, we conducted additional measurement campaigns at both sites, including flask sampling above the canopy at different levels in the towers and at Loobos also from aircraft (Vellinga et al., 2013). We measured the flasks for CO_2, O_2 and $\delta^{13}CO_2$. Atmospheric O_2 was measured as $\delta(O_2/N_2)$ on the Scripps Institution of Oceanography (SIO) 2017 scale, and converted to ppm equivalents (ppmEq) (Tohjima et al., 2005; Kozlova and Manning, 2009). $\delta^{13}CO_2$ was measured on the VPDB scale (Coplen, 2011; Wehr et al., 2013). See A5.7 for further details. $\delta^{13}CO_2$ was also measured continuously at ATTO together with surface flux measurements of $\delta^{13}CO_2$ (Moonen et al., 2023). Additionally, we collected vertical profiles of meteorological variables and CO_2, using radiosondes and an aircraft at different times of the day. Full details for these campaigns are given in A5.2-A5.3 and Table A5.1-A5.2.

The vertical profiles from flask and aircraft measurements enable us to estimate the entrainment flux (F_e), an atmospheric process that influences the measured mole fractions of carbon cycle tracers by mixing air with different composition from the FT or the residual layer into the ABL. The difference between the ABL and the FT or the residual layer of a species ϕ ($\Delta_{(ft-bl)} = \phi_{ft} - \phi_{bl}$), also referred to as the 'jump', allows to estimate F_e (Tennekes and Driedonks, 1981). Other atmospheric processes like the mass flux due to cloud ventilation (F_M, note that this does not include rain), subsidence, and horizontal advection of air also affect measured mole fractions and influence the diurnal cycle. We integrate these atmospheric processes in the total atmospheric flux (F_a) for a scalar ϕ (Ouwersloot et al., 2013):

$$\begin{aligned} F(\phi)_a = F(\phi)_e + F(\phi)_M = -w_e \cdot \Delta_{(ft-bl)\phi} + F(\phi)_M = \\ -\left(\frac{dh}{dt} - w_s\right) \cdot \Delta_{(ft-bl)\phi} + M \cdot (\phi_{cc} - \overline{\phi}(h^+)). \end{aligned} \tag{5.1}$$

where w_e is the entrainment velocity [m s^{-1}], dh/dt is the ABL growth [m s^{-1}], w_s is the subsidence velocity [m s^{-1}], M is the mass flow [m s^{-1}], ϕ_{cc} is the cloud core mole fraction, and $\overline{\phi}(h^+)$ is the mole fraction just above the sub-cloud layer. When boundary-layer clouds are present we assume that the mole fraction in the free troposphere is equal to the mole fraction in the sub-cloud layer (i.e. $\phi_{ft} = \overline{\phi}(h^+)$). Note that we ignore advection in this equation. Assuming $F_M = 0$, F_e provides a first estimate of F_a based on observations (using a direct and inferred approach, see A5.5). The complete derivation of Equation 5.1 is given in A5.8.

Similar to DTR, DR of carbon cycle tracers is modeled using the governing equations of the atmospheric boundary layer using the CLASS model (Stratum et al., 2014; Vilà-Guerau de Arellano et al., 2015). CLASS assumes that under convective conditions, meteorological and carbon cycle tracers are well-mixed within the boundary layer, maintaining a constant mole fraction with height (Lilly, 1968a; Tennekes, 1973). Studies have shown that the mixed-layer equations hold for CO_2, O_2 and $\delta^{13}CO_2$ (Vilà-Guerau de Arellano et al., 2019; Faassen et al., 2024b). CLASS couples atmospheric conditions with a representation of the turbulent surface fluxes of energy, water and CO_2 and has been extensively validated for different forests, including the temperate Harvard forest in the US (Vilà-Guerau de Arellano et al., 2019), and the boreal forest at Hyytiälä in Finland (Ouwersloot et al., 2012a; Faassen et al., 2024b). To study DR we performed two case studies using CLASS: one for the Loobos campaign (18 May 2022) including subsidence and advection of cold air, and one for the ATTO campaign (15 August 2022) with boundary-layer clouds with shallow cumuli during the dry season. A5.4 provides details on the initializations and location-specific parameters and model validation (ECMWF, 2014; Vilà-Guerau de Arellano et al., 2015).

The diurnal range of carbon cycle tracers is influenced by surface processes (F_s), atmospheric contributions (F_a, Eq. 5.1), and boundary layer growth. We quantify these contributions using:

$$DR = \overbrace{\int_{t_{min}}^{t_{max}} \frac{F_s(t)}{h} dt}^{\text{Surface contribution}} - \overbrace{\int_{t_{min}}^{t_{max}} \frac{F_a(t)}{h} dt}^{\text{Atmospheric contribution}} \tag{5.2}$$

where t_{min} and t_{max} are the times of the day with the minimum and maximum tracer mole fraction values, and h is the boundary layer height. A5.8 includes the derivation of this equation. We define β to quantify the relative importance of atmospheric processes versus surface processes:

$$\beta = -\frac{F_a}{F_s} \tag{5.3}$$

Previous studies defined β as the ratio of F_e and F_s (Vilà-Guerau de Arellano et al., 2004), and we extend it to include F_M. To understand the diurnal variability, β is calculated for three periods during daytime based on ABL growth regimes (Martin et al., 1988) (see A5.4 and Fig. A5.5). In P1, the ABL is shallow; in P2, the ABL grows rapidly due to high surface buoyancy; in P3, the ABL reaches its highest altitude caused by the decrease of the surface buoyancy flux. In P3, other processes like cloud ventilation and subsidence could become more important.

5.3 Diurnal Ranges for CO$_2$, O$_2$ and δ^{13}CO$_2$

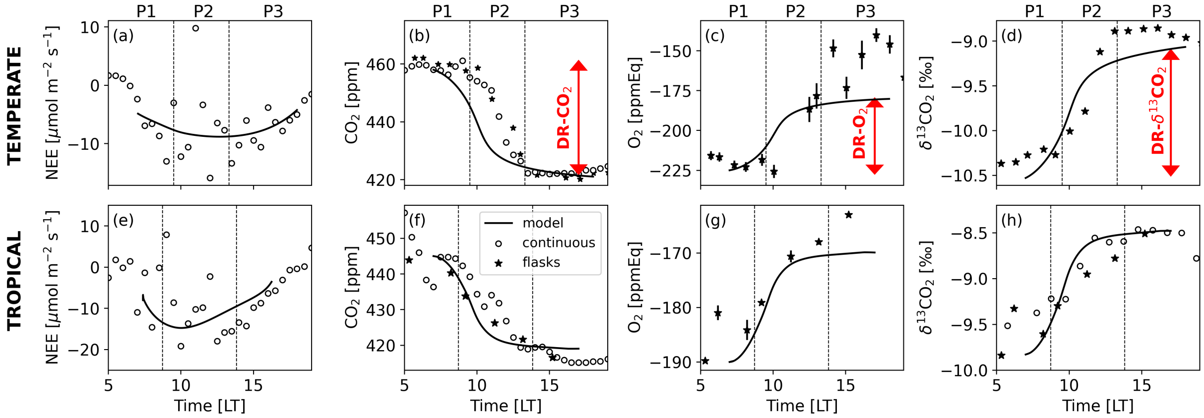

Figure 5.1: Observed diurnal cycles of Net Ecosystem Exchange (NEE), CO$_2$, O$_2$ and δ^{13}CO$_2$ for the temperate forest (a-d) and for the tropical forest (e-h) in comparison to CLASS model simulations. The vertical lines indicate the three periods as defined in Section 5.2. Measurements were made at 38 m for the temperate forest, and for the tropical forest at: 50 m (NEE and continuous CO$_2$), 60 m (flask samples), and 42 m (continuous δ^{13}CO$_2$). Time is reported as Local Time (LT) (winter time for the temperate forest).

Both flask and continuous observations of CO$_2$, O$_2$ and δ^{13}CO$_2$ showed similar diurnal variability for the temperate and the tropical site (Figure 5.1). For all three tracers, the rate of change was highest during P2 and decreased significantly in P3. This contrasts the diurnal pattern of NEE (Panels 5.1a and 5.1e), which showed the highest values during both P2 and P3, showing that DR of the carbon cycle tracers is not only driven by surface exchange, but also by atmospheric processes. We quantified this influence using vertical CO$_2$ flux turbulent measurements to derive β_{co2} (Eq. 5.3) representing the ratio of atmospheric to surface influence. Figures 5.2a and 5.2e show the change of the CO$_2$ flux with time and height, where the values at the BLH represent the entrainment flux, and the values above the canopy represent the surface fluxes. The entrainment flux obtained from flux measurements (directly observed for the temperate case and extrapolated from the surface for the tropical case) show a good agreement with the inferred method based on the 'jumps' from CO$_2$ flask measurements. We find a decrease in the entrainment flux and increase in surface flux, resulting in a decreasing β_{co2} throughout the day.

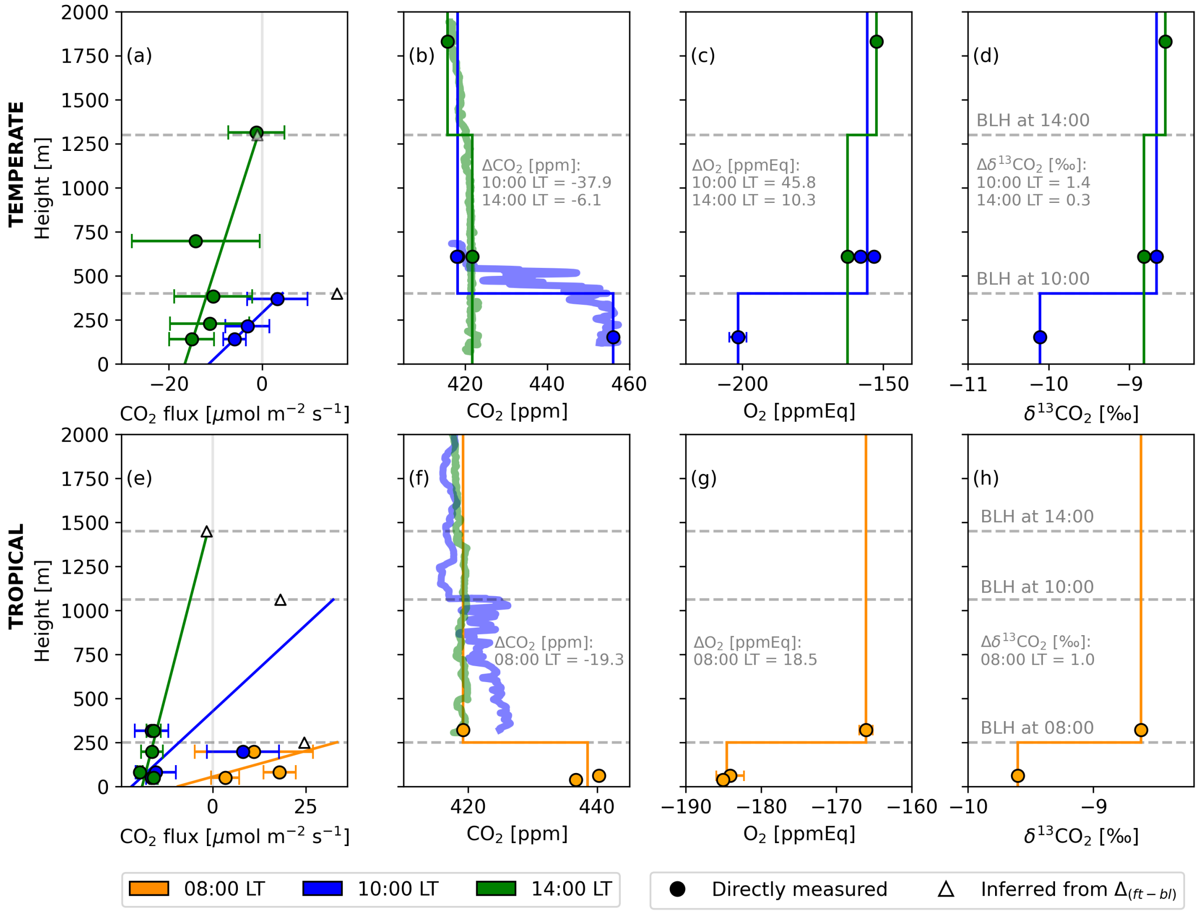

Figure 5.2: Observed vertical profiles of the CO_2 flux (a, e), CO_2 (b, f), O_2 (c, g) and $\delta^{13}CO_2$ (d, h) for the temperate and tropical forest cases at 8:00 (orange), 10:00 (blue) and 14:00 (green) LT. EC CO_2 flux measurements were made from aircraft (a) or from a tall tower (e). Continuous CO_2 measurements from aircraft are shown as bold transparent lines (b and f). Flask measurements are shown as circles, with their differences between the flask measurements in the free troposphere and the boundary layer (Δ) (b-d, f-h). The dashed grey horizontal lines show the boundary layer height (BLH) at the measurement times derived from radiosondes. Triangles represent the inferred entrainment fluxes using Δ (see A5.5).

In absence of direct observations of O_2 and $\delta^{13}CO_2$ fluxes, we used jumps ($\Delta_{(ft-bl)}$) to infer their entrainment fluxes. The satisfactory agreement between our continuous and flask observations of CO_2 (Figures 5.2b and 5.2f) show that our flask sampling strategy allows for an accurate representation of $\Delta_{(ft-bl)}$. At both sites, we found a decreasing $\Delta_{(ft-bl)}$ throughout the day, indicating a decreasing entrainment flux. The initial $\Delta_{(ft-bl)}$ of CO_2, O_2 and $\delta^{13}CO_2$ in the tropical forest were nearly twice as small as for the temperate forest, suggesting weaker entrainment in the tropical case compared to the temperate case. The observed $\Delta_{(ft-bl)}$ provides a unique opportunity to represent free troposphere conditions in the CLASS model, enabling accurate reproduction of surface fluxes and diurnal ranges (DR) for all carbon cycle tracers across both ecosystems (Figure 5.1).

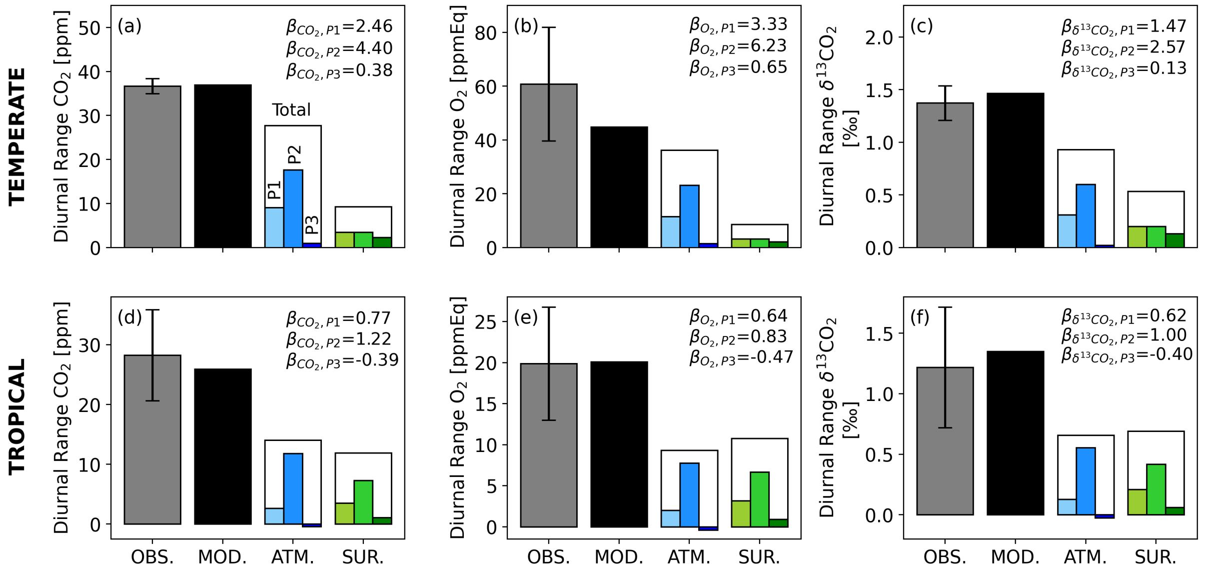

Figure 5.3: The diurnal ranges of observed (OBS.) and modeled (MOD.) CO_2, O_2 and $\delta^{13}CO_2$, and their partitioning into the contribution from atmospheric processes (ATM.) and surface exchange (SUR.) for the temperate (a-c) and tropical (d-f) forest cases. The contribution of the atmospheric and surface processes to the diurnal range is based on Eq. 5.2. The ratios between the atmospheric and surface processes (β) are given per period (see Figure 5.1).

Based on these CLASS model cases, we found that atmospheric processes significantly contributed to the diurnal range of carbon cycle tracers at both sites, with β values exceeding 1 (Figure 5.3). The β values followed a similar diurnal pattern for each tracer, with the strongest atmospheric influence in P1 and P2, where β_{P1} and β_{P2} ranged from 1.47 to 6.23 for the temperate forest and from 0.62 to 1.22 for the tropical forest. In P3, the β values decreased below 0.65 for both locations, indicating that the surface processes had a larger impact on the rate of change of the tracers than the atmospheric processes. In contrast to the β values for the carbon cycle tracers, β values for temperature and specific humidity were overall much lower (Figure A5.6).

Variations in jumps caused differences in the contributions of atmospheric processes between the tropical and temperate forest site and between the individual carbon cycle tracers. As shown in Eq. 5.1, the atmospheric flux depends on several factors. To compare the two sites, we focused on the differences of the components that form the entrainment flux F_e (see Eq. A5.6). While the entrainment velocities (w_e) were similar between the two locations (Figure A5.5), the jumps differed significantly (Figure 5.2). This resulted in a less dominant entrainment flux in the tropical forest, shown by lower β and smaller DR values compared to the temperate forest (Figure 5.1).

The dominance of atmospheric processes also varied between carbon cycle tracers. For the temperate forest, β values differed widely per period, with the highest values found for O_2 (P1: 3.33, P2: 6.23, P3: 0.65) and the lowest for $\delta^{13}CO_2$ (P1: 1.47, P2: 2.57, P3: 0.13).

The $\delta^{13}CO_2$ jump was relatively small, while the O_2 jump was relatively large compared to their total abundance (Figure 5.1), leading to different entrainment fluxes. In addition to entrainment, subsidence and cloud ventilation also impacted the atmospheric flux (Eq. 5.1). The magnitude of their influence differs between the two locations.

Depending on the case and time of the day, different atmospheric processes contributed to F_a shown in Figure 5.3. Boundary layer growth had the largest influence on the atmospheric flux and DR for both cases (Figure A5.4). At the temperate forest site, the subsidence velocity was significant, due to the influence of a high-pressure system during the campaign. The subsidence velocity limited boundary layer growth but increased entrainment velocity (Eq. A5.9). The influence of subsidence on DR was of similar magnitude as the surface flux. For the tropical forest case, cloud ventilation was significant because boundary layer clouds were formed in the morning and persisted into the late afternoon. Cloud ventilation transports air from the well-mixed boundary layer, which limited the boundary layer growth but added an extra ventilation flux for the carbon cycle tracers (Eq. A5.3 and A5.9) (Stratum et al., 2014; Vilà-Guerau de Arellano et al., 2020). Cloud ventilation was especially important during P2 and became as important as boundary layer dynamics during this period.

5.4 Impact of large-scale forcings on the diurnal range

The diurnal range is a result of a combination of surface, boundary-layer, synoptic and cloud processes (Figure 5.4a). These processes should be calculated simultaneously to understand the coupling between boundary layer and synoptic processes and their combined effect on DR and β. We analyzed the influence of high-pressure systems on DR as a representative example of typical synoptic events (see A5.6). High-pressure systems are characterized by high values for 1) the divergence of the mean wind (DivU), resulting in a high subsidence velocity (w_s, Eq. A5.10) and 2) the potential temperature lapse rate (γ_θ), which quantifies the FT stability (Pino et al., 2012).

γ_θ and w_s independently affect DR and β throughout the day (Figure 5.4 for CO_2 and Figure A5.8 for O_2 and $\delta^{13}CO_2$). Larger values of γ_θ (orange colors) lead to reduced boundary layer growth (Figure 5.4b) and entrainment velocity (w_e, Figure 5.4d) and as a result decreased both DR (Figure 5.4e) and β (Figure 5.4g). In turn, higher values of w_s (black colors) also limited boundary layer growth but increased w_e (Eq. 5.1). The increased w_e caused a high DR and therefore a low jump ($\Delta_{(ft-bl)}$, Figure 5.4f), resulting in a decreased β. With high values for both γ_θ and w_s (blue colors), DR increased because of an extremely shallow boundary layer height (Figure 5.4b) and β decreased because of a low w_e (Figure 5.4d) and a low $\Delta_{(ft-bl)}$ (Figure 5.4f). Cloud ventilation, which occurred in the tropical forest case, would also increase DR and decrease β, like subsidence. Our analysis shows that atmospheric processes cannot be ignored when analyzing DR, even when the surface flux is dominant, and therefore cloud ventilation, subsidence, free tropospheric lapse rate, and the jump should be considered.

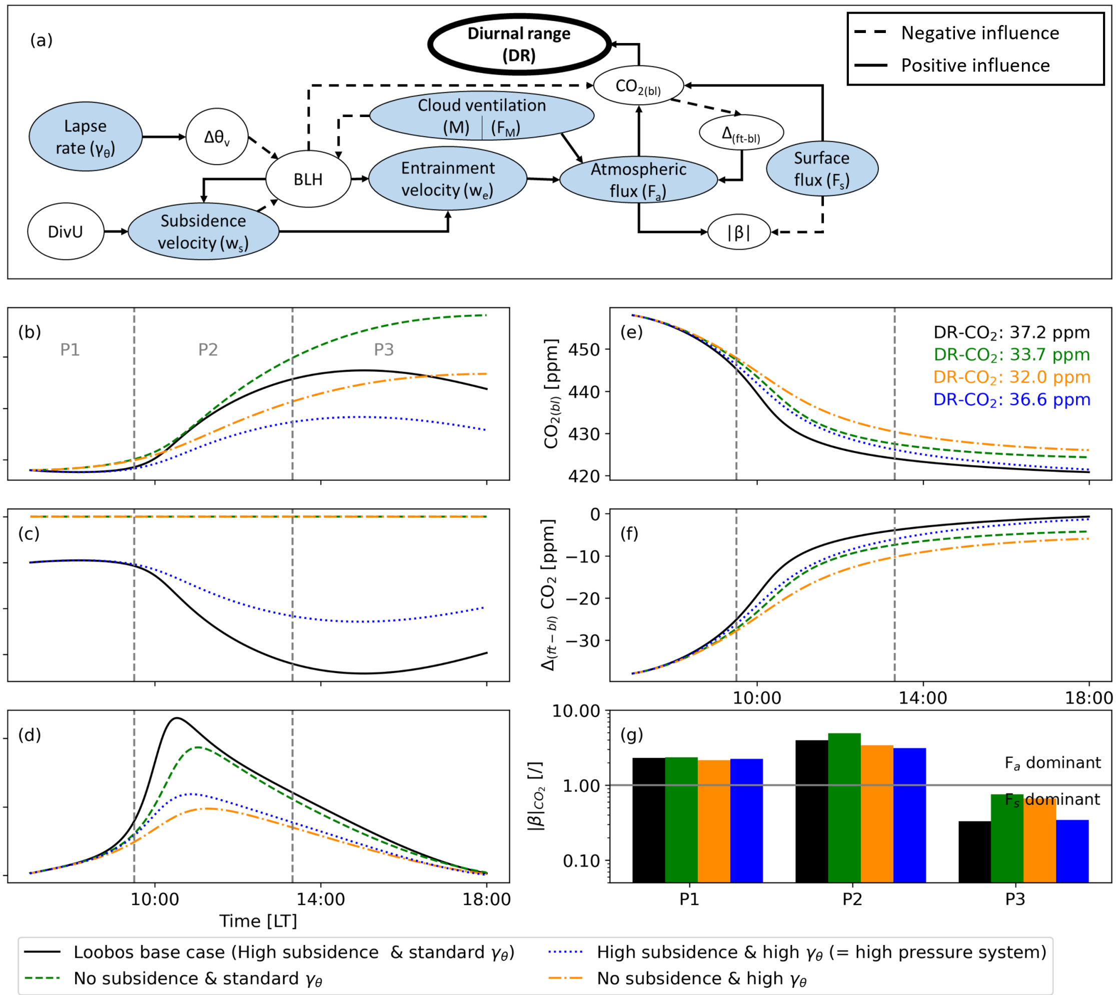

Figure 5.4: Schematic overview of the cause-effect relationships influencing the diurnal range (DR) for CO_2 (a), and results of our sensitivity analysis for the temperate forest case (b-g). Four model runs were included with either high or no subsidence (through DivU, the horizontal wind divergence) and high or standard lapse rate (γ_θ, free troposphere stability). Results are shown for the boundary layer height (BLH) (b), the subsidence velocity (w_s) (c), the entrainment velocity (w_e) (d), the boundary layer mole fraction ($CO_2(bl)$) (e), the jump ($\Delta_{(bl-ft)}$) (f), and β (the ratio between the atmospheric flux (F_a) and the surface flux (F_s)) (g).

5.5 Discussion

We propose using DR of carbon cycle tracers, similar to the widely-used DTR (e.g. Qu et al., 2014; Adekanmbi and Sizmur, 2022; Huang et al., 2023), as a metric to evaluate atmospheric models and analyze observations, as it integrates surface and atmospheric processes. DR of carbon cycle tracers is more complex to interpret compared to DTR due to individual processes associated to each tracer, but it still is a valuable constraint for observations and models because of the simplicity of its calculation. Network comparison of DR is also straightforward since it is less affected by biases in measurements. When models fail to capture DR, we recommend to use flux observations to identify inaccuracies of the model representations of surface and entrainment fluxes . This should be done for carbon cycle tracer individually, because the atmospheric influence is different for each of them. Comparing β values of the tracers with meteorological variables reveals the significantly larger role of atmospheric processes on DR of carbon cycle tracers, which was also found in previous studies (Davis et al., 1997; Vilà-Guerau de Arellano et al., 2004; Gibert et al., 2007; Casso-Torralba et al., 2008b). Thus, adding DR of individual carbon cycle tracers as an additional constraint to validate atmospheric models is highly beneficial, especially as models advance to finer spatial and temporal resolutions like those in the 6th Coupled Model Intercomparison Project (CMIP6) (Park et al., 2021; Martín-Gómez et al., 2023). To establish DR as a reliable metric, high-quality surface and upper-atmospheric observations are essential.

The observational data that we present here is unique because of the combination of carbon cycle tracer measurements (CO_2, O_2 and $\delta^{13}CO_2$), meteorological variables, and surface fluxes. Especially the combination of vertical atmospheric measurements from (tall) towers, radiosondes and aircraft for these tracers was unique in our campaign. Additional observations would have further strengthened our campaigns, including flux measurements for all the tracers (O_2 in both locations and $\delta^{13}CO_2$ in the temperate forest), further details on the oxidative ratio for O_2 and the process-specific fractionation coefficients for $\delta^{13}CO_2$, which would have better constrained the surface processes (Ishidoya et al., 2015; Wehr et al., 2016). More frequent vertical profiling would have allowed an even more detailed study of sub-daily variations during the morning and afternoon transitions on other days than the selected cases (Arrillaga et al., 2018; Dupont et al., 2024).

We call for systematic, long-term monitoring and trend analysis of DR and free tropospheric values of carbon cycle tracers to improve the use of atmospheric processes in carbon cycle partitioning methods. We showed that changes in DR result from differences in free troposphere values and large scale forcings, including subsidence and cloud ventilation, leading to differences in β values between our tropical and temperate forest cases. The surface dynamics and vertical profiles of the carbon cycle tracers vary daily (Ouwersloot et al., 2013) and differences between the ecosystems may fluctuate from day to day, which makes it difficult to generalize our ecosystem specific findings. Further research should explore the drivers of DR between ecosystems and over time, by investigating DR variations from weekly to seasonal and yearly trends (Graven et al., 2013). We advocate for more experimental ‘super sites’ with measurements at various heights, including upper atmospheric measurements from tall towers or aircraft. These super sites significantly enhance future research on vegetation dynamics in a changing climate (Yi et al., 2004; Bonan et al., 2021; Bonan et al., 2024).

5.6 Conclusion

For a tropical (dry season) and a temperate forest (summer), we show that atmospheric processes like entrainment, subsidence, and cloud ventilation are essential to understand the diurnal range of carbon cycle tracers (DR). We combined our unique observations with a coupled forest-atmosphere model to reproduce and interpret the CO_2, O_2 and $\delta^{13}CO_2$ diurnal variability. Using aircraft, radiosonde, and above-canopy tower measurements, we quantify the ratio of atmosphere processes to surface processes (β) for both ecosystems. Atmospheric processes significantly influence the diurnal patterns of carbon cycle tracers and the dominance of the atmospheric processes varies throughout the day, with maximum β values above 1 for CO_2 (4.4), O_2 (6.23), and $\delta^{13}CO_2$ (2.57) during the morning transition periods. The high β values show the need to represent both atmospheric processes and surface processes when analyzing carbon cycle tracers. In particular, subsidence and cloud ventilation are key to interpret DR changes. Finally, we propose DR, which is easy to measure, as a metric to 1) validate how well (large-scale) atmospheric models represent the combination of surface and atmospheric processes and to 2) understand season to annual changes of the carbon tracer diurnal variability on site level.

Data availability. The observational data used in Figure 1 and 2 can be found in their respective data portals: 'https://maq-observations.nl' Molen et al., 2024 and 'https://www.attodata.org'. The flask measurements of CO_2, O_2 and $\delta^{13}CO_2$, vertical aircraft CO_2 flux and mole fraction measurements for the Loobos campaign can be found in Faassen et al., 2024a. The CO_2, O_2 and $\delta^{13}CO_2$ flask measurements and the vertical aircraft CO_2 mole fraction measurements for the ATTO campaign can be found at in Faassen et al., 2024a. The model code for the CLASS model is available on 'https://classmodel.github.io/'.

5.7 Appendix

A5.1 Introduction

This supplementary information includes further information on the measurement campaigns (A5.2 and A5.3), the initial and boundary conditions of the model setup and validation (A5.4), the vertical CO_2 profiles and the observation based entrainment flux (A5.5), the sensitivity analyses (A5.6), the definition of O_2 and $\delta^{13}CO_2$ (A5.7), and the mixed layer equations (A5.8). The Figures A5.1 to A5.7 and the Tables A5.1 to A5.4 support the completes text and the main text. We therefore ensure the reproducibility of our observational and modeling findings.

A5.2 Loobos: site and field campaign

Loobos is an ecosystem measurement site located in the Veluwe natural area in the center of the Netherlands (52.1664° N, 5.7436° E, 33 m AMSL). The site is dominated by Scotts pine (*Pinus sylvestris*) with an understorey of Black Cherry (*Prunus serotina*) on podzol on fine sandy soil. The ground water level is 3-6 m below ground level. The trees are 20-22 m tall. The measurements in our campaign were done in a 36 m tall tower. In May 2023, the site was given the official ICOS Class 2 Ecosystem Site label (https://meta.icos-cp.eu/resources/stations/ES_NL-Loo).

During our campaign in May 2022 (17th and 18th of May), the eddy covariance measurements were already compliant with the ICOS ETC guidelines, using a Gill HS-50 sonic anemometer and a LI-7200 closed path CO_2 and H_2O analyzer installed at 38.2 m, which is 2.2 m above the highest platform of the tower. The raw data were collected at 20 Hz by a Licor Smartflux-2 system. Table A5.1 shows the extra measurements that were done during the field campaign.

During the campaign, the weather was relatively calm, influenced by high pressure conditions located above the Netherlands on that day. The conditions were partly cloudy, with varying degrees of shallow cumulus cover. In the night and morning of 18 May 2022 a weak warm and cold front passed over the site, after which the weather cleared up. On the 18th, the winds were from the south west, with an average value of 2.8 m s^{-1} above the canopy and temperatures ranged from 14 to 28 °C (KNMI, Deelen, https://www.knmi.nl/nederland-nu/klimatologie-metingen-en-waarnemingen).

A5.3 CloudRoots-Amazon22: site and field campaign

The campaign in the Amazon (CloudRoots-Amazon22) was conducted from August 8 to 21, 2022, at and around the Amazon Tall Tower Observatory (ATTO; 2.1819° S, 59.0217° W). This location is situated approximately 150 km northeast of the city of Manaus and approximately 1000 km inland from the Atlantic Ocean. As described by Andreae et al.

(2015), the site is located at the Uatumã Sustainable Development Reserve (USDR) in the central Amazon. This region is characterized by different ecosystems: non-flooded upland forests ('terra firme') plateaus and on ancient river terraces, 'campinas' (savanna on white-sand soils) and 'campinaranas' (white-sand forest) (Andreae et al., 2015). For the 'terra firme' rainforest, the canopy height ranges between 35 to 45 above ground level. In our study we take 40 m as the average reference canopy height.

Our observational strategy during the campaign aimed to extend and complete the comprehensive measurements taken routinely at ATTO. In short, there are three tall towers at ATTO: the ATTO tower (323 m), the Triangle tower (81 m) and the INSTANT tower (80 m) at which profiles of key atmospheric state variables (wind, temperature, and specific humidity) and their turbulent fluxes are continuously measured (Andreae et al., 2015). Shortwave and longwave radiation was measured at 75 m and light interception profiles of photosynthetic active radiation (PAR) are gathered across and above the canopy (INSTANT tower). Turbulent fluxes were measured using eddy covariance (EC) and integrated to 30-minute averages. To quantify changes in the state variables between the canopy, the sub-cloud and cloud layers, and the free troposphere, we launched balloon soundings with high temporal frequency (every three hours) over the course of the campaign. On August 18, we extended these measurements by additional aircraft measurements of vertical profiles (up to 5000 m) and horizontal spatial distribution of atmospheric composition (H_2O, CO_2, CO, CH_4) observations during the morning (09-11 LT) and afternoon transition (13-15 LT), respectively. The aircraft flew in a horizontal grid around the ATTO facility at constant height. Both in the morning and afternoon flights, we selected three representative heights in the sub-cloud layer, the cloud layer, and the free troposphere and integrated the measurements at constant heights for long, horizontal paths ($\approx$ 20 km). Table A5.2 shows more details on the extra measurements that were done during the campaign days.

During the ATTO campaign, the weather was characterized by clear skies during the morning that transitioned to cloudy skies during the afternoon, which on 6 days were categorized as shallow-cumulus. Complete information of the continuous measurements, the field campaign and its main goals can be found in Vilà-Guerau de Arellano et al. (2024).

A5.4 Model setup and validation

In the CLASS model, the ABL dynamics and carbon cycle tracers are calculated using three vertically integrated equations (i.e. a 0-dimensional slab only depending on time). We assume horizontally homogeneous conditions. (Lilly, 1968a). The first equation describes the time evolution of the slab variable and second equation describes the time evolution for the interface jump $\Delta_{(ft-bl)}$. More specifically, the ABL dynamics are represented by the mixed-layer equations of potential temperature (heat), specific humidity (moisture) and two wind components (momentum). The final equation calculates the boundary layer growth, from morning till late afternoon, using the limitation that the buoyancy flux at the canopy top should remain positive to ensure well-mixed conditions.

The initial settings and parameters used for our numerical experiments for the Loobos and Amazon cases in CLASS are shown in Tables A5.3 and A5.4. Table A5.3 describes the initial vertical profiles of temperature, specific humidity, wind, carbon cycle tracers (CO_2,O_2 and $\delta^{13}CO_2$) as well as the canopy height and boundary conditions of the free troposphere. The initial vertical profiles for the CLASS model are based on a combination of radiosonde, flasks and continuous tower measurements. Advection of colder air and subsidence at Loobos was estimated based on the results of a downscaled Large Eddy Simulation using the method of (Stratum et al., 2014) (Figure A5.1). Advection of colder air and divergence were taken constant during the CLASS run with -0.5 K h^{-1} and 2.5 $\cdot$ 10^{-5} s^{-1} respectively. The divergence is related to the subsidence, see Eq. A5.10. For the Amazon case, there was no subsidence, but instead the occurrence of clouds was added and the initialization is based on a previous study by Vilà-Guerau de Arellano et al. (2020). Table A5.4 describes the location, initial time and the vegetation and soil parameters. Vegetation and soil parameters are based on (1) prescribed values for the corresponding type of forest (ECMWF, 2014; Vilà-Guerau de Arellano et al., 2015) (2) previous observations at the sites or (3) leaf gas exchange observations acquired during the campaigns.

An elaborate comparison between the model and the observations for both locations is shown in Figure A5.2. The diurnal cycle of the surface fluxes, potential temperature and specific humidity compare well to observations for both locations. The surface flux of $\delta^{13}CO_2$ was measured during the Amazon campaign (Figure A5.2j) (Moonen et al., 2023). The comparison between the modelled and observed $\delta^{13}CO_2$ surface flux shows that the CLASS model can reproduce the processes behind the DR of $\delta^{13}CO_2$ well. Unfortunately, no O_2 gradient or surface flux measurements where done, and therefore we could not validate the O_2 fluxes from CLASS for these cases. However, Faassen et al. (2024b) already showed that CLASS is able to reproduce satisfactory the processes behind the DR of O_2 for a campaign in a forest in Finland.

Three periods (P1, P2, P3) were determined based on the growth of the boundary layer height to represent typical periods during daytime that have different strengths of entrainment (Figure A5.5). We define the periods wether the boundary layer growth is more or less than 100 m h^{-1}. P1 corresponds to the beginning of the day when the ABL grows slowly and the vegetation slowly starts to take up CO_2. In our classification, we define this period from the beginning of the day until the moment that the ABL starts growing at a rate larger than 100 m h^{-1}. P2 corresponds to the highest growth of the ABL, this part of the day is associated with high entrainment of air from the free troposphere into the ABL and high surface fluxes. P2 is defined as the period where the growth of the boundary layer exceeds 100 m h^{-1}. The last period, P3, occurs when the ABL growth reduces below 100 mh^{-1} again, or the ABL even starts to shrink. P3 reflects the period when both the entrainment and surface fluxes decrease, together with a high ABL. The resulting periods for the temperate forest case are:

- P1: sunrise - 09:30 LT
- P2: 09:30 LT - 13:18 LT
- P3: 13:18 - sunset

and for the tropical forest case:

- P1: sunrise - 08:43 LT
- P2: 08:43 LT - 13:50 LT
- P3: 13:50 LT - sunset.

A5.5 Vertical CO_2 flux profiles and entrainment calculations

Directly measured and inferred methods were used to calculate the entrainment flux from different sets of observational data. For the temperate forest case, we could directly estimate the entrainment for CO_2 flux using the vertical CO_2 fluxes measured from the aircraft (Figure 5.2a). During the temperate forest campaign, the aircraft measured CO_2 (and H_2O) fluxes with a Li-Cor 7500 open path, high frequency trace gas analyser in combination with a Best Aircraft Turbulence (BAT) probe to measure the high frequency 3D wind (for further details see Vellinga et al. (2013)). Covariances between the vertical velocity and temperature, moisture or CO_2 were integrated over 2 km horizontal windows or roughly one-minute intervals to derive the turbulent fluxes for heat, moisture and CO_2. First, vertical profiles were flown to identify the ABL height. Subsequently, two sets of horizontal laps were flown at constant heights, one in the morning, and one in the afternoon. Morning laps were flown from 7:00 to 7:41 UTC, at heights of 200, 500 and 1000 ft. Afternoon laps were flown from 12:19 to 12:56 UTC at heights of 200, 500, 1000, 2000 and 4000 ft. All laps were about 10 km long and made by flying back and forth between [52.20° N, 5.850° E] and [52.11° N, 5.953° E], producing 11 individual high-frequency meteorological and CO_2 flux measurements. We used these to calculate the horizontal turbulent fluxes at each level, shown in Figure 5.2a. Making use of the assumption that under well-mixed conditions the increase/decrease of turbulent flux of conserved variables is constant with height, the relationship between the average CO_2 flux and height was determined using a linear regression and extrapolated to the estimated BLH to determine the entrainment flux (Vilà-Guerau de Arellano et al., 2004). Only flux measurements made below the BLH were included in this regression. Continuous CO_2 concentration profiles were also measured onboard the aircraft (Figure 5.2b). These measurements were obtained with a Li-Cor 7815 closed path trace gas analyser for CO_2 and H_2O.

For the tropical forest case, we did not have flux measurements from aircraft. Therefore, we used the Eddy covarience (EC) measurements of the ATTO tower to determine the vertical profile of CO_2 fluxes for the Amazon (Figure 5.2e). We calculated the average of EC-measurements at heights of 50 m, 81 m, 196 m and 316 m during the 6 days that were characterized by shallow convection (Vilà-Guerau de Arellano et al., 2024). We used the measurements between 07:30-08:30, 09:30-10:30 and 13:30-14:30 to determine the average flux for the time periods that are presented in Figure 5.2e. Again a linear regression was used to determine the relationship between the average CO_2 flux and height, and determine the entrainment flux at the BLH.

Without EC measurements available we needed to inferre the entrainment flux. We inferred the entrainment flux using flask measurements of the carbon cycle tracers in and above the boundary layer, in combination with the boundary layer height (the triangles in Figure 5.2a and 5.2e). The calculation is based on the representation of the entrainment flux as a function of an entrainment velocity ($\mathrm{w_e}$) and the jump at the interface between the mixed-layer and the free troposphere (Eq. A5.6). We estimated the BLH growth using a linear interpolation of boundary layer height measurements of potential temperature or ceilometer measurements (Figure A5.5). The slope of the linear regression line was assumed to be the entrainment velocity during P1, P2 or P3 (Figure A5.5b and A5.5d). Figure A5.5 shows that this approach works well for a first estimate of the entrainment velocity because the modeled and observed $\mathrm{w_e}$ are relatively close.

The vertical continuous and flask measurements of CO_2, shown in Figure 5.2b and 5.2f were used to calculate the jump ($\Delta_{(ft-bl)}$). For the temperate forest case, the values from the free troposphere aircraft flask measurements were used together with the assumption that the lapse rate of the carbon cycle tracers is zero. For the Amazon case only the morning tower flask measurements could be used to get a value for the free troposphere, with the assumption that the highest height is located in the residual layer and the lower heights in the boundary layer. Both the CO_2 jump and the observed boundary layer growth are used in Eq. A5.6 to calculate the CO_2 entrainment flux for both the temperate and tropical forest case. Figure 5.2a shows how this inferred entrainment flux (the triangles) satisfactorily agrees with the directly measured method of aircraft measurements (where the linear regression ends at the BLH).

A5.6 DR under different free tropospheric conditions

For the sensitivity analysis of the temperate forest case in Sect. 5.4 of the main text, we changed the model input of the lapse rate of potential temperature (γ_θ) and the divergence term (DivU) (Figure A5.7) to understand the influence of a high pressure system. DivU represents the vertical motions of air and in CLASS it is linked to the subsidence velocity (air masses moving towards the surface) through Eq. A5.10. We initialised the divergence term at values between 0 $\mathrm{s^{-1}}$ and $3.15{\cdot}10^{-5}$ $\mathrm{s^{-1}}$ for the sensitivity analysis. We based this range on the study by Williams et al. (2011), the initial value of DivU in Table A5.3 and a typical boundary layer height of 1000 m. We based the range of γ_θ on the study by Pino et al. (2012) and initialised it at values between 10^{-4} K m^{-1} (less stable) and 10^{-3} K m^{-1} (strong thermodynamically stable). Figure A5.7 gives the complete overview of the resulting diurnal ranges and the β values of P1 and P3 for every combination of the changing values for γ_θ and DivU. The cross indicates the temperate forest case and the circles are the cases that are shown in Figure 5.4 of the main text. The O_2 and $\delta^{13}CO_2$ results can be found in Figure A5.8.

A5.7 Oxygen and ^{13}C stable isotope measurements

The flask measurements of O_2 are expressed in 'per meg' on the Scripps Institution of Oceanography (SIO) 2017 scale and normally given in $\delta O_2/N_2$, which is defined as:

$$\delta(O_2/N_2) = \left(\frac{(O_2/N_2)_{\text{sample}}}{(O_2/N_2)_{\text{reference}}} - 1\right) \cdot 10^6 \tag{A5.1}$$

To directly compare the O_2 and CO_2 measurements, we converted the $\delta O_2/N_2$ per meg values to ppm equivalents (ppmEq) by multiplying with 0.20946 (Machta and Hughes, 1970; Kozlova and Manning, 2009). In the main text, we refer to $\delta O_2/N_2$ as O_2.

The $\delta^{13}CO_2$ stable isotopes are on the VPDB scale and are expressed in per mil [‰], which is defined as:

$$\delta^{13}CO_2 = \left(\frac{(^{13}CO_2/^{12}CO_2)_{\text{sample}}}{(^{13}CO_2/^{12}CO_2)_{\text{reference}}} - 1\right) \cdot 10^3 \tag{A5.2}$$

Where $^{13}CO_2/^{12}CO_2$ is the ratio of the stable isotopes ^{13}C to ^{12}C.

A5.8 Mixed-layer equations

In the section, we show the different governing equations that the CLASS model uses or that we used in calculations in this study next to Eqs. 5.1, 5.2, 5.3 that are already mentioned in the main text. The following equation describes the budget of the tendency of a specific species (ϕ):

$$\frac{d\phi}{dt} = \frac{F(\phi)_s - F(\phi)_e - F(\phi)_M}{h} \tag{A5.3}$$

Where $F(\phi)_s$ is the surface flux, $F(\phi)_e$ is the entrainment flux and includes the effect of subsidence, $F(\phi)_M$ is the mass flux that we refer to as the cloud ventilation flux. By combining $F(\phi)_e$ and $F(\phi)_M$ into $F(\phi)_a$ and integrating over time between the minimum value of ϕ (occurred at t_{min}; $\phi_{min} = \phi(t_{min})$) and the maximum value of ϕ (occurred at t_{max}; $\phi_{max} = \phi(t_{max})$), we obtain:

$$\int_{t_{min}}^{t_{max}} \frac{d\phi}{dt} dt = \int_{t_{min}}^{t_{max}} \frac{F(\phi)_s}{h} dt - \int_{t_{min}}^{t_{max}} \frac{F(\phi)_a}{h} dt \tag{A5.4}$$

By integrating the change of ϕ over time we get the expression for the diurnal range (DR):

$$\int_{t_{min}}^{t_{max}} \frac{d\phi}{dt} dt = \phi(t_{max}) - \phi(t_{min}) = DR \tag{A5.5}$$

By combing Eq. A5.4 and A5.5, we obtain Eq. 5.1 of the main text. The entrainment flux can be written as:

$$F(\phi)_e = -w_e \cdot \Delta_{(ft-bl)}\phi \tag{A5.6}$$

Where w_e is the entrainment velocity and $\Delta_{(ft-bl)}$ is the jump. The jump is the difference between the free troposphere concentration just above the sub-cloud layer ($\overline{\phi}(h^+)$) and the mixed-layer concentration ($< \phi >$):

$$\Delta_{(ft-bl)}\phi = \overline{\phi}(h^+) - < \phi > \tag{A5.7}$$

The cloud ventilation flux can be determined with:

$$F(\phi)_M = M \cdot (\phi_{cc} - < \phi >) \tag{A5.8}$$

Where M is the mass flow at the cloud base in m s^{-1}, ϕ_{cc} is the mole fraction within the cloud core. The difference between ϕ_{cc} and $< \phi >$ is normally represented as a function of the deviation of ϕ. For more details see Stratum et al. (2014). Both M and w_e and the subsidence velocity (w_s) influence the growth of the boundary layer (h):

$$\frac{dh}{dt} = w_e + w_s - M \tag{A5.9}$$

Note that in absence of subsidence and mass flow, the entrainment velocity can be calculated with only the boundary layer growth (dh/dt). The subsidence velocity is not a constant value but depends on the boundary layer height:

$$w_s = -Div(U_h) \cdot h \tag{A5.10}$$

Where $Div(U_h)$ is the horizontal wind divergence in s^{-1} and (U_h) is the horizontal mean wind in m s^{-1} at the BLH.

By combining Eq. A5.3, A5.6, A5.7, A5.8 and A5.9, we obtain the final budget equation of ϕ that can be used to disentangle the different processes of the surface, subsidence, boundary layer dynamics and the cloud ventilation. The equation reads:

$$\frac{d\phi}{dt} = \overbrace{\frac{F(\phi)_s}{h}}^{\text{Surface}} - \overbrace{\frac{w_s \cdot \Delta_{(ft-bl)}\phi}{h}}^{\text{Subsidence}} + \overbrace{\frac{dh/dt \cdot \Delta_{(ft-bl)}\phi}{h}}^{\text{Boundary layer dynamics}} - \overbrace{\frac{M \cdot (\phi_{cc} - \overline{\phi}(h^+))}{h}}^{\textit{Cloud ventilation}} \tag{A5.11}$$

This is a general equation that is valid for any tracers. In our study CO_2, O_2 and $^{13}CO_2$. To determine the budget of $\delta^{13}CO_2$ some extra steps have to be calculated because it also depends on the budget of CO_2.

The CLASS model calculates the budget of $^{13}CO_2$ in ppb and the budget of $^{12}CO_2$ in ppm. Observations are normally presented by $\delta^{13}CO_2$ in permil, as a relative value between ^{13}C and ^{12}C. Eq. A5.2 is used to convert ppb values to permil by using a constant value for $(^{13}CO_2/^{12}CO_2)_{\mathrm{reference}}$ of 0.011057 (Coplen, 2011; Wehr et al., 2013). To calculate $\delta^{13}CO_2$ from Eq. A5.3 the following equation has to be solved:

$$\frac{d(\delta^{13}C)}{d(t)} = \frac{d}{dt}\left(\frac{^{13}C/^{12}C}{R_{ref}} - 1\right) = \frac{1}{R_{ref}}\frac{d}{dt}\left(\frac{^{13}C}{^{12}C}\right) = \frac{1}{R_{ref}}\frac{1}{(^{12}C)^2}\left(^{12}C\frac{d^{13}C}{dt} -^{13} C\frac{d^{12}C}{dt}\right) \tag{A5.12}$$

The budget equation for $\delta^{13}C$ can be determined by combining Eq. A5.12 and A5.11 applied to ^{13}C and ^{12}C. An example for the surface contribution is given:

$$\left[\frac{d(\delta^{13}C)}{d(t)}\right]_{surf} = \overbrace{\frac{1}{R_{ref}}\frac{1}{^{12}C}\left(\frac{F(^{13}C)_s}{h} - \frac{^{13}C}{^{12}C}\frac{F(^{12}C)_s}{h}\right)}^{\text{Surface}} \tag{A5.13}$$

The budget components of the $\delta^{13}C$ tendency for the subsidence, boundary layer dynamics and cloud ventilation can be obtained similarly by combining Eq. A5.12 and A5.11.

A5.9 Figures and Tables

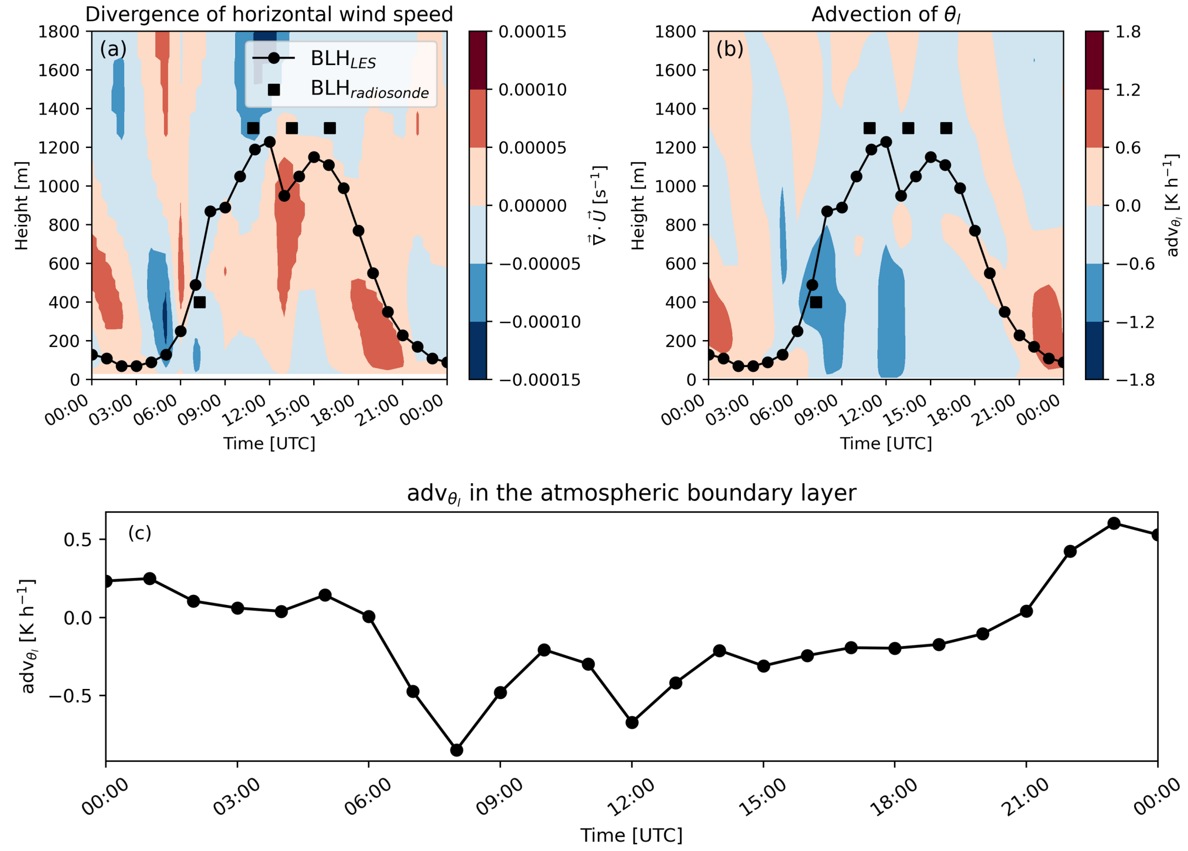

Figure A5.1: The divergence of wind speed (∇·U) (a) and advection of liquid potential temperature (adv$_{\theta_l}$) (b) per height and adv$_{\theta_l}$ averaged inside the boundary layer over time (c) as a results of the downscaling of ERA5 data with Large Eddy Simulation (LES) for the temperate forest case. The Boundary Layer Height (BLH) based on the downscaling and observed from the radiosondes is also shown in (a) and (b) with dots and squares. The advection and divergence of wind are used to initialise the temperate forest case.

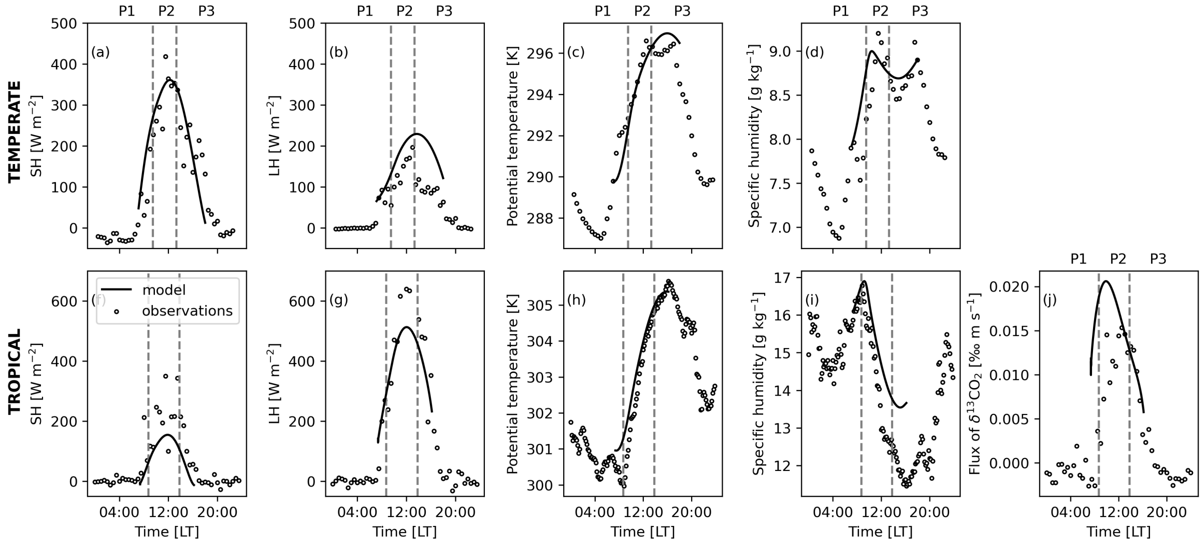

Figure A5.2: Comparison between the CLASS model output and the observations for the temperate forest case (panels a-d) and for the tropical forest case (panels f-j). The Sensible Heat flux (SH), Latent Heat flux (LH), potential temperature and specific humidity are compared for both cases. The surface flux of $\delta^{13}CO_2$ is specifically modelled and compared with observations that were taking for the tropical forest case (j). The periods P1, P2 and P3 are indicated with the vertical dotted lines. All observations of the temperate forest case are made at 38 m. The SH and LH flux of the Amazon case are measured at 81 m, potential temperature and specific humidity are measured at 316 m and the $\delta^{13}CO_2$ flux at 56 m.

Table A5.1: Additional variables measured during the temperate forest campaign in May 2022 next to the existing routine measurements.

Measurement technique	Variables measured	Frequency	Heights
Soundings	temperature, relative humidity, pressure	Hourly	0 to ∼14000 m
Vertical profiles airplane	temperature, CO_2, relative humidity, pressure	10:00 LT and 14:00 LT	0 to ∼6000 m
Flux measurements airplane	SH, $(\overline{w'CO_2'})$	10:00 LT and 14:00 LT	0 to ∼6000 m
Flask measurements airplane	CO_2, O_2, $\delta^{13}CO_2$	10:00 LT and 14:00 LT	below + above the boundary layer height
Flask measurements tower	CO_2, O_2, $\delta^{13}CO_2$	Hourly	38 m

Table A5.2: Variables measured during the CloudRoots-Amazon22 campaign in addition to the routine measurements collected at the measurement site ATTO that were used in this study. For a complete overview see Vilà-Guerau de Arellano et al., 2024.

Measurement technique	Variables measured	Frequency	Heights
Soundings	temperature, relative humidity, pressure	Hourly	0 to ∼14000 m
Vertical profiles airplane	temperature, CO_2, relative humidity, pressure	10:00 LT and 14:00 LT	0 to ∼6000 m
Flask measurements tower	CO_2, O_2, $\delta^{13}CO_2$	Hourly	60 m

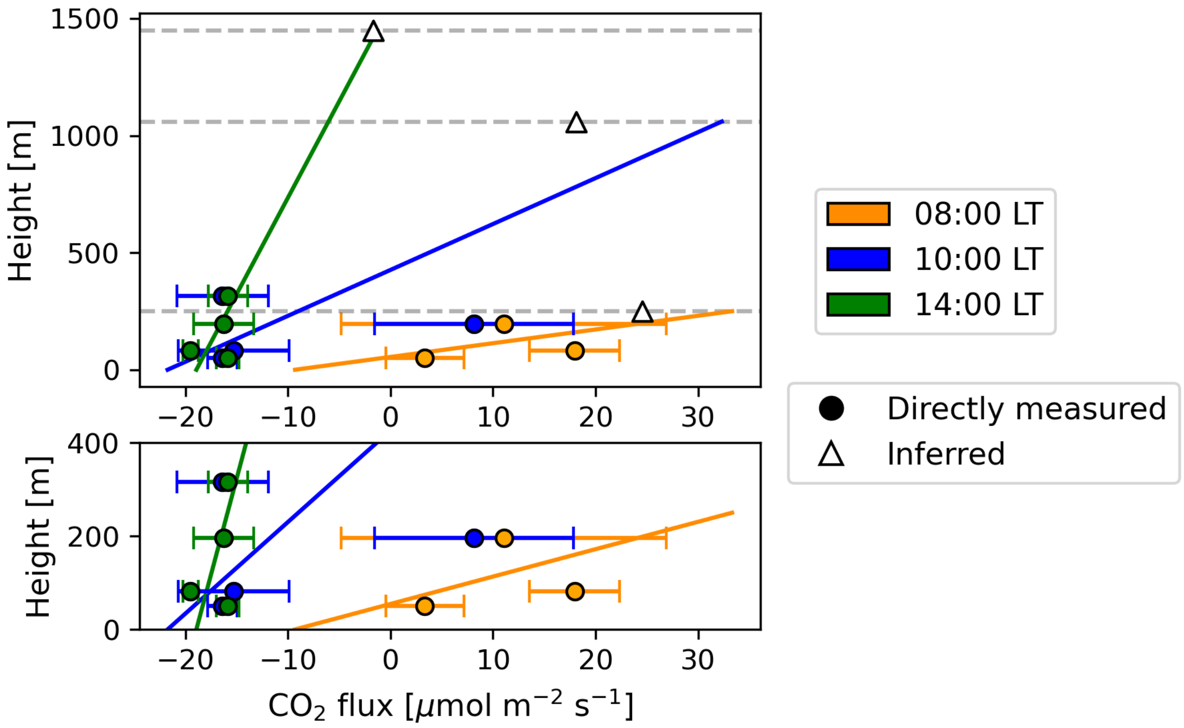

Figure A5.3: A zoomed-in version of Figure 5.2 from the main text, focusing on the first 400 m. With vertical flux observations of CO_2 for the tropical forest cases (circles) and Inferred fluxes calculated using observations and Eq. A5.6 are indicated with the triangles (see A5.5).

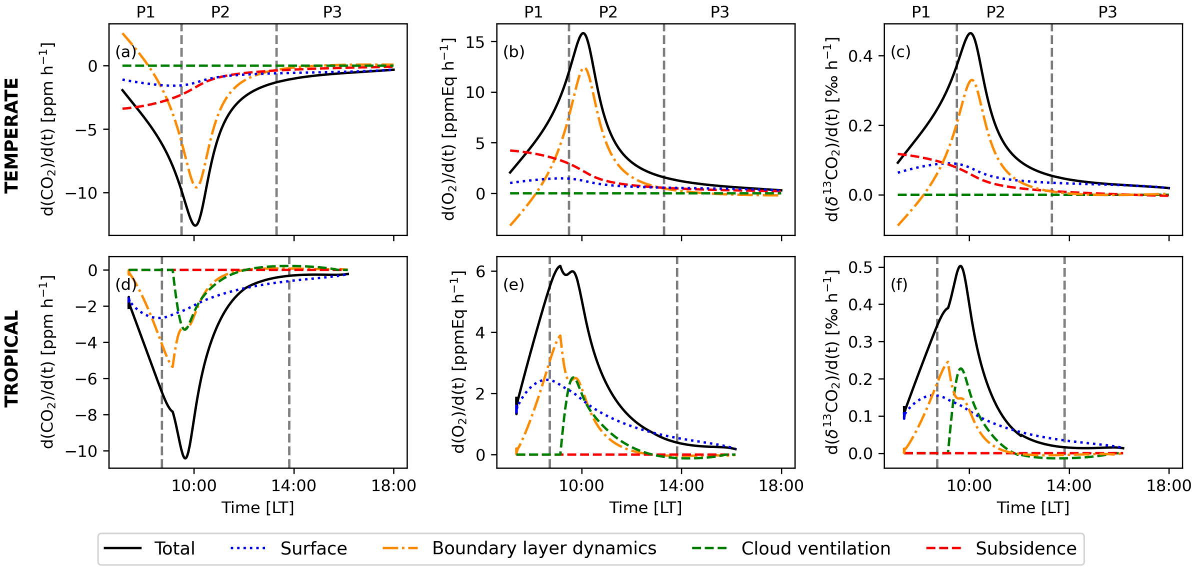

Figure A5.4: Contribution of the biophysical processes to the diurnal variability of CO_2, O_2 and $\delta^{13}CO_2$ calculated by the CLASS model for the temperate forest (panels a-c) and the tropical forest (panels d-f) cases. The different budget components are based on Eq. A5.11. A more detailed example for $\delta^{13}CO_2$ is given by Eq. A5.13.

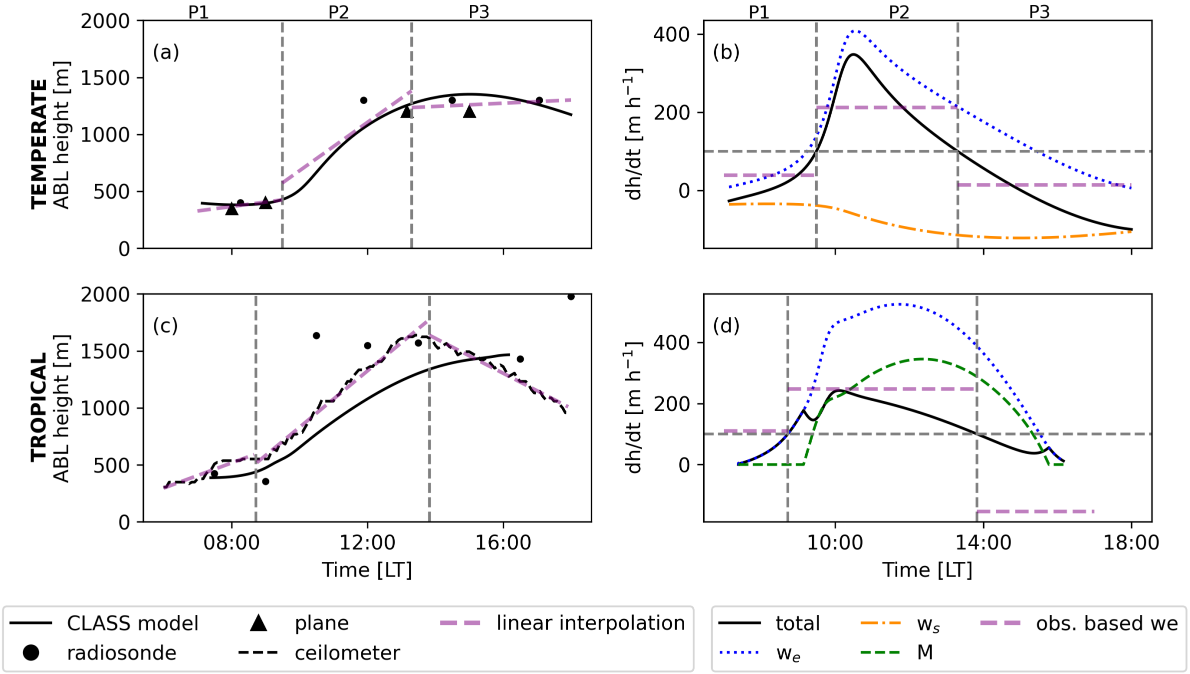

Figure A5.5: The comparison between the CLASS model output and the observations for the Atmospheric Boundary Layer (ABL) height based on radiosondes, aircraft measurements and ceilometer measurements (left panels), together with the budget components that contribute to the boundary layer height (h) growth (right panels). The purple dotted lines in the left panels indicate the linear regression line through the observations for the three periods (P1, P2 and P3). The purple dotted lines in the right panels indicate the slope of the linear regression line and indicate the entrainment velocity (w_e) based on observations. The budget components of the boundary layer growth are: entrainment velocity ($\mathrm{w_e}$), subsidence velocity ($\mathrm{w_s}$) and the cloud ventilation (M) (see Eq. A5.9).

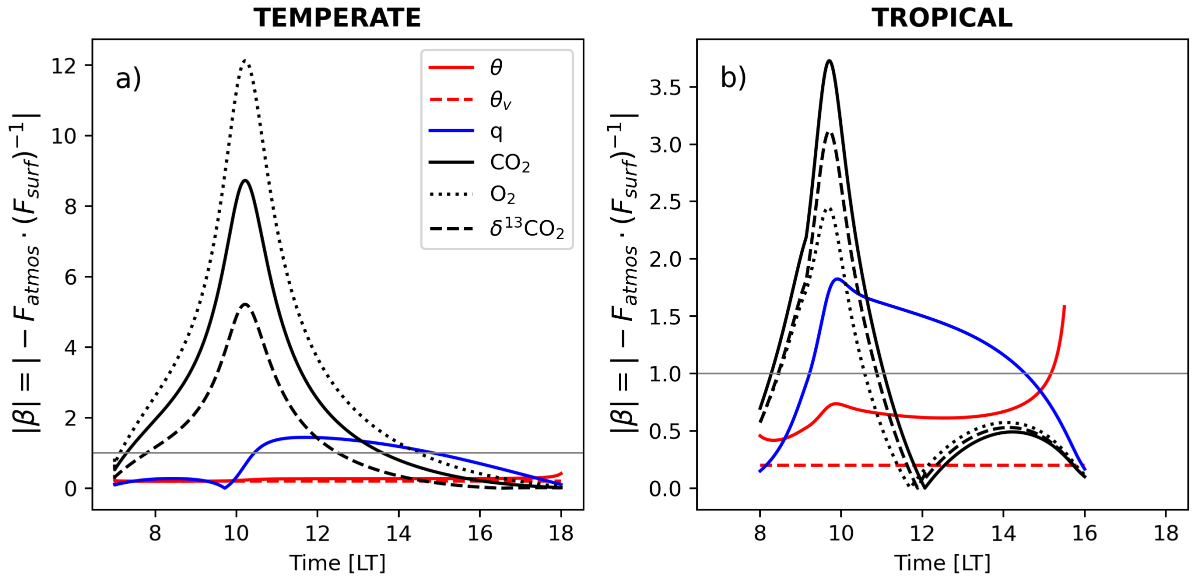

Figure A5.6: The ratio between the entrainment and the surface flux (β) over time for different meteorological variables and carbon cycle tracers for the modelled temperate (a) and tropical forest cases (b).

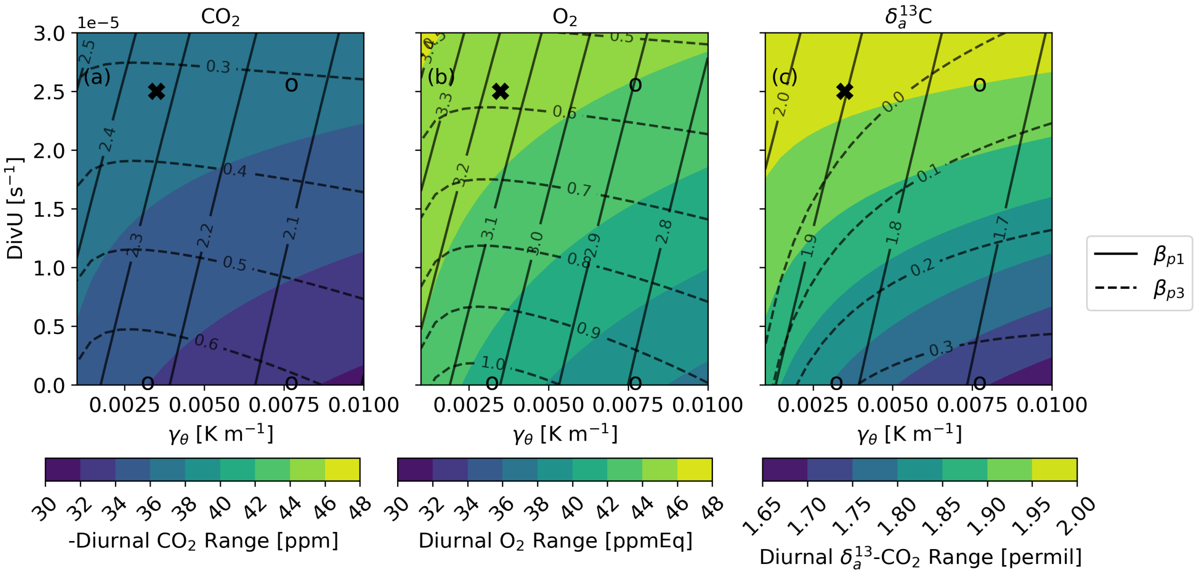

Figure A5.7: Sensitivity analysis for the temperate forest case, including different combinations of the diurnal range (colors) and the average ratio between the atmospheric flux and the surface flux for P1 (β_{p1}, continuous lines) and P3 (β_{p3}, dashed lines) for CO_2 (a), O_2 (b) and $\delta^{13}CO_2$ (c) by changing the divergence (DivU) and the lapse rate of potential temperature (γ_θ). The cross indicates the base case for the temperate forest as presented in the main text. The circles indicate the cases that are shown in more detail in Figure 5.4 in the main text.

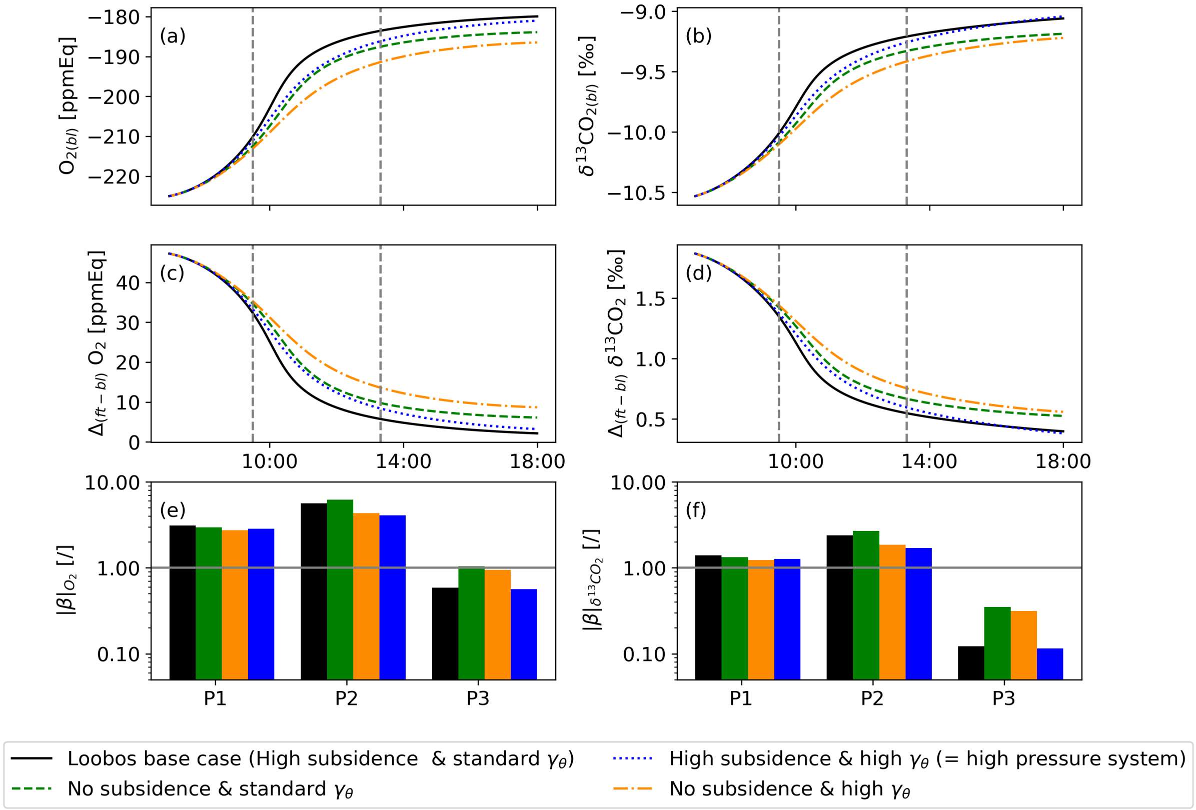

Figure A5.8: Similar as Figure 5.4, 5.4f and 5.4g in the main text but now for O_2 and $\delta^{13}CO_2$.

Table A5.3: Initial and boundary conditions of atmospheric variables, CO_2, O_2, $\delta^{13}CO_2$ used to represent the temperate forest case (May 18, 2022) and tropical forest case (August 15, 2022) numerical experiments in CLASS. The initial conditions are prescribed in CLASS at 6:00 UTC (7:00 local winter time) for temperate forest case and at 11:00 UTC (7:00 LT) for the tropical forest case. z indicates the height of the modelled variable: in the mixed layer ($h_0 > z > h_c$), or in the free troposphere ($z > h_0$).

	Loobos	Amazon
Initial boundary layer height (h_0)	400 m	385 m
Canopy height (h_c)	22 m	40 m
Horizontal large scale divergence of wind ($\nabla \cdot U$)	$2.5 \cdot 10^{-5}$ s^{-1}	0 s^{-1}
Entrainment ratio of virtual potential temperature	0.2	0.2
Potential temperature		
$h_0 >$ z $> h_c$	289.8 K	301 K
z $> h_0$	$293.1 + 3.5 \cdot 10^{-3}(z - h_0)$	$301.9 + 3.8 \cdot 10^{-3}$ $(z - h_0)$ K
Specific humidity		
$h_0 >$ z $> h_c$	7.9 g_w kg_a^{-1}	16 g_w kg_a^{-1}
z $> h_0$	$9.1 - 1.6 \cdot 10^{-3}(z - h_0)$ g_w kg_a^{-1}	$15.2 - 3.3 \cdot 10^{-3}(z - h_0)$ g_w kg_a^{-1}
Zonal wind		
$h_0 >$ z $> h_c$	non-applicable	-1
z $> h_0$	non-applicable	$-3.14 - 7.8 \cdot 10^{-4}(z - h_0)$ m s^{-1}
Meridional wind		
$h_0 >$ z $> h_c$	non-applicable	-2
z $> h_0$	non-applicable	$-2.85 - 3.0 \cdot 10^{-4}(z - h_0)$ m s^{-1}
Carbon dioxide		
$h_0 >$ z $> h_c$	458.02 ppm	445.00 ppm
z $> h_0$	420.12 ppm	420.72 ppm
Oxygen using $ER_A = -0.96$ *and* $ER_R = -1.03^{(1)}$		
$h_0 >$ z $> h_c$	-225 ppmEq	-190.00 ppmEq
z $> h_0$	-177.8 ppmEq	-171.46 ppmEq
$^{13}CO_2$ *using* $R^{13}_{VPDB} = 0.011057^{(2)}$		
$h_0 >$ z $> h_c$	5.011 ppm, $\delta = -10.53$ ‰	4.872 ppm, $\delta = -9.83$ ‰
z $> h_0$	4.603 ppm, $\delta = -9.10$ ‰	4.612 ppm, $\delta = -8.58$ ‰
Advection		
Advection of potential temperature	-0.5 K h−1	0 K h^{-1}
Shallow cumulus		
Transition layer thickness (Δz)	non-applicable	193 m
Cloud cover fraction	non-applicable	0

(1) The oxygen exchange ratios for assimilation (ER_A) and respiration (ER_R) were derived by Faassen et al., 2023 for Hyytiälä forest

(2) This value is for $CO_2 = {}^{12}CO_2 + {}^{13}CO_2$. The value for $^{12}CO_2$ as basis is R^{13}_{VPDB}=0.0111797.

Table A5.4: Initial and boundary conditions for the vegetation and soil parameterizations used to represent the temperate forest (May 18, 2022) and tropical forest (August 15, 2022) numerical experiments in CLASS.

Variable	Description and units	Loobos	Amazon
Geographic and time			
Lat	Latitude [deg]	52.17	-2.14
Lon	Longitude [deg]	5.74	-59.00
f_c	Coriolis parameter [s^{-1}]	10^{-4}	$-5.5 \cdot 10^{-6}$
DOY	Day of year [-]	138	226
Time	Initial time [h in UTC]	6	11
Vegetation			
z_{0m}	Roughness length for momentum [m]	2	0.5
z_{0h}	Roughness length for heat and moisture [m]	2	0.11
α	Surface albedo [-]	0.11	0.12
LAI	Leaf area index of vegetated surface fraction [-]	1.5	5
C_{veg}	Vegetation cover [-]	0.75	0.9
c3c4	Plant type [-]	c3	c3
c_β	Curvature plant-water stress factor [-]	0.25	0
a_d	Regression coefficient to calculate C_{frac} [kPa^{-1}]	0.07	0.07
f_0	Maximum value of C_{frac} [-]	0.89	0.89
g_{min}	Cuticular (minimum) conductance to water vapor [mm s^{-1}]	0.25	0.25
$A_{max,298}$	CO_2 maximal primary productivity at 298 K [mg CO_2 m^2_{leaf} s^{-1}]	2.2	1.83
$g_{m,298}$	Mesophyll conductance at 298 K [mm s^{-1}]	3	2
α_0	Light use efficiency at low light conditions [mg J^{-1}]	0.017	0.017
Γ_{298}	CO_2 compensation concentration at 298 K [mg CO_2 m^{-2}]	82.2	82.2
K_x	Extinction coefficient of PAR inside the canopy [m_{ground} m^{-1}_{leaf}]	0.7	0.7
$Q_{10,CO2}$	Temperature response coefficient to calculate Γ [-]	1.5	1.5
$Q_{10,gm}$	Temperature response coefficient to calculate g_m [-]	2.0	2.0
$Q_{10,Ammax}$	Temperature response coefficient to calculate A_{mmax} [-]	2.0	2.0
$T_{1,gm}$	Low reference temperature to calculate g_m [K]	278	301
$T_{1,Ammax}$	Low reference temperature to calculate A_{mmax} [K]	281	281
$T_{2,gm}$	High reference temperature to calculate g_m [K]	305	301
$T_{2,Ammax}$	High reference temperature to calculate A_{mmax} [K]	311	311
W_l	Equivalent water layer depth for wet vegetation [m]	0	0
Soil			
T_S	Initial surface temperature [K]	288	299
T_{soil1}	Temperature top soil layer [K]	286	298.6
T_{soil2}	Temperature deeper soil layer [K]	284	298.7
w_{sat}	Saturated volumetric water content [m^3 m^{-3}]	0.22	0.472
w_{fc}	Volumetric water content field capacity [m^3 m^{-3}]	0.17	0.4
w_{wilt}	Volumetric water content wilting point [m^3 m^{-3}]	0.02	0.171
w_{soil1}	Volumetric water content top soil layer [m^3 m^{-3}]	0.04	0.3
w_{soil2}	Volumetric water content deeper soil layer [m^3 m^{-3}]	0.04	0.34
a	Clapp and Hornberger retention curve parameter [–]	0.387	0.219
b	Clapp and Hornberger retention curve parameter [–]	4.05	4.9
p	Clapp and Hornberger retention curve parameter [–]	4	4
CG_{sat}	Saturated soil conductivity for heat [K m^{-2} J^{-1}]	$3.22 \cdot 10^{-6}$	$3.56 \cdot 10^{-6}$
$C1_{sat}$	Coefficient force term moisture [-]	0.082	0.132
$C2_{ref}$	Coefficient restore term moisture [-]	3.9	1.8
Λ	Thermal diffusivity skin layer [W m^{-2} K^{-1}]	20	40
R_{10}	Soil respiration at 10°C [mg CO_2 m^{-2} s^{-1}]	0.1	0.1
$r_{s,soil,min}$	Minimum resistance soil evaporation [s m^{-1}]	50	50

Chapter 6

Assessing the variability of O_2 and CO_2 biosphere exchange using the SiB4 biosphere model

This chapter is in preparation with contributions from:

A. van der Woude, J. Hooghiem, A.-W. van den Berg, B. Hilman, L. M. Hulsman, A. Kaushik, R. de Kok, M. van de Sande, W. Peters and I. T. Luijkx.

Abstract

Atmospheric oxygen (O_2) is used to partition the components of the carbon budget at both global and regional scales. In these partitioning methods, the net biospheric exchange ratio between O_2 and CO_2 (ER_{net}) is commonly assumed to be a constant value of 1.1 in O_2 partitioning methods used to constrain the carbon balance. ER_{net} is the result of assimilation and respiration processes, each characterized by distinct exchange ratios (ER_a and ER_r respectively). Studies have previously demonstrated that ER_a and ER_r vary across ecosystems and over time, suggesting that ER_{net} is also likely to exhibit temporal and spatial variability, and not a constant as assumed. To test this hypothesis, we implemented O_2 fluxes into the Simple Biosphere Model (SiB4), assigning different ER_a and ER_r values to various carbon pools and plant functional types, based on limited available observations. This implementation allows us to derive the first set of global O_2 biosphere fluxes that vary over space (lon×lat = 0.5° × 0.5°) and time ($\Delta t = 3$ hours). Our results reveal distinct seasonal patterns in ER_{net}, with high values around 1.1 in the winter and low values around 0.8 in the summer, and a pronounced spatial distribution, with values around 0.9 during summer in northern Europe and values around 1.01 in southern Europe. The modeled temporal variations are primarily caused by shifts in the ratio between the photosynthesis and respiration fluxes, while the spatial variability is the result of regional differences in dominant plant functional types. On regional scale, our findings highlight the importance of incorporating ER_{net} variability in O_2 partitioning methods, such as those estimating fossil fuel CO_2 signals using atmospheric potential oxygen (APO). When this variability in ER_{net} is not considered, the local atmospheric CO_2 fossil fuel signal could be overestimated. For example at a location with a large influence of the biosphere, the fossil fuel signal was overestimated by nearly 12 ppm and this resulted in an overestimation of more than 700% of the surface CO_2 fossil fuel fluxes. These insights enhance our understanding of the dynamics of biosphere O_2 and CO_2 exchange and underscore the necessity of accounting for biospheric contributions in O_2 partitioning methods.

6.1 Introduction

Atmospheric oxygen (O_2) is used to partition the components of the carbon budget at both global and regional scales. This is possible because O_2 and carbon dioxide (CO_2) are directly coupled in the major carbon cycle processes; fossil fuel burning and biosphere exchange (Keeling and Manning, 2014). This coupling is quantified by the Exchange Ratio (ER), which represents the number of moles of O_2 exchanged per mole of CO_2 (Keeling et al., 1998), defined in this study as a positive number when the exchange of O_2 and CO_2 is of opposite sign. Globally, the ER of the biosphere (α_b) is generally assumed to be 1.1 ± 0.05 (Severinghaus, 1995) and the ER of fossil fuel combustion (α_f) is estimated at 1.38 (Keeling and Manning, 2014). On a global decadal scale, these constant ER values are used to partition carbon sinks between the land and the ocean (Manning and Keeling, 2006; Friedlingstein et al., 2024), with a relatively small uncertainty of 0.1 to the assumed ratio (Manning and Keeling, 2006; Keeling and Manning, 2014). Furthermore, the biospheric ER value of 1.1 has also been used on the regional scale, to determine the contribution of fossil fuel emissions to the observed atmospheric CO_2 signal through Atmospheric Potential Oxygen (APO) (Stephens et al., 1998; Pickers et al., 2022; Rödenbeck et al., 2023). In all global and regional O_2-based partitioning methods, the ER of the biosphere has typically been treated as a constant value across space and time, and for vegetation and soil types.

Studies measuring the O_2 and CO_2 exchange of different soil and vegetation types indicate that the biospheric ER is not a constant value. The net ER signal of the biosphere ($\mathrm{ER_{net}}$) based on net surface exchange of O_2 and CO_2 results from the contributions of the ER of the assimilation flux ($\mathrm{ER_a}$) and the respiration flux ($\mathrm{ER_r}$), expressed as:

$$NEE = -GPP + TER \tag{6.1}$$

$$-ER_{net} \cdot NEE = ER_a \cdot GPP - ER_r \cdot TER \tag{6.2}$$

$$ER_{net} = \frac{ER_a \cdot GPP - ER_r \cdot TER}{-NEE} \tag{6.3}$$

Where NEE is the net ecosystem exchange, GPP is the gross primary productivity and TER is the total ecosystem respiration. We assume that NEE can be determined from GPP and TER because fires and disturbances are not taken into account. Both GPP and TER are defined as positive fluxes and NEE is negative when carbon is taken up at the surface and positive when carbon is released to the atmosphere. We emphasize that $\mathrm{ER_{net}}$ is the result of both assimilation and respiration processes, but in itself is a mathematical construct and not a process-specific ER itself, and even becomes infinite when NEE equals zero. $\mathrm{ER_a}$ can be measured *in situ* using branch bags or in the laboratory with plant or leaf chambers and varies temporally and across vegetation types (Seibt et al., 2004; Ishidoya et al., 2013; Bloom, 2015). Similarly, $\mathrm{ER_r}$ can be quantified *in situ* with soil chambers and also varies temporally and among soil types (Seibt et al., 2004; Angert et al., 2015; Ishidoya et al., 2013; Hicks Pries et al., 2020; Hilman et al., 2022). When ER_a and ER_r differ, their values can be used to partition NEE into the gross fluxes of GPP and TER (Ishidoya et al., 2015; Faassen et al., 2023). Moreover, differences between ER_a and ER_r lead to a varying ER_{net} over time as GPP and TER themselves fluctuate over time. This temporal variability of ER_{net} has been measured and demonstrated in a few studies (Stephens et al., 2007; Ishidoya et al., 2015; Battle et al., 2019; Faassen et al., 2023).

Variability in ER_{net} can have significant implications for O_2 partitioning methods. The constant biospheric ER value of 1.1 is derived from oxidative ratios (ORs) based on elemental composition analysis and has an uncertainty of ± 0.05 (Manning and Keeling, 2006; Keeling and Manning, 2014). Studies by Manning and Keeling (2006), Keeling and Manning (2014) and Rödenbeck et al. (2023) demonstrated that on decadal timescales, variability in ER_{net} within the range of 1.05 to 1.1 has minimal impact on O_2 partitioning methods. However, Randerson et al. (2006) argued that using the individual gross fluxes of GPP and TER and their respective ER signals, rather than the aggregated NEE and ER_{net}, has significant consequences for global O_2 partitioning on decadal timescales. Specifically, a difference of 0.0175 between ER_a and ER_r could lead to a shift of 1 PgC yr^{-1} from the global land to the ocean sink. Moreover, Rödenbeck et al. (2023) showed that when moving from decadal to seasonal timescales, varying ER_{net} between 1.05 and 1.1 increases the uncertainty of estimated fossil fuel CO_2 emissions through APO, to the extent that the uncertainty may become comparable to the magnitude of the signal itself. This could be especially relevant for studies such as Pickers et al. (2022) which used a constant ER for the biosphere in the calculation of APO to determine changes in regional fossil fuel CO_2 emissions over a year, based on local atmospheric O_2 and CO_2 measurements at Weybourne.

To evaluate the consequences of the variability between ER_a and ER_r on O_2 partitioning methods, biosphere O_2 fluxes over larger scales are required. Models can help to assess this in the absence of O_2 flux observations. Studies by Huang et al. (2018) and Ding et al. (2022) provided the first global gridded (1.0° x 1.0° resolution) estimates of O_2 biosphere fluxes by linking constant OR values to simulated NEE fluxes from the fifth and sixth coupled model intercomparison project (CMIP5 and CMIP6). Although interesting, this approach misses the influence of vegetation- and soil specific and temporally variable ER_a and ER_r values. Implementing these variable values remains challenging because measurements of these ER's have only been conducted over relatively short timescales and in a limited number of ecosystems. Furthermore, there is no clear consensus on the drivers of the temporal variability of ER_a and ER_r, making it difficult to even parameterize them in a model. Only a few studies have explicitly incorporated biospheric O_2 fluxes into models by linking ER_a and ER_r separately to gross CO_2 fluxes (Yan et al., 2023; Faassen et al., 2024b). However, these studies were limited in scope, covering only specific ecosystems and focusing on diurnal time scales.

In this study we make a first attempt to link local variability in biosphere ER signals to larger scale O_2 partitioning methods, by integrating O_2 dynamics into the Simple Biosphere model (SiB4) (Haynes et al., 2019). We thereby provide modeled O_2 (and CO_2) biosphere fluxes, but our study does not include validation with observations due to the limited availability of observations and the current lack of understanding of the drivers of the variability of $\mathrm{ER_a}$ and $\mathrm{ER_r}$. Through our model framework, we aim to gain insights on potential consequences for $\mathrm{ER_{net}}$ when considering distinct $\mathrm{ER_a}$ and $\mathrm{ER_r}$ signals. Moreover, we evaluate the impact of a variable $\mathrm{ER_{net}}$ on the fossil fuel O_2 partitioning method when applied at atmospheric observational sites, by using an atmospheric transport model together with our simulated biosphere O_2 and CO_2 fluxes. The 'pseudo-observations' from the model, allow full or partial reconstructions of APO, ER_{net}, and fossil fuel fractions of local mole fractions.

In this chapter, we first describe the O_2 implementation in the SiB4 model (Sect. 6.2). In Sect. 6.3 we analyze the resulting O_2 and CO_2 biosphere fluxes where we focus on the temporal and spatial variability of their ratios. We end this section with an evaluation on the sensitivity of the APO partitioning method with a variable $\mathrm{ER_{net}}$ to estimate CO_2 fossil fuel signals. A detailed discussion of our findings is presented in Sect. 6.4, where we discuss the potential consequences of our study for different O_2 partitioning methods. Finally, in Sect. 6.5 we conclude what the impact was on the temporal and spatial variability of $\mathrm{ER_{net}}$ by implementing O_2 into the SiB4 model.

6.2 Methods

In this section, we describe the setup of the SiB4 model and the implementation of O_2. The O_2 implementation was done for each individual carbon pool. We provide a detailed explanation of our approach to implementing O_2 for each of these pools. Finally, we outline the methodology for the sensitivity study, in which we assess how sensitive the O_2 partitioning method described by Pickers et al. (2022) is to variations in the biosphere ERs.

6.2.1 Terminology used for the ratio between O_2 and CO_2

We integrate information from previous studies that measured O_2 at various parts of the ecosystem, including the atmosphere, the soil and vegetation. These studies do not always define the $O_2 : CO_2$ ratio as the Exchange Ratio (ER), but different terms are used depending on the measurement approach. For simplicity, we use a consistent terminology throughout this study based on the ER. However, it is important to clarify the different terms in use, as we combine results from multiple measurement studies.

The Oxidative Ratio (OR) represents the O_2:CO_2 ratio derived from elemental analysis of organic materials, such as wood or soil samples. OR reflects the stoichiometry of the sampled material and provides an indication of the O_2 and CO_2 exchange required to have formed the material (Randerson et al., 2006; Gallagher et al., 2014; Clay and Worrall, 2015). Consequently, OR represents processes occurring over time scales of years to decades. In contrast, the Exchange Ratio (ER) refers to the O_2:CO_2 ratio that captures the direct O_2 and CO_2 exchange at the time of measurement, reflecting the specific time scale of the measurement period. Atmospheric ER measurements just above the canopy can be categorized into ER values based on O_2 and CO_2 mole fraction measurements (ER_{atmos}) or based on surface flux measurements (ER_{net}, Eq. 6.2) (Seibt et al., 2004; Ishidoya et al., 2013; Faassen et al., 2023). Studies measuring direct O_2 and CO_2 exchange from soils, stems and vegetation often use the inverse of ER (CO_2:O_2). In this case, different terms are used depending on the process being investigated. The Respiration Quotient (RQ) is used for respiration processes (Angert et al., 2015), and the Assimilation Quotient (AQ) is used to study assimilation processes (Cousins and Bloom, 2004; Bloom, 2015; Fischer et al., 2015). In soil studies, the Apparent Respiration Quotient (ARQ) is used when O_2 or CO_2 follow different pathways out of the soil (Angert et al., 2015; Hicks Pries et al., 2020; Hilman et al., 2022). Under such conditions, ARQ provides an approximation of RQ.

In this study, we only use the terms OR and ER. Values for RQ, AQ and ARQ are converted to ER signals, because RQ, AQ and ARQ represent O_2 and CO_2 exchange at the moment of measurement, similar to ER. OR is used when discussing processes over long time scales and referring to the measurements using elemental analysis. OR is frequently associated with the global biosphere ER (α_b), used in O_2 partitioning methods (Keeling and Manning, 2014). However, we explore the use of ER values directly for α_b and evaluate the difference between these approaches.

6.2.2 SiB4 set-up

The O_2 biosphere fluxes are implemented in the Simple Biosphere Version 4 (SiB4) model (Haynes et al., 2019). Vegetation in the model is categorized into 10 plant function types (PFTs), as summarized in Table A6.1. The PFTs include different forest types, shrubs, and crops, each forming distinct carbon pools that drive the carbon fluxes. Each carbon pool stores carbon and allocates it to the next pool. Table A6.1 shows the individual live carbon pools responsible for assimilation and autotrophic respiration. For simplicity, we grouped the various dead carbon pools that contribute to heterotrophic respiration.

The SiB4 model calculates surface flux outputs every 10 minutes and we average them to 3-hourly means on a global grid with a resolution of 0.5° by 0.5°. The flux outputs are based on a weighted average of the PFTs within each grid cell. The model uses meteorological data from the ECMWF Reanalysis 5th Generation (ERA5) as input (Hersbach et al., 2020). Consistent with previous studies, the carbon pools were initialized and brought to a steady state using a first-guess quasi-steady-state solution followed by a spin-up of 5 x

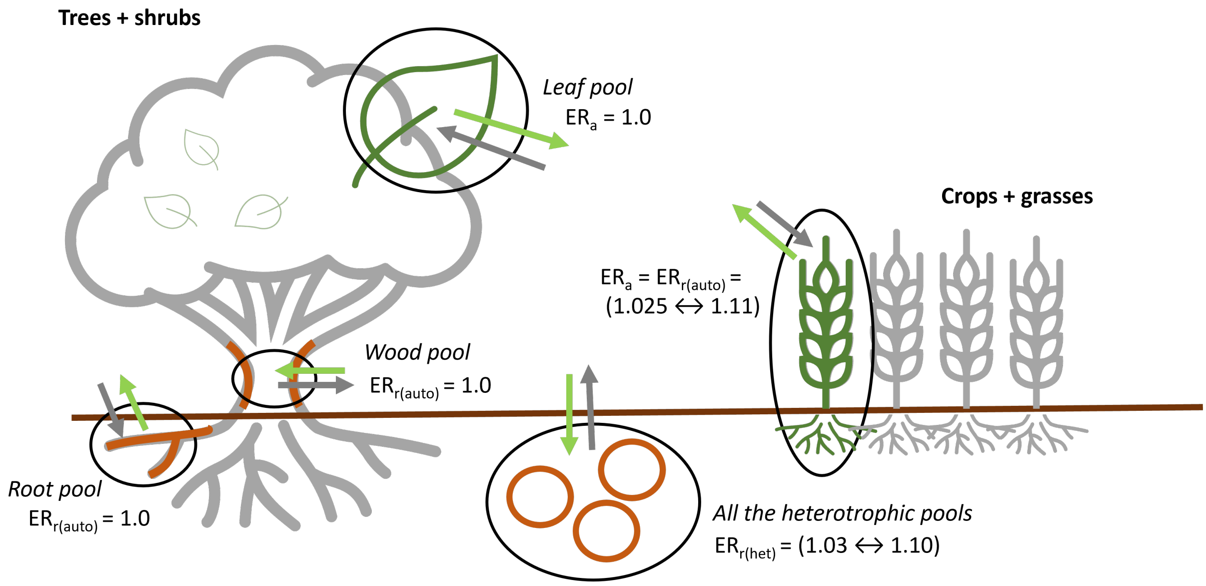

Figure 6.1: Schematic overview of the different exchange ratios (ER) that are coupled to the carbon pools found in the SiB4 model. ER values are specific for the processes: assimilation (ER_a), autotrophic respiration ($ER_{r(auto)}$) and heterotrophic respiration ($ER_{r(het)}$). The green arrows indicate the O_2 fluxes and the grey arrows indicate the CO_2 fluxes.

20 years with a constant atmospheric CO_2 mole fraction of 370 ppm (Haynes et al., 2019; Kooijmans et al., 2021; Van Der Woude et al., 2023a). This study focuses on the year 2021, a period characterized by relatively normal conditions, such as no extreme drought in Europe and La Niña conditions in the tropics.

6.2.3 O_2 implementation

The implementation of O_2 into the SiB4 model directly links O_2 fluxes to the final CO_2 fluxes for each carbon pool and PFT, using an ER signal:

$$F(O_2)_{pool} = -ER \cdot F(CO_2)_{pool} \tag{6.4}$$

The CO_2 fluxes ($F(CO_2)_{pool}$) include a GPP flux from the leaf pool, autotrophic respiration fluxes from the leaf, fine roots, coarse roots, wood and product pools and heterotrophic respiration fluxes from the dead pools. The autotrophic and heterotrophic respiration fluxes can be combined into the TER flux (Eq. 6.2). Table A6.1 outlines the ER values used to construct O_2 fluxes from CO_2 fluxes. In the following sections, we provide a detailed reasoning for the selection of ER values for each carbon pool and discuss the specific differences in ER values between grasslands and crops and other PFTs.

Our aim is to generate biosphere O_2 fluxes using a relatively simple model implementation to assess the implications of spatially and temporally varying ER_a and ER_r values. For this purpose, we assume that the individual ER_a and ER_r values remain constant over time.

While it is highly likely that the ER_a and ER_r values fluctuate due to factors such as light availability (Fischer et al., 2015), vapor pressure deficit, temperature variations, changes in soil moisture (Hicks Pries et al., 2020; Hilman et al., 2022) or vegetation development (Randerson et al., 2006; Gallagher et al., 2014), these dynamics are not accounted for in this study. Instead, we focus only on spatial and temporal variations in the resulting ER signals (ER_{net}, ER_a and ER_r) caused by e.g. shifts in dominance of the carbon pools or spatial differences in PFT coverage.

The resulting biosphere O_2 fluxes are not validated in this study. This was not possible due to the lack of O_2 flux observations. We discuss this further in Sect. 6.4. In contrast, the CO_2 biospheric fluxes from the SiB4 model have been validated in previous studies and agree well with observational data (Haynes et al., 2019; Kooijmans et al., 2021; Van Der Woude et al., 2023a).

Table A6.1: Implementation of O_2 into the SiB4 model by linking exchange ratio (ER) signals of assimilation (ER_a), autotrophic respiration ($ER_{r(auto)}$ and heterotrophic respiration ($ER_{r(het)}$) to the different carbon pools of specific plant functional types (PFT).

PFT	$\mathbf{ER_a}$	$\mathbf{ER_{r(auto)}}$					$\mathbf{ER_{r(het)}}$
	Leaf	Leaf	Fine Roots	Coarse Roots	Wood	Product	All dead pools
Evergreen Needleleaf	1.0	1.0	1.0	1.0	1.0	1.0	1.07^a
Deciduous Needleleaf	1.0	1.0	1.0	1.0	1.0	1.0	1.08^a
Evergreen Broadleaf	1.0	1.0	1.0	1.0	1.0	1.0	1.07^a
Deciduous Broadleaf	1.0	1.0	1.0	1.0	1.0	1.0	1.08^a
Shrubs	1.0	1.0	1.0	1.0	1.0	1.0	1.10^a
Tundra	1.0	1.0	1.0	1.0	1.0	1.0	1.10^a
Grassland	1.025^b	$=ER_a$	$=ER_a$	$=ER_a$	$=ER_a$	$=ER_a$	1.03^a
Cropland	1.03^c	$=ER_a$	$=ER_a$	$=ER_a$	$=ER_a$	$=ER_a$	1.05^a
Maize	1.03^c	$=ER_a$	$=ER_a$	$=ER_a$	$=ER_a$	$=ER_a$	1.05^a
Soybeans	1.11^c	$=ER_a$	$=ER_a$	$=ER_a$	$=ER_a$	$=ER_a$	1.05^a
Winter Wheat	1.03^c	$=ER_a$	$=ER_a$	$=ER_a$	$=ER_a$	$=ER_a$	1.05^a

a: Clay and Worrall (2015), b: Randerson et al. (2006), c: Gallagher et al. (2014)

Leaf and product pool

The ER_a and $ER_{r(auto)}$ values of the leaf pool are both set to 1.0 (Table A6.1). This assumption is based on the assumption that glucose, which has an OR of 1.0, is the main compound that is formed and burned during assimilation and respiration in leaves. Additionally, other carbon-compounds synthesize in leaves, such as starch and larger carbohydrates, again with an OR of 1.0 (De Vries et al., 1974; McDermitt and Loomis, 1981). Compounds with an OR differing from carbohydrates, such as lignin, proteins, amino acids, and lipids, are predominantly produced during the growth stage of vegetation (De Vries et al., 1974; Plaxton and Podestá, 2006). Since the current implementation does not account for growth-stage processes, the production of these compounds is excluded.

Previous studies have measured from plant and branch chambers and found an ER of approximately 1.0 for leaf O_2 and CO_2 exchange (Cousins and Bloom, 2004; Seibt et al., 2004; Ishidoya et al., 2013; Fischer et al., 2015). However, variations in leaf ER may occur depending on the source of nitrogen available to the plant (Cousins and Bloom, 2004; Bloom, 2015).

The product pool has a minimal impact on respiration fluxes and is difficult to measure. Therefore, we have kept the $ER_{r(auto)}$ for this pool at 1.0 to avoid unnecessary complexity.

Root pool

The $ER_{r(auto)}$ values for both the fine and course root pools are set to 1.0 (Table A6.1), under the assumption that root respiration primarily involves the burning of carbohydrates (Saglio and Pradet, 1980; Hoch et al., 2003; Zhalnina et al., 2018). However, direct measurements of O_2 and CO_2 exchange from both fine and course roots show a large range for $ER_{r(auto)}$ with values both above and below 1.0 (Shane et al., 2004; Rachmilevitch et al., 2006; Bathellier et al., 2009; Hicks Pries et al., 2020; Hilman et al., 2021; Hilman et al., 2022). This inconsistency challenges the assumption and remains unexplained. One hypothesis is that respiratory substrates other than carbohydrates are utilized. However, studies measuring $\delta^{13}C$ next to O_2 and CO_2 exchange have not found evidence of such changes, supporting the dominance of carbohydrate oxidation (Bowling et al., 2008; Bathellier et al., 2009; Hilman et al., 2021). Other potential explanations for the observed variability include: (1) nitrate assimilation, which reduces ER (Shane et al., 2004; Rachmilevitch et al., 2006); (2) carbon re-fixation within the root system, which increases ER (Bathellier et al., 2009; Hilman et al., 2021); and (3) carbon dissolution in xylem water, which also increases ER (Aubrey and Teskey, 2009). Given the unexplained nature of the observed ER values in roots, we base our implementation on theoretical assumptions and set the $ER_{r(auto)}$ to 1.0 as an initial approximation.

Wood pool

The $ER_{r(auto)}$ value for the wood pool is set to 1.0 (Table A6.1), under the theoretical assumption that stem respiration primarily oxidizes carbohydrates (Hoch et al., 2003; Plaxton and Podestá, 2006). However, field measurements report $ER_{r(auto)}$ values exceeding 1.0, with some studies observing values higher than 2.0 (Hilman et al., 2019; Hilman et al., 2022; Helm et al., 2023), contradicting the theoretical assumption. Similar to root respiration, the oxidation of alternative substrates, such as lipids, is considered unlikely because of low lipid concentration in woody samples (Hoch et al., 2003) and no indication in ER measurements that lipids are produced before they are oxidized (Hilman et al., 2019). Potential explanations for elevated ER values are similar to those for root respiration: (1) carbon re-fixation within the stem (Hilman et al., 2019) and (2) carbon dissolution in xylem water after respiration (Teskey et al., 2008; Hilman et al., 2022). Despite these hypotheses, no clear consensus has been reached on the mechanisms underlying the observed high $ER_{r(auto)}$ values in stem respiration (Helm et al., 2023). Given this uncertainty, we use an $ER_{r(auto)}$ value of 1.0 for the wood pool as a theoretical baseline.

Heterotrophic respiration pools

For the dead pools, we use a single $ER_{r(het)}$ value for their heterotrophic respiration, which is derived from the OR of the associated plant functional type. The dead pools include: dead biomass, metabolic litter, structural litter, soil litter, and the slow and armored pools. While these individual pools can be conceptually distinguished, direct measurements in bulk soil often make it difficult to determine specific ER values for each of them. Consequently, we grouped them together and assigned a unified ER value for the heterotrophic respiration. The underlying hypothesis is that the ER of bulk soil processes closely reflects the OR of the soil. This is based on the assumption that the compounds contributing to the soil's OR are decomposed during microbial respiration. The smaller and more oxidized compounds are favored, making the soil more reduced over time and increasing the OR above 1. As a result, the ER of heterotrophic respiration has been hypothesized to be higher than that of autotrophic respiration.

This hypothesis is supported by *in situ* measurements that found $ER_{r(het)}$ values consistently exceeding 1.0 (Angert et al., 2015; Hicks Pries et al., 2020; Hilman et al., 2022). These measurements also indicate that $ER_{r(het)}$ remains relatively constant over time except during periods with low respiration rates caused by low temperatures. Under such conditions, $ER_{r(het)}$ values can increase dramatically (exceeding 2.0), as slower processes becomes more apparent, including the oxidation of Fe^{2+} or the higher dissolution of CO_2 into groundwater relative to O_2 (Hicks Pries et al., 2020; Hilman et al., 2022). For the purposes of this study, we neglect this temperature-driven variability and assume a constant $ER_{r(het)}$ over time per PFT. The $ER_{r(het)}$ values of the PFT's are derived from the OR measurements reported by Clay and Worrall (2015) (Table A6.1).

Crops and grasses

We approach the ER signals of ER_a and $ER_{r(auto)}$ for crops and grasses differently than for the other PFTs, by which we introduce more variability in the resulting net O_2 fluxes. The reason for this choice is that forest types, shrubs and tundra represent relatively slow-growing vegetation compared to crops and grasses which grow faster. Our focus is on the changes in the net ER of the biosphere over a one-year period. This time scale is too short to reliably correlate the OR of slow-growing vegetation with the ER. However, grasses and crops complete their growth within a single year, making it plausible to link the OR to the ER, as hypothesized by Gallagher et al. (2014). By assuming that the OR reflects the net O_2 and CO_2 exchange required to form the complete organic matter of the vegetation (either the grasses or the crops), we propose that ER_a and $ER_{r(auto)}$ should have the same value (Table A6.1). The OR values for grasses and crops are based on the limited studies that present them: Randerson et al. (2006) for herbaceous plant parts, which we assume are representative values for grass, and Gallagher et al. (2014) for the different types of crops (Table A6.1).

6.2.4 Fossil fuel sensitivity study

The implementation of O_2 into the SiB4 model offers the opportunity to test the consequence of using a variable ER for the biosphere, both spatially and temporally, for estimating fossil fuel CO_2 signals through atmospheric potential oxygen (APO), as compared to using a constant ER value of 1.1 ($\alpha_b = 1.1$) (Severinghaus, 1995). We tested the impact of a variable α_b on fossil fuel flux estimates using APO (Pickers et al., 2022). APO is defined as (Stephens et al., 1998):

$$APO = \overbrace{O_2}^{\text{TotalO}_2} - \alpha_b \cdot \overbrace{CO_2}^{\text{TotalCO}_2} \tag{6.5}$$

The total atmospheric mole fraction signals of O_2 and CO_2 include the processes: fossil fuel combustion (ff), biosphere exchange (bio), ocean uptake and outgassing and the background values, i.e. the accumulated CO_2 in the atmosphere from all historical exchange with fossil, terrestrial, and oceanic reservoirs. The study by Pickers et al. (2022) used this definition of APO to calculate CO_2 fossil fuel fluxes based on O_2:

$$ff_{CO_2}[APO] = \frac{APO - APO_{BL}}{\alpha_f - \alpha_b} \tag{6.6}$$

Where α_f is the oxidative ratio of fossil fuel combustion and corresponds to $ff_{O_2} = \alpha_f \cdot ff_{CO_2}$, and APO_{BL} is the APO baseline, which mainly represents changes due to the ocean processes of both O_2 and CO_2, as well as the background value of O_2. Pickers et al. (2022) estimated APO_{BL} by curve fitting the seasonal variations of APO.

For the purpose of this study, we focus solely on the effect of not taking into account the variability of α_b in Eq. 6.6 on the estimated ff_{CO_2}[APO]. As a result, ocean fluxes and background values are not of importance for our analysis and are therefore not included. Incorporating them would introduce the same terms that we would subsequently remove. Consequently, we are able to exclude APO_{BL} from the equation. Without accounting for oceanic processes and background contributions, we can rewrite Eq. 6.5 into a new version:

$$APO_{wo} = \overbrace{ff_{O_2} + bio_{O_2}}^{\text{TotalO}_2} - \alpha_b \cdot \overbrace{ff_{CO_2} + bio_{CO_2}}^{\text{TotalCO}_2} \tag{6.7}$$

Where APO_{wo} is APO without ocean and the background signal and it represents the original APO through: $APO_{wo} = APO - APO_{BL}$. APO_{wo} can then be used to estimate ff_{CO_2}[APO] without considering ocean fluxes:

$$ff_{CO_2}[APO] = \frac{APO_{wo}}{\alpha_f - \alpha_b} \tag{6.8}$$

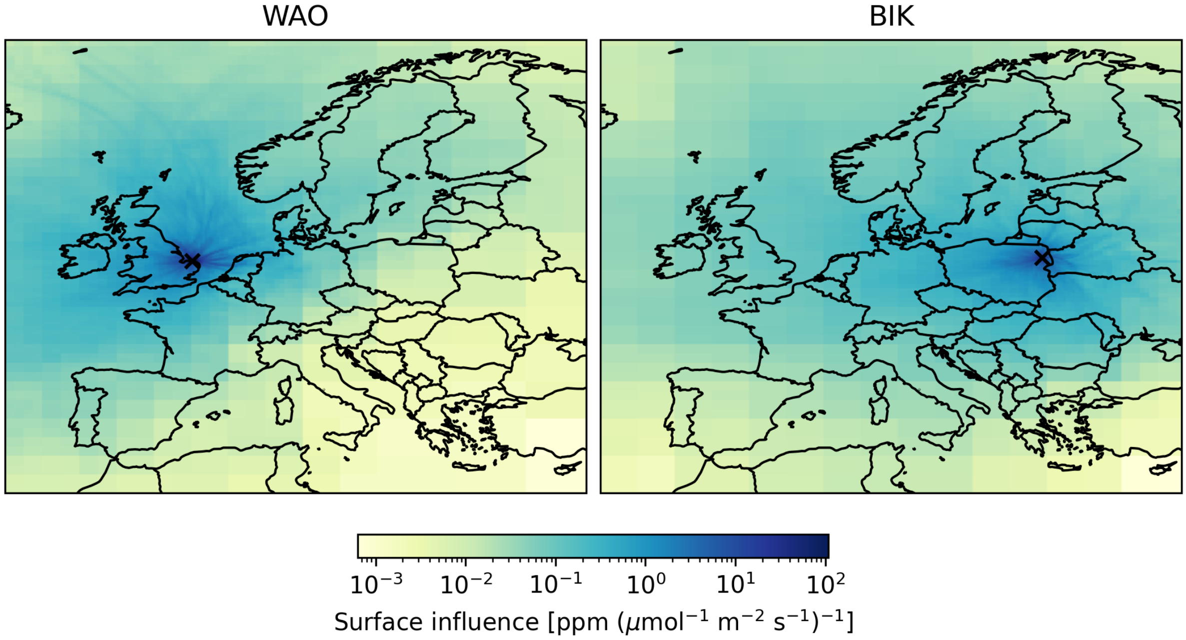

Figure 6.2: Sum of the footprint influence during 2021, for the stations: Weybourne (WAO) in the UK and Bialystok (BIK) in Poland, calculated by the STILT model.

To simulate a ff_{CO_2}[APO] signal, we used the regional atmospheric Stochastic Time-Inverted Lagrangian model (STILT) (Gerbig et al., 2003; Lin et al., 2003). STILT simulates the transport of fossil fuel and biosphere O_2 and CO_2 fluxes, generating a 3-hourly atmospheric signal that can be used to calculate a simulated $\mathrm{APO}_{\mathrm{wo}}$ signal. STILT uses ECMWF-IFS meteorological fields to calculate the footprint from a receptor location with a resolution of 0.1° by 0.2° (Roberts et al., 2018). At this receptor location, 250 particles are released and followed through the meteorological fields backwards in time for 10 days, until they get within a specified altitude of the surface (currently 0.5 times the height of the boundary layer) or go outside the domain, similar to the approach described by Van Der Woude et al. (2023a). Our domain of this study is Europe (15°W - 35°E; 33°N - 72°N) and any signal from outside the domain is considered to be non-local background. The footprint of the receptor locations determines which biospheric and fossil fuel surface fluxes are taken into account. The biosphere fluxes from the SiB4 model are used, together with fossil fuel fluxes from the GridFED dataset (Steinbach et al., 2011; Jones et al., 2021). GridFED categorizes fossil fuel emissions into four types, each with a specific OR: coal (OR = 1.17), oil (OR = 1.44), natural gas (OR = 1.95) and cement (OR = 0, indicating no O_2 uptake).

The resulting atmospheric O_2 and CO_2 signals from two stations were analyzed; Weybourne (WAO, at 15 m height above the surface), a coastal station in a rural part of the United Kingdom used by (Pickers et al., 2022), and Bialystok (BIK, at 300 m height above the surface), a station in Poland mostly influenced by biosphere fluxes (Popa et al., 2010). Figure 6.2 shows the yearly sum of the footprint influence for both stations, based on

STILT. APO_{wo} was calculated for both stations using the transported surface fluxes and α_b based on the transported biosphere fluxes within these footprints. To assess the impact of using a constant value for α_b instead of the actual biosphere O_2 and CO_2 flux ratios provided by the SiB4 model, APO_{wo} was also calculated using a fixed value of 1.1 for α_b. The difference in $ff_{CO_2}[APO]$ between the two methods offers insight into the significance of accounting for a variable α_b both over time and space.

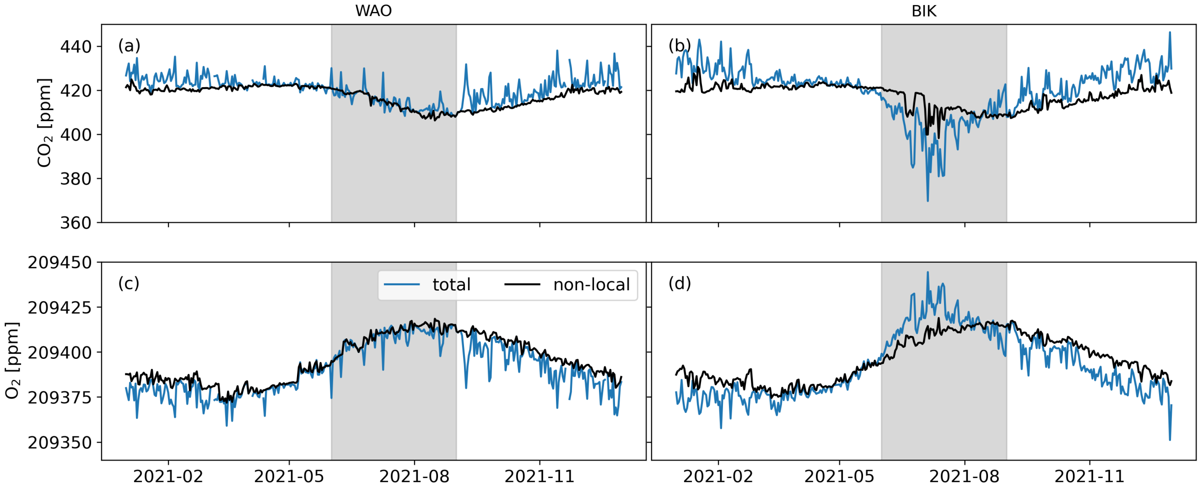

Figure 6.3: Time series of the mole fractions that result from transported surface fluxes by STILT for Weybourne (left column, WAO) and Bialystok (right column, BIK) for CO_2 (a-b), O_2 (c-d). The non-local signal is the result of TM5 simulations of global mole fractions resulting from fluxes from outside the European domain and transported by STILT from the boundaries to the two locations. The total signal is both the non-local signal and the fluxes from the footprint inside the European domain, transported by STILT. The grey shading indicates the summer period between 2021-06-01 and 2021-09-01.

To simulate the complete atmospheric signal at WAO and BIK, the non-local signal originating from outside the European domain has to be combined with the local signal. To achieve this, we use the global chemistry Transport Model version 5 (TM5) (Krol et al., 2005). TM5 is an Eulerian atmospheric transport model that operates on a 1° by 1° grid and, like the SiB4 model, uses ERA5 meteorological data as input. The surface fluxes from SiB4 and of GridFED are used to generate the biological and fossil fuel signals, respectively. Additionally, ocean fluxes and a background concentration are included. By transporting both the non-local signal from TM5 and the local signal resulting from surface fluxes within the footprint using STILT, we reconstruct the total atmospheric signal at the receptor location (Figure 6.3). The modeled seasonal cycles of atmospheric CO_2 and O_2 exhibit amplitudes that are of similar magnitudes as observations at the measurement stations (Pickers et al., 2022; Popa et al., 2010). In this study, we focus exclusively on the local signal, defined as the total signal minus the non-local contribution.

We analyze the difference between the fossil fuel atmospheric signal obtained with APO using either a value for α_B of 1.1 ($\mathrm{ff}_{CO_2}[\mathrm{APO}_{(\alpha_B\,=\,1.1)}]$) or using the variable α_B values from SiB4 (ff_{CO_2}[true]). We focus on individual days to compare the derived ff_{CO_2} with the original CO_2 fossil fuel emissions used in the model (from GridFED). These are the CO_2 fossil fuel emissions of ff_{CO_2}[true] and can be linked to the atmospheric fossil fuel signal by:

$$ff_{CO_2}[true] = \sum(FI \cdot F(ff_{CO_2})_s[true]) \tag{6.9}$$

Where FI is the footprint influence in ppm (μmol m^{-2} s^{-1})$^{-1}$, $\mathrm{F(ff}_{CO_2})_s$[true] is the surface flux of the CO_2 fossil fuel emissions in μmol m^{-2} s^{-1} and ff_{CO_2}[true] is the atmospheric fossil fuel signal in ppm. For the atmospheric signal of $\mathrm{ff}_{CO_2}[\mathrm{APO}_{(\alpha_B\,=\,1.1)}]$, the footprint stays the same. However, the fossil fuel fluxes that would have formed this signal are now modified $\mathrm{F(ff}_{CO_2})_s[\mathrm{APO}_{(\alpha_B\,=\,1.1)}]$:

$$ff_{CO_2}[APO_{(\alpha_B=1.1)}] = \sum(FI \cdot F(ff_{CO_2})_s[APO_{(\alpha_B=1.1)}]) \tag{6.10}$$

To calculate the $\mathrm{F(ff}_{CO_2})_s[\mathrm{APO}_{(\alpha_B\,=\,1.1)}]$ surface fluxes, the ratio between the atmospheric signal of $\mathrm{ff}_{CO_2}[\mathrm{APO}_{(\alpha_B\,=\,1.1)}]$ and ff_{CO_2}[true] can be used:

$$F(ff_{CO_2})_s[APO_{(\alpha_B=1.1)}] = \frac{ff_{CO_2}[APO_{(\alpha_B=1.1)}]}{ff_{CO_2}[true]} \cdot (FI \cdot F(ff_{CO_2})_s[true]) \tag{6.11}$$

With Eq. 6.11 the effect of using a constant α_B of 1.1 on fossil fuel emission estimates can be quantified.

6.3 Results

In this section we present the results of incorporating O_2 into the SiB4 model. We begin by examining the O_2 and CO_2 fluxes averaged over 2021 for the entire globe (Section 6.3.1). To gain better insights into the behavior of the resulting ER signal from these fluxes, we furthermore focus on Europe and analyze seasonal variations. Our analysis shows that the $\mathrm{ER_{net}}$ signal exhibits distinct temporal and spatial patterns, and we discuss the underlying drivers of these patterns. Finally, we assess the effect of using a variable α_B on the APO method used to estimate fossil fuel emissions (Section 6.3.2).

6.3.1 Spatial and temporal variability of $\mathrm{ER_{net}}$

Global biospheric O_2 fluxes exhibit both large spatial and large temporal variability, with elevated O_2 fluxes found in tropical regions and during the summer months. The choices made for the implementation of O_2 into the model are evident from the strong anti-correlation between O_2 and CO_2 fluxes, as shown in Figure 6.4a and 6.4b. Using the O_2 and CO_2 fluxes, we calculated $\mathrm{ER_{net}}$ signals for the entire globe. However, it is challenging to represent the biospheric $\mathrm{ER_{net}}$ with a single averaged value for the entire world. At first

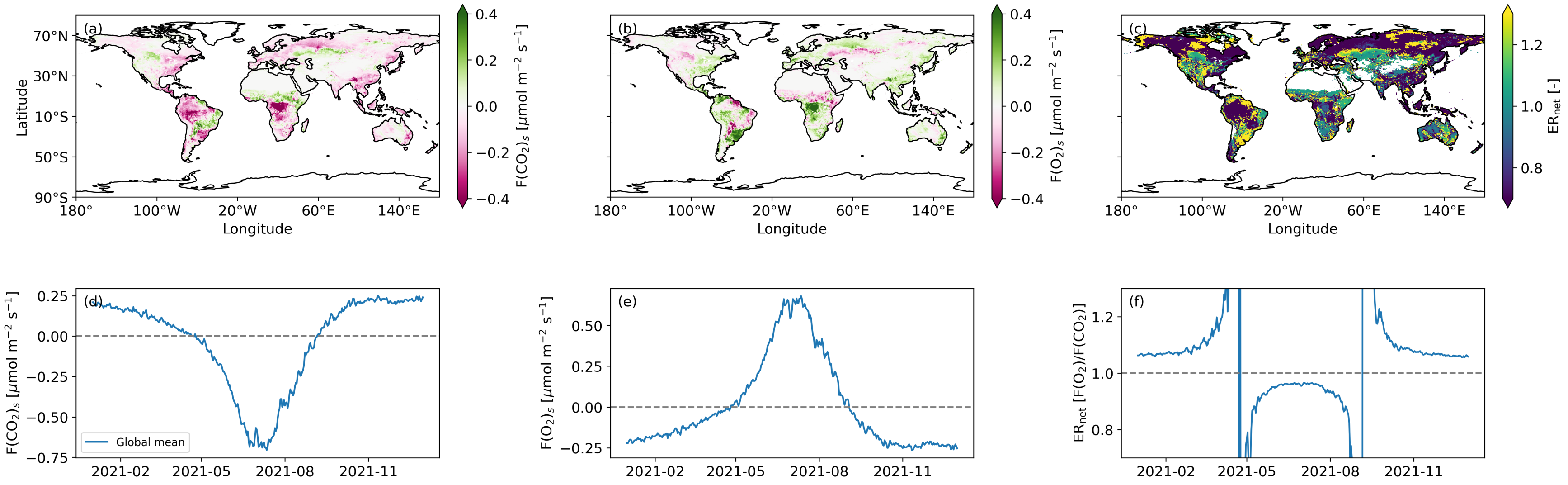

Figure 6.4: SiB4 model results for the year 2021 including the net CO_2 flux (a), net O_2 flux (b) and their exchange ratio (ER, c), together with the corresponding globally averaged time series over 2021 (d-f).

glance, the anti-correlated O_2 and CO_2 fluxes appear similar. However, when their ratios are calculated, the resulting ER_{net} signals reveal differences both temporally (Figure 6.4f) and spatially (Figure 6.4c), including the aforementioned asymptotic values when NEE ≈ 0.0 μmol m^{-2} s^{-1} in spring and fall (see eq. 6.2). Globally, ER_{net} fluctuates above 1.0 during winter and below 1.0 in summer. By dividing the globally averaged O_2 flux by the globally averaged CO_2 flux for 2021, a single global ER_{net} value is obtained: 0.42. This low global ER_{net} value can be explained by its spatial pattern, which shows extremely low ER_{net} values in tropical and boreal regions (below 0.7 or even lower than 0.0). These extremely low ER_{net} values cannot be directly linked to any of the implemented ER_a or ER_r values (Table A6.1). To fully understand the global ER_{net} patterns, we have to look at the individual gross processes that form the ER_{net}.

The ratio between the gross fluxes of GPP and TER can lead to extreme values of ER_{net}. The extreme values of ER_{net} can be explained by reformulating Eq. 6.2 to:

$$ER_{net} = \frac{ER_a \cdot \frac{GPP}{TER} - ER_r}{\frac{GPP}{TER} - 1} \tag{6.12}$$

From this equation it becomes evident that ER_{net} depends on three primary variables: ER_a, ER_r and the GPP/TER ratio. In contrast to the global ER_{net} values (Figure 6.4c), the global values for ER_a (Figure 6.5a) and ER_r (Figure 6.5b) remain within the expected ranges prescribed in Table A6.1 and exhibit only a small annual cycle, caused by changes in PFT dominance (Figure 6.5d and 6.5e). The globally averaged GPP/TER ratios are close to 1.0 (Figure 6.5c), showing that the modeled biosphere is approximately in a steady state if one integrates over long time periods. As indicated by Eq. 6.12, when the GPP/TER ratio approaches 1.0, ER_{net} can experience extreme values. This relationship becomes apparent when comparing the global time series of GPP/TER (Figure 6.5f) with ER_{net} (Figure 6.4f), where ER_{net} shows asymptotic values when GPP/TER crosses 1.0 (NEE ≈ 0.0 μmol m^{-2} s^{-1}). Consequently, ER_{net} is not linked to a single biological process, but is mathematical a combination of the individual gross fluxes, showing unexpected values, similar to isofluxes of $\delta^{13}C$ or $\delta^{18}O$ analyses (Miller and Tans, 2003). To further investigate ER_{net}, we focus on regional dynamics in Europe.

ER_{net} in Europe exhibits distinct temporal and spatial patterns, with each season characterized by unique features (Figure 6.6). During the winter months (December - February, DJF), ER_{net} shows minimal spatial variation across Europe (Figure 6.6a). In spring (March - May, MAM), ER_{net} values become extreme reflecting dynamic changes in ecosystem processes (Figure 6.6b). Summer (June - August, JJA) is characterized by low ER_{net} values compared to winter, with a clear gradient from lower values in the north to higher values in the south (Figure 6.6c). By fall (September - November, SON) ER_{net} returns to values closer to those found in winter (Figure 6.6d). As with the global analysis, the seasonal and spatial patterns of ER_{net} can be explained using Eq. 6.12, highlighting the role of variations in ER_a, ER_r and the GPP/TER ratio in driving these dynamics.

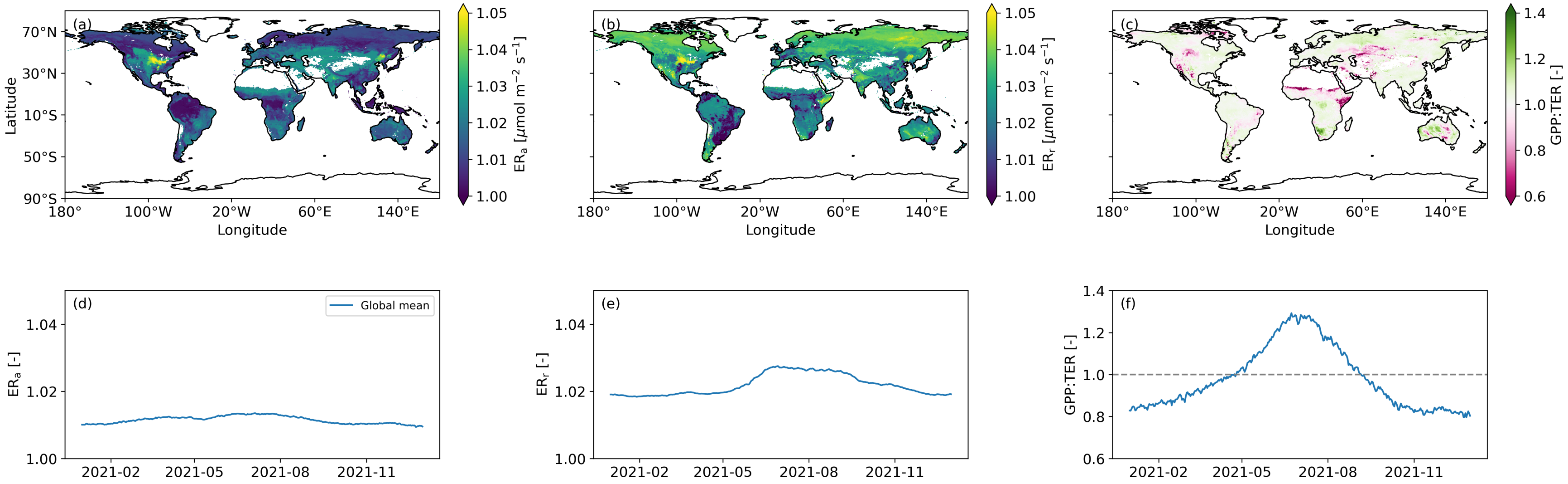

Figure 6.5: SiB4 model results for the year 2021 for the exchange ratio of assimilation ($\mathrm{ER_a}$) (a), exchange ratio of respiration ($\mathrm{ER_r}$) (b) and the ratio between gross primary productivity (GPP) and total ecosystem respiration (TER) (c), together with the corresponding globally averaged time series over 2021 (d-f).

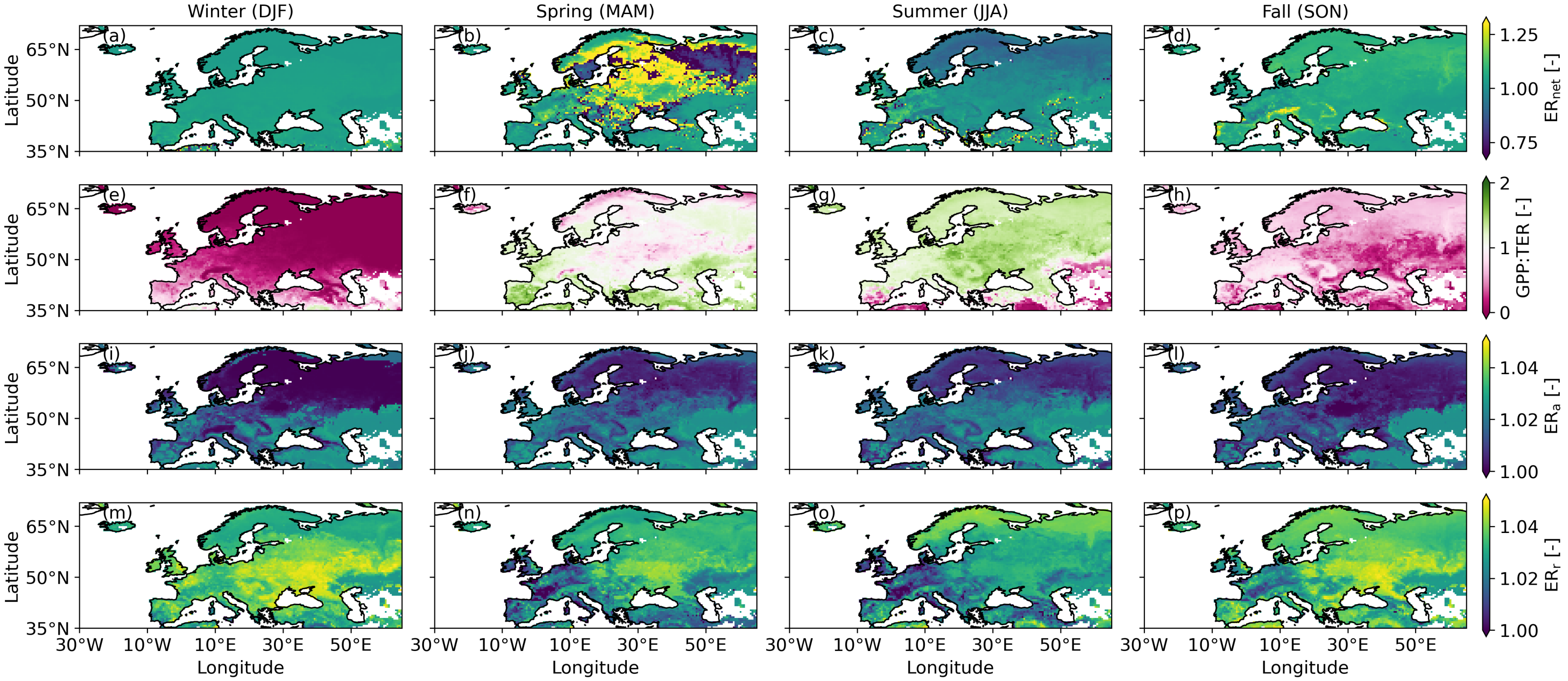

Figure 6.6: Averaged values of the SiB4 model results during the seasons (from left to right column): winter (December - February, DJF), spring (March - May, MAM), summer (June - August, JJA) and fall (September - November, SON) for the variables (from top to bottom row): the net Exchange Ratio (ER_{net}, a-d), the ratio between gross primary productivity (GPP) and total ecosystem respiration (TER) (e-h), the Exchange Ratio of assimilation (ER_a, i-l) and the Exchange Ratio of respiration (ER_r, m-p).

The temporal variation in ER_{net} can be attributed to changes in the GPP/TER ratio (Figures 6.6e-h). The variability of GPP/TER ratio depends on environmental changes, such as temperature, amount of light and soil moisture, which creates a clear seasonal pattern. During winter, TER dominates with minimal influence of GPP. According to Eq. 6.12, when TER is the dominant flux, ER_{net} should approach ER_r (around 1.04), as confirmed by Figure 6.6. In spring, the GPP/TER ratio approaches 1.0, resulting in extreme ER_{net} values, comparable to the behavior shown in Figure 6.4 for the global scale. During summer, GPP becomes the dominant flux, but TER remains significant. Eq. 6.12 suggests that when the GPP/TER ratio is around 1.5, the resulting ER_{net} lies slightly below ER_a (below 1.0). The summer ER_{net} values depend on all components of Eq. 6.12, including ER_a, ER_r and the individual gross fluxes.

The spatial variation in ER_a and ER_r explains the found spatial variation in ER_{net} during summer. While both ER_a (Figures 6.6i-l) and ER_r (Figures 6.6m-p) exhibit less pronounced seasonal variation compared to the GPP/TER ratio, they both display distinct spatial patterns. In particular, a clear north-south gradient is visible during summer, similar to the spatial variation in ER_{net}. In northern Europe (between 60°N and 80°N), ER_a is relatively low and ER_r is relatively high, leading to a low ER_{net} value. In contrast, in southern Europe (between 30°N and 60°N) ER_a is relatively high and ER_r is relatively low, resulting in higher ER_{net} values. These spatial patterns are consistent with the relationships described by Eq. 6.12.

The spatial variation in ER_a and ER_r is driven by differences in the dominant PFTs. Following our implementation of O_2 in SiB4, variations in ER_a arise from the influence of grasses crops, while variations in ER_r can result from either crop influence or the relative contributions of autotrophic and heterotrophic respiration (Table A6.1). The dominant influence is determined by the dominance of the gross fluxes associated with individual PFTs, which are combined in a weighted average net flux. During summer, a clear difference in the contributions of crops and heterotrophic respiration is evident between northern and southern Europe (Figure 6.7). Crops are more dominant in the south, leading to increased ER_a values. In the north, the more dominant role of trees increases $ER_{r(het)}$ and additionally a more dominant heterotrophic flux increases the ER_r further. The more dominant heterotrophic flux in the north can again be explained by the less dominant role of grasses crops, which have a relative high autotrophic respiration flux in the summer due to their fast growing cycle (Suleau et al., 2011). The GPP/TER ratio does not show a significant difference between northern and southern Europe.

Overall, the spatial and temporal variability of ER_{net} is primarily determined by the gross fluxes, suggesting that similar variability can be expected for real-world ecosystems. Temporal variability in ER_{net} arises from fluctuations in the ratio between GPP and TER, while spatial variability is driven by the dominance of the gross fluxes of specific PFTs. Although the individual ER values from Table A6.1 and the biospheric O_2 fluxes have not

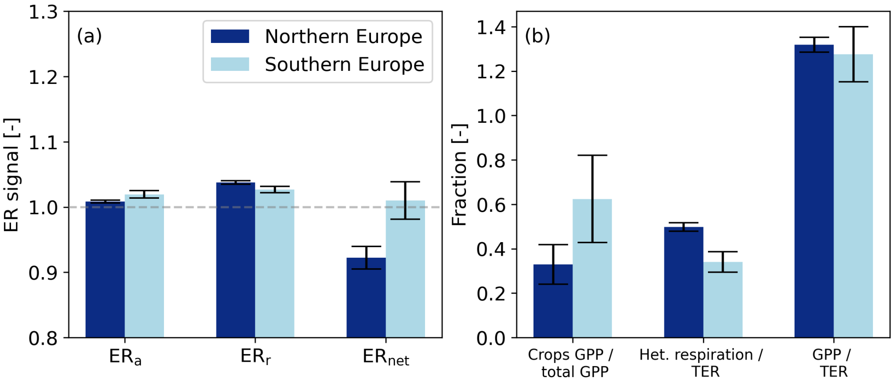

Figure 6.7: The median values and their median absolute deviation (shown as error bars) for different variables compared between the northern (between 60°N and 80°N) and southern (between 30°N and 60°N) part of Europe during summer for the: exchange ratios of assimilation (ER_a), respiration (ER_r) and the net fluxes (ER_{net}) (a) and for the ratio between heterotrophic respiration (Het. respiration) and autotrophic respiration (Auto. respiration), the ratio between crops gross primary productivity (GPP) and non-cops GPP, and the ratio the ratio between GPP and total ecosystem respiration (TER) (b).

been validated with observations, the gross CO_2 fluxes simulated by the model are known to be realistic. Previous studies have demonstrated that the spatial and temporal patterns of these CO_2 fluxes and their anomalies align well with observations (Haynes et al., 2019; Smith et al., 2020; Kooijmans et al., 2021; Van Der Woude et al., 2023b). Additionally, the implemented ER_a and ER_r values are based on theoretically established assumptions and OR measurements. We therefore argue that the temporal and spatial variability found for ER_{net} is realistic, even though the O_2 fluxes from model themselves have not been explicitly validated with observations. However, the absolute values of ER_{net} still require validation to confirm their accuracy. This variability has potential implications for O_2 partitioning methods, particularly those that rely on a constant value for α_B, as we demonstrate next.

6.3.2 Application of the fossil fuel partitioning method

We confirm that fossil fuel CO_2 signals (ff_{CO_2}) can be calculated correctly from APO when the correct α_b is used in both the numerator and denominator of Eq 6.8. This true α_B value is obtained with our O_2 and CO_2 surface fluxes from SiB4 by transporting them, along with the GridFED fossil fuel fluxes, to the generate a local signal at two locations using STILT (Figure 6.8c and 6.8d). This gave use the temporal variability of both α_b and α_F for WAO and BIK as shown in Figure 6.8e and 6.8f, to use in Eq 6.8. With all components of Eqs. 6.7 and 6.8 transported to WAO and BIK, the APO_{wo} signal (Figure 6.8g and 6.8h) and ff_{CO_2}[APO] (Figure 6.8i and 6.8j) are calculated. We subsequently confirmed that these values of ff_{CO_2}[APO] are exactly equal to the CO_2 signal resulting

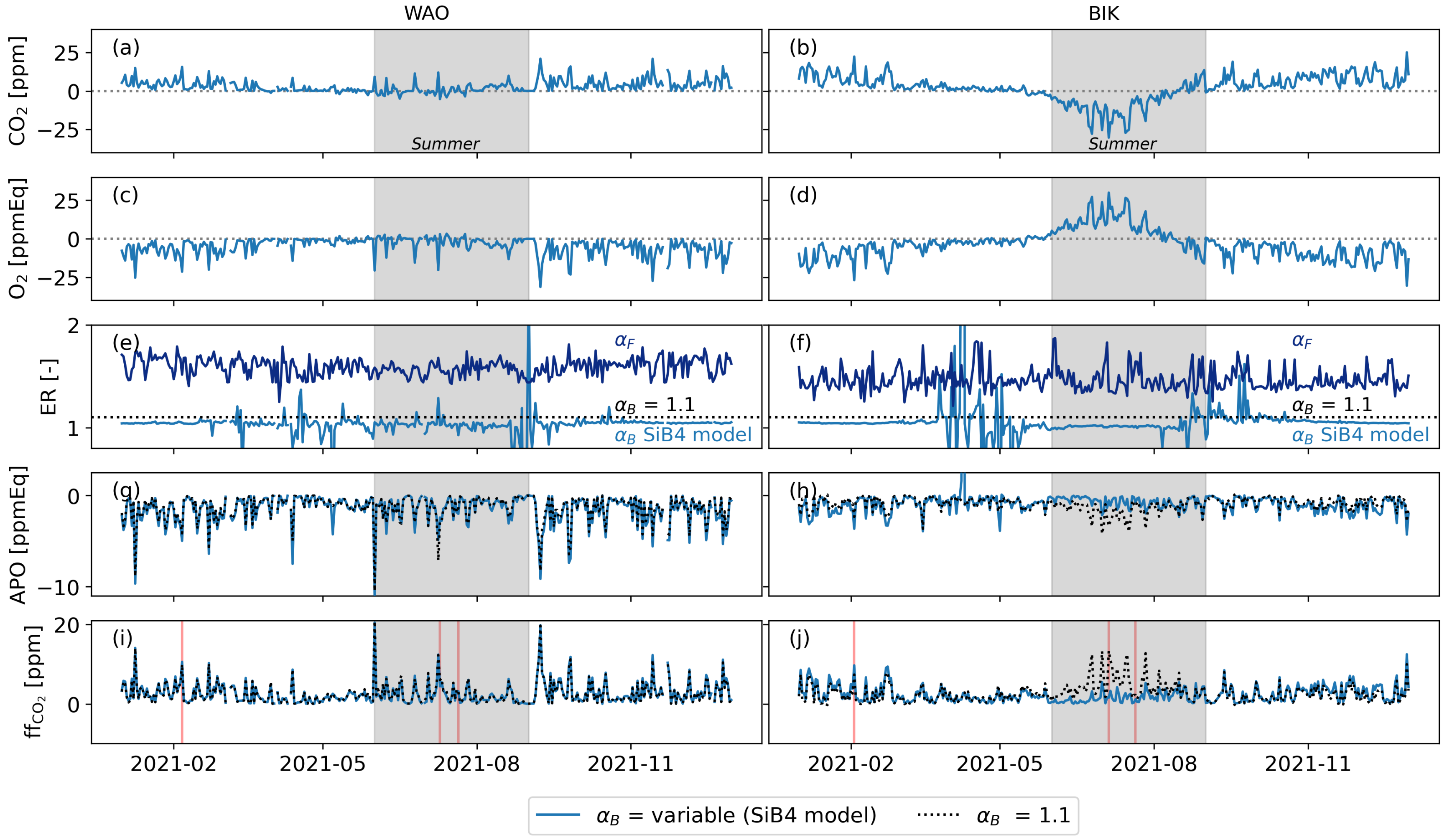

Figure 6.8: Time series of the transported surface fluxes by STILT for Weybourne, UK (left column, WAO) and Bialystok, Poland (right column, BIK) for CO_2 (a-b), O_2 (c-d), exchange ratios (ER, e-f), atmospheric potential oxygen (APO, g-h) and the fossil fuel signal of CO_2 (ff_{CO_2}, i-j). The grey shading indicates the summer period between 2021-06-01 and 2021-09-01. The red vertical lines indicate the three days chosen to evaluate the surface fluxes (Figure A6.2).

from transported fossil fuel fluxes ($\mathrm{ff_{CO_2}}$[true], not shown). The APO method worked in this regional case because the variability of both α_B and α_F were taken into account when calculating $\mathrm{APO_{wo}}$. For WAO, α_B fluctuates around 1.0 and for BIK α_B has a value around 1.0 during winter and below 1.0 in summer. WAO has a higher α_B compared to BIK because it is situated in an area with a higher contribution from crops and a lower contribution from heterotrophic respiration (Figure 6.6c). α_f also exhibits temporal variability but does not have a clear seasonal cycle at either WAO or BIK.

APO generally uses a constant value for α_B of 1.1 (or 1.05), which is valid only when the transported biosphere fluxes have an $\mathrm{ER_{net}}$ value of 1.1 (or 1.05). If we would have implemented O_2 into the SiB4 model with constant ER values of 1.1, the resulting transported α_B would also have been a constant value of 1.1 over space and time. In that case, using a constant α_B of 1.1 in Eq. 6.7 and 6.8 would again produce the same results with $\mathrm{ff_{CO_2}}$[APO] compared to the true transported fossil fuel fluxes ($\mathrm{ff_{CO_2}}$[true]). However, as we showed in Sect. 6.3.1, it is highly unlikely that the ER of the biosphere is constant. Therefore, we investigate the implications of assuming a constant α_B of 1.1 in reconstructing $\mathrm{ff_{CO_2}}$[APO], while the transported biosphere fluxes produce a variable α_B over time.

CO_2 fossil fuel signals derived using APO are overestimated when a constant α_B of 1.1 is applied instead of an α_B calculated from the variable transported biosphere fluxes from the SiB4 model. A constant α_B of 1.1 often is higher compared to the 'true' transported α_B (Figure 6.8e and 6.8f). This overestimation leads to too negative APO values (Eq. 6.6) and consequently, $\mathrm{ff_{CO_2}}$[APO] is also overestimated (Figure 6.8h). Overestimating α_B has more effect when the biosphere influence is higher (Figure A6.2). As a result, the difference between $\mathrm{ff_{CO_2}}[\mathrm{APO}_{(\alpha_B\,=\,1.1)}]$ and $\mathrm{ff_{CO_2}}$[true] signal is largest at BIK because BIK is located in a region with forests (Popa et al., 2010), whereas WAO is situated along the coast with less surrounding vegetation. Additionally, α_B at BIK is lower than at WAO, increasing the overestimation of α_B and increasing the bias at BIK.

APO-based fossil fuel CO_2 flux estimates are biased when using wrong values for α_B. The extent of this bias depends on the footprint that forms the atmospheric signal. To illustrate this, we selected three days for WAO and BIK based on the atmospheric difference between the atmospheric fossil fuel CO_2 signal calculated using a constant α_B of 1.1 ($\mathrm{ff_{CO_2}}[\mathrm{APO}_{(\alpha_B\,=\,1.1)}]$) and the true fossil fuel CO_2 signal ($\mathrm{ff_{CO_2}}$[true]) (Figure A6.2). The difference in fossil fuel CO_2 mole fraction is not directly proportional to the bias in surface CO_2 flux estimations (Figure 6.9), but also includes the footprint of the observation (see Equation 6.9). When the atmospheric fossil fuel CO_2 signal is formed by a footprint covering a region with relatively low fossil fuel emissions (Figure A6.3b and A6.3e) and strong biosphere influence (Figure A6.2), the relative difference between $\mathrm{ff_{CO_2}}$[true] to $\mathrm{ff_{CO_2}}[\mathrm{APO}_{(\alpha_B\,=\,1.1)}]$ increases. This leads to a corresponding increase in the estimated surface flux (Figures 6.9b and 6.9e). As a result, an overestimation of

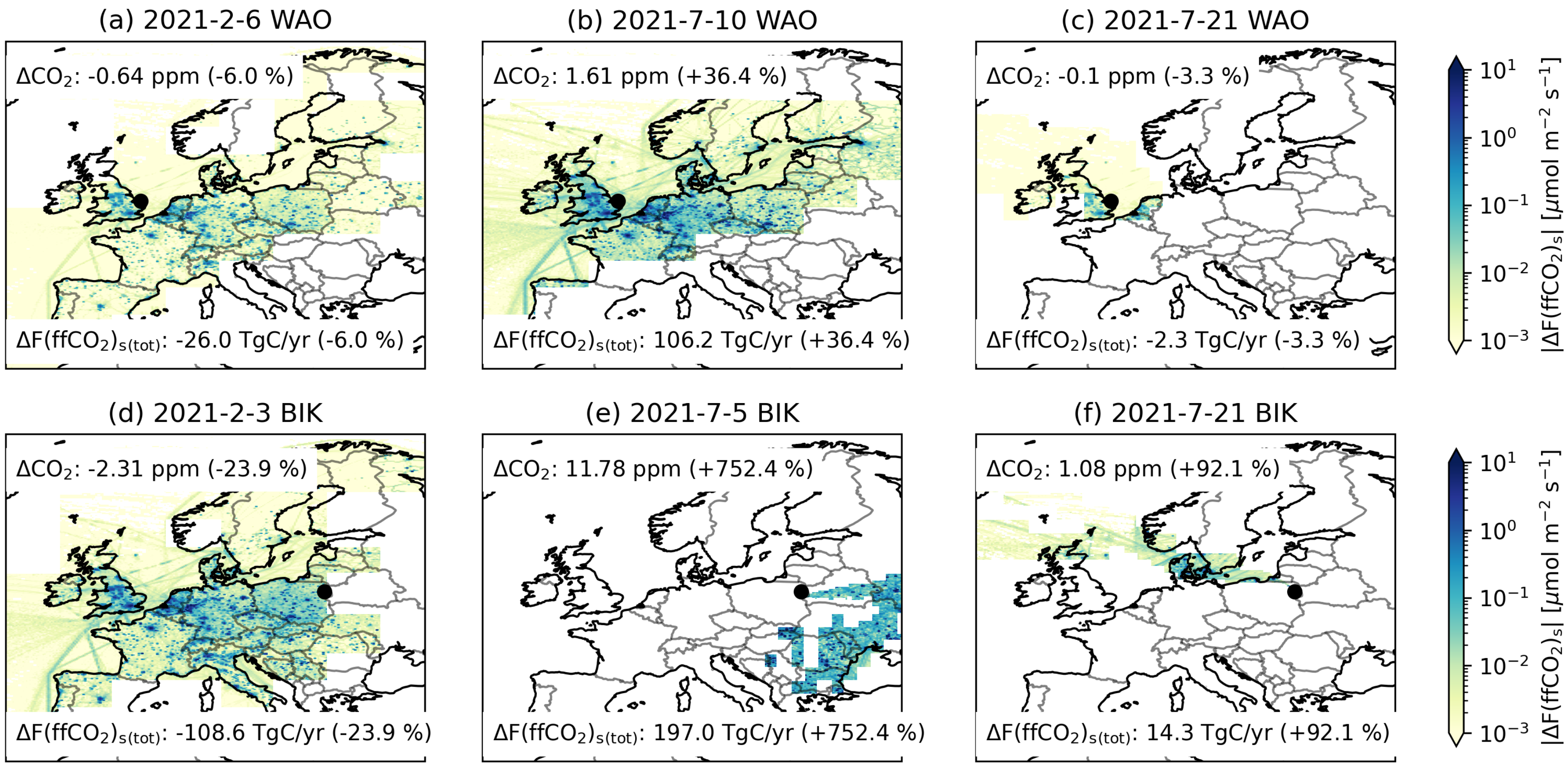

Figure 6.9: Difference between the fossil fuel CO_2 surface fluxes of the true input fluxes from GridFED ($F(ff_{CO_2})_s[true]$) and the surface fluxes based on the APO fossil fuel signal with an α_B of 1.1 ($F(ff_{CO_2})_s[APO_{(\alpha_B\,=\,1.1)}]$), calculated with Eq. 6.11, for three days at Weybourne (WAO, a-c) and three days at Bialystock (BIK, d-f) in units of μmol m^{-2} s^{-1}. Text labels: ΔCO_2 is the difference between the atmospheric signals of $ff_{CO_2}[APO_{(\alpha_B\,=\,1.1)}]$ and $ff_{CO_2}[true]$ (Figure A6.2), $\Delta F(ffCO2)_{s(tot)}$ is the integrated difference between the surface fluxes of $F(ff_{CO_2})_s[APO_{(\alpha_B\,=\,1.1)}]$ and $F(ff_{CO_2})_s[true]$ inside the footprint, scaled to an annual flux.

$\mathrm{ff}_{CO_2}[\mathrm{APO}_{(\alpha_B\,=\,1.1)}]$ by 1.6 ppm at WAO leads to an increase of 37% in fossil fuel surface fluxes, and an overestimation of 11.8 ppm at BIK results in a 754% increase. Conversely, when the footprint is dominated by regions with high fossil fuel emissions (Figure A6.3a and A6.3d), the relative difference in CO_2 mole fraction is smaller, reducing the bias in surface flux estimation (Figures 6.9a and 6.9d). Overall, when using an assumed α_B value of 1.1 instead of the 'true' α_B from SiB4 simulations, fossil fuel surface fluxes at BIK experience a greater bias compared to WAO. This is due to a stronger biospheric influence and lower fossil fuel contribution within the footprint at BIK.

It is important to note that while we directly link biases in atmospheric CO_2 signals to biases in surface flux estimations, additional uncertainties may also arise from the STILT transport model.

6.4 Discussion

We presented first insights into global biospheric O_2 fluxes and the variability of $\mathrm{ER_{net}}$ by incorporating distinct exchange ratios for assimilation and respiration processes into the SiB4 model. This implementation revealed that $\mathrm{ER_{net}}$ shows a pronounced temporal variability at both global and European scales, alongside distinct spatial variations during the summer months in Europe. The modeled temporal and spatial variability of $\mathrm{ER_{net}}$ could significantly impact the application of the O_2 partitioning method for estimating fossil fuel CO_2 signals using APO, especially in situations where the biosphere signals are large. In this section, we discuss the implementation of O_2 into the SiB4 model, explore how this approach can be validated and improved, and clarify the implications of our findings for other O_2 partitioning methods.

6.4.1 Evaluation of the O_2 implementation

The O_2 implementation into the SiB4 model should be validated with observations before using the resulting ER values. Several measurement locations are available that could provide above-vegetation O_2 observations to support validation of the SiB4 model. These locations include: the WLEF-TV tower in Park Falls, Wisconsin, USA (Stephens et al., 2007), the Takayama tower (TKY) in Japan (Ishidoya et al., 2013), the Zotino Tall Tower Observatory (ZOTTO) in Russia (Kozlova and Manning, 2009), the Bialystok tower in Poland (Popa et al., 2010), the Ochsenkopf tower in Germany (Thompson et al., 2009), the Reinshof site in Germany (Knohl et al., 2020) and the Hyytiälä tower in Finland (Faassen et al., 2023). Data from these measurement towers could be used to evaluate the seasonal and annual patterns of $\mathrm{ER_{net}}$ by calculating O_2 and CO_2 surface fluxes based on their vertical gradients (Ishidoya et al., 2015; Faassen et al., 2023). Similar to the approach described in Faassen et al. (2023), $\mathrm{ER_a}$ and $\mathrm{ER_r}$ could be estimated at these locations using the GPP and TER fluxes. However, some of the above mentioned stations miss the necessary meteorological data to directly infer the surface fluxes. Additionally, inferring

O_2 surface fluxes from a vertical gradient has shown to be challenging (Ishidoya et al., 2015; Faassen et al., 2023), making validation of the ER_{net} values based on observational data difficult.

A few additional improvements to the model implementation could help evaluate its accuracy without solely relying on observational data. The individual ER values in Table A6.1 are currently difficult to validate because of measurement challenges. However, theoretical approaches have demonstrated that O_2 uptake by the soil can be modeled independently from the CO_2 flux, using a vertical diffusion approach (Cook and Knight, 2003; Cook et al., 2013). Incorporating this modeling approach as a separate total O_2 soil flux into the SiB4 model and comparing it with the resulting O_2 soil fluxes derived from the current ER implementation could provide valuable insights. Discrepancies between these methods would serve as an initial indication of the model's capacity to reproduce O_2 soil fluxes accurately. Another method to support validation is the inclusion of stable isotope measurements, specifically $\delta^{13}C$ in CO_2. Studies have shown that $\delta^{13}C$ measurements can be used to explain ER measurements (Bowling et al., 2008; Hilman et al., 2019). For instance, when analyzing whether different substrates are being burned or formed, both $\delta^{13}C$ and ER_r or ER_a should have a similar change over time. By using the SiB4 implementation of $\delta^{13}C$ alongside O_2 (A. Kaushik, personal communication; Van der Velde et al., 2014), we could assess if ER and $\delta^{13}C$ behave similarly.

6.4.2 Additional measurements

More local biospheric measurements are essential to enhance our understanding of O_2 biosphere fluxes and to support our implementation of O_2 into the SiB4 model. Our findings highlight the priorities for such measurements. Existing measurement locations that have measured long-term atmospheric O_2 and CO_2 time series above the biosphere are limited, and are mainly located in temperate forest regions (as discussed above). Furthermore, our understanding of the different ER_a and ER_r signals from the biosphere remains limited due to measurement challenges. While it is impractical to measure every ER signal in detail for all plant functional types, our study offers valuable insights into prioritizing measurement efforts. Specifically, we have identified regions and ER signals that exert the most significant influence on the ER_{net} signal, guiding future research towards areas with the highest potential impact.

We found that especially more measurements are needed for crops and in the tropical region. Figure 6.7 demonstrates that crops significantly contribute to the spatial pattern of ER_{net} during the summer. This pattern arises from the assumption that ER_a and $ER_{r(auto)}$ values of crops are equal to their OR values (Gallagher et al., 2014). This assumption could be validated by measuring O_2 and CO_2 fluxes over a complete growing season of a specific crop and comparing it with the observed OR at the end of the growing season. If the net O_2 and CO_2 exchange aligns with the OR, then the assumption holds. Additionally, the tropical region requires more attention. Figure A6.1 reveals no clear seasonal pattern for this region, with extreme ER values fluctuating above 1.3 and below 0.7 throughout the year. The tropical ER signals might be influenced by factors other than seasonal changes of temperature (summer vs winter), such as El Niño events (Schaik et al., 2018), dry and wet periods (Restrepo-Coupe et al., 2013; Baldocchi et al., 2018) or biological changes (Wu et al., 2017). Given the high gross fluxes in the tropics compared to other regions (Luyssaert et al., 2007; Baldocchi et al., 2018), their impact on biospheric ER_{net} values is potentially substantial. However, the absence of long-term O_2 above canopy gradient measurements from tropical regions, and lack of CO_2 measurements as well, makes detailed analysis and model validation difficult.

When measuring ER values of an ecosystem, it is crucial to ensure that the correct measurements are taken by focusing on both the net exchange at the canopy level and the individual ER_a and ER_r values from for leafs, stems and roots and heterotrophic respiration. To accurately calculate ER_{net} signals for the biosphere, measurements at a minimum of two heights and additional meteorological variables such as the sensible heat flux are required to infer the net O_2 and CO_2 exchange (Faassen et al., 2023), in absence of direct O_2 flux measurement methods. Relying on a single-height measurements could lead to incorrect ER_{net} values Faassen et al. (2024b). Additionally, individual ER_a and ER_r signals must also be measured to fully understand the ER_{net} signal. Particular emphasis should be placed on measuring ER signals from stems and roots, as there is currently no consensus on the processes shaping these signals. For the SiB4 implementation, we based stem and root ER signals on theoretical assumptions, with a constant value of 1.0. However, if the ER values of stems and roots deviate from this assumption, as some measurements suggest (Shane et al., 2004; Bathellier et al., 2009; Hilman et al., 2019; Hilman et al., 2022), differences in spatial patterns would arise.

6.4.3 Consequences for O_2 partitioning methods

Our first calculations of biosphere O_2 and CO_2 fluxes derived with SiB4 cannot yet replace the use of a constant value used for α_B in global-scale O_2 partitioning methods. When we average the global O_2 and CO_2 fluxes over 2021 (Figure 6.4), we found that the resulting ER_{net} value was approximately 0.4. Global-scale O_2 partitioning methods, which operate on decadal timescales, assume that ER_a and ER_r are equal and that OR values provide a reasonable proxy for the global ER_{net} value, resulting in the choice to use a constant value of around 1.1 for α_B based on OR measurements (Keeling, 1988; Severinghaus, 1995; Stephens et al., 1998; Worrall et al., 2013). With our current O_2 implementation in the SiB4 model, we cannot assess whether ER_a approaches ER_r over longer timescales, as we did not implement dynamical changes over time in the individual ER signals that show evolution over time associated with development of the vegetation and soil pools. With our current implementation, the global ER_{net} value consistently remains lower than ER_a, yielding α_B values below 1.0, even over decadal timescales. This outcome may not reflect reality, as it is often hypothesized that $\mathrm{ER_{net}}$ should converge to the OR when considering the complete development of a vegetation type.

To re-evaluate the accuracy of the value of 1.1 for α_B, used on decadal timescales globally, temporal changes in $\mathrm{ER_a}$ and $\mathrm{ER_r}$ values associated with the current growth stage of the vegetation and carbon pools needs to be incorporated into the SiB4 model. This would require a more detailed implementation of vegetation development and of the corresponding molecular carbon (C), hydrogen (H), nitrogen (N) and oxygen (O) composition of the pools. Currently, the spin-up of the model ensures that the forest types and soil pools are in a steady state and further increases of the pools occur only due to environmental changes such as increases in temperature or atmospheric CO_2 mole fraction (Haynes et al., 2019). For grass and crop types, a complete growing cycle is already included (Haynes et al., 2019). If the complete development from seedling to fully grown vegetation were implemented for all vegetation types, such as is done in Dynamic Global Vegetation Models (DGVMs) (Sitch et al., 2024), ER values could vary between different stages of the development of the vegetation. Another method would be model the molecular composition (C:H:N:O) of the carbon pool over time, which is now only done for carbon in the SiB4 model. This would make it possible to link the ER flux directly to the OR. Both implementations would allow for a more accurate representation of temporal changes in $\mathrm{ER_a}$ and $\mathrm{ER_r}$, caused by an ecosystem with changing carbon pool compositions. This could lead to a more reliable estimate of a single global $\mathrm{ER_{net}}$ value and provide insight into the appropriate value for α_B.

For O_2 partitioning methods applied to smaller timescales or regional estimates of carbon budgets, it is essential to account for the variability of $\mathrm{ER_{net}}$ (or α_B). At the Weybourne site, the impact of incorporating a variable $\mathrm{ER_{net}}$ was less pronounced compared to Bialystok, since there is less local vegetation activity. Other locations might experience a greater impact from using a variable $\mathrm{ER_{net}}$ due to higher biosphere contributions or reduced crop influence. It is important to note that this analysis does not account for non-local biospheric signals originating from outside Europe (Figure 6.3). Consequently, not all biospheric influence is taken into account. However, we assume that any discrepancies introduced by using an incorrect α_B for the non-local biosphere signal would be mitigated when subtracting the background, as outlined in the method by Pickers et al. (2022). Additionally, when using APO to determine fossil fuel CO_2 emissions on a regional scale, as demonstrated by Rödenbeck et al. (2023), it is essential to recognize that $\mathrm{ER_{net}}$ is likely lower than $\mathrm{ER_a}$. This results in α_B deviating from the assumed value of 1.1 to approximately 1.0 or even lower. Rödenbeck et al. (2023) highlighted that such a change in α_B substantially increases the uncertainty of APO signals on a seasonal scale to almost the magnitude of the signal itself.

When O_2 partitioning methods are applied to smaller timescales, we recommend to use a biosphere model that is able to model net O_2 and CO_2 net surface fluxes of the biosphere based on separate ER_a and ER_r implementation, to account for the α_B variability, such as our approach shown here. By using the SiB4 O_2 and CO_2 biosphere surface fluxes, the variability of α_B can be taken into account and the APO method for estimating fossil fuel CO_2 signals could achieve better accuracy and reliability. Additionally, we advise to use the APO method at locations with relatively low influence from the biosphere to reduce the bias in CO_2 fossil fuel signal estimates.

6.5 Conclusions

By incorporating O_2 into the simple biosphere model (SiB4), we demonstrated that the net O_2 to CO_2 exchange ratio (ER_{net}) of the biosphere is not a constant value but is characterized by temporal and spatial variability. The temporal variability arises from differences in the ratio between gross primary productivity (GPP) and total ecosystem respiration (TER), leading to a distinct seasonal pattern. We find large differences between regions, corresponding to differences in plant functional types between e.g the tropics and the boreal regions. Although our O_2 implementation in SiB4 was based on theoretical assumptions and limited available measurements of the oxidative ratios, we argue that the found temporal and spatial variability in ER_{net} is realistic, as the SiB4 model generates accurate GPP and TER fluxes and uses a credible spatial distribution of plant functional types.

Atmospheric potential oxygen (APO) based calculations of fossil fuel CO_2 can lead to overestimated atmospheric fossil fuel CO_2 signals and emissions, when variability in ER_{net} in regional partitioning methods is not accounted for. The overestimation is highest when the influence from the biosphere is high and when the true ER_{net} value deviates further from the constant 1.1 value. Additionally, the relative bias in the fossil fuel emissions increases when the footprint of the signal includes less fossil fuel fluxes. For future applications of O_2 partitioning methods, our O_2 implementation in SiB4 could provide a first estimate to use as a variable ER_{net}.

Due to the lack of temporal changes in the ER_a and ER_r values in our model implementation, associated with carbon pool growth, it is not possible to link the ER_{net} from SiB4 to global O_2 partitioning methods. In global scale partitioning methods that are applied on decadal time periods, it is assumed that ER_a and ER_r have the same value resulting in a constant ER_{net}. We could not validate this assumption with the current set-up of the model because the implemented ER_a and ER_r values stay constant over time. Consequently, we cannot address the potential temporal variability of the 1.1 value linked to the global scale and decadal time scales. Further improvement of the SiB4 implementation is needed to evaluate the 1.1 value, and this improvement should be rooted in expanded high-precision multi-level observations of O_2 and CO_2, as demonstrated and discussed throughout the chapters of this thesis.

6.6 Appendix

A6.1 Figures

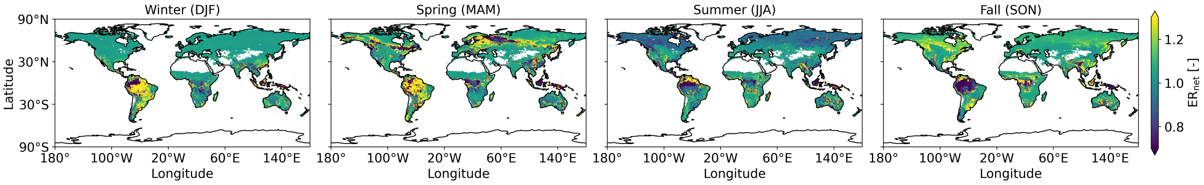

Figure A6.1: Averaged values of the SiB4 model results during the seasons: winter (December - February, DJF), spring (March - May, MAM), summer (June - August, JJA) and fall (September - November, SON) for the net exchange ratio (ER$_{net}$).

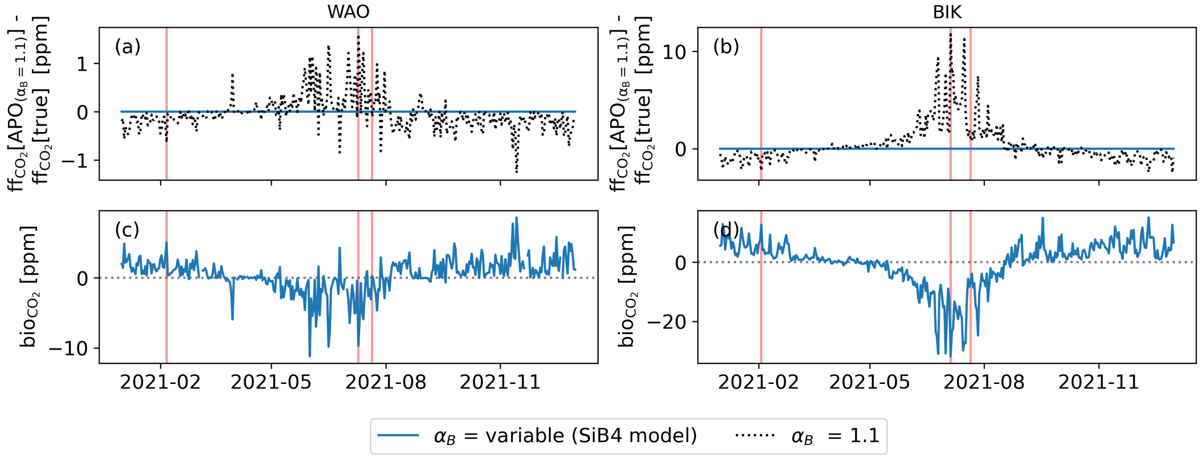

Figure A6.2: Timeseries of the transported surface fluxes by STILT and the resulting difference between the fossil fuel signal estimated with atmospheric potential oxygen (ff$_{CO_2}$[APO$_{(\alpha_B = 1.1)}$]) and the true fossil fuel signal (ff$_{CO_2}$[true]) (a,b), together with the biosphere signals (c,d) for the stations Weybourne (WAO, a, c) and Bialystok (BIK, b, d)

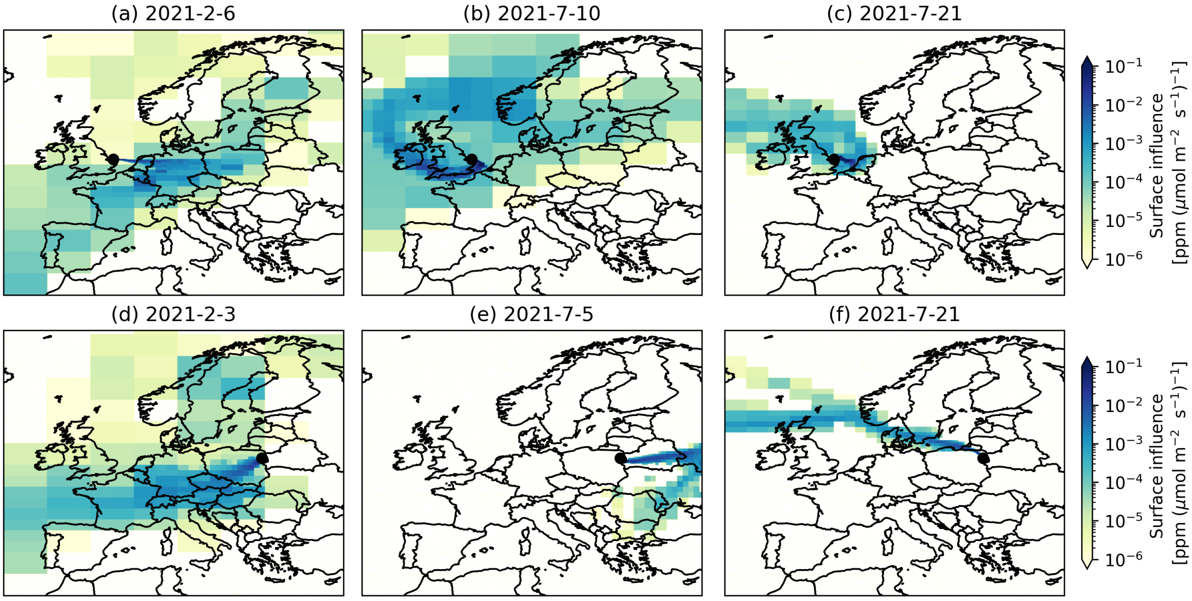

Figure A6.3: The footprint influence for three individual days at Weybourne (a-d) and Bialystok (d-f).

Chapter 7

Synthesis

7.1 Introduction

Throughout this thesis, we improved the understanding of the Exchange Ratio (ER) of the biosphere by integrating observations with models across various ecosystems and spatial scales. In **Chapter 3**, we used our observations in a boreal forest in Finland to calculate: the ER value based on inferred O_2 and CO_2 fluxes from their vertical gradient (ER_{net}), the ER value of assimilation (ER_a) and the ER value of respiration (ER_r). We demonstrated that our obtained ER signals allow to partition net ecosystem exchange (NEE) measurements into gross primary productivity (GPP) and total ecosystem respiration (TER).

In **Chapter 4**, we reproduced the diurnal pattern of atmospheric O_2 and CO_2 measurements from Finland using an atmospheric one-box mixed-layer model with a coupled surface scheme, and showed that it is not straightforward to link the ER value based on a mole fractions at a single measurement height (ER_{atmos}) to the ER that represents the net surface exchange (ER_{net}) because ER_{atmos} is influenced by additional atmospheric processes.

Chapter 5 expanded the focus to other ecosystems: by combining observations from our field campaigns in temperate and tropical forests with the atmospheric mixed-layer model, we showed the importance of accounting for atmospheric processes when analyzing the diurnal cycles of CO_2, O_2 and $\delta^{13}CO_2$. We quantified the importance of atmospheric processes compared to surface processes and showed, similar to Chapter 4, that single height mole fraction measurements cannot be linked directly to surface processes, and that fluxes should be used instead.

In **Chapter 6**, we scaled up both temporally and spatially by implementing O_2 into a global biosphere model, using specific ER_a and ER_r values for individual carbon pools and plant functional types. We demonstrated that the ER of the biosphere (ER_{net}) exhibits significant variability over time and space, and that this variability strongly impacts O_2-based fossil fuel CO_2 estimates in regions with large biosphere contributions to the observed CO_2 and O_2 mole fractions.

In this synthesis chapter we integrate the findings from the four preceding chapters by comparing their methods and conclusions. By combining these chapters we identify the remaining significant knowledge gaps and propose future research directions for the ER of the biosphere. The synthesis is structured around four themes:

1. Variability of ER_a and ER_r
2. Linking temporal and spatial scales, focusing on:
    (a) stomata-atmosphere exchange
    (b) upscaling from soil and leaf to the atmosphere

   (c) connecting $\mathrm{ER_a}$ and $\mathrm{ER_r}$ values based on flux measurements to the oxidative ratio (OR) values based on molecular composition of organic materials
   (d) the link between $\mathrm{ER_{net}}$ and $\mathrm{ER_{atmos}}$
3. The role of biospheric O_2 in the global carbon budget, focusing on:
   (a) the level of detail needed for biosphere variability in O_2 partitioning methods
   (b) using O_2 in atmospheric inversions
   (c) fires and land-use change
4. Recommendations for future measurement strategies

Within each theme, we first synthesize the chapters and then provide recommendations for future research.

7.2 Variability of $\mathrm{ER_a}$ and $\mathrm{ER_r}$

Accurate accounting for the temporal and spatial variability of $\mathrm{ER_a}$ and $\mathrm{ER_r}$ is important for both measurement and modeling studies. These exchange ratios determine the overall ER signal of NEE, referred to in this thesis as $\mathrm{ER_{forest}}$ or $\mathrm{ER_{net}}$:

$$-ER_{net} \cdot NEE = ER_a \cdot GPP - ER_r \cdot TER \tag{7.1}$$

A comprehensive understanding of $\mathrm{ER_{net}}$ is essential for different partitioning methods, such as separating NEE into GPP and TER (Chapter 3) or isolating the fossil fuel signal from atmospheric measurements (Chapter 6). Consequently, it is important to understand the processes that form $\mathrm{ER_{net}}$.

As we discussed in this thesis, there is relatively little information available on the spatiotemporal variability of the exchange ratios of assimilation ($\mathrm{ER_a}$) and respiration ($\mathrm{ER_r}$). We therefore assumed in all chapters that $\mathrm{ER_a}$ and $\mathrm{ER_r}$ are constant over time. In summary, the assumptions we made in the chapters are:

- Chapter 3: we assumed that the $\mathrm{ER_r}$ and $\mathrm{ER_a}$ that we obtained from the inferred O_2 and CO_2 fluxes from our measurements of vertical gradients above the canopy remained constant throughout the day, and applied them in the partitioning method to estimate GPP and TER fluxes. Nighttime O_2 and CO_2 fluxes supported the assumption that $\mathrm{ER_r}$ is constant during the night. However, the inferred fluxes could not confirm whether $\mathrm{ER_r}$ and $\mathrm{ER_a}$ remain constant during daytime.
- Chapters 4 and 5: We used temporally constant $\mathrm{ER_r}$ and $\mathrm{ER_a}$ values to incorporate O_2 into the CLASS model to generate daytime O_2 surface fluxes. We multiplied the observed $\mathrm{ER_a}$ and $\mathrm{ER_r}$ values from Chapter 3 with model-generated GPP and TER fluxes to calculate the O_2 fluxes.

- Chapter 6: here we similarly implemented $\mathrm{ER_a}$ and $\mathrm{ER_r}$ to simulate O_2 fluxes with the SiB4 model. However, in this case, we introduced additional spatial variability by assigning different $\mathrm{ER_a}$ and $\mathrm{ER_r}$ values to different plant functional types. This approach made a distinction between ER values for autotrophic and heterotrophic respiration and between crops and non-crops. The gross fluxes at a given location were calculated as a weighted average of the different plant functional type fluxes present in the grid box, creating indirect temporal variability when different plant functional types dominate. This implementation was not possible in Chapters 4 and 5 because the CLASS model uses one plant function type per location and does not differentiate between autotrophic and heterotrophic respiration.

Expanding our knowledge on the variability of $\mathrm{ER_a}$ and $\mathrm{ER_r}$ remains challenging due to a lack of measurements. The limited data available indicate that both $\mathrm{ER_a}$ and $\mathrm{ER_r}$ exhibit variability across time and space (e.g. Cousins and Bloom, 2004; Randerson et al., 2006; Hicks Pries et al., 2020; Hilman et al., 2022). However, a comprehensive explanation of the factors driving this variability has yet to be established. Addressing these gaps through further investigation is essential to enhance the accuracy of both measurement-based and model-based approaches. In the next sections, we discuss how to address these for both $\mathrm{ER_a}$ and $\mathrm{ER_r}$.

7.2.1 The exchange ratio of assimilation ($\mathrm{ER_a}$)

The exchange ratio of assimilation ($\mathrm{ER_a}$) can be determined through laboratory measurements or using *in situ* branch bag experiments. To date, *in situ* branch bag measurements have been conducted at only a limited number of sites, providing a single $\mathrm{ER_a}$ value for the duration of the measurements (Seibt et al., 2004; Ishidoya et al., 2013). At these sites (N=2), $\mathrm{ER_a}$ values ranged from 1.02 ± 0.03 to 1.19 ± 0.12, indicating variability between different ecosystems (deciduous broad leaf and coniferous evergreen forest respectively). However, a single $\mathrm{ER_a}$ value does not provide insights into whether or how $\mathrm{ER_a}$ varies over time. To address this, long-term observations are needed to capture $\mathrm{ER_a}$ variability between seasons or under different environmental conditions, such as during periods of drought or heat waves.

Measuring $\mathrm{ER_a}$ variability using branch bags presents several challenges. Extreme environmental conditions, such as high temperatures and high vapor pressure deficit, can occur rapidly, making it difficult to control the measurement conditions and establish clear relationships between these conditions and $\mathrm{ER_a}$. Furthermore, branch bag measurements include both leaf respiration and assimilation processes, which complicates isolating $\mathrm{ER_a}$ needed to link this value to GPP (Ishidoya et al., 2015). To estimate the contribution of leaf respiration, nighttime measurements could provide insights into the $\mathrm{ER_r}$ signal of leaf respiration. However, low respiration fluxes during the night complicate accurate measurements of the $\mathrm{ER_r}$ signal (Seibt et al., 2004).

Laboratory measurements provide a controlled environment that can help mitigate some of the challenges associated with branch bag measurements. A few studies have examined ER_a signals in plant chambers and found relationships between ER_a and factors such as nitrogen sources (Bloom, 2015) or light intensity (Cousins and Bloom, 2004; Fischer et al., 2015). However, very few studies evaluated the relationship between ER_a and environmental variables such as temperature or humidity. Only Fischer et al. (2015) did a first study to evaluate the effect of drought on ER_a and found no significant impact.

Preliminary results from leaf-chamber experiments in our group at Wageningen University show that it is possible to measure O_2 and CO_2 exchange on the leaf level, and derive light-response curves. Figure 7.1 shows preliminary results from measurements of O_2 and CO_2 exchange for varying light levels, for 9 sun flowers grown under controlled conditions (Hulsman et al., in prep.). The resulting ER values are relatively constant for the different light-levels, but the exact values are still preliminary due to pending calibration of the measurements.

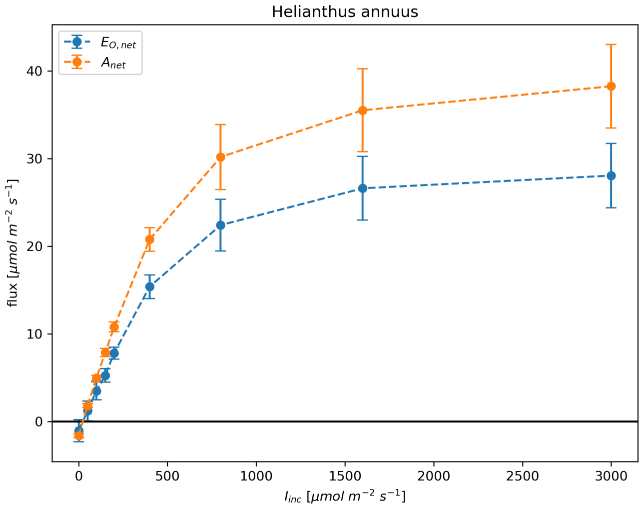

Figure 7.1: Light response curves for net carbon assimilation (A_{net}) and oxygen evolution ($E_{O,net}$) for a set of 9 sun flowers (*Helianthus annuus*). The net flux is given in µmol m^{-2} s^{-1} for different light levels (I_{inc}). Negative values indicate net consumption of O_2 and net respiration of CO_2 and positive values indicate net evolution (release) of O_2 and assimilation of CO_2. Figure from Hulsman et al. (in prep.).

Additional whole plant and leaf level chamber measurements are needed. Compared to branch bag measurements, chamber experiments allow for gradual and controlled changes in environmental conditions (e.g. temperature, vapor pressure deficit), making it easier to establish relationships between ER_a and external factors compared to field measurements. Improving our understanding of ER_a variability would improve O_2 partitioning methods, by allowing ER_a variability to be calculated using relationships to meteorological variables.

Also, model studies benefit from a deeper understanding of ER_a, by allowing ER_a to be implemented with greater detail. Ultimately, laboratory measurements should be compared with branch bag measurements to ensure that results obtained under controlled conditions are consistent with real-world behavior, and additionally they can inform on how to upscale ER_a from leaf measurements to plant level and canopy level (see also Sect. 7.3.2).

Finally, other tracers should be measured alongside O_2 and CO_2 exchange, to enhance our understanding of ER_a. A key challenge with laboratory chamber measurements is that they inherently include contributions of respiration processes in the calculation of ER_a. Combining O_2 measurements with that of other tracers such as $\delta^{13}CO_2$ could help. $\delta^{13}CO_2$ allows to separately estimate dark and photo-respiration, since these processes have different $\delta^{13}CO_2$ signatures (Ghashghaie et al., 2003; Igamberdiev et al., 2004; Lanigan et al., 2008). These differences could help disentangle respiration fluxes from assimilation fluxes (Wehr and Saleska, 2015; Wehr et al., 2016) and to subsequently establish the correct value for ER_a for the GPP flux.

7.2.2 The exchange ratio of respiration (ER_r)

The exchange ratio of respiration (ER_r) is more challenging to determine than ER_a, as it encompasses a greater variety of processes, each with distinct ER values. ER_r at canopy level includes both autotrophic and heterotrophic respiration, which can be further subdivided into specific components. At ecosystem level, autotrophic respiration consists of processes such as stem and root respiration, while heterotrophic respiration involves various soil organic matter pools. To fully understand the spatial and temporal variability of ER_r, these individual components should be analyzed independently. Such a comprehensive approach is necessary to capture the complexity of ER_r dynamics and to improve its representation in both measurement-based and model-based studies.

ER_r values for individual respiration processes can be determined using laboratory measurements or *in situ* measurements such as using soil and stem chambers. Similar to ER_a, laboratory measurements should be employed to further investigate the signals of ER_r originating from roots and leaves under different environmental conditions (Shane et al., 2004; Bloom, 2015; Fischer et al., 2015; Hicks Pries et al., 2020). However, measuring stem and heterotrophic respiration in laboratory settings is challenging, making *in situ* chamber measurements the primary approach for these components (Angert et al., 2015; Hilman et al., 2019; Hicks Pries et al., 2020; Hilman et al., 2022). As with ER_a, environmental conditions for *in situ* chamber measurements are difficult to control, making it challenging to obtain detailed information about ER_r for a range of environmental conditions. Furthermore, soil respiration depends on soil types, which have high spatial variability as respiration rates vary significantly within 1 to 10 m due to changes in soil composition (Rayment and Jarvis, 2000; Yim et al., 2003; Martin and Bolstad, 2009). Additionally, different soil organic matter pools have their own ER_r, complicating measurements and interpretation (Randerson et al., 2006; Hilman et al., 2022).

In addition to measuring ER_r itself, other methods can be used to improve our understanding of ER_r, such as combining O_2 with $\delta^{13}CO_2$ measurements and combining models with measurements. Several studies have demonstrated that O_2 can be modeled independently from CO_2 for soil processes (Cook and Knight, 2003; Cook et al., 2013), making it possible to model O_2 exchange without relying on ER measurements. They could provide valuable insights into spatial patterns of ER_r and improve the implementation of ER_r in biosphere models. Moreover, studies have shown that $\delta^{13}CO_2$ measurements are particularly useful to interpret ER_r measurements, because $\delta^{13}CO_2$ measurements help to verify which compounds are being respired (Bowling et al., 2008; Hilman et al., 2019). By combining multiple carbon cycle tracers, such as $\delta^{13}CO_2$ and O_2, we can significantly enhance our ability to disentangle the underlying processes and refine both models and measurements of the carbon cycle.

7.2.3 ER_a and ER_r in different ecosystems

With only a limited number of O_2 ecosystem measurements available, it is crucial to carefully select future measurement locations based on vegetation type, soil type and their relevance to key atmospheric and climate processes. Throughout this thesis we presented measurements from different ecosystems: Chapters 3 and 4 focused on a boreal forest, Chapter 5 on both a temperate and a tropical forest and in Chapter 6 we incorporated 15 plant function types in the SiB4 model. However, most existing studies that have measured O_2 above vegetation have focused on temperate forests in the Northern Hemisphere (Figure 1.6). There are therefore significant gaps in our understanding of ER signals for ecosystems that are less observed and are critical for atmospheric processes or are expected to experience substantial changes due to climate change, such as tropical and boreal forests. Long-term measurements in such ecosystems are therefore crucial to capture different environment conditions.

Lacking observations from certain ecosystems make it challenging to interpret atmospheric ER signals. Especially understanding the environmental response of both ER_r and ER_a and their variations from one ecosystem to another is essential to apply the O_2 partitioning method at various measurement sites without relying on difficult to obtain *in situ* ER_a and ER_r measurements. Additionally, to incorporate O_2 dynamics into biospheric models effectively, it is crucial to account for ecosystem-specific differences, as these models are often plant-type specific (Fisher et al., 2014). Chapter 6 demonstrated that ER_{net} was strongly influenced by the relative contribution of heterotrophic respiration compared to autotrophic respiration and crops compared to non-crops.

We recommend that future measurements focus on ecosystems with the potential for the largest variations in ER signals due to their gross fluxes (GPP and TER). This includes tropical forests, boreal forests, crops and the distinction between C3 and C4 plants. Tropical forests, with their high gross fluxes (Luyssaert et al., 2007; Baldocchi et al., 2018), likely have a significant influence on the temporal evolution of $\mathrm{ER_r}$, $\mathrm{ER_a}$ and $\mathrm{ER_{net}}$. Boreal forests are susceptible to changes in gross fluxes due to the ongoing effects of climate change, as the temperatures in these regions are increasing most rapidly (Price et al., 2013; Gauthier et al., 2015). Crops, with their relatively short growing seasons, may have a substantial influence on ER signals, as highlighted in Chapter 6. Lastly, no research so far has explored whether ER signals differ between C3 and C4 plants. Given that their photosynthesis pathways are different and therefore other processes govern the O_2 and CO_2 exchange, it is likely that differences also exist for their ER signals.

7.3 Crossing temporal and spatial scales

Throughout this thesis, we bridge several spatial and temporal scales. Chapter 3 focuses on above-canopy measurements on a single day for one ecosystem. The $\mathrm{ER_a}$ and $\mathrm{ER_r}$ values derived from these measurements where then used in Chapter 4 and 5 to model daytime O_2 fluxes from vegetation and soils. In Chapter 6, the analysis expands from small spatial and temporal scales to the global scale over the course of an entire year. Bridging these different scales comes with several challenges. In this section, we address four of these challenges that emphasize the importance of correctly bridging spatial and temporal scales. We start at a scale not yet addressed in this thesis, but relevant to ecosystem exchange of O_2 and CO_2 on the smallest scale: stomata-atmosphere exchange. Secondly, we discuss upscaling from the leaf and soil to the canopy scale within an ecosystem. Third, we discuss the connection between the oxidative ratio (OR) of organic material with the directly measured exchange ratios (ER), which is relevant to connect the different temporal scales that they each represent. Finally, we discuss the concept of the ER derived from atmosphere mole fractions ($\mathrm{ER_{atmos}}$), and put these into perspective against the ER of surface exchange ($\mathrm{ER_{net}}$ or $\mathrm{ER_{forest}}$).

7.3.1 O_2 on the smallest spatial scale: stomata-atmosphere

Throughout this thesis, we assumed that turbulent diffusion is the main mechanism that transports O_2 between a leaf and the atmosphere. However, two additional transport mechanisms become significant when looking at the leaf or stomatal exchange: molecular diffusion and the Stefan flow (also sometimes referred to as mass flow). Turbulent diffusion is driven by eddies caused by gradients in temperature and moisture (turbulent convection) or in velocity (mechanical turbulence). As discussed in Chapter 3, turbulent diffusion of trace gases can be described using the K-theory (Stull, 1988). Molecular diffusion is driven by the concentration gradient of a trace gas and can be described by Fick's law (Bird et al., 1960):

$$F_M = -D(\frac{\delta\phi}{\delta x}) \tag{7.2}$$

where ϕ is the mole fraction of the transported trace gas, D is the diffusion coefficient and $(\delta\phi/\delta x)$ is the concentration gradient of the trace gas over distance x. The third transport mechanism is caused by movement of other species influencing each other (e.g. Jarman, 1974) and we refer to this as Stefan flow. In context of stomata-atmosphere exchange of O_2 and CO_2, the large water vapor flux plays a dominant role in forming the Stefan flow in a stagnant atmosphere. As water vapor exits the stomata, it drags along other compounds, transporting them in the same direction. This makes water vapor the main driver of the Stefan flow. In other words, the velocity of the multi-species system (u) is dominated by the velocity of water (u_w), yielding transport from the stomata to the atmosphere and can be described as:

$$F_S = \phi \cdot u_w \tag{7.3}$$

The Stefan flow (F_S) and molecular diffusion (F_M) together form the net exchange between stomata and atmosphere:

$$F_{net(stomata)} = F_M + F_S = -D(\frac{\delta\phi}{\delta x}) + \phi \cdot u_w \tag{7.4}$$

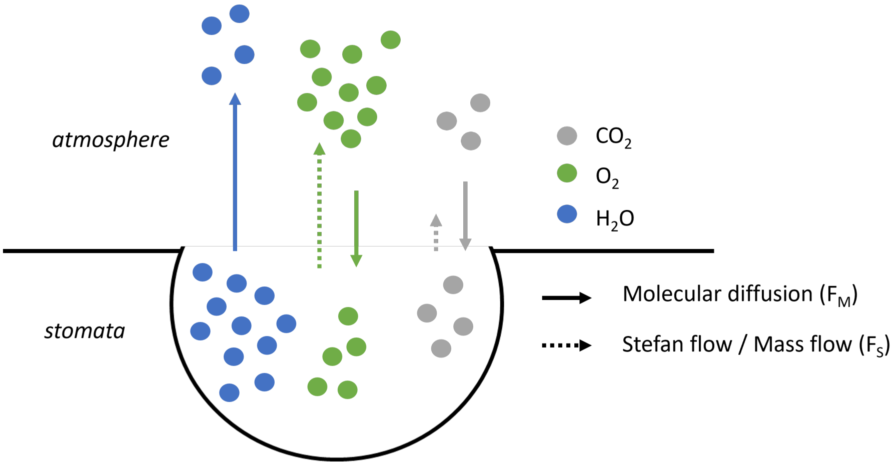

Figure 7.2: Schematic overview of the direction and size of the molecular diffusion (F_M) and Stefan flow (F_S) fluxes between a stomata and the atmosphere for CO_2, O_2 and H_2O.

On canopy scale, turbulent transport is the dominant mechanism over molecular diffusion and Stefan flow. It has been argued that turbulent flux calculations should account for Stefan flow, particularly for O_2 exchange (Kowalski, 2017; Kowalski et al., 2021). The reasoning is that the high water vapor flux between the canopy and the atmosphere could influence the exchange of other compounds. For O_2 this effect would be enormous because of its high mole fraction (Eq. 7.3). However, we disagree with the statements by Kowalski (2017) and Kowalski et al. (2021), and argue that this assumption does not hold at canopy level. We base our arguments on Reynolds number calculations and *in situ* measurements. It is well established that a high Reynolds number in the boundary layer indicates that turbulent diffusion is the dominant transport mechanism over molecular diffusion (Reynolds, 1894; Stull, 1988). Since Stefan flow arises from molecular diffusion of water vapor in a stagnant atmosphere, it is similarly negligible under conditions where turbulence dominates. Additionally, Lobos-Roco et al. (2021) demonstrated through *in situ* eddy covariance (EC) measurements at 1 meter above a saline lake, that exchange between the surface and the atmosphere was only detectable in the presence of wind. In stable conditions, there was no detectable flux of water vapor at 1 meter. This finding highlights that turbulence is the primary driver of transport, and without it, neither molecular diffusion nor Stefan flow generates sufficient flux to be measurable in the atmosphere.

On stomata scale, Stefan flow could become highly dominant for O_2 due to the absence of turbulence (a stagnant atmosphere). For CO_2 stomata-atmosphere exchange calculations, Stefan flow is already accounted for through the use of the so-called ternary correction, which includes both Stefan flow and molecular diffusion as an important transport mechanism for CO_2 (Jarman, 1974; Von Caemmerer and Farquhar, 1981b; Farquhar and Cernusak, 2012). To our knowledge, the ternary correction has not yet been applied for O_2. Given the high mole fraction of O_2 in the atmosphere ($\approx$ 209,392 ppm), Stefan flow for O_2 could generate substantial fluxes, effectively transporting O_2 out of the stomata (Figure 7.2, Eq. 7.3). The magnitude of this effect for O_2 would be approximately 500 times larger than for CO_2, based on the ratio of their mole fractions (209,392/420 $\approx$ 500). In contrast, net O_2 and CO_2 exchange measurements typically yield fluxes of similar magnitude at both leaf and canopy level (Cousins and Bloom, 2004; Bloom, 2015; Ishidoya et al., 2015). To yield an O_2 flux of similar magnitude as for CO_2, O_2 molecular diffusion must act counterintuitively because Stefan flow pushes O_2 out of the stomata, leading to a higher O_2 mole fraction in the atmosphere compared to the stomata. This would result in molecular diffusion of O_2 from the atmosphere into the stomata against its gradient, moving O_2 'uphill' (Figure 7.2, Eq. 7.4). This suggests that the mechanisms driving stomata-atmosphere exchange for O_2 and CO_2 are fundamentally different.

The importance of Stefan flow in O_2 stomata-atmosphere exchange needs further investigation. The potential decoupling of O_2 and CO_2 at stomatal level could have significant implications for interpretation of biospheric ER measurements, as biological processes might no longer be directly linked to ER_a values. To better understand this phenomenon, stomatal scale measurements could allow to further understand O_2 exchange at the smallest scale by for example validating if O_2 mole fractions are indeed higher outside the stomata compared to inside (Peralta Ogorek et al., 2021; Natale et al., 2024). Also, direct numerical simulations could provide valuable insights by incorporating both molecular diffusion and Stefan flow at the stomata-atmosphere interface (Sharma and García-Mayoral, 2020; Bannister et al., 2022). If Stefan flow is found to significantly influence O_2 exchange on leaf scale, this effect should be accounted for in biospheric models, such as the CLASS and SiB4 models, similar to the ternary correction for CO_2 and $\delta^{13}CO_2$ that is already commonly used (Von Caemmerer and Farquhar, 1981b; Farquhar and Cernusak, 2012).

7.3.2 Crossing spatial scales: from leaf and soil to canopy level

Throughout this thesis, we assumed that the ER signals originating from leaves and soil remain the same when going to above-canopy measurements, with no upscaling or downscaling applied. In Chapter 4 and 5, we assumed that the ER values derived from above-canopy flux measurements in Chapter 3 could directly be linked to leaf ($\mathrm{ER_a}$) and soil ($\mathrm{ER_r}$) contributions. A similar assumption was made in Chapter 6, although there the net flux above the canopy was formed by combining several respiration processes.

It is crucial to evaluate whether this choice to not apply upscaling or downscaling when moving to the larger scale is appropriate, as this can significantly impact interpretation of measurements and model implementation. Studies of biosphere CO_2 exchange have demonstrated that discrepancies can arise between leaf measurements and their resulting canopy fluxes due to vertical variations in vegetation properties and environmental conditions, such as shaded and sunlit leaves (Echer and Rosolem, 2015; González-Armas et al., 2024) or between old and new leaves (Echer and Rosolem, 2015; Bielczynski et al., 2017). These vertical variations could similarly influence O_2 fluxes and, consequently, ER signals (Fischer et al., 2015). Additionally, CO_2 emitted from soil respiration can sometimes remain trapped below the canopy and be taken up again by vegetation and therefore remain invisible to measurements in the atmosphere above the canopy (Kanani-Sühring and Raasch, 2015; Santana et al., 2018). Such below canopy mixing of ER signals could affect the above canopy $\mathrm{ER_r}$ and $\mathrm{ER_a}$ signals, deviating from expectations based solely on single leaf and soil chamber measurements. As a result, inaccurate upscaling may lead to incorrect estimates of the net ER originating from the ecosystem and more research is needed.

Validating the accuracy of upscaling is challenging due to measurement limitations. Above canopy flux measurements have a large footprint that includes processes from the complete ecosystem, making it difficult to directly compare them with small-scale measurements such as with leaf and soil chambers. To address this challenge, additional measurements are required to provide a better understanding of the vertical structure of O_2 and CO_2 fluxes and their ER. For example, conducting measurements at multiple heights could provide valuable insights (Sterck et al., 2013; González-Armas et al., 2025). However, this approach is difficult for O_2 because of its complex measurement technique. Only Ishidoya et al. (2013) and Battle et al. (2023) have measured O_2 below and above the canopy, however they only measured at one height below the canopy which would not allow to understand the vertical structure of O_2 and CO_2 fluxes. Additionally, at the Leinefelde site in Germany, below canopy O_2 mole fraction measurements have been started at different heights, but the vertical profile of ER signals have not yet been published (A. Knohl, personal communication). As a result, evaluating the vertical structure of ER signals below the canopy and linking them to above-canopy ER measurements remains a significant challenge.

To address the gap between the spatial scale of leaf and soil chamber measurements and above-canopy measurements, we recommend combining measurements with models and build further on the multi-level canopy modeling study by Yan et al. (2023). Additionally, multi-layer canopy Large Eddy Simulations (LES) would provide a more detailed understanding of how the O_2 and CO_2 fluxes mix within the canopy and how this mixing influences the resulting net ER signal from the ecosystem (Kanani-Sühring and Raasch, 2015; Ma and Liu, 2019; Pedruzo-Bagazgoitia et al., 2023). To validate LES models, additional measurements are needed at multiple vertical levels within the ecosystem.

7.3.3 Temporal scales: connecting OR and ER

In this thesis, we have discussed O_2:CO_2 ratios that represent different time scales and different processes. Specifically, we have discussed the O_2:CO_2 ratio defined by fluxes (the exchange ratios (ERs): ER_a, ER_r or ER_{net}), the O_2:CO_2 ratio defined by atmospheric mole fractions (ER_{atmos}), as well as the O_2:CO_2 ratio derived from the molecular composition of organic material (Oxidative Ratio, OR), see Figure 1.4. Throughout this thesis we have connected ER values based on fluxes with OR values. In Chapter 3, the OR measured in podzol soils was used to compare with our flux-based ER_r value. Additionally, in Chapter 6 we used OR values as a substitute for ER_r and ER_a values to estimate O_2 fluxes for crops, grasses and heterotrophic respiration. In this section, we further discuss how the ER (focusing on ER_a, ER_r and ER_{net}) and OR that represent different scales can be compared. In Section 7.3.4 we elaborate on the connection between ER values based on fluxes and ER_{atmos}.

Understanding the link between OR and ER is crucial, as OR measurements are often used to interpret O_2 and CO_2 measurements due to their relatively straightforward methodology. The OR is determined by the stoichiometry of the organic material, theoretically representing the net O_2 and CO_2 fluxes required to have formed that material during its lifespan. As a result, OR values reflect long timescales of years to decades (Worrall et al., 2013; Gallagher et al., 2014). In contrast, the ER is derived from flux measurements and therefore reflect the time scale over which the fluxes are observed, typically ranging from half hourly means and integrated up to days to a year (Cousins and Bloom, 2004; Hilman et al., 2022; Ishidoya et al., 2015). This distinction between OR and ER becomes particularly significant in studies measuring O_2 and CO_2 exchange from soils, where OR is frequently used to interpret ER measurements (Angert et al., 2015; Hicks Pries et al., 2020). Furthermore, on global scale, in partitioning ocean and biosphere sinks of CO_2, it is commonly assumed that the net exchange of the biosphere corresponds with its weighted OR values (Worrall et al., 2013; Keeling and Manning, 2014).

It is generally assumed that the time-integrated ER of assimilation (ER_a) and respiration (ER_r) should converge over time to OR, when the same organic material is measured. However, this assumption has never been validated. Theoretically, if fluxes were measured continuously during the formation of organic materials, the ratio of the cumulative net fluxes should align with the OR of the resulting organic materials. Unfortunately, such long-term datasets of continuous O_2 and CO_2 measurements above vegetation do currently not exist. Additionally, various processes in the soil and vegetation can cause O_2 and CO_2 fluxes to become decoupled, making them less directly relatable to the measured ER. Examples include differences in the solubility of O_2 and CO_2 in groundwater (Angert et al., 2015; Hicks Pries et al., 2020) and land-use changes, which lead to soil OR values that no longer reflect the vegetation growing above them (Randerson et al., 2006).

Despite the challenges in linking OR to ER, measurement studies could provide valuable insights into how OR might be used to validate the ERs. Evaluating longer time series of net O_2 and CO_2 fluxes above the biosphere (ER_{net}) could be helpful. Observing how ER_{net} evolves over time could clarify whether ER converges towards a constant value that reflects the OR. This might be more feasible in ecosystems with short lifespans, such as crops or grass fields. By measuring O_2 and CO_2 exchange throughout the entire growing cycle and comparing the results with the OR measured at the end of the cycle, we could better understand the relationship between ER and OR. Knohl et al. (2020) have recently made such measurements at the Reinshof site in a crop field in Germany, and these would therefore provide a unique opportunity to test this theory. Additionally, a theoretical modeling framework including O_2 fluxes resulting from carbon pools forming over time could further enhance our understanding of the formation of OR. The SiB4 model of Chapter 6 provides an excellent foundation for exploring these dynamics.

7.3.4 Exchange ratios based on atmospheric mole fractions

Deriving surface fluxes from atmospheric mole fraction measurements presents significant challenges, as we demonstrated in all four thesis chapters. In Chapter 3, we identified a mismatch between the forest ER signal based on surface fluxes above the canopy (ER_{net} or ER_{forest}), and the atmospheric ER signal based on changes in atmospheric mole fractions over time (ER_{atmos}, Figure 7.3). Chapter 4 explains this difference further using modeling, and we show that the influence of additional processes, such as entrainment, complicate the interpretation of ER_{atmos}. Similar conclusions were drawn in Chapter 5 for other ecosystems and tracers. Finally, in Chapter 6, we further studies this challenge by transporting surface fluxes to obtain atmospheric time series using a Lagrangian transport model.

Understanding the link between ER_{net} and ER_{atmos} is important because ER_{atmos} is used in several studies, e.g. focusing on O_2 partitioning methods to estimate fossil fuel CO_2 signals (Pickers et al., 2022; Rödenbeck et al., 2023) and to study ocean and land partitioning of global CO_2 sinks (Stephens et al., 1998; Manning and Keeling, 2006; Tohjima et al., 2019). Additionally, ER_{atmos} is sometimes used as a proxy to estimate ER_{net} (e.g. Battle et al., 2019). For global O_2 partitioning methods, detailed understanding of how surface ER signals translate to atmospheric ER signals is less critical, because most of the temporal

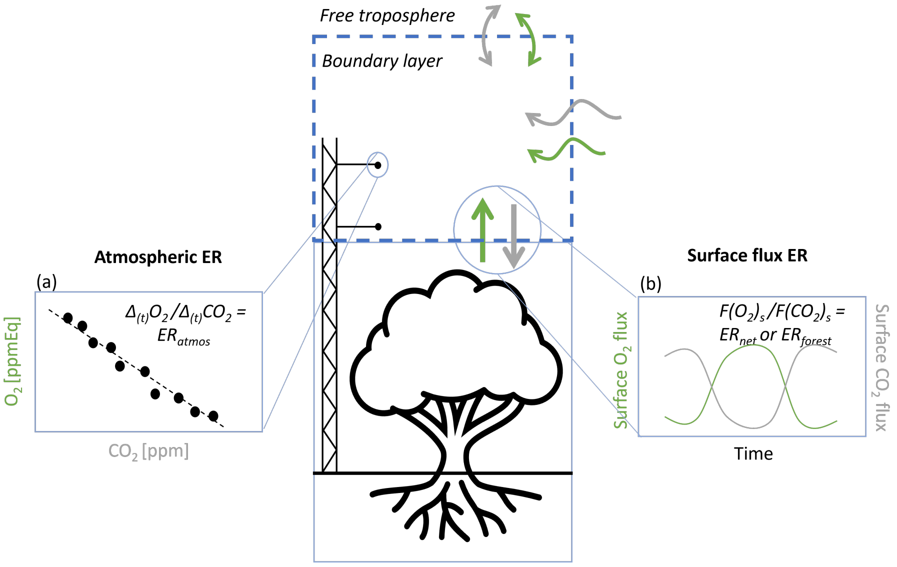

Figure 7.3: Schematic overview of the different definitions of the exchange ratio (ER) based on either: a) mole fraction measurements in the atmosphere (ER_{atmos}) and b) based on the net surface fluxes above the canopy (ER_{net} or ER_{forest}).

and spatial variability is smoothed out on the decadal time scales on which these methods are applied. However, for O_2 partitioning methods applied to regional or local scales, it becomes crucial to understand how the variability in ER_{net} translates into atmospheric ER signals. At these smaller sales, the variability in ER_{net} does not always align with the variability in ER_{atmos}, as was demonstrated in Chapters 4, 5 and 6.

Linking ER_{net} to ER_{atmos} is challenging due to the influence of multiple processes (such as entrainment and advection) on the atmospheric signal (Figure 7.3) and the inherent complexities of working with ratios (Chapter 3; Chapter 6; Miller and Tans, 2003). Atmospheric signals are formed by a combination of processes that act on different spatial scales, and some even lack distinct ER values, which makes atmospheric ERs difficult to link to surface processes and sometimes even impossible. For instance, diurnal time series of O_2 and CO_2 mole fractions are governed by surface and atmospheric processes, including stability changes, entrainment, clouds, and subsidence (Chapters 4 and 5). Longer seasonal time series are also affected by advection of air masses from other locations with varying atmospheric and surface characteristics (Chapter 6). Even under the hypothetical scenario where only surface processes influence atmospheric ER signals, discrepancies would still arise because ratios do not represent flux magnitudes. As demonstrated in Chapters 4 and 6, extreme surface ER value can occur when the gross fluxes (GPP and TER) are similar, for example during the early morning transition or in spring. However, because the net flux of these gross fluxes (NEE) is close to zero, these extreme ER_{net} values have minimal impact on ER_{atmos}. Instead, ER_{atmos} is influenced mostly by periods with higher net surface fluxes. Consequently, careful consideration is necessary when translating surface fluxes into surface ER signals and linking them to atmospheric ER values. Additionally, for the other way around, we strongly advise against using atmospheric ER values (ER_{atmos}) as a direct indication of surface ER signals.

More field campaigns and modeling studies are needed to fully understand the link between ER_{net} and ER_{atmos}. Chapter 5 demonstrated the added value of vertical measurements from aircraft in understanding diurnal cycles, while Chapter 4 highlighted how differences between O_2 and CO_2 entrainment can lead to significant discrepancies between the ER_{net} and ER_{atmos}. Therefore, vertical measurements of meteorological variables and O_2 and CO_2 from aircraft and/or using radiosondes should always be included in field campaigns. Combining these measurements with atmospheric transport models, such as STILT (Chapter 6), offers a powerful approach to investigate why certain atmospheric processes decouple O_2 and CO_2. Transport models also provide critical insights into how ER_{net} forms atmospheric ERs, making them invaluable tools for O_2 partitioning methods.

7.4 The role of biospheric O_2 in global carbon budget calculations

Throughout this thesis we focused on the O_2 and CO_2 exchange processes of the biosphere without delving into global carbon or oxygen budgets or the potential impact of our results on these large-scale calculations. We describe the methods used in the global partitioning of carbon sources and sink using O_2 in Chapter 1. Furthermore, we briefly addressed this topic in Chapter 6, where we discussed that our approach to examine the variability of the biosphere ER ratio operates on different time scales compared to the fixed value of 1.1 used in global O_2 partitioning methods. Although our studies are not directly applicable to global budget calculations yet, we believe there are several insights that could improve the integration of biospheric O_2 exchange into global O_2 partitioning methods. To this end, in this section, we highlight the importance of accounting for the variability in biospheric O_2:CO_2 ratios in three topics. We first address the level of detail of biosphere O_2 and CO_2 variability needed in global scale partitioning. Secondly, we discuss global atmospheric inversions using O_2. Finally, we discuss the role of fires and land-use change.

7.4.1 Level of detail needed for biosphere variability in O_2 partitioning methods

The O_2 partitioning method, as used to partition the global ocean and biosphere carbon sinks over decadal time periods, uses a constant ER_{net} value of 1.1 (or 1.05) without incorporating further biosphere-specific details. Figure 7.4 illustrates how results from the O_2 partitioning method compare with other estimates of the global ocean and biosphere carbon sinks based on bottom-up models and atmospheric inversions. The orange shaded area represents the uncertainty of the O_2 method, which accounts for the uncertainties in: fossil fuel emissions, the OR of fossil fuels α_F, O_2 ocean outgassing, measured trends in $\delta(O_2/N_2)$ and CO_2, and the ER of the biosphere α_B (see Chapter 1; Keeling and Manning, 2014; Friedlingstein et al., 2024). Among these, the largest uncertainties arise from ocean O_2 outgassing and fossil fuel emissions (Keeling and Manning, 2014), while α_B contributes minimally to the overall uncertainty due to its assumed uncertainty range of 0.05 to a maximum of 0.1 (Keeling and Manning, 2014; Rödenbeck et al., 2023). Consequently, incorporating a temporal variation in the ER_{net} value of 1.1, even within a range of 0.1, would have a negligible impact on the decadal-scale carbon sinks derived with this O_2 partitioning method.

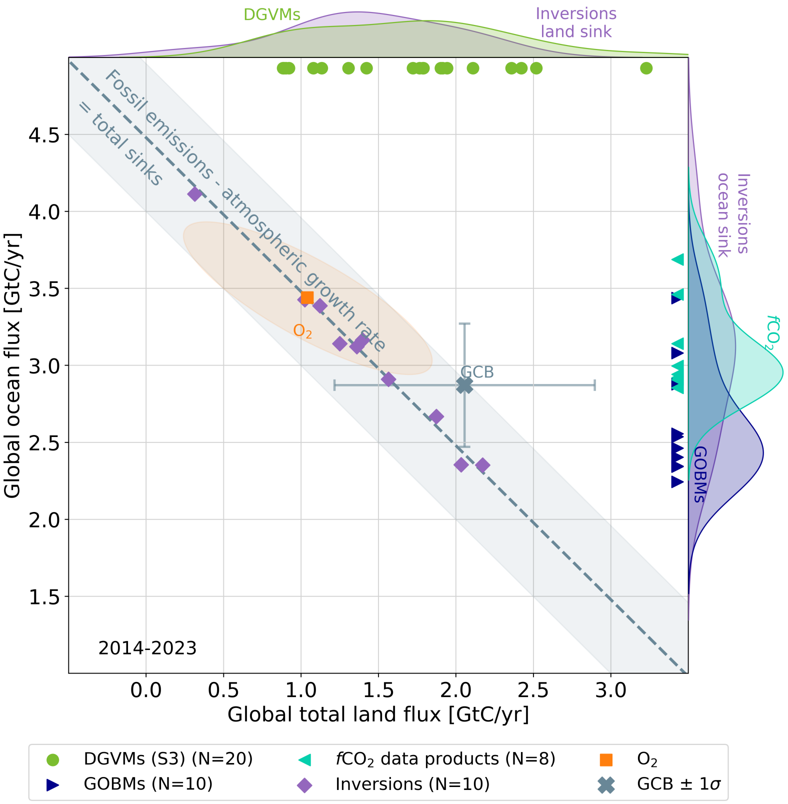

Figure 7.4: Global ocean and land carbon fluxes averaged over 2014-2023 as shown in Friedlingstein et al. (2024), derived from atmospheric O_2 observations (orange) and based on the global carbon budget (GCB, grey), in comparison to other methods: atmospheric inversions, dynamic global vegetation models (DGVMs), global ocean biogeochemical models (GOBMs) and ocean data products based on CO_2 measurements in the ocean water (fCO_2).

The level of detail needed for ER_{net} increases as the temporal scale of the O_2 partitioning method shortens below the decadal time scale. Rödenbeck et al. (2023) demonstrated that on seasonal time scales, a change in ER_{net} of just 0.05 can elevate the uncertainty in fossil fuel CO_2 emission estimates to match the magnitude of the signal itself. In this thesis, we showed that the ER_a and ER_r values differ both on diurnal (Chapter 3) and annual scales (Chapter 6). Specifically, Chapter 6 showed that on an annual scale, the global ER_{net} value can deviate substantially from the commonly assumed constant value of 1.1, with values ranging mostly between 0.8 and 1.2. These findings underscore the need for greater detail and representation of biospheric processes in global O_2 partitioning methods below the decadal time scale.

More research is needed to determine the temporal and spatial scales at which detailed biosphere ER_{net} modeling is necessary, to avoid the use of unnecessarily complex and resource-intensive biosphere models. In Chapter 6, we demonstrated that using a biosphere model is crucial to obtain improved estimates of α_B on an annual time scale and for regional O_2 partitioning methods. However, applying such detailed modeling to methods on decadal time-scales would introduce excessive complexity and undermine the simplicity that makes global O_2 partitioning methods advantageous. It is therefore important to define clear thresholds for the level of detail needed. For instance, key questions include identifying the time scales at which ER_a and ER_r converge towards the oxidative ratio (OR), and determining when regional dynamics significantly impact the temporal variability of ER_{net}.

7.4.2 Using O_2 in atmospheric inversions

Atmospheric CO_2 inversions are widely used to enhance estimates of the global carbon budget by constraining the CO_2 surface fluxes with atmospheric measurements (e.g. Figure 7.4; Friedlingstein et al., 2024). These methods achieve this by minimizing a cost function to find an optimized set of surface fluxes, using atmospheric observations and an atmospheric transport model (e.g. Peters et al., 2005). The integration of O_2 measurements into atmospheric inversions has proven to be a valuable addition, providing further constraints on the CO_2 budget (Rödenbeck et al., 2008; Rödenbeck et al., 2023). For example, inversions using atmospheric potential oxygen (APO) have been used to optimize APO ocean fluxes and therefore improve our understanding of global ocean characteristics (Gruber et al., 2001; Rödenbeck et al., 2008; Resplandy et al., 2018). APO inversions have also been used improve the estimated fossil fuel CO_2 fluxes in Europe (Rödenbeck et al., 2023).

Until now, O_2 inversion studies have primarily used APO in their analysis instead of the full atmospheric O_2 signal, thereby assuming that the biosphere influence is negligible. However, based on our findings in this thesis, we recommend incorporating the biospheric signal using the complete O_2 and CO_2 signals in the inverse systems. When applying the O_2 partitioning method on decadal time scale using only atmospheric measurements, the ‘true’ biosphere CO_2 fluxes that are actually emitted by the biosphere are inherently included in the atmospheric CO_2 signal. In this case, the main uncertainty associated with the biosphere is represented by α_B, which, as discussed in the previous section, has minimal influence. However, in atmospheric inverse systems, model-derived biosphere fluxes are used to create the APO signal. These biosphere fluxes already have an uncertainty associated with the model approach because there is always a certain degree of discrepancy between the modeled fluxes and the ‘true’ biosphere fluxes measured in the field. If APO is used without accounting for these discrepancies, an uncertainty is introduced through the biosphere fluxes, despite the assumption that the biosphere does not significantly influence the APO signal. To ensure a comprehensive understanding of uncertainties, we recommend including the biosphere signal explicitly in inversion analyses, as shown by Vertegaal (2023). Consequently, a more detailed representation of the spatial variability in ER_{net} is essential to accurately estimate O_2 biosphere fluxes.

Additionally, inversions could also provide valuable insights into the global O_2 budget itself. By optimizing biospheric O_2 surface fluxes, inversions can help to better characterize the spatial variability of ER signals, offering an improvement over the theoretical implementation in the SiB4 model. Enhancing our understanding of the spatial variability of ER_{net} would also clarify whether the biosphere should be explicitly included in O_2 inversions, instead of using APO. To apply these methods effectively, more atmospheric measurement stations are needed that observe O_2 mole fractions. Recently, the Integrated Carbon Observation System (ICOS) has started measuring O_2 from flasks at multiple stations in Europe (Apadula et al., 2025). These measurements have the potential to significantly advance the integration of O_2 data into inverse systems, as highlighted by Rödenbeck et al. (2023).

7.4.3 Fires and land-use change

α_B does not only represent the O_2:CO_2 exchange ratio of biospheric fluxes but also includes contributions from fires and land-use change fluxes (Keeling and Manning, 2014). Consequently, the ER values for fires and land-use change have so far been assumed to behave the same as photosynthesis and respiration when individual components of the global O_2 budget are calculated (Huang et al., 2018; Liu et al., 2020). However, throughout this thesis, we have demonstrated that ecosystem ER values vary over time and space due to the dynamics of different processes. It is therefore highly unlikely that the ER values associated with land-use change and fires are equivalent to those of ecosystem exchange, because different processes drive their CO_2 and corresponding O_2 flux. The O_2 exchange resulting from fires and land-use change has received limited attention in literature so far. As such, we can only hypothesize how their ER values might deviate from the biosphere processes analyzed in this thesis.

Theoretically, the ER of fires should approximately be the OR of the organic material being burned. To our knowledge, only Lueker et al. (2001) have measured the O_2:CO_2 ratios originating from fires to validate this assumption. Their findings indicate that atmospheric ER values increased above 1.1 on days with clear fire influence, and therefore deviating from the expected OR of 1.1. This elevated ER could be attributed to incomplete combustion, during which also carbon monoxide (CO) is formed instead of purely CO_2. In case of incomplete combustion, CO can become a significant component of the emitted carbon, altering the expected O_2:CO_2 ratio Lueker et al. (2001). The proportion of CO formed during combustion depends on various factors, such as fire conditions and fuel type (Van Leeuwen and Van Der Werf, 2011; Van Der Werf et al., 2017). Consequently, the ER of fires is likely influenced similarly. Further research is essential to quantify the ER values of fires accurately, enabling their incorporation into models and improving the interpretation of atmospheric measurements impacted by fire events.

The ER associated with land-use change fluxes is more challenging to quantify. These fluxes include contributions from deforestation, forest (re)growth, wood harvest and other forest management, peat drainage and peat fires (Friedlingstein et al., 2024). Even for CO_2, land-use change fluxes are difficult to determine due to challenges in defining and constraining these fluxes and the complexities involved in measuring them accurately (Grassi et al., 2023). Linking O_2 fluxes to these CO_2 fluxes based on known OR values is particularly complicated, as land-use change fluxes are not directly tied to specific biological processes. Therefore, further research is needed to investigate how the ER associated with land-use change might deviate from the standard α_B. Similar to fires, if the O_2 fluxes linked to land-use change can be disentangled from general biosphere fluxes, it would allow for a more detailed analysis of the global O_2 budget.

7.5 Recommendations for future measurement strategies

Throughout this thesis and this synthesis chapter, we have emphasized the need for more extensive measurements to enhance our understanding of biospheric O_2 and CO_2 exchange processes. The current lack of measurements limits our ability to fully assess the variability of ER_{net} across different spatial and temporal scales. In this section, we combine the recommendations about measurements outlined in the individual chapters and the previous sections in this synthesis to propose an ‘ideal’ measurement strategy for future campaigns and long-term observational sites (Figure 7.5).

To determine the ER_{net} signal of the biosphere, measurements should be made that make it possible to infer O_2 and CO_2 surface fluxes (Chapters 3 and 4). These fluxes can be inferred using a vertical gradient (e.g. the K-theory) (Stull, 1988), as demonstrated in Chapter 3. Implementing the K-theory approach requires continuous measurements of O_2

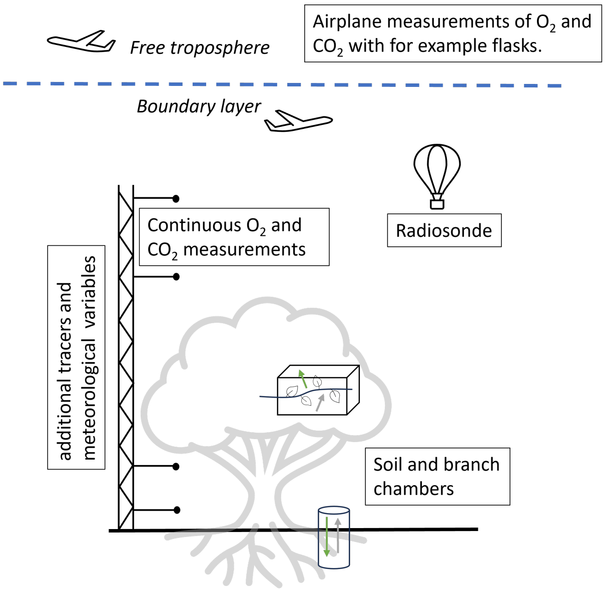

Figure 7.5: Schematic overview of all measurements that we recommend for an ideal measurement strategy.

and CO_2 at two heights *above* the canopy to derive vertical gradients. Additionally, eddy covariance measurements of either CO_2 or the sensible heat flux are necessary to allow calculation of the O_2 surface fluxes from these vertical gradients (Chapter 3). To obtain a comprehensive understanding of the turbulence driving these fluxes, these observations should be complemented with meteorological variables, including temperature, pressure, specific humidity, and latent heat flux. Alternatively, development of a system capable of eddy covariance O_2 measurements would be recommended over vertical profile measurements, but to date these have not yet been possible due to limitations in O_2 instruments response time and precision. The vacuum-ultraviolet absorption technique (VUV) seems to be the most promising candidate to achieve this (Stephens et al., 2003).

Below-canopy measurements are essential to explain the biological processes driving O_2 and CO_2 fluxes and their ER_{net} signal. *In situ* soil and branch chamber measurements should be employed, together with laboratory measurements of the vegetation type at the measurement location, to determine the individual ER values for assimilation (ER_a) and respiration (ER_r). *In situ* chamber measurements should be done at several locations to establish the heterogeneity of the measurements. Simultaneously quantifying ER_a and ER_r while inferring ER_{net} facilitates the application of the O_2 partitioning method to separate NEE into GPP and TER (Chapter 3). Moreover, this approach enhances our understanding of the temporal and spatial variability of ER_{net} (Chapter 6). Next to chamber measurements, additional below-canopy atmospheric measurements of O_2 and CO_2 at multiple heights further aid in linking chamber-derived ER_a and ER_r values to the above-canopy ER_{net} signal (this chapter).

Vertical atmospheric measurements above the canopy are essential to accurately analyze O_2 and CO_2 mole fractions. Entrainment of air from the free troposphere into the boundary layer can significantly influence the temporal variability of these mole fractions. To quantify this effect, atmospheric measurements at different heights are required, both inside and above the boundary layer in the free troposphere (Chapter 4 and 5). Such measurements can be conducted using flask sampling, as demonstrated in Chapter 5, or through continuous measurements, as shown by Stephens et al. (2021). In addition to vertical O_2 and CO_2 profiles, it is crucial to measure vertical meteorological profiles that quantify atmospheric processes, including boundary layer dynamics and free tropospheric lapse rates. Radiosondes can provide this information by measuring vertical profiles of temperature, relative humidity and pressure (Chapter 4 and 5).

Additional considerations are needed for measurement sites at which the primary objective is CO_2 emission verification through extracting the fossil fuel CO_2 signal from total atmospheric CO_2 mole fraction measurements using O_2. To minimize biases from biosphere O_2/CO_2 exchange with their temporally variable ER_{net}, measurement locations should be chosen with a relatively small biospheric and high fossil fuel influence (Chapter 6). Examples of locations with these criteria include sites at Heathfield (UK), Weybourne (UK), and Cabauw (Netherlands). At these sites, it is essential to conduct continuous O_2 measurements, as demonstrated by Pickers et al. (2022). Continuous O_2 monitoring enables the identification of fossil fuel combustion peaks and provides a critical dataset for comparison with atmospheric transport models (Chapter 6).

Furthermore, we advocate for multi-tracer measurement approaches that combine O_2 observations with additional carbon cycle tracers, such as $\delta^{13}CO_2$, COS and $\Delta^{14}CO_2$. These tracer measurements should be integrated into measurement strategies investigating ER_{net} variability as well as those focused on quantifying fossil fuel CO_2 signals using O_2. As highlighted throughout this synthesis chapter, the combined analysis of O_2:CO_2 ratios with other carbon cycle tracers provides valuable insights into the processes driving these ratios. This, in turn, enhances our understanding of how O_2 measurements can be effectively used to constrain the carbon budget.

7.6 Conclusion

Throughout this thesis, we demonstrated that the exchange of O_2 and CO_2 in the biosphere provides valuable information to enhance our understanding of the carbon budget from local to global scales. Our findings show that the O_2:CO_2 exchange ratio of biosphere exchange (ER_{net}) is not a fixed value but varies both temporally and spatially. By integrating observational data with modeling approaches, we enhanced the understanding of ER_{net} variability and improved methods for its quantification.

Our results highlight the importance of careful consideration when determining $\mathrm{ER}_{\mathrm{net}}$, as its variability has significant implications for partitioning methods. Figure 7.6 illustrates the different definitions used to quantify the exchange of O_2 and CO_2 in the biosphere across various spatial scales, similar to Figure 1.4. Previous studies often assumed a constant oxidative ratio (OR) as a proxy for the biosphere's exchange ratio at both regional and global scale, through the definition of Atmospheric Potential Oxygen (APO). In contrast, in this thesis we distinguish between the exchange ratio of assimilation (ER_{a}) and the exchange ratio of respiration (ER_{r}), that are both process-based, and can be combined into $\mathrm{ER}_{\mathrm{net}}$ with its resulting (non-process-based) spatial and temporal variability. Furthermore, we demonstrated that the exchange ratio based on single-height atmospheric mole fraction measurements ($\mathrm{ER}_{\mathrm{atmos}}$) should not be used as a direct indicator of surface exchange ($\mathrm{ER}_{\mathrm{net}}$). Further research is needed to link the variable $\mathrm{ER}_{\mathrm{net}}$ values identified in this thesis to global-scale applications. To advance this understanding, we recommend expanding O_2 and CO_2 biosphere measurements. By enhancing our understanding of biospheric O_2 exchange, this work strengthens the application of O_2 methods used to constrain the carbon budget and to verify fossil fuel emissions.

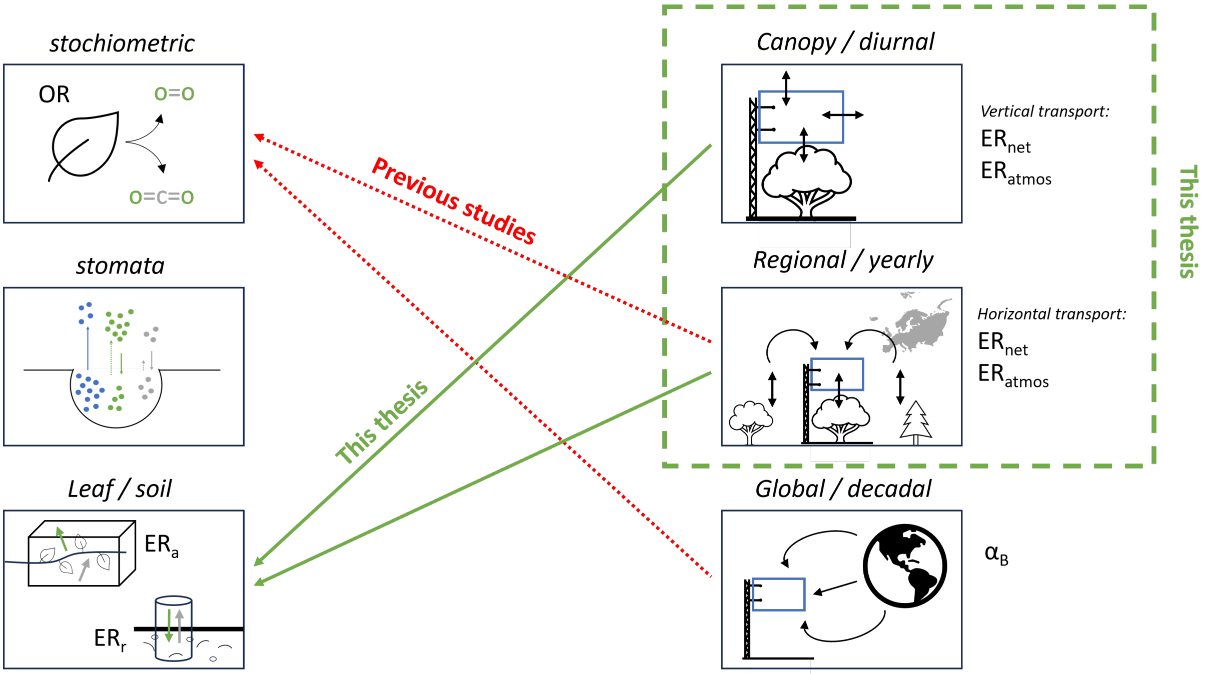

Figure 7.6: Schematic overview of the different O_2:CO_2 ratios of the biosphere at different spatial scales: oxidative ratio (OR) based on stoichiometry, exchange ratio of assimilation (ER_{a}), exchange ratio of respiration (ER_{r}), net exchange ratio of the biosphere ($\mathrm{ER}_{\mathrm{net}}$), atmospheric exchange ratio ($\mathrm{ER}_{\mathrm{atmos}}$) and the constant O_2:CO_2 ratio of the biosphere used in global partitioning methods (α_B). The arrows indicate which smaller spatial scale O_2:CO_2 ratios are used to determine the O_2:CO_2 ratios at canopy, regional or global scale in previous studies (red arrows) and recommended in this thesis (green arrows).

References

Adekanmbi, A. A. and T. Sizmur (2022). “Importance of Diurnal Temperature Range (DTR) for predicting the temperature sensitivity of soil respiration”. *Frontiers in Soil Science* 2. DOI: `10.3389/fsoil.2022.969077`.

Andreae, M. O., O. C. Acevedo, A. Araùjo, P. Artaxo, C. G. G. Barbosa, H. M. J. Barbosa, J. Brito, S. Carbone, X. Chi, B. B. L. Cintra, N. F. da Silva, N. L. Dias, C. Q. Dias-Júnior, F. Ditas, R. Ditz, A. F. L. Godoi, R. H. M. Godoi, M. Heimann, T. Hoffmann, J. Kesselmeier, T. Könemann, M. L. Krüger, J. V. Lavric, A. O. Manzi, A. P. Lopes, D. L. Martins, E. F. Mikhailov, D. Moran-Zuloaga, B. W. Nelson, A. C. Nölscher, D. Santos Nogueira, M. T. F. Piedade, C. Pöhlker, U. Pöschl, C. A. Quesada, L. V. Rizzo, C.-U. Ro, N. Ruckteschler, L. D. A. Sá, M. de Oliveira Sá, C. B. Sales, R. M. N. dos Santos, J. Saturno, J. Schöngart, M. Sörgel, C. M. de Souza, R. A. F. de Souza, H. Su, N. Targhetta, J. Tóta, I. Trebs, S. Trumbore, A. van Eijck, D. Walter, Z. Wang, B. Weber, J. Williams, J. Winderlich, F. Wittmann, S. Wolff, and A. M. Yáñez-Serrano (2015). “The Amazon Tall Tower Observatory (ATTO): overview of pilot measurements on ecosystem ecology, meteorology, trace gases, and aerosols”. *Atmospheric Chemistry and Physics* 15 (18), 10723–10776.

Andrew, R. M. (2020). “A comparison of estimates of global carbon dioxide emissions from fossil carbon sources”. *Earth System Science Data Discussions* 2020, 1–51.

Angert, A., D. Yakir, M. Rodeghiero, Y. Preisler, E. A. Davidson, and T. Weiner (2015). “Using O_2 to study the relationships between soil CO_2 efflux and soil respiration”. *Biogeosciences* 12 (7), 2089–2099. DOI: `10.5194/bg-12-2089-2015`.

Apadula, F., T. Biermann, A. Colomb, S. Conil, C. Couret, P. Cristofanelli, M. De Mazière, M. Delmotte, T. Di Iorio, L. Emmenegger, G. Forster, A. Frumau, L. Haszpra, J. Hatakka, M. Heliasz, A. Hensen, O. Hermansen, A. Hoheisel, T. Kneuer, and A. di Sarra (2025). “ICOS Atmosphere Release 2025-1 of Level 1 FastTrack Greenhouse Gas Mole Fractions of CO_2, CH_4, N_2O, CO, meteorology data and flask samples analysed for CO_2, CH_4, N_2O, CO, H_2, SF6 and ^{14}C (Version 1.0).” DOI: `https://doi.org/10.18160/1703-4FF1`.

Arrillaga, J. A., J. V.-G. de Arellano, F. Bosveld, H. K. Baltink, C. Yagüe, M. Sastre, and C. Román-Cascón (2018). “Impacts of afternoon and evening sea-breeze fronts on local turbulence, and on CO_2 and radon-222 transport”. *Quarterly Journal of the Royal Meteorological Society* 144 (713), 990–1011.

Aubinet, M., T. Vesala, and D. Papale (2012). *Eddy covariance: a practical guide to measurement and data analysis.* Springer Science & Business Media.

Aubrey, D. P. and R. O. Teskey (2009). “Root-derived CO_2 efflux via xylem stream rivals soil CO_2 efflux”. *New Phytologist* 184 (1), 35–40.

Baldocchi, D., H. Chu, and M. Reichstein (2018). “Inter-annual variability of net and gross ecosystem carbon fluxes: A review”. *Agricultural and Forest Meteorology* 249, 520–533.

Baldocchi, D. D. (2003). “Assessing the eddy covariance technique for evaluating carbon dioxide exchange rates of ecosystems: past, present and future”. *Global change biology* 9 (4), 479–492.

Ballantyne, A. á., C. á. Alden, J. á. Miller, P. á. Tans, and J. White (2012). “Increase in observed net carbon dioxide uptake by land and oceans during the past 50 years”. *Nature* 488 (7409), 70–72.

Bannister, E., A. R. MacKenzie, and X.-M. Cai (2022). “Realistic forests and the modeling of forest-atmosphere exchange”. *Reviews of Geophysics* 60 (1), e2021RG000746.

Bathellier, C., G. Tcherkez, R. Bligny, E. Gout, G. Cornic, and J. Ghashghaie (2009). “Metabolic origin of the δ13C of respired CO_2 in roots of Phaseolus vulgaris”. *New Phytologist* 181 (2), 387–399.

Battle, M. O., A. R. Raynor, S. E. Kesler, and R. F. Keeling (2023). “The Impact of Industrial Activity on the Amount of Atmospheric O_2”. *Tellus Series B Chemical and Physical Meteorology B* 75 (1), 65–75.

Battle, M. O., J. William Munger, M. Conley, E. Sofen, R. Perry, R. Hart, Z. Davis, J. Scheckman, J. Woogerd, K. Graeter, S. Seekins, S. David, and J. Carpenter (2019). “Atmospheric measurements of the terrestrial $O_2 : CO_2$ exchange ratio of a midlatitude forest”. *Atmospheric Chemistry and Physics* 19 (13), 8687–8701. DOI: `10.5194/acp-19-8687-2019`.

Bender, M., T. Ellis, P. Tans, R. Francey, and D. Lowe (1996). “Variability in the O_2/N_2 ratio of southern hemisphere air, 1991–1994: Implications for the carbon cycle”. *Global Biogeochemical Cycles* 10 (1), 9–21.

Bender, M. L., P. P. Tans, J. T. Ellis, J. Orchardo, and K. Habfast (1994). “A high precision isotope ratio mass spectrometry method for measuring the O_2/N_2 ratio of air”. *Geochimica et Cosmochimica Acta* 58 (21), 4751–4758.

Benedict, F. G. (1912). *The composition of the atmosphere with special reference to its oxygen content.* 166. Carnegie institution of Washington.

Berkelhammer, M., D. Asaf, C. Still, S. Montzka, D. Noone, M. Gupta, R. Provencal, H. Chen, and D. Yakir (2014). “Constraining surface carbon fluxes using in situ measurements of carbonyl sulfide and carbon dioxide”. *Global Biogeochemical Cycles* 28 (2), 161–179.

Bibby, R., P. Cleall-Harding, S. Rundle, S. Widdicombe, and J. Spicer (2007). “Ocean acidification disrupts induced defences in the intertidal gastropod Littorina littorea”. *Biology letters* 3 (6), 699–701.

Bielczynski, L. W., M. K. Lacki, I. Hoefnagels, A. Gambin, and R. Croce (2017). “Leaf and plant age affects photosynthetic performance and photoprotective capacity”. *Plant physiology* 175 (4), 1634–1648.

Bird, R. B., W. E. Stewart, and E. N. Lightfoot (1960). “Transport phenomena”, 780.

Blaine, T. W., R. F. Keeling, and W. J. Paplawsky (2006). “An improved inlet for precisely measuring the atmospheric Ar/N_2 ratio”. *Atmospheric Chemistry and Physics* 6 (5), 1181–1184. DOI: `10.5194/acp-6-1181-2006`.

Bloom, A. J. (2015). “Photorespiration and nitrate assimilation: a major intersection between plant carbon and nitrogen”. *Photosynthesis research* 123 (2), 117–128.

Bloom, A. J., R. M. Caldwell, J. Finazzo, R. L. Warner, and J. Weissbart (1989). “Oxygen and Carbon Dioxide Fluxes from Barley Shoots Depend on Nitrate Assimilation”. *Plant Physiology* 91 (1), 352–356. DOI: `10.1104/pp.91.1.352`.

Bloom, A. J., J. S. Rubio Asensio, L. Randall, S. Rachmilevitch, A. B. Cousins, and E. A. Carlisle (2012). “CO_2 enrichment inhibits shoot nitrate assimilation in C3 but not C4 plants and slows growth under nitrate in C3 plants”. *Ecology* 93 (2), 355–367. DOI: `10.1890/11-0485.1`.

Bolinius, D. J., A. Jahnke, and M. MacLeod (2016). “Comparison of eddy covariance and modified Bowen ratio methods for measuring gas fluxes and implications for measuring fluxes of persistent organic pollutants”. *Atmospheric Chemistry and Physics* 16 (8), 5315–5322. DOI: `10.5194/acp-16-5315-2016`.

Bonan, G. B., O. Lucier, D. R. Coen, A. C. Foster, J. K. Shuman, M. M. Laguë, A. L. Swann, D. L. Lombardozzi, W. R. Wieder, K. M. Dahlin, et al. (2024). “Reimagining Earth in the Earth system”. *Journal of Advances in Modeling Earth Systems* 16 (8), e2023MS004017.

Bonan, G. B., E. G. Patton, J. J. Finnigan, D. D. Baldocchi, and I. N. Harman (2021). “Moving beyond the incorrect but useful paradigm: reevaluating big-leaf and multilayer plant canopies to model biosphere-atmosphere fluxes–a review”. *Agricultural and Forest Meteorology* 306, 108435.

Bopp, L., L. Resplandy, J. C. Orr, S. C. Doney, J. P. Dunne, M. Gehlen, P. Halloran, C. Heinze, T. Ilyina, R. Seferian, et al. (2013). “Multiple stressors of ocean ecosystems in the 21st century: projections with CMIP5 models”. *Biogeosciences* 10 (10), 6225–6245.

Botía, S., S. Komiya, J. Marshall, T. Koch, M. Gałkowski, J. Lavric, E. Gomes-Alves, D. Walter, G. Fisch, D. M. Pinho, B. W. Nelson, G. Martins, I. T. Luijkx, G. Koren, L. Florentie, A. Carioca de Araújo, M. Sá, M. O. Andreae, M. Heimann, W. Peters, and C. Gerbig (2022). “The CO_2 record at the Amazon Tall Tower Observatory: A new opportunity to study processes on seasonal and inter-annual scales”. *Global Change Biology* 28 (2), 588–611. DOI: `https://doi.org/10.1111/gcb.15905`.

Bowling, D. R., D. E. Pataki, and J. T. Randerson (2008). “Carbon isotopes in terrestrial ecosystem pools and CO_2 fluxes”. *New Phytologist* 178 (1), 24–40.

Bowling, D., S. P. Burns, T. J. Conway, R. Monson, and J. White (2005). “Extensive observations of CO_2 carbon isotope content in and above a high-elevation subalpine forest”. *Global Biogeochemical Cycles* 19 (3).

Brown, J., M. Shapkalijevski, M. Krol, T. Karl, H. Ouwersloot, A. Moene, E. Patton, and J. Vilà-Guerau de Arellano (2020). “Ozone exchange within and above an irrigated Californian orchard”. *Tellus B: Chemical and Physical Meteorology* 72 (1), 1–17.

Buurman, P. and A. Jongmans (2005). “Podzolisation and soil organic matter dynamics”. *Geoderma* 125 (1-2), 71–83.

Carbon Portal ICOS RI (2022). *STILT station characterization for Hyytiälä at 17m.*

Casso-Torralba, P., J. V. G. de Arellano, F. Bosveld, M. R. Soler, A. Vermeulen, C. Werner, and E. Moors (2008a). "Diurnal and vertical variability of the sensible heat and carbon dioxide budgets in the atmospheric surface layer". *Journal of Geophysical Research Atmospheres* 113 (12). DOI: `10.1029/2007JD009583`.

Casso-Torralba, P., J. Vilà-Guerau de Arellano, F. Bosveld, M. R. Soler, A. Vermeulen, C. Werner, and E. Moors (2008b). "Diurnal and vertical variability of the sensible heat and carbon dioxide budgets in the atmospheric surface layer". *Journal of Geophysical Research: Atmospheres* 113 (D12).

Clay, G. D. and F. Worrall (2015). "Oxidative ratio (OR) of Southern African soils and vegetation: Updating the global OR estimate". *Catena* 126, 126–133.

Combe, M., J. Vilà-Guerau de Arellano, H. G. Ouwersloot, C. M. Jacobs, and W. Peters (2015). "Two perspectives on the coupled carbon, water and energy exchange in the planetary boundary layer". *Biogeosciences* 12 (1), 103–123.

Cook, F. and J. Knight (2003). "Oxygen transport to plant roots: modeling for physical understanding of soil aeration". *Soil Science Society of America Journal* 67 (1), 20–31.

Cook, F., J. Knight, and F. Kelliher (2013). "Modelling oxygen transport in soil with plant root and microbial oxygen consumption: depth of oxygen penetration". *Soil Research* 51 (6), 539–553.

Coplen, T. B. (2011). "Guidelines and recommended terms for expression of stable-isotope-ratio and gas-ratio measurement results". *Rapid communications in mass spectrometry* 25 (17), 2538–2560.

Cousins, A. and A. Bloom (2004). "Oxygen consumption during leaf nitrate assimilation in a C3 and C4 plant: the role of mitochondrial respiration". *Plant, Cell & Environment* 27 (12), 1537–1545.

Cox, P. M., D. Pearson, B. B. Booth, P. Friedlingstein, C. Huntingford, C. D. Jones, and C. M. Luke (2013). "Sensitivity of tropical carbon to climate change constrained by carbon dioxide variability". *Nature* 494 (7437), 341–344.

Crotwell, A., H. Lee, and M. Steinbacher (2020). *20th WMO/IAEA Meeting on Carbon Dioxide, Other Greenhouse Gases and Related Measurement Techniques (GGMT-2019).* Tech. rep. 255, 1–141.

Curiel Yuste, J., D. Baldocchi, A. Gershenson, A. Goldstein, L. Misson, and S. Wong (2007). "Microbial soil respiration and its dependency on carbon inputs, soil temperature and moisture". *Global Change Biology* 13 (9), 2018–2035.

Davis, K. J., D. H. Lenschow, S. P. Oncley, C. Kiemle, G. Ehret, A. Giez, and J. Mann (1997). "Role of entrainment in surface-atmosphere interactions over the boreal forest". *Journal of Geophysical Research: Atmospheres* 102 (D24), 29219–29230.

De Vries, F. P., A. Brunsting, and H. Van Laar (1974). "Products, requirements and efficiency of biosynthesis a quantitative approach". *Journal of theoretical Biology* 45 (2), 339–377.

Denning, A. S., D. A. Randall, G. J. Collatz, and P. J. Sellers (1996). "Simulations of terrestrial carbon metabolism and atmospheric CO_2 in a general circulation model: Part 2: Simulated CO_2 concentrations". *Tellus B* 48 (4), 543–567.

Ding, L., J. Huang, C. Li, D. Han, X. Liu, H. Li, Y. Bai, and J. Huang (2022). "Variations in terrestrial oxygen sources under climate change". *Science China Earth Sciences* 65 (9), 1810–1823.

Dolman, A., E. Moors, and J. Elbers (2002). "The carbon uptake of a mid latitude pine forest growing on sandy soil". *Agricultural and Forest Meteorology* 111 (3), 157–170. DOI: `https://doi.org/10.1016/S0168-1923(02)00024-2`.

Dupont, S., M. R. Irvine, and C. Bidot (2024). "Morning transition of the coupled vegetation canopy and atmospheric boundary layer turbulence according to the wind intensity". *Journal of the Atmospheric Sciences*.

Dyer, A. (1974). "A review of flux-profile relationships". *Boundary-Layer Meteorology* 7 (3), 363–372.

Echer, F. R. and C. A. Rosolem (2015). "Cotton leaf gas exchange responses to irradiance and leaf aging". *Biologia plantarum* 59 (2), 366–372.

ECMWF, I. (2014). "Documentation—Cy40r1 Part IV: Physical Processes". *European Centre for Medium-Range Weather Forecasts: Reading, UK.*

Elbers, J. A., C. M. Jacobs, B. Kruijt, W. W. Jans, and E. J. Moors (2011). "Assessing the uncertainty of estimated annual totals of net ecosystem productivity: A practical approach applied to a mid latitude temperate pine forest". *Agricultural and Forest Meteorology* 151 (12), 1823–1830. DOI: `https://doi.org/10.1016/j.agrformet.2011.07.020`.

Faassen, K., R. González Armas, G. Koren, G. A. Adnew, H. van Asperen, S. Botía, O. Hartogensis, R. Hutjes, J. Miller, M. van der Molen, I. T. Luijkx, and J. Vilà-Guerau de Arellano (2024a). *Tracing diurnal variations of atmospheric CO_2, O_2 and $\delta^{13}CO_2$ over a tropical and a temperate forest.* Data set.

Faassen, K. and I. Luijkx (2022). *Atmospheric O_2 and CO_2 measurements at Hyytiälä, Finland.* last accessed: 06-01-2023. DOI: `10.18160/SJ3J-PD38`.

Faassen, K. A. P., R. González-Armas, G. Koren, G. Agmuas Adnew, H. van Asperen, H. de Boer, S. Botía, V. S. de Feiter, O. Hartogensis, B. G. Heusinkveld, L. M. Hulsman, R. W. A. Hutjes, S. P. Jones, B. A. M. Kers, S. Komiya, L. A. T. Machado, G. Martins, J. B. Miller, W. Mol, M. van der Molen, R. Moonen, C. Q. Dias-Junior, T. Röckmann, H. Snellen, I. T. Luijkx, and J. Vilà-Guerau de Arellano (under review). "Tracing diurnal variations of atmospheric CO_2, O_2 and $\delta^{13}CO_2$ over a tropical and a temperate forest". *Geophysical Research Letters*.

Faassen, K. A. P., L. N. T. Nguyen, E. R. Broekema, B. A. M. Kers, I. Mammarella, T. Vesala, P. A. Pickers, A. C. Manning, J. Vilà-Guerau de Arellano, H. A. J. Meijer, W. Peters, and I. T. Luijkx (2023). "Diurnal variability of atmospheric O_2, CO_2, and their exchange ratio above a boreal forest in southern Finland". *Atmospheric Chemistry and Physics* 23 (2), 851–876.

Faassen, K. A. P., J. Vilà-Guerau de Arellano, R. González-Armas, B. G. Heusinkveld, I. Mammarella, W. Peters, and I. T. Luijkx (2024b). "Separating above-canopy CO_2 and O_2

measurements into their atmospheric and biospheric signatures". *Biogeosciences* 21 (12), 3015–3039.

Farquhar, G. D., S. v. von Caemmerer, and J. A. Berry (1980). "A biochemical model of photosynthetic CO_2 assimilation in leaves of C 3 species". *planta* 149, 78–90.

Farquhar, G. D. and L. A. Cernusak (2012). "Ternary effects on the gas exchange of isotopologues of carbon dioxide". *Plant, Cell & Environment* 35 (7), 1221–1231.

Fischer, S., S. Hanf, T. Frosch, G. Gleixner, J. Popp, S. Trumbore, and H. Hartmann (2015). "Pinus sylvestris switches respiration substrates under shading but not during drought". *New Phytologist* 207 (3), 542–550.

Fisher, J. B., D. N. Huntzinger, C. R. Schwalm, and S. Sitch (2014). "Modeling the terrestrial biosphere". *Annual review of environment and resources* 39 (1), 91–123.

Forster, P. M., C. J. Smith, T. Walsh, W. F. Lamb, R. Lamboll, M. Hauser, A. Ribes, D. Rosen, N. Gillett, M. D. Palmer, et al. (2023). "Indicators of Global Climate Change 2022: annual update of large-scale indicators of the state of the climate system and human influence". *Earth System Science Data* 15 (6), 2295–2327.

Friedlingstein, P., M. W. Jones, M. O'Sullivan, R. M. Andrew, D. C. E. Bakker, J. Hauck, C. Le Quéré, G. P. Peters, W. Peters, J. Pongratz, S. Sitch, J. G. Canadell, P. Ciais, R. B. Jackson, S. R. Alin, P. Anthoni, N. R. Bates, M. Becker, N. Bellouin, L. Bopp, T. T. T. Chau, F. Chevallier, L. P. Chini, M. Cronin, K. I. Currie, B. Decharme, L. M. Djeutchouang, X. Dou, W. Evans, R. A. Feely, L. Feng, T. Gasser, D. Gilfillan, T. Gkritzalis, G. Grassi, L. Gregor, N. Gruber, Ö. Gürses, I. Harris, R. A. Houghton, G. C. Hurtt, Y. Iida, T. Ilyina, I. T. Luijkx, A. Jain, S. D. Jones, E. Kato, D. Kennedy, K. Klein Goldewijk, J. Knauer, J. I. Korsbakken, A. Körtzinger, P. Landschützer, S. K. Lauvset, N. Lefèvre, S. Lienert, J. Liu, G. Marland, P. C. McGuire, J. R. Melton, D. R. Munro, J. E. M. S. Nabel, S.-I. Nakaoka, Y. Niwa, T. Ono, D. Pierrot, B. Poulter, G. Rehder, L. Resplandy, E. Robertson, C. Rödenbeck, T. M. Rosan, J. Schwinger, C. Schwingshackl, R. Séférian, A. J. Sutton, C. Sweeney, T. Tanhua, P. P. Tans, H. Tian, B. Tilbrook, F. Tubiello, G. R. van der Werf, N. Vuichard, C. Wada, R. Wanninkhof, A. J. Watson, D. Willis, A. J. Wiltshire, W. Yuan, C. Yue, X. Yue, S. Zaehle, and J. Zeng (2022). "Global Carbon Budget 2021". *Earth System Science Data* 14 (4), 1917–2005. DOI: `10.5194/essd-14-1917-2022`.

Friedlingstein, P., M. O'Sullivan, M. W. Jones, R. M. Andrew, J. Hauck, P. Landschützer, C. Le Quéré, H. Li, I. T. Luijkx, A. Olsen, G. P. Peters, W. Peters, J. Pongratz, C. Schwingshackl, S. Sitch, J. G. Canadell, P. Ciais, R. B. Jackson, S. R. Alin, A. Arneth, V. Arora, N. R. Bates, M. Becker, N. Bellouin, C. F. Berghoff, H. C. Bittig, L. Bopp, P. Cadule, K. Campbell, M. A. Chamberlain, N. Chandra, F. Chevallier, L. P. Chini, T. Colligan, J. Decayeux, L. Djeutchouang, X. Dou, C. Duran Rojas, K. Enyo, W. Evans, A. Fay, R. A. Feely, D. J. Ford, A. Foster, T. Gasser, M. Gehlen, T. Gkritzalis, G. Grassi, L. Gregor, N. Gruber, Ö. Gürses, I. Harris, M. Hefner, J. Heinke, G. C. Hurtt, Y. Iida, T. Ilyina, A. R. Jacobson, A. Jain, T. Jarníková, A. Jersild, F. Jiang, Z. Jin, E. Kato, R. F. Keeling, K. Klein Goldewijk, J. Knauer, J. I. Korsbakken, S. K. Lauvset, N. Lefèvre, Z. Liu, J. Liu, L. Ma, S. Maksyutov, G. Marland, N. Mayot, P. McGuire, N. Metzl, N. M. Monacci, E. J. Morgan, S.-I. Nakaoka, C. Neill, Y. Niwa, T. Nützel, L. Olivier, T. Ono, P. I. Palmer, D. Pierrot, Z. Qin, L. Resplandy,

A. Roobaert, T. M. Rosan, C. Rödenbeck, J. Schwinger, T. L. Smallman, S. Smith, R. Sospedra-Alfonso, T. Steinhoff, Q. Sun, A. J. Sutton, R. Séférian, S. Takao, H. Tatebe, H. Tian, B. Tilbrook, O. Torres, E. Tourigny, H. Tsujino, F. Tubiello, G. van der Werf, R. Wanninkhof, X. Wang, D. Yang, X. Yang, Z. Yu, W. Yuan, X. Yue, S. Zaehle, N. Zeng, and J. Zeng (2024). "Global Carbon Budget 2024". *Earth System Science Data Discussions* 2024, 1–133. DOI: `10.5194/essd-2024-519`.

Friedlingstein, P., M. O'sullivan, M. W. Jones, R. M. Andrew, D. C. Bakker, J. Hauck, P. Landschützer, C. Le Quéré, I. T. Luijkx, G. P. Peters, et al. (2023). "Global carbon budget 2023". *Earth System Science Data* 15 (12), 5301–5369.

Gallagher, M., C. Masiello, W. Hockaday, J. Baldock, S. Snapp, and C. McSwiney (2014). "Controls on the oxidative ratio of net primary production in agricultural ecosystems". *Biogeochemistry* 121, 581–594.

Gallagher, M. E., F. L. Liljestrand, W. C. Hockaday, and C. A. Masiello (2017). "Plant species, not climate, controls aboveground biomass O_2 :CO_2 exchange ratios in deciduous and coniferous ecosystems". *Journal of Geophysical Research: Biogeosciences* 122 (9), 2314–2324. DOI: `10.1002/2017JG003847`.

Gao, Y., T. Markkanen, M. Aurela, I. Mammarella, T. Thum, A. Tsuruta, H. Yang, and T. Aalto (2017). "Response of water use efficiency to summer drought in a boreal Scots pine forest in Finland". *Biogeosciences* 14 (18), 4409–4422.

Gauthier, S., P. Bernier, T. Kuuluvainen, A. Z. Shvidenko, and D. G. Schepaschenko (2015). "Boreal forest health and global change". *Science* 349 (6250), 819–822.

Gerbig, C., J. Lin, S. Wofsy, B. Daube, A. Andrews, B. Stephens, P. Bakwin, and C. Grainger (2003). "Toward constraining regional-scale fluxes of CO_2 with atmospheric observations over a continent: 2. Analysis of COBRA data using a receptor-oriented framework". *Journal of Geophysical Research: Atmospheres* 108 (D24).

Ghashghaie, J., F.-W. Badeck, G. Lanigan, S. Nogués, G. Tcherkez, E. Deléens, G. Cornic, and H. Griffiths (2003). "Carbon isotope fractionation during dark respiration and photorespiration in C 3 plants". *Phytochemistry reviews* 2, 145–161.

Gibelin, A.-L., J.-C. Calvet, and N. Viovy (2008). "Modelling energy and CO_2 fluxes with an interactive vegetation land surface model-Evaluation at high and middle latitudes". *Agricultural and forest meteorology* 148 (10), 1611–1628.

Gibert, F., M. Schmidt, J. Cuesta, P. Ciais, M. Ramonet, I. Xueref, E. Larmanou, and P. H. Flamant (2007). "Retrieval of average CO_2 fluxes by combining in situ CO_2 measurements and backscatter lidar information". *Journal of Geophysical Research: Atmospheres* 112 (D10).

González-Armas, R., D. Rikkers, O. Hartogensis, C. Quaresma Dias-Júnior, S. Komiya, G. Pugliese, J. Williams, H. van Asperen, J. Vilà-Guerau de Arellano, and H. J. de Boer (2025). "Daytime water and CO_2 exchange within and above the Amazon rainforest [Under review]". *Agricultural and Forest Meteorology.*

González-Armas, R., J. Vilà-Guerau de Arellano, M. R. Mangan, O. Hartogensis, and H. De Boer (2024). "Impact of canopy environmental variables on the diurnal dynamics of water and carbon dioxide exchange at leaf and canopy level". *Biogeosciences* 21 (10), 2425–2445.

Goudriaan, J., H. Van Laar, H. Van Keulen, and W. Louwerse (1985). “Photosynthesis, CO_2 and plant production”. In: *Wheat growth and modelling.* Springer, 107–122.

Grassi, G., C. Schwingshackl, T. Gasser, R. A. Houghton, S. Sitch, J. G. Canadell, A. Cescatti, P. Ciais, S. Federici, P. Friedlingstein, et al. (2023). “Harmonising the land-use flux estimates of global models and national inventories for 2000–2020”. *Earth System Science Data* 15 (3), 1093–1114.

Graven, H., R. Keeling, S. Piper, P. Patra, B. Stephens, S. Wofsy, L. Welp, C. Sweeney, P. Tans, J. Kelley, et al. (2013). “Enhanced seasonal exchange of CO_2 by northern ecosystems since 1960”. *Science* 341 (6150), 1085–1089.

Gruber, N., M. Gloor, S.-M. Fan, and J. L. Sarmiento (2001). “Air-sea flux of oxygen estimated from bulk data: Implications for the marine and atmospheric oxygen cycles”. *Global Biogeochemical Cycles* 15 (4), 783–803.

Hari, P., E. Nikinmaa, T. Pohja, E. Siivola, J. Bäck, T. Vesala, and M. Kulmala (2013). “Station for Measuring Ecosystem-Atmosphere Relations: SMEAR”. In: *Physical and Physiological Forest Ecology.* Ed. by P. Hari, K. Heliövaara, and L. Kulmala. Dordrecht: Springer Netherlands, 471–487. DOI: `10.1007/978-94-007-5603-8_9`.

Hauck, J., M. Zeising, C. Le Quéré, N. Gruber, D. C. Bakker, L. Bopp, T. T. T. Chau, Ö. Gürses, T. Ilyina, P. Landschützer, et al. (2020). “Consistency and challenges in the ocean carbon sink estimate for the global carbon budget”. *Frontiers in Marine Science* 7, 571720.

Haugan, P. M. and H. Drange (1996). “Effects of CO_2 on the ocean environment”. *Energy conversion and management* 37 (6-8), 1019–1022.

Haynes, K., I. Baker, A. Denning, R. Stöckli, K. Schaefer, E. Lokupitiya, and J. Haynes (2019). “Representing grasslands using dynamic prognostic phenology based on biological growth stages: 1. Implementation in the Simple Biosphere Model (SiB4)”. *Journal of Advances in Modeling Earth Systems* 11 (12), 4423–4439.

Heerwaarden, C. C. van and A. J. Teuling (2014). “Disentangling the response of forest and grassland energy exchange to heatwaves under idealized land–atmosphere coupling”. *Biogeosciences* 11 (21), 6159–6171.

Heinze, C., S. Meyer, N. Goris, L. Anderson, R. Steinfeldt, N. Chang, C. Le Quere, and D. C. Bakker (2015). “The ocean carbon sink–impacts, vulnerabilities and challenges”. *Earth System Dynamics* 6 (1), 327–358.

Heiskanen, L., J.-P. Tuovinen, H. Vekuri, A. Räsänen, T. Virtanen, S. Juutinen, A. Lohila, J. Mikola, and M. Aurela (2023). “Meteorological responses of carbon dioxide and methane fluxes in the terrestrial and aquatic ecosystems of a subarctic landscape”. *Biogeosciences* 20 (3), 545–572.

Helm, J., R. L. Salomón, B. Hilman, J. Muhr, A. Knohl, K. Steppe, Y. Gibon, C. Cassan, and H. Hartmann (2023). “Differences between tree stem CO_2 efflux and O_2 influx rates cannot be explained by internal CO_2 transport or storage in large beech trees”. *Plant, Cell & Environment* 46 (9), 2680–2693.

Hersbach, H., B. Bell, P. Berrisford, S. Hirahara, A. Horányi, J. Muñoz-Sabater, J. Nicolas, C. Peubey, R. Radu, D. Schepers, et al. (2020). "The ERA5 global reanalysis". *Quarterly Journal of the Royal Meteorological Society* 146 (730), 1999–2049.

Hicks Pries, C., A. Angert, C. Castanha, B. Hilman, and M. S. Torn (2020). "Using respiration quotients to track changing sources of soil respiration seasonally and with experimental warming". *Biogeosciences* 17 (12), 3045–3055.

Hilman, B. and A. Angert (2016). "Measuring the ratio of CO_2 efflux to O_2 influx in tree stem respiration". *Tree Physiology* 36 (11), 1422–1431.

Hilman, B., J. Muhr, J. Helm, I. Kuhlmann, E.-D. Schulze, and S. Trumbore (2021). "The size and the age of the metabolically active carbon in tree roots". *Plant, Cell & Environment* 44 (8), 2522–2535.

Hilman, B., J. Muhr, S. E. Trumbore, N. Kunert, M. S. Carbone, P. Yuval, S. J. Wright, G. Moreno, O. Pérez-Priego, M. Migliavacca, et al. (2019). "Comparison of CO_2 and O_2 fluxes demonstrate retention of respired CO_2 in tree stems from a range of tree species". *Biogeosciences* 16 (1), 177–191.

Hilman, B., T. Weiner, T. Haran, C. A. Masiello, X. Gao, and A. Angert (2022). "The apparent respiratory quotient of soils and tree stems and the processes that control it". *Journal of Geophysical Research: Biogeosciences* 127 (3), e2021JG006676.

Hoch, G., A. Richter, and C. Körner (2003). "Non-structural carbon compounds in temperate forest trees". *Plant, cell & environment* 26 (7), 1067–1081.

Hockaday, W., C. Masiello, J. Randerson, R. Smernik, J. Baldock, O. Chadwick, and J. Harden (2009). "Measurement of soil carbon oxidation state and oxidative ratio by 13C nuclear magnetic resonance". *Journal of Geophysical Research: Biogeosciences* 114 (G2).

Hockaday, W. C., M. E. Gallagher, C. A. Masiello, J. A. Baldock, C. M. Iversen, and R. J. Norby (2015). "Forest soil carbon oxidation state and oxidative ratio responses to elevated CO_2". *Journal of Geophysical Research: Biogeosciences* 120 (9), 1797–1811.

Huang, J., J. Huang, X. Liu, C. Li, L. Ding, and H. Yu (2018). "The global oxygen budget and its future projection". *Science Bulletin* 63 (18), 1180–1186.

Huang, X., R. J. H. Dunn, L. Z. X. Li, T. R. McVicar, C. Azorin-Molina, and Z. Zeng (2023). "Increasing Global Terrestrial Diurnal Temperature Range for 1980–2021". *Geophysical Research Letters* 50 (11), e2023GL103503. DOI: `10.1029/2023GL103503`.

Hulsman, L., L. Mossink, W. Peters, S. Driever, and I. Luijkx (in prep.). "A novel, highly precise method for measuring leaf-level oxygen and carbon dioxide fluxes".

Igamberdiev, A. U., T. N. Mikkelsen, P. Ambus, H. Bauwe, P. J. Lea, and P. Gardeström (2004). "Photorespiration contributes to stomatal regulation and carbon isotope fractionation: a study with barley, potato and Arabidopsis plants deficient in glycine decarboxylase". *Photosynthesis Research* 81, 139–152.

Ishidoya, S., S. Morimoto, S. Aoki, S. Taguchi, D. Goto, S. Murayama, and T. Nakazawa (2012). "Oceanic and terrestrial biospheric CO_2 uptake estimated from atmospheric potential oxygen observed at Ny-Ålesund, Svalbard, and Syowa, Antarctica". *Tellus B: Chemical and Physical Meteorology* 64 (1), 18924.

Ishidoya, S., S. Murayama, H. Kondo, N. Saigusa, A. W. Kishimoto-Mo, and S. Yamamoto (2015). "Observation of O_2:CO_2 exchange ratio for net turbulent fluxes and its application to forest carbon cycles". *Ecological Research* 30 (2), 225–234. DOI: `10.1007/s11284-014-1241-3`.

Ishidoya, S., S. Murayama, C. Takamura, H. Kondo, N. Saigusa, D. Goto, S. Morimoto, N. Aoki, S. Aoki, and T. Nakazawa (2013). " O_2:CO_2 exchange ratios observed in a cool temperate deciduous forest ecosystem of central Japan ". *Tellus B: Chemical and Physical Meteorology* 65 (1), 21120. DOI: `10.3402/tellusb.v65i0.21120`.

Ishidoya, S., H. Sugawara, Y. Terao, N. Kaneyasu, N. Aoki, K. Tsuboi, and H. Kondo (2020). "O_2: CO_2exchange ratio for net turbulent flux observed in an urban area of Tokyo, Japan, and its application to an evaluation of anthropogenic CO_2 emissions". *Atmospheric Chemistry and Physics* 20 (9), 5293–5308.

Ishidoya, S., K. Tsuboi, H. Kondo, K. Ishijima, N. Aoki, H. Matsueda, and K. Saito (2022a). "Measurement report: Method for evaluating CO_2 emission from a cement plant by atmosphere O_2/N_2 and CO_2 measurements and its applicability to the detection of CO_2 capture signals". *Atmospheric Chemistry and Physics Discussions*, 1–26.

Ishidoya, S., K. Tsuboi, Y. Niwa, H. Matsueda, S. Murayama, K. Ishijima, and K. Saito (2022b). "Spatiotemporal variations of the δ (O_2/ N_2), CO_2 and δ (APO) in the troposphere over the western North Pacific". *Atmospheric Chemistry and Physics* 22 (10), 6953–6970.

Jacobs, C., B. Van den Hurk, and H. De Bruin (1996). "Stomatal behaviour and photosynthetic rate of unstressed grapevines in semi-arid conditions". *Agricultural and Forest Meteorology* 80 (2-4), 111–134.

Jarman, P. (1974). "The diffusion of carbon dioxide and water vapour through stomata". *Journal of Experimental Botany* 25 (5), 927–936.

Jin, Y., B. B. Stephens, R. F. Keeling, E. J. Morgan, C. Rödenbeck, P. K. Patra, and M. C. Long (2023). "Seasonal Tropospheric Distribution and Air-Sea Fluxes of Atmospheric Potential Oxygen From Global Airborne Observations". *Global Biogeochemical Cycles* 37 (10), e2023GB007827.

Jones, M. W., R. M. Andrew, G. P. Peters, G. Janssens-Maenhout, A. J. De-Gol, P. Ciais, P. K. Patra, F. Chevallier, and C. Le Quéré (2021). "Gridded fossil CO_2 emissions and related O_2 combustion consistent with national inventories 1959–2018". *Scientific Data* 8 (1), 2.

Jones, M. W., G. P. Peters, T. Gasser, R. M. Andrew, C. Schwingshackl, J. Gütschow, R. A. Houghton, P. Friedlingstein, J. Pongratz, and C. Le Quéré (2023). "National contributions to climate change due to historical emissions of carbon dioxide, methane, and nitrous oxide since 1850". *Scientific Data* 10 (1), 155.

Jürgensen, J., J. Muhr, and A. Knohl (2021). "Variations of the Oxidative Ratio across Ecosystem Components and Seasons in a Managed Temperate Beech Forest (Leinefelde, Germany)". *Forests* 12 (12), 1693.

Kaimal, J. C. and J. J. Finnigan (1994). *Atmospheric boundary layer flows: their structure and measurement.* Oxford university press.

Kaiser, E., J. Kromdijk, J. Harbinson, E. Heuvelink, and L. F. Marcelis (2017). “Photosynthetic induction and its diffusional, carboxylation and electron transport processes as affected by CO_2 partial pressure, temperature, air humidity and blue irradiance”. *Annals of Botany* 119 (1), 191–205.

Kaiser, E., A. Morales, J. Harbinson, J. Kromdijk, E. Heuvelink, and L. F. Marcelis (2015). “Dynamic photosynthesis in different environmental conditions”. *Journal of Experimental Botany* 66 (9), 2415–2426.

Kanani-Sühring, F. and S. Raasch (2015). “Spatial variability of scalar concentrations and fluxes downstream of a clearing-to-forest transition: a large-eddy simulation study”. *Boundary-Layer Meteorology* 155 (1), 1–27.

Keeling, R. F. and A. C. Manning (2014). *Studies of Recent Changes in Atmospheric O_2 Content.* 2nd ed. Vol. 5. Elsevier Ltd., 385–404. DOI: `10.1016/B978-0-08-095975-7.00420-4`.

Keeling, R. (1988). “Development of an Interferometric Oxygen Analyzer for Precise Measurement of the Atmospheric O_2 Mole Fraction.” PhD thesis. Harvard University.

Keeling, R., R. Najjar, M. Bender, and P. Tans (1993). “What atmospheric oxygen measurements can tell us about the global carbon-cycle”. *Global Biogeochemical Cycles* 7, 37–67. DOI: `10.1029/92GB02733`.

Keeling, R. (2024). *Flask O_2/N_2 and flask CO_2 data taken at Mauna Loa Observatory.* url: https://scrippso2.ucsd.edu/data/mlo.html, last accessed: 01-15-2025.

Keeling, R. F. and H. E. Garcia (2002). “The change in oceanic O_2 inventory associated with recent global warming”. *Proceedings of the National Academy of Sciences* 99 (12), 7848–7853.

Keeling, R. F., A. C. Manning, E. M. McEvoy, and S. R. Shertz (1998). “Methods for measuring changes in atmospheric O_2 concentration and their application in southern hemisphere air”. *Journal of Geophysical Research: Atmospheres* 103 (D3), 3381–3397.

Keeling, R. F. and S. R. Shertz (1992). “Seasonal and interannual variations in atmospheric oxygen and implications for the global carbon cycle”. *Nature* 358 (6389), 723–727.

Keeling, R. F., A. C. Manning, W. J. Paplawsky, and A. C. Cox (2007). “On the long-term stability of reference gases for atmospheric O_2/N_2 and CO_2 measurements”. *Tellus B: Chemical and Physical Meteorology* 59 (1), 3–14. DOI: `10.1111/j.1600-0889.2006.00196.x`.

Kirschbaum, M. U. (1995). “The temperature dependence of soil organic matter decomposition, and the effect of global warming on soil organic C storage”. *Soil Biology and biochemistry* 27 (6), 753–760.

Kljun, N., P. Calanca, M. Rotach, and H. P. Schmid (2015). “A simple two-dimensional parameterisation for Flux Footprint Prediction (FFP)”. *Geoscientific Model Development* 8 (11), 3695–3713.

Knohl, A., J. Muhr, M. J. Deventer, E. Blei, J. Braden-Behrens, E. Tunsch, M. Bonazza, P. A. Pickers, D. Nelson, M. Zahniser, et al. (2020). “Measuring oxygen fluxes in a European beech forest-results from the OXYFLUX project”. In: *EGU General Assembly Conference Abstracts*, 18822.

Kohonen, K.-M., R. Dewar, G. Tramontana, A. Mauranen, P. Kolari, L. M. Kooijmans, D. Papale, T. Vesala, and I. Mammarella (2022). "Intercomparison of methods to estimate gross primary production based on CO_2 and COS flux measurements". *Biogeosciences* 19 (17), 4067–4088.

Kooijmans, L. M., A. Cho, J. Ma, A. Kaushik, K. D. Haynes, I. Baker, I. T. Luijkx, M. Groenink, W. Peters, J. B. Miller, et al. (2021). "Evaluation of carbonyl sulfide biosphere exchange in the Simple Biosphere Model (SiB4)". *Biogeosciences* 18 (24), 6547–6565.

Koren, G., L. Schneider, I. R. van der Velde, E. van Schaik, S. S. Gromov, G. A. Adnew, D. J. Mrozek Martino, M. E. Hofmann, M.-C. Liang, S. Mahata, et al. (2019). "Global 3-D Simulations of the Triple Oxygen Isotope Signature Δ17O in Atmospheric CO_2". *Journal of Geophysical Research: Atmospheres* 124 (15), 8808–8836.

Korhonen, J., M. Pihlatie, J. Pumpanen, H. Aaltonen, P. Hari, J. Levula, A.-J. Kieloaho, E. Nikinmaa, T. Vesala, and H. Ilvesniemi (2013). "Nitrogen balance of a boreal Scots pine forest". *Biogeosciences* 10 (2), 1083–1095.

Kowalski, A. S. (2017). "The boundary condition for vertical velocity and its interdependence with surface gas exchange". *Atmospheric Chemistry and Physics* 17 (13), 8177–8187.

Kowalski, A. S., P. Serrano-Ortiz, G. Miranda-García, and G. Fratini (2021). "Disentangling turbulent gas diffusion from non-diffusive transport in the boundary layer". *Boundary-Layer Meteorology* 179, 347–367.

Kozlova, E. A. and A. C. Manning (2009). "Methodology and calibration for continuous measurements of biogeochemical trace gas and O_2 concentrations from a 300-m tall tower in central Siberia". *Atmospheric Measurement Techniques* 2 (1), 205–220. DOI: `10.5194/amt-2-205-2009`.

Kozlova, E. A., A. C. Manning, Y. Kisilyakhov, T. Seifert, and M. Heimann (2008). "Seasonal, synoptic, and diurnal-scale variability of biogeochemical trace gases and O_2 from a 300-m tall tower in central Siberia". *Global Biogeochemical Cycles* 22 (4).

Kretschmer, R., C. Gerbig, U. Karstens, G. Biavati, A. Vermeulen, F. Vogel, S. Hammer, and K. Totsche (2014). "Impact of optimized mixing heights on simulated regional atmospheric transport of CO_2". *Atmospheric Chemistry and Physics* 14 (14), 7149–7172.

Krol, M., S. Houweling, B. Bregman, M. Van den Broek, A. Segers, P. Van Velthoven, W. Peters, F. Dentener, and P. Bergamaschi (2005). "The two-way nested global chemistry-transport zoom model TM5: algorithm and applications". *Atmospheric Chemistry and Physics* 5 (2), 417–432.

Kulmala, L., J. Pumpanen, P. Kolari, S. Dengel, F. Berninger, K. Köster, L. Matkala, A. Vanhatalo, T. Vesala, and J. Bäck (2019). "Inter-and intra-annual dynamics of photosynthesis differ between forest floor vegetation and tree canopy in a subarctic Scots pine stand". *Agricultural and Forest Meteorology* 271, 1–11.

Laan, S. van der, I. T. van der Laan-Luijkx, C. Rödenbeck, A. Varlagin, I. Shironya, R. E. Neubert, M. Ramonet, and H. A. Meijer (2014a). "Atmospheric CO_2, $\delta(O_2/N_2)$, APO and oxidative ratios from aircraft flask samples over Fyodorovskoye, Western Russia". *Atmospheric Environment* 97, 174–181. DOI: `10.1016/j.atmosenv.2014.08.022`.

Laan, S. van der, I. Van der Laan-Luijkx, C. Rödenbeck, A. Varlagin, I. Shironya, R. Neubert, M. Ramonet, and H. Meijer (2014b). "Atmospheric CO_2, δ (O_2/N_2), APO and oxidative ratios from aircraft flask samples over Fyodorovskoye, Western Russia". *Atmospheric environment* 97, 174–181.

Lanigan, G. J., N. Betson, H. Griffiths, and U. Seibt (2008). "Carbon isotope fractionation during photorespiration and carboxylation in Senecio". *Plant Physiology* 148 (4), 2013–2020.

Larson, V. E. and H. Volkmer (2008). "An idealized model of the one-dimensional carbon dioxide rectifier effect". *Tellus B: Chemical and Physical Meteorology* 60 (4), 525–536.

Lasslop, G., M. Reichstein, D. Papale, A. D. Richardson, A. Arneth, A. Barr, P. Stoy, and G. Wohlfahrt (2010). "Separation of net ecosystem exchange into assimilation and respiration using a light response curve approach: critical issues and global evaluation". *Global change biology* 16 (1), 187–208.

Leeuwen, C. van (2015). "Highly precise atmospheric oxygen measurements as a tool to detect leaks of carbon dioxide from Carbon Capture and Storage sites". PhD thesis. University of Groningen.

Leeuwen, C. van and H. A. Meijer (2015). "Detection of CO_2 leaks from carbon capture and storage sites with combined atmospheric CO_2 and O_2 measurements". *International Journal of Greenhouse Gas Control* 41, 194–209. DOI: `10.1016/j.ijggc.2015.07.019`.

Lilly, D. K. (1968a). "Models of cloud-topped mixed layers under s strong inversion". *Quart. J. Roy. Meteorol. Soc.* 94, 292–309.

Lilly, D. K. (1968b). "Models of cloud-topped mixed layers under a strong inversion". *Quarterly Journal of the Royal Meteorological Society* 94 (401), 292–309.

Lin, J., C. Gerbig, S. Wofsy, A. Andrews, B. Daube, K. Davis, and C. Grainger (2003). "A near-field tool for simulating the upstream influence of atmospheric observations: The Stochastic Time-Inverted Lagrangian Transport (STILT) model". *Journal of Geophysical Research: Atmospheres* 108 (D16).

Lindroth, A., J. Holst, M.-L. Linderson, M. Aurela, T. Biermann, M. Heliasz, J. Chi, A. Ibrom, P. Kolari, L. Klemedtsson, et al. (2020). "Effects of drought and meteorological forcing on carbon and water fluxes in Nordic forests during the dry summer of 2018". *Philosophical Transactions of the Royal Society B* 375 (1810), 20190516.

Lindroth, A., F. Lagergren, M. Aurela, B. Bjarnadottir, T. Christensen, E. Dellwik, A. Grelle, A. Ibrom, T. Johansson, H. Lankreijer, et al. (2008). "Leaf area index is the principal scaling parameter for both gross photosynthesis and ecosystem respiration of Northern deciduous and coniferous forests". *Tellus B: Chemical and Physical Meteorology* 60 (2), 129–142.

Liu, X., J. Huang, J. Huang, C. Li, L. Ding, and W. Meng (2020). "Estimation of gridded atmospheric oxygen consumption from 1975 to 2018". *Journal of Meteorological Research* 34 (3), 646–658.

Liu, X., J. Huang, L. Wang, X. Lian, C. Li, L. Ding, Y. Wei, S. Chen, Y. Wang, S. Li, et al. (2023a). ""Urban Respiration" Revealed by Atmospheric O_2 Measurements in an Industrial Metropolis". *Environmental Science & Technology* 57 (6), 2286–2296.

Liu, X., L. Wang, J. Huang, Y. Wang, C. Li, L. Ding, X. Lian, and J. Shi (2023b). “Revealing the Covariation of Atmospheric O_2 and Pollutants in an Industrial Metropolis by Explainable Machine Learning”. *Environmental Science & Technology Letters.*

Lobos-Roco, F., O. Hartogensis, J. Vilà-Guerau de Arellano, A. De La Fuente, R. Muñoz, J. Rutllant, and F. Suárez (2021). “Local evaporation controlled by regional atmospheric circulation in the Altiplano of the Atacama Desert”. *Atmospheric Chemistry and Physics* 21 (11), 9125–9150.

Lueker, T. J., R. F. Keeling, and M. K. Dubey (2001). “The oxygen to carbon dioxide ratios observed in emissions from a wildfire in northern California”. *Geophysical research letters* 28 (12), 2413–2416.

Luyssaert, S., I. Inglima, M. Jung, A. D. Richardson, M. Reichstein, D. Papale, S. Piao, E.-D. Schulze, L. Wingate, G. Matteucci, et al. (2007). “CO_2 balance of boreal, temperate, and tropical forests derived from a global database”. *Global change biology* 13 (12), 2509–2537.

Ma, Y. and H. Liu (2019). “An advanced multiple-layer canopy model in the WRF model with large-eddy simulations to simulate canopy flows and scalar transport under different stability conditions”. *Journal of Advances in Modeling Earth Systems* 11 (7), 2330–2351.

Machta, L. and E. Hughes (1970). “Atmospheric oxygen in 1967 to 1970”. *Science* 168 (3939), 1582–1584.

Manning, A. C. (2001). *Temporal variability of atmospheric oxygen from both continuous measurements and a flask sampling network: Tools for studying the global carbon cycle.* University of California, San Diego.

Manning, A. C. and R. F. Keeling (2006). “Global oceanic and land biotic carbon sinks from the scripps atmospheric oxygen flask sampling network”. *Tellus, Series B: Chemical and Physical Meteorology* 58 (2), 95–116. DOI: `10.1111/j.1600-0889.2006.00175.x`.

Martin, C. L., D. Fitzjarrald, M. Garstang, A. P. Oliveira, S. Greco, and E. Browell (1988). “Structure and growth of the mixing layer over the Amazonian rain forest”. *Journal of Geophysical Research: Atmospheres* 93 (D2), 1361–1375.

Martin, J. G. and P. V. Bolstad (2009). “Variation of soil respiration at three spatial scales: components within measurements, intra-site variation and patterns on the landscape”. *Soil Biology and Biochemistry* 41 (3), 530–543.

Martín-Gómez, V., Y. Ruprich-Robert, E. Tourigny, R. Bernardello, P. Ortega, M. G. Donat, and M. S. Cabré (2023). “Large spread in interannual variance of atmospheric CO_2 concentration across CMIP6 Earth System Models”. *npj Climate and Atmospheric Science* 6 (1), 206.

Masiello, C., M. Gallagher, J. Randerson, R. Deco, and O. Chadwick (2008). “Evaluating two experimental approaches for measuring ecosystem carbon oxidation state and oxidative ratio”. *Journal of Geophysical Research: Biogeosciences* 113 (G3).

Mayer, J. C., A. Bargsten, U. Rummel, F. X. Meixner, and T. Foken (2011). “Distributed Modified Bowen Ratio method for surface layer fluxes of reactive and non-reactive trace gases”. *Agricultural and Forest Meteorology* 151 (6), 655–668. DOI: `10.1016/j.agrformet.2010.10.001`.

McClintock, J. B., R. A. Angus, M. R. Mcdonald, C. D. Amsler, S. A. Catledge, and Y. K. Vohra (2009). “Rapid dissolution of shells of weakly calcified Antarctic benthic macroorganisms indicates high vulnerability to ocean acidification”. *Antarctic Science* 21 (5), 449–456.

McDermitt, D. and R. Loomis (1981). “Elemental composition of biomass and its relation to energy content, growth efficiency, and growth yield”. *Annals of Botany* 48 (3), 275–290.

Meyers, T. P., M. E. Hall, S. E. Lindberg, and K. Kim (1996). “Use of the modified Bowen-ratio technique to measure fluxes of trace gases”. *Atmospheric Environment* 30 (19), 3321–3329.

Miller, J. B. and P. P. Tans (2003). “Calculating isotopic fractionation from atmospheric measurements at various scales”. *Tellus B: Chemical and Physical Meteorology* 55 (2), 207–214.

Molen, M. van der, J. Barten, H. Snellen, W. Peters, and J. Vilà-Guerau de Arellano (2024). *MAQ-Observations v1.0: Loobos.*

Moonen, R. P., G. A. Adnew, O. K. Hartogensis, J. Vilà-Guerau de Arellano, D. J. Bonell Fontas, and T. Röckmann (2023). “Data treatment and corrections for estimating H_2O and CO_2 isotope fluxes from high-frequency observations”. *Atmospheric Measurement Techniques* 16 (23), 5787–5810.

Morgan, E. J., B. B. Stephens, M. C. Long, R. F. Keeling, J. D. Bent, K. McKain, C. Sweeney, M. S. Hoecker-Martínez, and E. A. Kort (2019). “Summertime Atmospheric Boundary Layer Gradients of O_2 and CO_2 over the Southern Ocean”. *Journal of Geophysical Research: Atmospheres* 124 (23), 13439–13456.

Natale, S., L. L. Peralta Ogorek, L. Caracciolo, T. Morosinotto, H. van Amerongen, V. Casolo, O. Pedersen, and A. Nardini (2024). “Net O_2 exchange rates under dark and light conditions across different stem compartments”. *New Phytologist* 243 (1), 72–81.

Nguyen, L. N., H. A. Meijer, C. van Leeuwen, B. A. Kers, H. A. Scheeren, A. E. Jones, N. Brough, T. Barningham, P. A. Pickers, A. C. Manning, et al. (2022). “Two decades of flask observations of atmospheric δ (O_2/N_2), CO_2, and APO at stations Lutjewad (the Netherlands) and Mace Head (Ireland), and 3 years from Halley station (Antarctica)”. *Earth System Science Data* 14 (2), 991–1014.

Ouwersloot, H. G., J. V.-.-G. de Arellano, B. H. van Stratum, M. Krol, and J. Lelieveld (2013). “Quantifying the transport of subcloud layer reactants by shallow cumulus clouds over the Amazon”. *Journal of Geophysical Research: Atmospheres* 118 (23), 13–041.

Ouwersloot, H. G., J. Vilà-Guerau de Arellano, A. C. Nölscher, M. Krol, L. N. Ganzeveld, C. Breitenberger, I. Mammarella, J. Wlliams, and J. Lelieveld (2012a). “Characterization of a boreal convective boundary layer and its impact on atmospheric chemistry during HUMPPAC-COPEC-2010”. *Atmospheric Chemistry and Physics* 12, 9335–9353.

Ouwersloot, H., J. Vilà-Guerau de Arellano, A. Nölscher, M. Krol, L. Ganzeveld, C. Breitenberger, I. Mammarella, J. Williams, and J. Lelieveld (2012b). “Characterization of a boreal convective boundary layer and its impact on atmospheric chemistry during HUMPPA-COPEC-2010”. *Atmospheric Chemistry and Physics* 12 (19), 9335–9353.

Park, S.-W., J.-S. Kug, S.-Y. Jun, S.-J. Jeong, and J.-S. Kim (2021). “Role of cloud feedback in continental warming response to CO_2 physiological forcing”. *Journal of Climate* 34 (22), 8813–8828.

Paulson, C. A. (1970). “The mathematical representation of wind speed and temperature profiles in the unstable atmospheric surface layer”. *Journal of Applied Meteorology and Climatology* 9 (6), 857–861.

Pedruzo-Bagazgoitia, X., E. Patton, A. Moene, H. Ouwersloot, T. Gerken, L. Machado, S. Martin, M. Sörgel, P. Stoy, M. Yamasoe, et al. (2023). “Investigating the Diurnal Radiative, Turbulent, and Biophysical Processes in the Amazonian Canopy-Atmosphere Interface by Combining LES Simulations and Observations”. *Journal of Advances in Modeling Earth Systems* 15 (2), e2022MS003210.

Peralta Ogorek, L. L., E. Pellegrini, and O. Pedersen (2021). “Novel functions of the root barrier to radial oxygen loss–radial diffusion resistance to H2 and water vapour”. *New Phytologist* 231 (4), 1365–1376.

Peters, W., J. Miller, J. Whitaker, A. Denning, A. Hirsch, M. Krol, D. Zupanski, L. Bruhwiler, and P. Tans (2005). “An ensemble data assimilation system to estimate CO_2 surface fluxes from atmospheric trace gas observations”. *Journal of Geophysical Research: Atmospheres* 110 (D24).

Peters, W., A. Bastos, P. Ciais, and A. Vermeulen (2020). “A historical, geographical and ecological perspective on the 2018 European summer drought”. *Philosophical transactions of the royal society B* 375 (1810), 20190505.

Peters, W., I. R. van der Velde, E. Van Schaik, J. B. Miller, P. Ciais, H. F. Duarte, I. T. van der Laan-Luijkx, M. K. van der Molen, M. Scholze, K. Schaefer, et al. (2018). “Increased water-use efficiency and reduced CO_2 uptake by plants during droughts at a continental scale”. *Nature geoscience* 11 (10), 744–748.

Physick, W. and J. Garratt (1995). “Incorporation of a high-roughness lower boundary into a mesoscale model for studies of dry deposition over complex terrain”. *Boundary-Layer Meteorology* 74 (1), 55–71.

Piao, S., X. Wang, K. Wang, X. Li, A. Bastos, J. G. Canadell, P. Ciais, P. Friedlingstein, and S. Sitch (2020). “Interannual variation of terrestrial carbon cycle: Issues and perspectives”. *Global Change Biology* 26 (1), 300–318. DOI: `https://doi.org/10.1111/gcb.14884`.

Pickers, P. A., A. C. Manning, C. Le Quéré, G. L. Forster, I. T. Luijkx, C. Gerbig, L. S. Fleming, and W. T. Sturges (2022). “Novel quantification of regional fossil fuel CO_2 reductions during COVID-19 lockdowns using atmospheric oxygen measurements”. *Science advances* 8 (16), eabl9250.

Pickers, P. A., A. C. Manning, W. T. Sturges, C. Le Quéré, S. E. Mikaloff Fletcher, P. A. Wilson, and A. J. Etchells (2017). “In situ measurements of atmospheric O_2 and CO_2 reveal an unexpected O_2 signal over the tropical Atlantic Ocean”. *Global Biogeochemical Cycles* 31 (8), 1289–1305.

Pino, D., J. Vilà-Guerau de Arellano, W. Peters, J. Schröter, C. van Heerwaarden, and M. Krol (2012). “A conceptual framework to quantify the influence of convective boundary layer development on carbon dioxide mixing ratios”. *Atmospheric Chemistry and Physics* 12 (6), 2969–2985.

Plaxton, W. C. and F. E. Podestá (2006). “The functional organization and control of plant respiration”. *Critical Reviews in Plant Sciences* 25 (2), 159–198.

Popa, M. E., M. Gloor, A. C. Manning, A. Jordan, U. Schultz, F. Haensel, T. Seifert, and M. Heimann (2010). “Measurements of greenhouse gases and related tracers at Bialystok tall tower station in Poland”. *Atmospheric Measurement Techniques* 3 (2), 407–427. DOI: `10.5194/amt-3-407-2010`.

Price, D. T., R. Alfaro, K. Brown, M. Flannigan, R. A. Fleming, E. Hogg, M. Girardin, T. Lakusta, M. Johnston, D. McKenney, et al. (2013). “Anticipating the consequences of climate change for Canada’s boreal forest ecosystems”. *Environmental Reviews* 21 (4), 322–365.

Qu, M., J. Wan, and X. Hao (2014). “Analysis of diurnal air temperature range change in the continental United States”. *Weather and Climate Extremes* 4, 86–95. DOI: `https://doi.org/10.1016/j.wace.2014.05.002`.

Rachmilevitch, S., H. Lambers, and B. Huang (2006). “Root respiratory characteristics associated with plant adaptation to high soil temperature for geothermal and turf-type Agrostis species”. *Journal of Experimental Botany* 57 (3), 623–631.

Randerson, J. T., C. A. Masiello, C. J. Still, T. Rahn, H. Poorter, and C. B. Field (2006). “Is carbon within the global terrestrial biosphere becoming more oxidized? Implications for trends in atmospheric O_2 ”. *Global Change Biology* 12 (2), 260–271. DOI: `10.1111/j.1365-2486.2006.01099.x`.

Rayment, M. and P. Jarvis (2000). “Temporal and spatial variation of soil CO_2 efflux in a Canadian boreal forest”. *Soil Biology and Biochemistry* 32 (1), 35–45.

Reichstein, M., E. Falge, D. Baldocchi, D. Papale, M. Aubinet, P. Berbigier, C. Bernhofer, N. Buchmann, T. Gilmanov, A. Granier, et al. (2005). “On the separation of net ecosystem exchange into assimilation and ecosystem respiration: review and improved algorithm”. *Global change biology* 11 (9), 1424–1439.

Resplandy, L., R. Keeling, Y. Eddebbar, M. Brooks, R. Wang, L. Bopp, M. Long, J. Dunne, W. Koeve, and A. Oschlies (2018). “Quantification of ocean heat uptake from changes in atmospheric O_2 and CO_2 composition”. *Nature* 563 (7729), 105–108.

Restrepo-Coupe, N., H. R. da Rocha, L. R. Hutyra, A. C. da Araujo, L. S. Borma, B. Christoffersen, O. M. Cabral, P. B. de Camargo, F. L. Cardoso, A. C. L. da Costa, et al. (2013). “What drives the seasonality of photosynthesis across the Amazon basin? A cross-site analysis of eddy flux tower measurements from the Brasil flux network”. *Agricultural and Forest Meteorology* 182, 128–144.

Reynolds, O. (1894). “II. On the dynamical theory of incompressible viscous fluids and the determination of the criterion”. *Proceedings of the Royal Society of London* 56 (336-339), 40–45.

Ridder, K. de (2010). “Bulk transfer relations for the roughness sublayer”. *Boundary-Layer Meteorology* 134 (2), 257–267. DOI: `10.1007/s10546-009-9450-y`.

Roberts, C. D., R. Senan, F. Molteni, S. Boussetta, M. Mayer, and S. P. Keeley (2018). “Climate model configurations of the ECMWF Integrated Forecasting System (ECMWF-IFS cycle 43r1) for HighResMIP”. *Geoscientific model development* 11 (9), 3681–3712.

Rödenbeck, C., K. E. Adcock, M. Eritt, M. Gachkivskyi, C. Gerbig, S. Hammer, A. Jordan, R. F. Keeling, I. Levin, F. Maier, et al. (2023). "The suitability of atmospheric oxygen measurements to constrain western European fossil-fuel CO_2 emissions and their trends". *Atmospheric Chemistry and Physics* 23 (24), 15767–15782.

Rödenbeck, C., C. Le Quéré, M. Heimann, and R. F. Keeling (2008). "Interannual variability in oceanic biogeochemical processes inferred by inversion of atmospheric O_2/N_2 and CO_2 data". *Tellus, Series B: Chemical and Physical Meteorology* 60 B (5), 685–705. DOI: `10.1111/j.1600-0889.2008.00375.x`.

Ronda, R., H. De Bruin, and A. Holtslag (2001). "Representation of the canopy conductance in modeling the surface energy budget for low vegetation". *Journal of Applied Meteorology and Climatology* 40 (8), 1431–1444.

Rousseeuw, P. J. and S. Verboven (2002). "Robust estimation in very small samples". *Computational Statistics & Data Analysis* 40 (4), 741–758.

Ryan, M. G. and B. E. Law (2005). "Interpreting, measuring, and modeling soil respiration". *Biogeochemistry* 73, 3–27.

Saglio, P. H. and A. Pradet (1980). "Soluble sugars, respiration, and energy charge during aging of excised maize root tips". *Plant physiology* 66 (3), 516–519.

Santana, R. A., C. Q. Dias-Júnior, J. T. da Silva, J. D. Fuentes, R. S. do Vale, E. G. Alves, R. M. N. dos Santos, and A. O. Manzi (2018). "Air turbulence characteristics at multiple sites in and above the Amazon rainforest canopy". *Agricultural and Forest Meteorology* 260, 41–54.

Schaik, E. van, L. Killaars, N. E. Smith, G. Koren, L. Van Beek, W. Peters, and I. T. van der Laan-Luijkx (2018). "Changes in surface hydrology, soil moisture and gross primary production in the Amazon during the 2015/2016 El Niño". *Philosophical Transactions of the Royal Society B: Biological Sciences* 373 (1760), 20180084.

Schuh, A. E. and A. R. Jacobson (2023). "Uncertainty in parameterized convection remains a key obstacle for estimating surface fluxes of carbon dioxide". *Atmospheric Chemistry and Physics* 23 (11), 6285–6297.

Schulte, R., M. van Zanten, S. Rutledge-Jonker, D. Swart, R. W. Kruit, M. Krol, W. van Pul, and J. V.-G. de Arellano (2021). "Unraveling the diurnal atmospheric ammonia budget of a prototypical convective boundary layer". *Atmospheric Environment* 249, 118153.

Seibt, U., W. A. Brand, M. Heimann, J. Lloyd, J. P. Severinghaus, and L. Wingate (2004). "Observations of $O_2 : CO_2$ exchange ratios during ecosystem gas exchange". *Global Biogeochemical Cycles* 18 (4), 1–18. DOI: `10.1029/2004GB002242`.

Seibt, U., A. Rajabi, H. Griffiths, and J. A. Berry (2008). "Carbon isotopes and water use efficiency: sense and sensitivity". *Oecologia* 155 (3), 441–454. DOI: `10.1007/s00442-007-0932-7`.

Seneviratne, S. I., X. Zhang, M. Adnan, W. Badi, C. Dereczynski, A. D. Luca, S. Ghosh, I. Iskandar, J. Kossin, S. Lewis, et al. (2021). "Weather and climate extreme events in a changing climate".

Severinghaus, J. P. (1995). "Studies of the Terrestrial O_2 and Carbon Cycles in Sand Dune Gases and in Biosphere". PhD thesis. Columbia University, 159.

Shane, M. W., M. D. Cramer, S. Funayama-Noguchi, G. R. Cawthray, A. H. Millar, D. A. Day, and H. Lambers (2004). "Developmental physiology of cluster-root carboxylate synthesis and exudation in harsh hakea. Expression of phospho enol pyruvate carboxylase and the alternative oxidase". *Plant Physiology* 135 (1), 549–560.

Sharma, A. and R. García-Mayoral (2020). "Turbulent flows over dense filament canopies". *Journal of Fluid Mechanics* 888, A2.

Sitch, S., M. O'sullivan, E. Robertson, P. Friedlingstein, C. Albergel, P. Anthoni, A. Arneth, V. K. Arora, A. Bastos, V. Bastrikov, et al. (2024). "Trends and drivers of terrestrial sources and sinks of carbon dioxide: An overview of the TRENDY project". *Global Biogeochemical Cycles* 38 (7), e2024GB008102.

Smith, N. E., L. M. Kooijmans, G. Koren, E. Van Schaik, A. M. Van Der Woude, N. Wanders, M. Ramonet, I. Xueref-Remy, L. Siebicke, G. Manca, et al. (2020). "Spring enhancement and summer reduction in carbon uptake during the 2018 drought in northwestern Europe". *Philosophical Transactions of the Royal Society B* 375 (1810), 20190509.

Steinbach, J., C. Gerbig, C. Rödenbeck, U. Karstens, C. Minejima, and H. Mukai (2011). "The CO_2 release and Oxygen uptake from Fossil Fuel Emission Estimate (COFFEE) dataset: effects from varying oxidative ratios". *Atmospheric Chemistry and Physics* 11 (14), 6855–6870.

Stephens, B. B., R. F. Keeling, and W. J. Paplawsky (2003). "Shipboard measurements of atmospheric oxygen using a vacuum-ultraviolet absorption technique". *Tellus B: Chemical and Physical Meteorology* 55 (4), 857–878.

Stephens, B. B., E. J. Morgan, J. D. Bent, R. F. Keeling, A. S. Watt, S. R. Shertz, and B. C. Daube (2021). "Airborne measurements of oxygen concentration from the surface to the lower stratosphere and pole to pole". *Atmospheric Measurement Techniques* 14 (3), 2543–2574.

Stephens, B. B., P. S. Bakwin, P. P. Tans, R. M. Teclaw, and D. D. Baumann (2007). "Application of a differential fuel-cell analyzer for measuring atmospheric oxygen variations". *Journal of Atmospheric and Oceanic Technology* 24 (1), 82–94. DOI: `10.1175/JTECH1959.1`.

Stephens, B. B., R. F. Keeling, M. Heimann, K. D. Six, R. Murnane, and K. Caldeira (1998). "Testing global ocean carbon cycle models using measurements of atmospheric O_2 and CO_2 concentration". *Global Biogeochemical Cycles* 12 (2), 213–230. DOI: `10.1029/97GB03500`.

Stephens, B. B. (1999). *Field-based atmospheric oxygen measurements and the ocean carbon cycle.* University of California, San Diego.

Sterck, F. J., R. A. Duursma, R. W. Pearcy, F. Valladares, M. Cieslak, and M. Weemstra (2013). "Plasticity influencing the light compensation point offsets the specialization for light niches across shrub species in a tropical forest understorey". *Journal of Ecology* 101 (4), 971–980.

Stratum, B. J. van, J. Vilà-Guerau de Arellano, C. C. van Heerwaarden, and H. G. Ouwersloot (2014). "Subcloud-layer feedbacks driven by the mass flux of shallow cumulus convection over land". *Journal of the Atmospheric Sciences* 71 (3), 881–895.

Stull, R. B. (1988). *An introduction to boundary layer meteorology.* Vol. 13. Springer Science & Business Media.

Sturm, P., M. Leuenberger, and M. Schmidt (2005). “Atmospheric O_2, CO_2 and $\delta^{13}C$ observations from the remote sites Jungfraujoch, Switzerland, and Puy de Dôme, France”. *Geophysical research letters* 32 (17).

Suleau, M., C. Moureaux, D. Dufranne, P. Buysse, B. Bodson, J.-P. Destain, B. Heinesch, A. Debacq, and M. Aubinet (2011). “Respiration of three Belgian crops: partitioning of total ecosystem respiration in its heterotrophic, above-and below-ground autotrophic components”. *Agricultural and Forest Meteorology* 151 (5), 633–643.

Tennekes, H. and A. Driedonks (1981). “Basic entrainment equations for the atmospheric boundary layer”. *Boundary-Layer Meteorology* 20 (4), 515–531.

Tennekes, H. (1973). “A model for the dynamics of the inversion above a convective boundary layer”. *Journal of Atmospheric sciences* 30 (4), 558–567.

Teskey, R. O., A. Saveyn, K. Steppe, and M. A. McGuire (2008). “Origin, fate and significance of CO_2 in tree stems.” *New Phytologist* 177 (1).

Thompson, R., A. Manning, E. Gloor, U. Schultz, T. Seifert, F. Hänsel, A. Jordan, and M. Heimann (2009). “In-situ measurements of oxygen, carbon monoxide and greenhouse gases from Ochsenkopf tall tower in Germany”. *Atmospheric Measurement Techniques* 2 (2), 573–591.

Thompson, R. L., A. C. Manning, D. C. Lowe, and D. C. Weatherburn (2007). “A ship-based methodology for high precision atmospheric oxygen measurements and its application in the Southern Ocean region”. *Tellus B: Chemical and Physical Meteorology* 59 (4), 643–653.

Tohjima, Y. (2000). “Method for measuring changes in the atmospheric O_2/N_2 ratio by a gas chromatograph equipped with a thermal conductivity detector”. *Journal of Geophysical Research: Atmospheres* 105 (D11), 14575–14584.

Tohjima, Y., T. Machida, T. Watai, I. Akama, T. Amari, and Y. Moriwaki (2005). “Preparation of gravimetric standards for measurements of atmospheric oxygen and reevaluation of atmospheric oxygen concentration.” *Journal of Geophysical Research–Atmospheres* 110, D11302. DOI: `10.1029/2004JD005595`.

Tohjima, Y., H. Mukai, T. Machida, Y. Hoshina, and S.-I. Nakaoka (2019). “Global carbon budgets estimated from atmospheric $\delta O_2/N_2$ and CO_2 observations in the western Pacific region over a 15-year period”. *Atmospheric Chemistry and Physics* 19 (14), 9269–9285.

van der Laan-Luijkx, I. T., R. E. Neubert, S. van der Laan, and H. A. Meijer (2010). “Continuous measurements of atmospheric oxygen and carbon dioxide on a North Sea gas platform”. *Atmospheric Measurement Techniques* 3 (1), 113–125. DOI: `10.5194/amt-3-113-2010`.

Van der Laan-Luijkx, I., R. Neubert, S. Van der Laan, and H. Meijer (2010). “Continuous measurements of atmospheric oxygen and carbon dioxide on a North Sea gas platform”. *Atmospheric Measurement Techniques* 3 (1), 113–125.

Van der Velde, I., J. Miller, K. Schaefer, G. Van Der Werf, M. Krol, and W. Peters (2014). “Terrestrial cycling of 13 CO_2 by photosynthesis, respiration, and biomass burning in SiBCASA”. *Biogeosciences* 11 (23), 6553–6571.

Van Der Werf, G. R., J. T. Randerson, L. Giglio, T. T. Van Leeuwen, Y. Chen, B. M. Rogers, M. Mu, M. J. Van Marle, D. C. Morton, G. J. Collatz, et al. (2017). "Global fire emissions estimates during 1997–2016". *Earth System Science Data* 9 (2), 697–720.

Van Der Woude, A. M., R. De Kok, N. Smith, I. T. Luijkx, S. Botía, U. Karstens, L. M. Kooijmans, G. Koren, H. A. Meijer, G.-J. Steeneveld, et al. (2023a). "Near-real-time CO_2 fluxes from CarbonTracker Europe for high-resolution atmospheric modeling". *Earth System Science Data* 15 (2), 579–605.

Van Der Woude, A. M., W. Peters, E. Joetzjer, S. Lafont, G. Koren, P. Ciais, M. Ramonet, Y. Xu, A. Bastos, S. Botía, et al. (2023b). "Temperature extremes of 2022 reduced carbon uptake by forests in Europe". *nature communications* 14 (1), 6218.

Van Diepen, K., J. Goudriaan, J. Vilà-Guerau de Arellano, and H. De Boer (2022). "Comparison of C3 Photosynthetic Responses to Light and CO_2 Predicted by the Leaf Photosynthesis Models of Farquhar et al.(1980) and Goudriaan et al.(1985)". *Journal of Advances in Modeling Earth Systems* 14 (9), e2021MS002976.

Van Leeuwen, T. and G. Van Der Werf (2011). "Spatial and temporal variability in the ratio of trace gases emitted from biomass burning". *Atmospheric Chemistry and Physics* 11 (8), 3611–3629.

Vellinga, O. S., R. J. Dobosy, E. J. Dumas, B. Gioli, J. A. Elbers, and R. W. Hutjes (2013). "Calibration and quality assurance of flux observations from a small research aircraft". *Journal of Atmospheric and Oceanic Technology* 30 (2), 161–181.

Vertegaal, D. (2023). "Global O_2 exchange modelling in TM5 as a proxy for the carbon cycle". MA thesis. Wageningen University.

Vilà-Guerau de Arellano, J., O. K. Hartogensis, H. de Boer, R. Moonen, R. González-Armas, M. Janssens, G. A. Adnew, D. J. Bonell-Fontás, S. Botía, S. P. Jones, H. van Asperen, S. Komiya, V. S. de Feiter, D. Rikkers, S. de Haas, L. A. T. Machado, C. Q. Dias-Junior, G. Giovanelli-Haytzmann, W. I. D. Valenti, R. C. Figueiredo, C. S. Farias, D. H. Hall, A. C. S. Mendonça, F. A. G. da Silva, J. L. M. da Silva, R. Souza, G. Martins, J. N. Miller, W. B. Mol, B. Heusinkveld, C. C. van Heerwaarden, F. A. F. D'Oliveira, R. R. Ferreira, R. A. Gotuzzo, G. Pugliese, J. Williams, A. Ringsdorf, A. Edtbauer, C. A. Quesada, B. T. T. Portela, E. G. Alves, C. Pöhlker, S. Trumbore, J. Lelieveld, and T. Röckmann (2024). "CloudRoots-Amazon22: Integrating clouds with photosynthesis by crossing scales". *Bulletin of the American Meteorological Society*. DOI: `10.1175/BAMS-D-23-0333.1`.

Vilà-Guerau de Arellano, J., X. Wang, X. Pedruzo-Bagazgoitia, M. Sikma, A. Agustí-Panareda, S. Boussetta, G. Balsamo, L. A. T. Machado, T. Biscaro, P. Gentine, S. T. Martin, J. D. Fuentes, and T. Gerken (2020). "Interactions Between the Amazonian Rainforest and Cumuli Clouds: A Large-Eddy Simulation, High-Resolution ECMWF, and Observational Intercomparison Study". *Journal of Advances in Modeling Earth Systems* 12 (7). e2019MS001828 10.1029/2019MS001828. DOI: `https://doi.org/10.1029/2019MS001828`. eprint: `https://agupubs.onlinelibrary.wiley.com/doi/pdf/10.1029/2019MS001828`.

Vilà-Guerau de Arellano, J., B. Gioli, F. Miglietta, H. J. Jonker, H. K. Baltink, R. W. Hutjes, and A. A. Holtslag (2004). "Entrainment process of carbon dioxide in the atmospheric boundary layer". *Journal of Geophysical Research: Atmospheres* 109 (D18).

Vilà-Guerau de Arellano, J., C. C. van Heerwaarden, B. J. H. van Stratum, and K. van den Dries (2015). *Atmospheric Boundary Layer: Integrating Air Chemistry and Land Interactions.* Cambridge University Press.

Vilà-Guerau de Arellano, J., G. Koren, H. G. Ouwersloot, I. van der Velde, T. Röckmann, and J. B. Miller (2019). "Sub-diurnal variability of the carbon dioxide and water vapor isotopologues at the field observational scale". *Agricultural and Forest Meteorology* 275, 114–135.

Vilà-Guerau de Arellano, J., C. C. Van Heerwaarden, and J. Lelieveld (2012). "Modelled suppression of boundary-layer clouds by plants in a CO_2-rich atmosphere". *Nature geoscience* 5 (10), 701–704.

Visser, A. J., L. N. Ganzeveld, I. Goded, M. C. Krol, I. Mammarella, G. Manca, and K. F. Boersma (2021). "Ozone deposition impact assessments for forest canopies require accurate ozone flux partitioning on diurnal timescales". *Atmospheric Chemistry and Physics* 21 (24), 18393–18411.

Von Caemmerer, S. v. and G. D. Farquhar (1981a). "Some relationships between the biochemistry of photosynthesis and the gas exchange of leaves". *Planta* 153, 376–387.

– (1981b). "Some relationships between the biochemistry of photosynthesis and the gas exchange of leaves". *Planta* 153, 376–387.

Wehr, R., J. Munger, J. McManus, D. Nelson, M. Zahniser, E. Davidson, S. Wofsy, and S. Saleska (2016). "Seasonality of temperate forest photosynthesis and daytime respiration". *Nature* 534 (7609), 680–683.

Wehr, R., J. Munger, D. Nelson, J. McManus, M. Zahniser, S. Wofsy, and S. Saleska (2013). "Long-term eddy covariance measurements of the isotopic composition of the ecosystem–atmosphere exchange of CO_2 in a temperate forest". *Agricultural and forest meteorology* 181, 69–84.

Wehr, R. and S. Saleska (2015). "An improved isotopic method for partitioning net ecosystem–atmosphere CO_2 exchange". *Agricultural and Forest Meteorology* 214, 515–531.

Whelan, M. E., S. T. Lennartz, T. E. Gimeno, R. Wehr, G. Wohlfahrt, Y. Wang, L. M. J. Kooijmans, T. W. Hilton, S. Belviso, P. Peylin, R. Commane, W. Sun, H. Chen, L. Kuai, I. Mammarella, K. Maseyk, M. Berkelhammer, K.-F. Li, D. Yakir, A. Zumkehr, Y. Katayama, J. Ogée, F. M. Spielmann, F. Kitz, B. Rastogi, J. Kesselmeier, J. Marshall, K.-M. Erkkilä, L. Wingate, L. K. Meredith, W. He, R. Bunk, T. Launois, T. Vesala, J. A. Schmidt, C. G. Fichot, U. Seibt, S. Saleska, E. S. Saltzman, S. A. Montzka, J. A. Berry, and J. E. Campbell (2018). "Reviews and syntheses: Carbonyl sulfide as a multi-scale tracer for carbon and water cycles". *Biogeosciences* 15 (12), 3625–3657. DOI: `10.5194/bg-15-3625-2018`.

Williams, I., W. Riley, M. Torn, J. Berry, and S. Biraud (2011). "Using boundary layer equilibrium to reduce uncertainties in transport models and CO_2 flux inversions". *Atmospheric Chemistry and Physics* 11 (18), 9631–9641.

Wolf, A., N. Saliendra, K. Akshalov, D. A. Johnson, and E. Laca (2008). "Effects of different eddy covariance correction schemes on energy balance closure and comparisons with the modified Bowen ratio system". *Agricultural and Forest Meteorology* 148 (6-7), 942–952. DOI: `10.1016/j.agrformet.2008.01.005`.

Worrall, F., G. D. Clay, C. A. Masiello, and G. Mynheer (2013). "Estimating the oxidative ratio of the global terrestrial biosphere carbon". *Biogeochemistry* 115 (1-3), 23–32. DOI: `10.1007/s10533-013-9877-6`.

Wu, J., K. Guan, M. Hayek, N. Restrepo-Coupe, K. T. Wiedemann, X. Xu, R. Wehr, B. O. Christoffersen, G. Miao, R. Da Silva, et al. (2017). "Partitioning controls on Amazon forest photosynthesis between environmental and biotic factors at hourly to interannual timescales". *Global Change Biology* 23 (3), 1240–1257.

Yan, Y., A. Klosterhalfen, F. Moyano, M. Cuntz, A. C. Manning, and A. Knohl (2023). "A modeling approach to investigate drivers, variability and uncertainties in O_2 fluxes and O_2: CO_2 exchange ratios in a temperate forest". *Biogeosciences* 20 (19), 4087–4107.

Yi, C., K. J. Davis, P. S. Bakwin, A. S. Denning, N. Zhang, A. Desai, J. C. Lin, and C. Gerbig (2004). "Observed covariance between ecosystem carbon exchange and atmospheric boundary layer dynamics at a site in northern Wisconsin". *Journal of Geophysical Research: Atmospheres* 109 (D8).

Yim, M. H., S. J. Joo, K. Shutou, and K. Nakane (2003). "Spatial variability of soil respiration in a larch plantation: estimation of the number of sampling points required". *Forest Ecology and Management* 175 (1-3), 585–588.

Zhalnina, K., K. B. Louie, Z. Hao, N. Mansoori, U. N. Da Rocha, S. Shi, H. Cho, U. Karaoz, D. Loqué, B. P. Bowen, et al. (2018). "Dynamic root exudate chemistry and microbial substrate preferences drive patterns in rhizosphere microbial community assembly". *Nature microbiology* 3 (4), 470–480.

Acknowledgements

It is often said that doing a PhD is a solo project, like working alone on your own little island. While that description may hold true at times, there were only a few moments when it truly felt that way. For the most part, I was far from alone and I definitely could not have completed this thesis on my own. The support of many different people has guided me through the past four years, and I would like to take this opportunity to thank them. First and foremost, I would like to thank my supervisors, all of whom have supported me tremendously throughout this journey. Without their guidance, this book would not have been possible.

Ingrid, I would like to start with you. You made my PhD journey truly enjoyable, and for that, I am deeply grateful. I genuinely believe that having the right supervisor is one of the most important factors for a successful PhD, and I was incredibly fortunate to have you. You brought a human touch to the entire process, always making sure that my well-being came before the work that needed to be done. I always looked forward to our meetings, which often turned into two-hour conversations, whether we were talking about life, science, or anything in between. You showed me that being a “good scientist” doesn’t mean fitting into a narrow mold, and that lesson has stayed with me. Beyond academia, I also really appreciated the sports we did together, especially the triathlons and the long bike rides. You encouraged me to step outside my comfort zone, both in science and in life, and that has helped me grow in confidence. I’m truly grateful to have had you as my supervisor.

Wouter, although you were less involved throughout my entire PhD process, I always appreciated your input. Your ability to see the bigger picture and continually question the significance of the research was both inspiring and thought-provoking. I learned a great deal from our discussions, particularly about the importance of critical thinking in science and, more specifically, about why we should even be using atmospheric O_2 in the first place.

Jordi, although you officially became part of my PhD team only a few months ago, you were unofficially already involved in my thesis from the very beginning. Your enthusiasm for science has always been infectious, and your genuine care for others and their well-being is truly admirable. I always enjoyed our meetings. Your ability to quickly recognize the unique and innovative aspects of the research, and your excitement about them, never failed to impress me. As a result, I consistently left our conversations feeling more confident than when they began. I also want to thank you for introducing me to Ingrid during my MSc and for encouraging me to do my thesis with her. Without that, I don't think I would have ever pursued a PhD.

In addition to my supervisors, there were several others with whom I could discuss the "O_2" topic. It all began with a small group in Groningen: Harro, Linh, and Bert. It was truly enjoyable to meet with you and have the opportunity to explore this topic together. It helped me feel less isolated in this research area, where only a handful of people worldwide are working on similar questions. Especially since we always seemed to arrive at the same conclusion: *"O_2 is more complicated than we thought…"*. Lucas, Katja, and Lois, you joined later in my PhD, and I greatly valued our O_2 meetings. Your insights were always incredibly helpful. Finally, the O_2 team wouldn't be complete without Andrew, Penelope, Karina, and Anh. Our discussions about my O_2 work and calculating with ratios kept me on my toes, and I truly appreciated the exchange. It was always a pleasure to be surrounded by people with whom we could not only tackle the shared challenge of O_2, but also talk about our mutual love of cats.

The O_2 topic would be incomplete without considering the carbon cycle, and the same can be said for the carbon cycle group. Anne-Wil, Ara, Auke, Daan, Firmin, Ida, Joram, Marnix, Peiyi, Peter, Remco, Ruben and Xiaoting, thank you all for the great Tuesday meetings we've had over the years. Although your work didn't always align directly with my own research, I really appreciated these breaks and the opportunity to hear about what you were all working on. The meetings, especially in the early days of my PhD during COVID, were invaluable for staying connected with familiar faces and having some much-needed human interaction. Furthermore, Chapter 6 of this thesis would not have come together, or even been completed, without all of your help. Your insightful contributions on setting up models and running transport models for me were crucial and deeply appreciated.

I would also like to thank all my colleagues at MAQ. It has been a truly enjoyable and supportive environment to work in. I appreciated the ease with which we could collaborate, or simply take a coffee break together and chat about life. The various sporting activities we did as a group helped me tremendously throughout my PhD. The morning swims, Monday runs, and even the 250 km bike ride were not only fun but also helped me stay sane. I especially want to thank all my office mates over the years: Christoph, Esther, Farhan, Martin, Mary Rose, Menno, Raquel, Ruben, Sjoerd, Thomas, and Wouter. I'm not great at working from home, so being greeted by friendly faces in the morning made a big difference and was always something I appreciated deeply.

Beyond my colleagues, there were many others who helped me maintain a healthy work-life balance. To the Boorwurmpjes, thank you for always being up for fun activities, whether it was crafting, mudflat walking or simply relaxing in the sauna. To the Supersukkols, high school feels like a lifetime ago, and although we've all moved to different places, I really appreciate our catch-up talks and seeing where life has taken each of you. Maaike, I enjoyed the step classes and outdoor sports sessions we did at the beginning of my PhD. It was always fun to reflect on our weeks together. Elise, thank you for your great company and for the conversations about our shared experiences as PhD students. I'm also grateful you introduced me to bouldering. And finally, Jochem, Renkse, Bart and Marlieke, thank you for introducing me to a hobby outside of sports. Playing D&D on Friday nights was always a joy. It pushed me out of my comfort zone and helped me clear my mind.

Harro and Judith, the past few years have been a rollercoaster, and I'm so glad we got to experience them together. Our Friday nights were always a welcome constant, something to look forward to and rely on. I especially appreciated having that human connection during the COVID period, as well as the evenings when we could talk about science and life. I'm truly grateful to have such close friends to share life with, and I sincerely hope that continues, even as we now live in different countries.

Finally, I would like to thank my family. Even if you didn't always fully understand what I was working on, your constant encouragement and belief in me meant a great deal.

Christoph, I couldn't have made it through this PhD without your support. You are truly my *"rots in de branding"*, and you helped me through the most stressful moments. You always knew how to calm my anxious, overthinking mind. You are my safe haven, and I'm so happy to see where the future will take us together.

SENSE

Netherlands Research School for the
Socio-Economic and Natural Sciences of the Environment

DIPLOMA

for specialised PhD training

The Netherlands research school for the
Socio-Economic and Natural Sciences of the Environment
(SENSE) declares that

Kim Anna Petronella Faassen

born on 28 November 1996 in Beesel, The Netherlands

has successfully fulfilled all requirements of the
educational PhD programme of SENSE.

Wageningen, 08 July 2025

SENSE coordinator PhD education

Dr Ir Peter Vermeulen

The SENSE Director

Dr Jampel Dell'Angelo

The SENSE Research School declares that **Kim Anna Petronella Faassen** has successfully fulfilled all requirements of the educational PhD programme of SENSE with a work load of 40.2 EC, including the following activities:

SENSE PhD Courses

- Environmental research in context (2021)
- Research in context activity: ‘Organizing land atmosphere interaction meetings’ (2022)

Other PhD and Advanced MSc Courses

- Code refinery workshop, Nordic e-Infrastructure Collaboration (2021)
- Challenges in measurement and interpretation of greenhouse gas concentrations and fluxes, ICOS (2021)
- Scientific writing, Wageningen Graduate Schools (2021)
- New Advances in Land Carbon Cycle Modelling, North Arizona University (2022)
- Supervising BSc and MSc thesis students, Wageningen University (2023)
- Big data analysis and object-oriented programming with python, WIMEK (2023)

Management and Didactic Skills Training

- Supervising two BSc student with thesis entitled ‘Comparison of Boundary Layer Characteristics between radiosonde measurements and LES output for modelling CO$_2$ concentrations in Hyytiäla, Finland’ (2022) and ‘No reduction in carbon uptake during the 2018 drought in a boreal forest in Finland’(2022)
- Supervising MSc student with thesis entitled ‘Global O2 exchange modelling in TM5 as a proxy for the carbon cycle’ (2023)
- Teaching assistant in the BSc course ‘Meteorology and Climate’ (2021-2023)
- Teaching in the MSc course ‘Interdisciplinary Topics in Earth and Environment’ (2021-2023)

Selection of Oral Presentations

- *Using atmospheric O$_2$ to better understand the carbon cycle*. NACgeo, 5- 6 September 2022, Utrecht, The Netherlands
- *How to determine O$_2$ and CO$_2$ fluxes together with their ER above a forest*. GGMT, 19 – 21 September 2022, Wageningen, The Netherlands
- *The diurnal cycle of O$_2$ above a forest*. WAO4 workshop, 23- 25 August 2023, Brunswick, United States of America
- *Variability of the net exchange of O$_2$ and CO$_2$ of the biosphere*, ICOS science conference, 10- 12 September 2024, Versailles, France

The presented research was financially supported by funding from the Meteorology and Air Quality Department at Wageningen University. The measurement campaigns in Hyytiälä, Finland were support by a Veni grant awarded to dr. I.T. Luijkx by the Netherlands Organisation for Scientific Research (grant no. 016.Veni.171.095).

Cover design by Kim Faassen